From Terahertz to X-ray:
Excitations in two-dimensional Materials

vorgelegt von

M. Sc.

Dominik Christiansen

an der Fakultät II – Mathematik und Naturwissenschaften

der Technischen Universität Berlin

zur Erlangung des akademischen Grades

Doktor der Naturwissenschaften

- Dr. rer. nat. -

genehmigte Dissertation

Promotionsausschuss:

Vorsitzende: Prof. Dr. Birgit Kanngießer

1. Gutachter: Prof. Dr. Andreas Knorr

2. Gutachter: Prof. Dr. Torsten Meier

Tag der wissenschaftlichen Aussprache: 10. Dezember 2021

Berlin, 2022

Für Papa und Mama

Abstract

The recent rise of two-dimensional materials attracted a tremendous amount of interest in the fields of photonics and optoelectronics, as they are promising candidates for next-generation devices. Materials, which are under extensive investigation, are graphene and monolayer transition-metal dichalcogenides (TMDC). While graphene is a semi-metal, certain monolayer TMDCs are semiconductors exhibiting tightly bound electron-hole pairs – excitons, which dominate their optical response to a large extent. The light-matter interaction of two-dimensional materials composes the footing of their excitation dynamics. This incorporates the excitation of excitons in the visible range of the electromagnetic spectrum. Because of exciton-phonon interaction a subsequent transfer from optically excited coherent to incoherent excitons occurs. For molybdenum-based TMDCs calculations and optical experiments suggest that the excitons at the optical active $K_{\pm}$ points form the global minimum. In contrast, for tungsten-based TMDCs it seems that momentum-indirect dark excitons with electron and hole at different valleys in the Brillouin zone are the energetically lowest lying states. Time and angle resolved photoemission spectroscopy (tr-ARPES) is a method to measure the ultrafast electron dynamics directly in momentum space. In case that tr-ARPES is also able to access Coulomb-correlated two-particle states this experimental method might be the smoking gun to proof the presence of the momentum-indirect states. In this thesis, we develop a microscopic description of the temporal dynamics of excitonic time and angle resolved photoemission spectroscopy with the focus on phonon-mediated relaxation of optically excited excitons. We show that tr-ARPES is able to access excitons and quantify the spectroscopic signatures of coherent and incoherent excitons in tr-ARPES. Additionally, we suggest coherent pump Fourier transform ARPES to measure the exciton coherence lifetime with great accuracy. Here, we combine a coherent tr-ARPES experiment with a second pump pulse and investigate the tr-ARPES signal as function of the time delay to the second pump pulse.

Moreover, van der Waals materials enable the construction of heterostructures of different atomically-thin materials. Here, after excitation of the distinct materials different interfacial energy and charge transfer mechanisms occur. In particular, we investigate a WSe_2-graphene stack and study the coupling mechanisms of Förster, Dexter, and phonon-assisted tunneling. In addition, we propose a new energy transfer mechanism: interlayer Meitner-Auger energy transfer. Here, a non-radiative exciton recombination leads to intraband transitions in graphene and therefore to a hot hole distribution deep in the valence band.

Besides intralayer excitons, van der Waals heterostructures exhibit also interlayer excitons, where electron and hole are in different materials. We propose that interlayer excitons in certain hybrid inorganic/organic systems might form a new many-body excitonic ground state. Therefore, semiconductors functionalized by organic molecules might be the ideal candidate for the experimental realization of the elusive excitonic insulator. Using a proper description for the new many-body ground state based on a Bogoliubov description, we calculate the excitonic phase diagram of a WS_2-F6TCNNQ stack as function of the relevant experimental parameters band gap (tunable by applied voltage), temperature, and dielectric environment. We show that all excitonic phases, namely semi-metal, semiconductor, and excitonic insulator have unique optical signatures in the far-infrared to terahertz (THz) regime.

Besides monolayer TMDC excitons excited by visible wavelengths and intraexcitonic transitions, present in excitonic insulators, and excited by long wavelength radiation, also core electrons can be excited by X-ray radiation. X-ray absorption spectroscopy is divided into X-ray absorption near edge spectroscopy (XANES) and extended X-ray absorption fine structure spectroscopy (EXAFS). The former constitute transitions of core electrons into

unoccupied conduction band states and is typically described by Fermi's golden rule. The latter accounts for ionization of core electrons from the material and is typically described in a high-order multiple-scattering theory. Here, we aim for a consistent description of both processes within a Maxwell coupled spatio-temporal Bloch formalism. Within this formalism we describe the polarization dependence of core transitions, the radiative and Meitner-Auger recombination channels of core electrons and give microscopic insights into the spectral signatures observed in EXAFS beyond point scattering theory. Moreover, the correct inclusion of the Bloch character of solid state core electrons allows us to assign so far uninterpreted features in the Fourier transformed EXAFS spectrum of graphene.

Deutsche Zusammenfassung

Die Möglichkeit der Herstellung vielfältiger zweidimensionaler Materialien hat enormes Interesse in den Feldern der Photonik und Optoelektronik hervorgerufen. Materialien, welche unter großflächiger Untersuchung stehen, sind Graphen und Übergangsmetall-Dichalgenoide (TMDC). Während Graphen ein Semimetall ist, besitzen halbleitende TMDCs Exzitonen mit sehr großen Bindungsenergien, welche die optischen Eigenschaften des Materials bestimmen. Diese Exzitonen werden im sichtbaren Bereich des elektromagnetischen Spektrum angeregt. Folgende Exziton-Phonon Wechselwirkung führt zu einem Transfer von optisch induzierten kohärenten zu inkohärenten Exzitonen. Für molybdänbasierte TMDCs legen Rechnungen und optische Experimente nahe, dass Exzitonen an den optisch aktiven $K_\pm$ Punkten das globale Minimum bilden. Im Gegensatz scheinen in wolframbasierten TMDC impulsindirekte Exzitonen mit Elektron und Loch an verschiedenen Orten in der Brillouin Zone das energetische Minimum zu bilden. Zeit und Winkel aufgelöste Photoemissionsspektroskopie (tr-ARPES) ist eine Methode um die ultraschnelle Dynamik von Elektronen direkt im Impulsraum zu messen. Im Falle, dass tr-ARPES auch Coulomb-korrelierte Zweiteilchenzustände abbilden könnte, würde dieses Verfahren den unwiederlegbaren Beweis für die Präsenz dieser Zustände geben. Wir entwickeln daher eine mikroskopische Beschreibung von impuls- und energieaufgelöster exzitonischer Photoemission und berücksichtigen dabei die phononvermittelte Relaxation von optisch induzierten Exzitonen. Wir zeigen, dass tr-ARPES in der Tat Exzitonen direkt abbilden kann und quantifizierten die spektroskopischen Signaturen von kohärenten und inkohärenten Exzitonen im tr-ARPES. Außerdem schlagen wir vor mittels kohärentem Pump fouriertransformiertem ARPES die Exzitonkohärenzlebenszeit mit großer Genauigkeit zu messen. Hierbei kombinieren wir ein kohärentes ARPES mit einem zweiten Pumppuls und betrachten das ARPES signal als Funktion der Zeitverschiebung zu dem zweiten Pumppuls.

Einen Vorteil den van der Waals Materialien haben, ist dass sie zu Heterostrukturen gestapelt werden können. Nach der optischen Anregung der konstituierenden Materialien kommt es zu Energie- und Teilchentransfer zwischen den Materiallagen. Wir untersuchen im speziellen eine WSe_2-Graphen Heterostruktur und berechnen den Förster, Dexter und phononassistierten Tunnel zwischen den Lagen. Weiterhin schlagen wir einen neuen Energietransfermechanismus vor: Den Interlagen Meitner-Auger Energietransfer. Hier rekombiniert ein TMDC Exziton nichtradiativ und regt Intrabandübergänge im Graphen an. Dies führt zu heißen Lochverteilungen im Graphen.

Neben Intralagenexzitonen gibt es in Heterostrukturen auch Interlagenexzitonen. Hier sind Elektron und Loch in verschiedenen Materialien. Wir schlagen vor, dass Interlagenexzitonen in gewissen Hybridstrukturen aus inorganischem Halbleiter und organischen Molekülen einen neuen exzitonischen Vielteilchengrundzustand bilden könnten. Damit sind diese Hybridstrukturen der ideale Kandidat für die experimentelle Realisierung eines exzitonischen Insulators. Wir verwenden eine angemessene Beschreibung des Vielteilchengrundzustandes mittels eines Bogoliubovformalismuses und berechnen das exzitonische Phasendiagramm einer WS_2-F6TCNNQ Heterostruktur als Funktion der experimentell relevanten Parameter Bandlücke (verstellbar durch ein angelegtes elektrisches Feld), Temperatur und dielektrischer Umgebung. Wir zeigen, dass alle exzitonischen Phasen, nämlich Semimetall, Halbleiter und exzitonischer Insulator, einzigartige optische Signaturen im Infrarot- bis Terahertzbereich aufweisen.

Neben einzellagen TMDC-Exzitonen, anregbar mit sichtbaren Wellenlängen, und Interlagenexzitonen, ansprechbar mit langwelliger Strahlung, können auch Kernelektronen mittels Röntgenstrahlung angeregt werden. Röntgenabsorptionsspektroskopie is unterteilt in

Röntgenabsorption nahe der Kante (XANES) und erweiterter Röntgenabsorptionsfeinstruktur-spektroskopie (EXAFS). Ersteres besteht aus Kernelektronübergängen in unbesetzte Leitungs-bandzustände und wird üblicherweise mittels Fermi's goldener Regel beschrieben. Letzteres betrachtet die Ionisierung von Kernelektronen in das Vakuum und wird in einer Multistreutheo-rie höherer Ordnung beschrieben. Wir zielen in dieser Arbeit darauf ab eine gemeinsame Beschreibung beider Prozesse zu geben. Dafür nutzen wir einen gekoppelten Formalismus aus den Maxwell Gleichungen und zeit- und raumaufgelösten Blochgleichungen. In diesem Formal-ismus beschreiben wir die Polarisationsabhängigkeit von Kernübergängen, die radiativen und Meitner-Auger Rekombinationskanäle von Kernelektronen und geben mikroskopische Einblicke in die spektroskopischen Signaturen von EXAFS über Punktstreutheorie hinaus. Darüber hinaus ermöglicht uns die korrekte Berücksichtigung des Blochcharakters von Kernelektronem im Festkörper bisher uninterpretierte Signaturen im fouriertransformiertem EXAFS von Graphen zu bestimmen.

Publications

- **D. Christiansen**, M. Selig, G. Berghäuser, R. Schmidt, I. Niehues, R. Schneider, A. Arora, S. M. de Vasconcellos, R. Bratschitsch, E. Malic, A. Knorr. *Phonon sidebands in monolayer transition metal dichalcogenides*, Phys. Rev. Lett. **119**, 187402 (2017)

- E. Malic, M. Selig, M. Feierabend, S. Brem, **D. Christiansen**, F. Wendler, A. Knorr, G. Berghäuser. *Dark excitons in transition metal dichalcogenides*, Phys. Rev. Mat. **2**, 014002 (2018) (Top 10 most cited PRM articles 2017-2019 and 2018-2020)

- I. Niehues, R. Schmidt, M. Drüppel, P. Marauhn, **D. Christiansen**, M. Selig, G. Berghäuser, D. Wigger, R. Schneider, L. Braasch, R. Koch, A. Castellanos-Gomez, T. Kuhn, A. Knorr, E. Malic, M. Rohlfing, S. M. de Vasconcellos, R. Bratschitsch. *Strain control of exciton–phonon coupling in atomically thin semiconductors*, Nano Lett. **18**, 1751 (2018)

- **D. Christiansen**, M. Selig, E. Malic, R. Ernstorfer, A. Knorr. *Theory of exciton dynamics in time-resolved ARPES: Intra-and intervalley scattering in two-dimensional semiconductors*, Phys. Rev. B **100**, 205401 (2019) (Editors suggestion)

- S. Brem, A. Ekman, **D. Christiansen**, F. Katsch, M. Selig, C. Robert, X. Marie, B. Urbaszek, A. Knorr, E. Malic. *Phonon-assisted photoluminescence from indirect excitons in monolayers of transition-metal dichalcogenides*, Nano Lett. **20**, 2849 (2020)

- F. Katsch, **D. Christiansen**, R. Schmidt, S. M. de Vasconcellos, R. Bratschitsch, A. Knorr, M. Selig. *Theory of the coherent response of magneto-excitons and magneto-biexcitons in monolayer transition metal dichalcogenides*, Phys. Rev. B **102**, 115420 (2020)

- S. Dong, M. Puppin, T. Pincelli, S. Beaulieu, **D. Christiansen**, H. Hübener, C. W. Nicholson, R. P. Xian, M. Dendzik, Y. Deng, Y. W. Windsor, M. Selig, E. Malic, A. Rubio, A. Knorr, M. Wolf, L. Rettig, R. Ernstorfer. *Direct measurement of key exciton properties: Energy, dynamics, and spatial distribution of the wave function*, Nat. Sci. **1**, e10010 (2021).

- S. Dong, S. Beaulieu, M. Selig, P. Rosenzweig, **D. Christiansen**, T. Pincelli, M. Dendzik, J. D. Ziegler, J. Maklar, R. P. Xian, A. Neef, A. Mohammed, A. Schulz, M. Stadler, M. Jetter, P. Michler, T. Taniguchi, K. Watanabe, H. Takagi, U. Starke, A. Chernikov, M. Wolf, H. Nakamura, A. Knorr, L. Rettig, R. Ernstorfer. *Observation of ultrafast interfacial Meitner-Auger energy transfer in a van der Waals heterostructure*, under review (2021); arXiv preprint: 2108.06803.

- **D. Christiansen**, M. Selig, J. Biegert, A. Knorr. *Theory of X-ray absorption spectroscopy: a microscopic Bloch equation approach for two-dimensional solid states*, under

review (2021).

- **D. Christiansen**, M. Selig, M. Rossi, A. Knorr. *Excitonic insulator states in molecular functionalized atomically-thin semiconductors*, under review (2021); arXiv preprint: 2112.03135.

Proceedings

- **D. Christiansen**, F. Katsch, A. Knorr, M. Selig. *Exciton dynamics in atomically thin semiconductors: optical lineshape, intervalley coupling, and luminescence dynamics*, Proc. SPIE **10916**, 109160B (2019)

Contents

Chapter 1

Introduction

In 1959 Richard Feynman asked in his famous lecture „There's plenty of room at the bottom": „*What could we do with layered structures with just the right layers?*" [1]. Since the synthesis of graphene [2], the monolayer limit of graphite, in 2004 a new branch of solid state physics and material science opened investigating exactly the answers to this question.

Quickly after the discovery of graphene many other layered materials were found and reduced to their monolayer limit as was previously done for graphene. A very prominent family, which attracted keen attention over the last decade, are monolayer transition-metal dichalcogenides (TMDC) [3, 4]. It turned out that, when going from bulk to monolayer, semiconducting TMDCs undergo an indirect to direct band gap transition at the edges of the Brillouin zone, namely the K_+ and K_- points [5–7]. Because of the two-dimensionality of the material, monolayer TMDCs exhibit a low dielectric environment screening leading to exceptionally strongly bound electron-hole pairs or excitons with binding energies of hundreds of meV [8–10]. At the same time, the material exhibits a strong light-matter interaction that excitons can absorb about 10% of the irradiated light in the visible range of the electromagnetic spectrum [3, 4, 11]. This makes the material of special interest for optoelectronic applications. Interestingly, monolayer TMDCs have even more fascinating properties. Their strong spin-orbit interaction [12, 13] leads to splitting of the optical transition at the $K_\pm$ points into A and B exciton transition. A time-reversal symmetry leads to the fact that the K_+ and K_- point are non-equivalent causing opposite spins in the energetically same bands at both high symmetry points [12, 14]. Paired with a valley selective circular dichroism [15–17] this gives rise to interesting spin-valley exciton physics [12, 18, 19].

This work investigates optical excitations of two-dimensional materials such as monolayer TMDCs from low-energy light as terahertz up to high-energy X-ray radiation. Figure 1.1 draws the examined part of the electromagnetic spectrum with investigated scenarios. The excitation energy of optically bright excitons at the $K_\pm$ points corresponds to red light. Moreover, the complex quasi-particle band structure of monolayer TMDCs with different side valleys influences the excitonic properties of the optically injected excitons at the $K_\pm$ points. These side valleys can lead to momentum-indirect excitons, where electron and hole are at different points in the Brillouin zone, and are of extensive discussion in the literature [20–25]. Here, we aim to finally end the discussion about momentum-indirect excitons by combining the theoretically expected exciton dynamics of monolayer TMDCs with an excitonic theory for time and angle resolved photoemission spectroscopy (tr-ARPES). Tr-ARPES is a spectroscopic technique, which possesses time, momentum, and energy resolution and enables direct access to the single-particle Brillouin zone [26]. Here, electrons are photoemitted from the sample with extreme ultraviolet light, cf. Fig. 1.1. If tr-ARPES has also access to bound two-particle

WS$_2$-F6TCNNQ
intraexcitonic
transition

WSe$_2$ exciton
formation

WSe$_2$
free electron-hole
pair formation

Exciton ionization

Graphene core
transition

Graphene core
ionization

0.1eV 2 eV 3 eV 20 eV 300 eV 500 eV

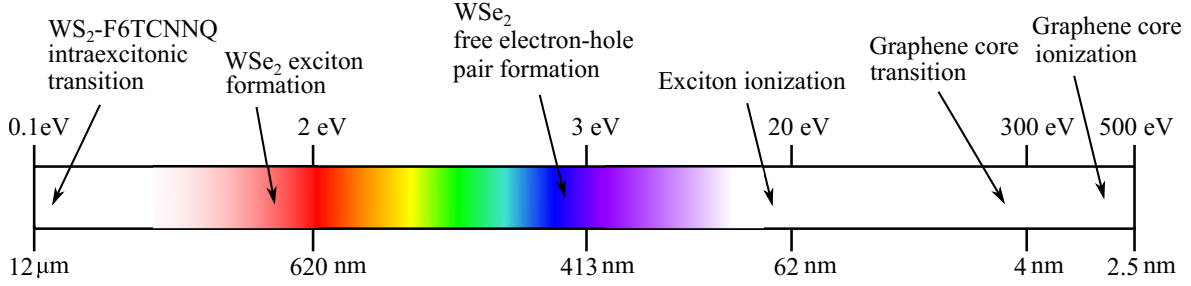12 µm 620 nm 413 nm 62 nm 4 nm 2.5 nm

Figure 1.1: Investigated part of the electromagnetic spectrum with studied optical excitations. Low-energy light excites intraexcitonic transitions, in the visible range of the electromagnetic spectrum we find exciton and free electron-hole pair formation, and high-energy light induces exciton and core electron ionization. All those scenarios are discussed in the following chapters.

states not only the existence of momentum-indirect excitons can be proven but it will also trigger new experiments and boost the understanding of exciton physics in monolayer TMDCs and other two-dimensional materials.

An advantage of layered materials is that they can be combined and stacked in desired way forming van der Waals heterostructures with totally different properties than their single-layer parts [27–30]. A promising heterostructure are TMDC and graphene stacks since they combine strongly bound excitons and their high light-matter interaction with the high carrier mobility of graphene [31–33]. Therefore, we investigate the different possible interfacial energy and charge transfer mechanisms coupling the two layers. We study in detail Förster and Dexter energy transfer, phonon-assisted tunneling of electrons and holes and find a new energy transfer mechanism, which we term as interlayer Meitner-Auger energy transfer.

A different type of heterostructure are hybrid inorganic/organic systems (HIOS). Here, an inorganic semiconductor is functionalized by a layer of self-assemble organic molecules. Such heterostructures are a grand hope in device research [34–36]. We predict that they are the ideal candidate to form a new phase of matter, namely the excitonic insulator [37]. This intriguing phase was first predicted in the 1960's and since then searched. The phase is characterized by spontaneous formation of excitons since their binding energy exceeds the single-particle band gap. Although spectroscopic signatures were observed over the time [38, 39] compelling evidence are still missing. With the appearance of monolayer TMDCs with exciton binding energy of hundreds of meV and the possibility to built van der Waals heterostructures the interest in the excitonic insulator skyrised in recent years [40–42]. We investigate in detail the heterostructure WS$_2$-F6TCNNQ, which we predict to have a many-body ground state of excitonic nature. The fundamental excitations are addressed by far-infrared to terahertz wavelengths, which correspond to intraexcitonic transitions, cf. Fig. 1.1.

The last part of the thesis puts a larger emphasis on a proper theoretical description of the spectroscopic technique of X-ray absorption spectroscopy (XAS). X-ray absorption spectroscopy is a technique, which played an important role at the beginning of the 20th century in the establishment of the atomic energy level model [43, 44] and the discovery of rare-earth elements [45]. XAS is situated at the opposite end of the electromagnetic spectrum, cf. Fig. 1.1, and uses X-ray light of several hundred up to thousands of eV to probe the core electrons of the investigated material. Core electronic transitions in the material (atom, molecule, or crystalline solid) constitute the X-ray absorption near edge spectroscopy (XANES) and is comparable to typical absorption experiments but involving core electrons. When

the core electrons are photoemitted from the sample we talk of extended X-ray absorption fine structure (EXAFS). In case of molecules or solids here the absorption cross section is modulated by oscillations [46–49]. First theoretical attempts to explain this phenomenon were performed in 1931 and 1932 by R. de L. Kronig [50, 51]. But it took further 40 years to relate these oscillation with the local geometry of the irradiated material. This breakthrough, achieved by D. E. Sayers and coworkers [52, 53], promoted XAS from a spectroscopic to a structural technique and gave a rebirth to XAS experiments. Within a point scattering theory D. E. Sayers *et. al.* interpret the oscillation as interferences of scattered X-ray waves. However, the derived formalism, which is the standard of EXAFS analysis nowadays, does not fulfill the Bloch theorem. Although this might be appropriate for the analysis of molecules, for crystalline solids the basis functions need to satisfy the Bloch theorem, which was not included so far. Therefore, we aim to derive a self-consistent Maxwell-Bloch formalism for X-ray absorption, which gives a unified description of XANES and EXAFS, so far missing in the literature. Within this framework we can extend the accomplishments of atomic and molecular XAS investigations concerning recombination channels [54, 55] or polarization dependent core transitions [56, 57] to solid states. Further, we find that the oscillations, although correctly related to the local structure of the material, stem from interference of electronic Bloch waves of neighbored atoms, which gives rise to additional so far uninterpreted features in the Fourier transformed EXAFS spectra. Such an analysis is performed in the last chapter for graphene.

Chapter 2

Exciton dynamics in tr-ARPES

2.1 General solid state Hamiltonian

A crystal consists of atoms arranged in a regular lattice. As consequence, we find an underlying repeating structure, which minimal repeating unit is called the unit cell. The crystal symmetries are represented by the space group, which contains all symmetry operations leaving the crystal invariant, such as translations, rotations, inversion, or combinations. The unit cell is spanned by a basic set of primitive lattice vectors $\{\boldsymbol{a}_i\}$. Translation in the space group are represented by linear combinations of these lattice vectors connecting all lattice points $\{\boldsymbol{R}_n\}$.

The neutral atoms forming the crystal can be separated into atomic nuclei and the electrons. As starting point for a quantitative investigation of solid state properties we use the Hamiltonian. The Hamiltonian describing a perfect crystal, with nuclei, electrons, and their mutual interaction reads [58, 59]

$$\mathcal{H} = -\sum_i \frac{\hbar^2 \nabla_i^2}{2m_i} - \sum_j \frac{\hbar^2 \nabla_j^2}{2M_j} + \frac{e^2}{4\pi\epsilon_0} \sum_{j<j'} \frac{Z_j Z_{j'}}{|\boldsymbol{R}_j - \boldsymbol{R}_{j'}|} - \frac{e^2}{4\pi\epsilon_0} \sum_{i,j} \frac{Z_j}{|\boldsymbol{r}_i - \boldsymbol{R}_j|}$$

$$+ \frac{e^2}{4\pi\epsilon_0} \sum_{i<i'} \frac{1}{|\boldsymbol{r}_i - \boldsymbol{r}_{i'}|} + \sum_{i,j} \frac{\hbar}{4c^2 m_i^2} \left(\nabla V(\boldsymbol{r}_i, \boldsymbol{R}_j) \times \boldsymbol{p}_i \right) \cdot \boldsymbol{\sigma} . \tag{2.1}$$

The indices i and j denote the electrons and nuclei, respectively. The electrons in an atom see a magnetic field because of their own orbital motion, which gives rise to a spin-orbit interaction. In a non-relativistic limit $v \ll c$, the spin-orbit coupling is described by the last term of the Hamiltonian acting on the spin wave function. The momentum operator and the Pauli spin matrices are denoted by $\boldsymbol{p}_i$ and $\boldsymbol{\sigma}$, respectively. Since the effect depends on the gradient of the potential generated by the nuclei and felt by the electrons, corresponding to the fourth term of the Hamiltonian and abbreviated by $V(\boldsymbol{r}_i, \boldsymbol{R}_j)$, it scales with the atomic number Z of the crystal compounds. The complex Hamiltonian can be simplified by a variety of largely valid approximations. Often the electrons are separated into two groups: core and valence electrons. The former are electrons occupying the filled orbitals being mostly localized at the nuclei. In most optical spectroscopic experiments these electrons do not contribute in contrast to the valence electrons of incompletely filled shells. In consequence, the core electrons can be treated together with the nuclei [60, 61]. This reduces the sum i over all electrons only to the valence electrons. However, experiments involving extreme ultraviolet (XUV) light with excitation energy around $100\,\mathrm{eV}$ or X-ray radiation can access the core electrons. Therefore, this typical approximation is not performed. A widely valid

approximation is the Born-Oppenheimer approximation [62]. Because of the heavy weight of the nuclei compared to the electrons, the latter react much faster to an external perturbation than the nuclei. Therefore, the nuclei may be regarded as fixed in space on the time scale of electronic interactions. The response time of ionic vibrations in solids are typically on the order of $10^{12}\,\mathrm{s}$ [58]. To estimate the electron response time we consider the external excitation of electrons. For semiconductors at least the band gap energy has to be fed. For an energy of $1\,\mathrm{eV}$ we can estimate the frequency of electronic motion to the order of $10^{15}\,\mathrm{s}^{-1}$ [58]. We see that with increasing energy of the excitation light the adiabatic approximation becomes better. Within the Born-Oppenheimer approximation we can express the Hamiltonian in Eq. (2.1) as

$$\mathcal{H} = \mathcal{H}_{\mathrm{nuc}}(\boldsymbol{R}_j) + \mathcal{H}_{\mathrm{el}}(\boldsymbol{r}_i, \boldsymbol{R}_{j0}) + \mathcal{H}_{\mathrm{el\text{-}nuc}}(\boldsymbol{r}_i, \delta\boldsymbol{R}_j)\,. \tag{2.2}$$

The nucleus motion under the influence of the atomic potential is described by H_{nuc}. The Hamiltonian for the electron motion with the nuclei in their equilibrium position $\boldsymbol{R}_{j0}$ and electron-electron interaction is described by H_{el}, which absorbs also the spin-orbit interaction. Since in this work the spin plays only a secondary role, the spin-orbit coupling is neglected from now on. Finally, $H_{\mathrm{el\text{-}nuc}}$ describes the change of electronic energy due to the displacement $\boldsymbol{R}_j$ of the nuclei from their equilibrium position, which is known as electron-phonon interaction. At last, we will assume that every electron experiences the same average potential $V(\boldsymbol{r}) = \sum_j V(\boldsymbol{r} - \boldsymbol{R}_j)$. The potential is by construction lattice periodic, i.e. $V(\boldsymbol{r}) = V(\boldsymbol{r} + \boldsymbol{R})$ with lattice vector $\boldsymbol{R}$. Thus, the Schrödinger equation, describing the motion of the electrons in the potential landscape of the nuclei background, reads

$$\mathcal{H}_{\mathrm{el}}\Psi_\alpha(\boldsymbol{r}) = \left(-\frac{\hbar^2\nabla^2}{2m} + V(\boldsymbol{r})\right)\Psi_\alpha(\boldsymbol{r}) = \varepsilon_\alpha\Psi_\alpha(\boldsymbol{r})\,, \tag{2.3}$$

where $\Psi_\alpha(\boldsymbol{r})$ and ε_α denote the wave function and energy of an electron in the eigenstate α. After having introduced the fundamentals of solid state physics, we see that the solution of the Schrödinger equation is the basic task of quantum theory in solids. To tackle the solution of the Schrödinger equation it is convenient to exploit the symmetry of the crystal.

2.2 Bloch theorem

In a crystal a periodic potential appears because the ions are arranged with the periodicity of their Bravais lattice. Usually, the problem is simplified by assuming a very large crystal, where the precise form does not affect the physical description. We may then choose periodic or Born-von Karman boundary conditions, where the value of any wave function is the same at equivalent points on opposite sites of the crystal. Counting along the direction of each primitive translation brings us to a point not only physically but also mathematically identical to the original point. In the case of two-dimensional materials the assumption of an infinite extended crystal can only be performed within the plane. In normal direction to the plane translation invariance is broken. Consequently, also the unit cell is semi-infinite in direction normal to the surface. Since the Schrödinger equation can be restricted to a fixed finite volume described by a single primitive cell of the crystal we expect to find an infinite family of solutions with discretely spaced eigenvalues. They are labeled by a band index λ and the corresponding wave function is denoted by $\Psi_\lambda(\boldsymbol{r})$.

We define a translation operator $T_{\boldsymbol{R}}$ acting in the crystal plane that $T_{\boldsymbol{R}}\Psi_\lambda(\boldsymbol{r}) = \Psi_\lambda(\boldsymbol{r} + \boldsymbol{R})$. Note that $\boldsymbol{R}$ is two-dimensional. Since the lattice potential shows the same lattice

periodicity, the translation operator and the Hamiltonian commute. This implies that any function obtained by applying the translation operator to an eigenfunction Ψ_λ will also be an eigenfunction with the same energy as the original one. If we assume that the eigenenergy ε_λ is l_λ-fold degenerate, we may choose a set of l_λ orthonormal eigenfunctions Ψ_λ^κ with $\kappa = 1, 2, \ldots, l_\lambda$ belonging to ε_λ. In other words, the l_λ degenerate functions form basis vectors of a subspace of the entire Hilbert space of the Hamiltonian. We can therefore construct a matrix, which executes the effect of the translation operator as [63, 64]

$$T_R \Psi_\lambda^\nu = \sum_{\kappa=1}^{l_\lambda} \Psi_\lambda^\kappa \Gamma_{\kappa\nu}^{(\lambda)}(R) \,, \tag{2.4}$$

where Eq. (2.4) holds for a one-dimensional translation. The sum includes all l_λ degenerate eigenfunctions Ψ_λ^κ having the same energy ε_λ as Ψ_λ^ν with ν labelling the degeneracy and $\Gamma_{\kappa\nu}^{(\lambda)}(R)$ is an irreducible representation matrix, which defines the linear combination. We know that all eigenfunctions of the Hamiltonian with the translation symmetry of the lattice must transform according to some representation of the group. Since we assume periodic boundary conditions for the crystal description, the cyclic group of order N is the symmetry group of the Hamiltonian. N corresponds to the number of unit cells along one axis forming the crystal. We can then write for the solutions from the pth representation

$$\Psi_\lambda^p(\boldsymbol{r} + \boldsymbol{R}) = T_{\boldsymbol{R}} \Psi_\lambda^p(\boldsymbol{r}) = \Gamma^{(p_x)}(R_x) \Gamma^{(p_y)}(R_y) \Psi_\lambda^p(\boldsymbol{r}) = e^{2\pi i p_x / N} e^{2\pi i p_y / N} \Psi_\lambda^p(\boldsymbol{r}) \,. \tag{2.5}$$

We used that the crystal is periodic within the plane and the well known representation of the cyclic group $\Gamma^{(p)}(R) = \exp(2\pi i p / N)$ with $p = 1, 2, \ldots, N$ [63]. If we introduce the crystal length $L_i = R_i N$ with $i = \{x, y\}$, relate k_i to p_i by $k_i = 2\pi p_i / L_i$, and relabel the function with equivalent index we obtain

$$\Psi_{\lambda,\boldsymbol{k}}(\boldsymbol{r} + \boldsymbol{R}) = e^{i\boldsymbol{k} \cdot \boldsymbol{R}} \Psi_{\lambda,\boldsymbol{k}}(\boldsymbol{r}) \,, \tag{2.6}$$

which is the fundamental Bloch condition. We see that both functions just differ by a phase factor. Consequently, physical quantities such as the probability distribution $|\Psi_{\lambda,\boldsymbol{k}}|^2$ are conserved. Introducing a lattice periodic function $u_{\lambda,\boldsymbol{k}}(\boldsymbol{r})$, the electronic wave function can be written as Bloch wave function

$$\Psi_{\lambda,\boldsymbol{k}}(\boldsymbol{r}) = \frac{1}{\sqrt{A}} e^{i\boldsymbol{k} \cdot \boldsymbol{r}_\parallel} u_{\lambda,\boldsymbol{k}}(\boldsymbol{r}) \tag{2.7}$$

constituting the solution of the Schödinger equation Eq. (2.3). The normalization constant carries the unit cell area A. The quantization volume in z-direction is merged into the periodic lattice function, which includes also the orbital out-of-plane extension often described in an envelope function approximation [65, 66]. We see that the electronic wave function can be written as a plane wave modulated by a lattice periodic function $u_{\lambda,\boldsymbol{k}}(\boldsymbol{r} + \boldsymbol{R}) = u_{\lambda,\boldsymbol{k}}(\boldsymbol{r})$. The Bloch waves are normalized since the periodic functions are orthogonal over a single unit cell of volume $V_{UC} : \langle u_{\lambda,\boldsymbol{k}} | u_{\lambda',\boldsymbol{k}} \rangle = V_{UC} \delta_{\lambda,\lambda'}$. Bloch's theorem follows solely from the translation symmetry of the crystal, holding true for any particle in a periodic lattice without any assumption about the strength of the potential. The two-dimensional wave vector $\boldsymbol{k}$ can be regarded as quantum number of translation. In a broader sense, the wave vector could also be seen as a crystal momentum. Finally, the electronic state is characterized by the quantum numbers band and wave vector $\{\lambda, \boldsymbol{k}\}$. The corresponding energy levels $\varepsilon_{\lambda,\boldsymbol{k}}$ vary in $\boldsymbol{k}$ forming the electronic dispersion. Note that the wave vector lies within the 1st Brillouin zone. Thus,

if we consider a vector in the extended zone $\boldsymbol{k} + \boldsymbol{G}$, the appropriate phase factor in Bloch's theorem is

$$e^{i(\boldsymbol{k}+\boldsymbol{G})\cdot\boldsymbol{R}} = e^{i\boldsymbol{k}\cdot\boldsymbol{R}} \tag{2.8}$$

since $\boldsymbol{G} \cdot \boldsymbol{R} = 2\pi n$, $n \in \mathbb{N}$. Similar to the lattice vector $\boldsymbol{R}$ connecting identical sites in real space, the reciprocal lattice vector $\boldsymbol{G}$ connects identical sites in reciprocal space. To have further insights into the Bloch function, we can express it in terms of a discrete plane wave basis, whose wave vectors are the reciprocal lattice vectors of the crystal because the Bloch function has the same periodicity as the direct lattice. The electronic wave function can then be expanded in terms of a linear combination of plane waves

$$\Psi_{\lambda,\boldsymbol{k}}(\boldsymbol{r}) = \frac{1}{\sqrt{A}} \sum_{\boldsymbol{G}} \xi_{\lambda,\boldsymbol{k}+\boldsymbol{G}} e^{i(\boldsymbol{k}+\boldsymbol{G})\cdot\boldsymbol{r}_\parallel} \, . \tag{2.9}$$

This approach takes explicitly the extended nature of Bloch waves into account. The coefficients $\xi_{\lambda,\boldsymbol{k}+\boldsymbol{G}}$ are obtained from the Schrödinger equation. An advantage of solving the Schrödinger equation for the coefficients of Eq. (2.9) over solving Eq. (2.3) directly is that the reciprocal space representation of the kinetic energy is diagonal and the potential can be described in terms of their Fourier components.

For photoemitted electrons leaving the sample we use the free kinetic energy $\hbar^2\mathbf{k}^2/2m_0$ with free electron mass m_0. Correspondingly, the electronic wave function should be describable by a plane wave. However, for pure plane waves the orthogonality to the material wave functions would be violated. One possibilty to overcome this problem is to use orthogonalized plane waves (OPW) [67–69]. Here, the plane wave is orthogonalized to the bound electronic wave functions $\Psi_{\lambda,\boldsymbol{k}}(\boldsymbol{r})$ exploiting the Gram-Schmidt procedure:

$$\Psi_{k_\perp,\boldsymbol{k}}(\boldsymbol{r}) = \frac{1}{\sqrt{V}} e^{i\boldsymbol{k}\boldsymbol{r}_\parallel} e^{ik_\perp z} - \sum_\lambda \eta_{\lambda,\boldsymbol{k},k_\perp} \Psi_{\lambda,\boldsymbol{k}}(\boldsymbol{r}) \, . \tag{2.10}$$

For the photoemitted electrons, the wave vector is now three-dimensional. We choose as notation that the out-of-plane component $k_\perp$ is used additionally as band index for the unbound states. Then, $\boldsymbol{k}$ still describes a two-dimensional in-plane wave vector. The band sum runs over all states within the material and $\eta_{k_\perp,\lambda,\boldsymbol{k}} = \langle k_\perp, \boldsymbol{k} | \Psi_{\lambda,\boldsymbol{k}} \rangle$ denotes the orthogonalization coefficient with the notation $\langle \boldsymbol{r} | k_\perp, \boldsymbol{k} \rangle = \exp(i\boldsymbol{k} \cdot \boldsymbol{r}_\parallel + ik_\perp z)/\sqrt{V}$ stemming from the unorthogonalized plane wave character of the final state.

However, the crystal potential is not perfectly cut at the surface that a plane wave description can also be to simple. For instance, approximating the final states by plane waves certain effects such as circular dichroism vanish [70, 71]. Alternatively, we construct the final states, such that they are Bloch states with respect to the in-plane wave vector and obey time-reversed LEED asymptotic boundary conditions in the out-of-plane direction. A time-reversed LEED approach is most commonly used in theoretical descriptions of photoemission spectroscopy [72–75]. LEED stands for low energy electron diffraction and denotes a technique from surface science. Here, electrons in the energy range from 20-50 eV are sent to the material surface, where they interact with matter, that a diffraction pattern can be measured. We can therefore consider in LEED an electron coming from a detector, arriving at the surface, where they will be reflected and transmitted, matching the free wave function at the surface [76]. Now, considering that state to be time-reversed we obtain a free electron propagating from the material towards a detector referred to as time-reversed LEED [77, 78]. We expand the final states as

$$\Psi_{k_\perp,\boldsymbol{k}}(\boldsymbol{r}) = \sum_{\boldsymbol{G}} e^{i(\boldsymbol{k}+\boldsymbol{G})\cdot\boldsymbol{r}_\parallel} \xi_{k_\perp,\boldsymbol{k},\boldsymbol{G}}(z) \, . \tag{2.11}$$

The expansion coefficients in Eq. (2.11) are fixed by [70]

$$\Psi_{k_\perp,\boldsymbol{k}}(\boldsymbol{r}) \to e^{i\boldsymbol{k}\cdot\boldsymbol{r}_\parallel} + \sum_{\boldsymbol{G}} R_{\boldsymbol{G}} e^{-i(\boldsymbol{k}+\boldsymbol{G})\cdot\boldsymbol{r}_\parallel} \quad (z \to \infty)$$

$$\Psi_{k_\perp,\boldsymbol{k}}(\boldsymbol{r}) \to \sum_{\boldsymbol{G}} T_{\boldsymbol{G}} \to e^{i(\boldsymbol{k}+\boldsymbol{G})\cdot\boldsymbol{r}_\parallel} \quad (z \to -\infty)$$

(2.12)

where $R_{\boldsymbol{G}}$ and $T_{\boldsymbol{G}}$ are reflection and transmission coefficients, respectively. This description of photoemitted electronic waves can be seen in comparison to an electron wave passing a potential step. At the finite barrier the wave is elastically scattered and diffracted. Such a behavior is absorbed into the coefficients $R_{\boldsymbol{G}}$ and $T_{\boldsymbol{G}}$, whereby the potential step corresponds to the sample surface. The coefficients of the final states Eq. (2.11) are determined by the Schrödinger equation Eq. (2.3):

$$\sum_{\boldsymbol{G}'} \left[\left(-\frac{\hbar^2 \partial_z^2}{2m} + \frac{\hbar^2(\boldsymbol{k}+\boldsymbol{G})}{2m} \right) \delta_{\boldsymbol{G},\boldsymbol{G}'} + V_{\boldsymbol{G}-\boldsymbol{G}'}(z) \right] \xi_{k_\perp,\boldsymbol{k},\boldsymbol{G}'}(z) = \left(\frac{\hbar^2 \boldsymbol{k}^2}{2m} + \frac{\hbar^2 k_\perp^2}{2m} \right) \xi_{k_\perp,\boldsymbol{k},\boldsymbol{G}}(z).$$

(2.13)

Here, we see the earlier discussed diagonality of the kinetic energy and the Fourier transformed Coulomb potential. It would now be necessary to solve Eq. (2.13) together with the boundary conditions (2.12), which requires computational expensive methods [79].

2.3 Electronic Hamiltonian

Generally, the modes of the electromagnetic field and a simple harmonic oscillator satisfy the same classical equations. This fact suggests that it is possible to quantize both in the same way. By defining annihilation and creation operators for each wave vector $\boldsymbol{k}$ and integrating over them yields a Hamiltonian for the free theory [80]. This procedure is known as second quantization. Within this framework the Hilbert space is forwarded to the Fock space. A direct sum of the Hilbert spaces of n-particle states at each time constitutes the Fock space [81]. We can define field operators, which are constructed from creation and annihilation operators for each momentum. The second quantized electronic Hamilton operator can be calculated from a Hamiltonian density, which is a functional of field and their conjugate momenta [80,82].

Knowing the complete set of eigenstates from the stationary single-particle Schrödinger equation, the electronic field operators can be expanded by

$$\hat{\Psi}^{(\dagger)}(\boldsymbol{r},t) = \sum_{\lambda,\boldsymbol{k}} \Psi^{(*)}_{\lambda,\boldsymbol{k}}(\boldsymbol{r}) \lambda^{(\dagger)}_{\boldsymbol{k}}(t)$$

(2.14)

with the single-particle wave function $\Psi_{\lambda,\boldsymbol{k}}(\boldsymbol{r})$ and the electronic annihilation (creation) operator $\lambda^{(\dagger)}_{\boldsymbol{k}}(t)$. For the sake of readability, we introduce the notation $\lambda^{(\dagger)}_{\boldsymbol{k}}$ annihilating (creating) an electron in band λ with in-plane wave vector $\boldsymbol{k}$. The creation and annihilation operators fulfill the fundamental commutation relations of fermions

$$\left[\lambda_{\boldsymbol{k}}, \lambda'^{\dagger}_{\boldsymbol{k}'} \right]_+ = \delta^{\lambda,\lambda'}_{\boldsymbol{k},\boldsymbol{k}'}, \quad \left[\lambda^{(\dagger)}_{\boldsymbol{k}}, \lambda'^{(\dagger)}_{\boldsymbol{k}'} \right]_+ = 0.$$

(2.15)

This ensures the antisymmetry of the many-particle wave function and that a state cannot be occupied by more than one particle.

Free Hamiltonian: With the expansion we obtain the single-particle Hamiltonian in second quantization

$$H = \sum_{\lambda,\lambda,\boldsymbol{k},\boldsymbol{k}'} \int d^3r \ \Psi_{\lambda,\boldsymbol{k}}^*(\boldsymbol{r}) \left(-\frac{\hbar^2\nabla^2}{2m} + V(\boldsymbol{r}) \right) \Psi_{\lambda',\boldsymbol{k}'}(\boldsymbol{r}) \lambda_{\boldsymbol{k}}^\dagger \lambda'_{\boldsymbol{k}'} = \sum_{\lambda,\boldsymbol{k}} \varepsilon_{\lambda,\boldsymbol{k}} \lambda_{\boldsymbol{k}}^\dagger \lambda_{\boldsymbol{k}} , \qquad (2.16)$$

where we used the orthogonality of the wave functions bringing the Hamiltonian into diagonal form. The dispersion of the electrons in band λ is described by $\varepsilon_{\lambda,\boldsymbol{k}}$.

Carrier-light coupling: On the same footage, we include the interaction of solid state electrons with an external classical light field. The radiation acts as a source for the investigated excitation dynamics. Further, we are interested in the description of spectroscopy, which refers to the study of matter through its interaction with light fields. We will treat the interaction semi-classically, where the light presents only a time-dependent interaction potential that acts on the matter. The electric dipole Hamiltonian reads [66, 83]

$$H = - \sum_{\lambda,\lambda',\boldsymbol{k},\boldsymbol{k}'} \boldsymbol{d}_{\boldsymbol{k},\boldsymbol{k}'}^{\lambda\lambda'} \cdot \boldsymbol{E}(t) \lambda_{\boldsymbol{k}}^\dagger \lambda'_{\boldsymbol{k}'} . \qquad (2.17)$$

The Hamiltonian describes the transition from a band λ into the band λ', optically induced by an electric field $\boldsymbol{E}(t)$. The electric field is assumed to propagate perpendicular to the sample. Consequently, the polarization vector of the incident light is parallel to the sample plane. The dipole matrix element [84, 85] reads formally

$$\boldsymbol{d}_{\boldsymbol{k},\boldsymbol{k}'}^{\lambda\lambda'} = e\langle \Psi_{\lambda,\boldsymbol{k}} | \boldsymbol{r} | \Psi_{\lambda',\boldsymbol{k}'} \rangle \qquad (2.18)$$

with elementary charge e. The dipole matrix element describes the strength and selection rules of the optical transitions. The latter is determined by the crystal symmetry and the symmetry of the involved initial and final states. In order to derive the used dipole matrix element, we insert the Bloch wave functions for the bands λ and λ'. Then we substitute $\boldsymbol{r}_\parallel \exp(i\boldsymbol{k} \cdot \boldsymbol{r}_\parallel) = -i\nabla_{\boldsymbol{k}} \exp(i\boldsymbol{k} \cdot \boldsymbol{r}_\parallel)$. The integral is shifted into the first unit cell and summed over all unit cells. A detailed derivation is shown in the appendix A.2. Finally, we obtain the dipole matrix operator

$$\boldsymbol{d}_{\boldsymbol{k},\boldsymbol{k}'}^{\lambda\lambda'} = -ie\langle u_{\lambda,\boldsymbol{k}} | \begin{pmatrix} \nabla_{\boldsymbol{k}} \\ iz \end{pmatrix} | u_{\lambda',\boldsymbol{k}'} \rangle \ \delta_{\boldsymbol{k},\boldsymbol{k}'}^{\lambda',\bar{\lambda}} - ie\delta_{\boldsymbol{k},\boldsymbol{k}'}^{\lambda,\lambda'} \nabla_{\boldsymbol{k}} . \qquad (2.19)$$

Generally throughout this thesis, integrals in this notation involving the periodic lattice functions $u_{\lambda,\boldsymbol{k}}(\boldsymbol{r})$ or atomic orbitals extend over the 1st Brillouin zone. The first term describes interband transitions from one band λ into a different band $\bar{\lambda}$. The second term is band conserving and specifies therefore intraband transitions, where the gradient acts onto the creation operator in Eq. (2.17). The intraband term describes an acceleration of carriers and polarization by the external electric field. The motion of the carriers induces a macroscopic current, which contributes in addition to the macroscopic polarization to the optical response [86, 87]. The external field of the laser changes the crystal momentum of electrons according to the acceleration theorem [88]. Usually, exciting light in the near infrared and of higher excitation energy is used to probe the optical response of a material. Due to the fast oscillation of the electric fields, the wave vector changes are small compared to the electronic wave vector [86, 89]. Therefore, the optical response is not strongly altered and the intraband source is usually neglected. Besides restrictions for the band indices, we find also a selection rule for the wave vectors. In Eq. (2.17) we see that the spatial extension of the
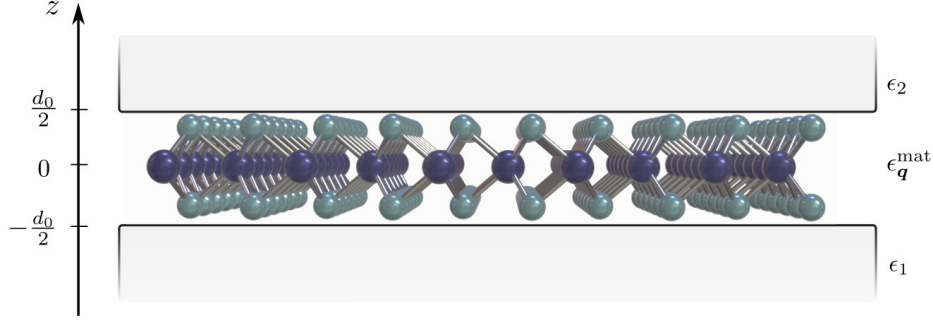
Figure 2.1: An atomically-thin material of finite thickness d_0 with substrate and supstrate characterized by the dielectric constants ϵ_1 and ϵ_2, respectively.

electric field is neglected. In more detail, the spatial phase is expanded in orders of $\boldsymbol{r}_\parallel$ around the nuclei position, which yields a series of multipole moments of increasing order [90]. Due to its dominating contribution only the zeroth order is kept, i.e. $\exp(i\boldsymbol{Q}\cdot\boldsymbol{r}_\parallel)\approx 1$ with light wave vector $\boldsymbol{Q}$. The underlying reason is that for light in the visible and XUV (here considered up to $20\,\mathrm{eV}$) regime the wavelength $\lambda = 2\pi/k$ is largely smaller than the extension of the unit cell lying in the range of the lattice constant. Therefore, for the first order holds $\boldsymbol{r}_\parallel\cdot\boldsymbol{Q}\ll 1$ compared to the zeroth order. Consequently, the electric field can be considered constant throughout the unit cell. This explains also why the dipole Hamiltonian is diagonal in the wave vector and describes only vertical transitions within the Brillouin zone with conserving wave vector. Inserting the dipole matrix operator into Eq. (2.17) we recognize that the minus sign cancels.

Carrier-carrier coupling: As third, the interaction between carriers is investigated. In principle, intra- and interband Coulomb interaction is possible described by

$$H = \frac{1}{2}\sum_{\substack{\lambda,\lambda',\nu,\nu'\\ \boldsymbol{k},\boldsymbol{k}',\boldsymbol{q}}} V_{\boldsymbol{k},\boldsymbol{k}',\boldsymbol{q}}^{\lambda\lambda'\nu'\nu}\lambda^\dagger_{\boldsymbol{k}+\boldsymbol{q}}\lambda'^\dagger_{\boldsymbol{k}'-\boldsymbol{q}}\nu'_{\boldsymbol{k}'}\nu_{\boldsymbol{k}} \tag{2.20}$$

with the Coulomb matrix element [91]

$$V_{\boldsymbol{k},\boldsymbol{k},\boldsymbol{q}}^{\lambda\lambda'\nu'\nu} = V_{\boldsymbol{q}}\sum_{\boldsymbol{G}}\langle u_{\lambda,\boldsymbol{k}+\boldsymbol{q}}|e^{i\boldsymbol{G}\cdot\boldsymbol{r}_\parallel}|u_{\nu,\boldsymbol{k}}\rangle\langle u_{\lambda',\boldsymbol{k}'-\boldsymbol{q}}|e^{-i\boldsymbol{G}\cdot\boldsymbol{r}_\parallel}|u_{\nu',\boldsymbol{k}'}\rangle\,. \tag{2.21}$$

To obtain the presented matrix element, we shifted the integrals into the 1st Brillouin zone and summed over all unit cells. Equation (2.21) describes the probability of a Coulomb-induced transition between the states $(\lambda,\boldsymbol{k}+\boldsymbol{q})$ and $(\lambda',\boldsymbol{k}'-\boldsymbol{q})$ to $(\nu,\boldsymbol{k})$ and $(\nu',\boldsymbol{k}')$. The momentum transfer $\boldsymbol{q}$ corresponds to the distance in momentum space between the interacting carriers. $V_{\boldsymbol{q}}$ denotes the Fourier transform of the Coulomb potential. It can be derived by solving the Poisson equation for a three layer model [92–95], as sketched in Fig. 2.1. While the substrates are approximately described by dielectric constants [96], the investigated atomically-thin material is described by a non-local dielectric function [97]. The screened Coulomb potential reads

$$V_{\boldsymbol{q}} = \frac{\mathcal{V}_{\boldsymbol{q}}}{\epsilon_{\boldsymbol{q}}}\,. \tag{2.22}$$

11

It constitutes of the bare Coulomb potential [98]

$$\mathcal{V}_{\boldsymbol{q}} = \frac{e^2}{\epsilon_0 A d_0 |\boldsymbol{q}|^2} \left(1 - \frac{1}{d_0 |\boldsymbol{q}|} \left(1 - e^{-d_0 |\boldsymbol{q}|} \right) \right) \tag{2.23}$$

with dielectric vacuum permittivity ϵ_0 and unit cell area A. $\mathcal{V}_{\boldsymbol{q}}$ corresponds to a quasi two-dimensional Coulomb potential including the finite thickness d_0 of the investigated material. Interestingly, for $q d_0 \ll 1$ the expression recovers the ideal two-dimensional Coulomb potential $\mathcal{V}_{\boldsymbol{q}} = e^2 / \epsilon_0 A |\boldsymbol{q}|$. In contrast, for $q d_0 \gg 1$ we obtain the three-dimensional Coulomb potential $\mathcal{V}_{\boldsymbol{q}} = e^2 / \epsilon_0 A |\boldsymbol{q}|^2$. Therefore, the quasi two-dimensional potential interpolates between the strict two-dimensional and three-dimensional case [99]. The Coulomb potential is statically screened by the dielectric environment. The corresponding macroscopic dielectric function $\epsilon_{\boldsymbol{q}}$ includes a non-linear wave vector dependence, which is in agreement with *ab initio* calculations [98, 100–102], and reads [96]

$$\epsilon_{\boldsymbol{q}} = \frac{\epsilon_{\boldsymbol{q}}^{\mathrm{mat}} \tilde{\epsilon}_{\boldsymbol{q}} \left(d_0 |\boldsymbol{q}| - 1 + e^{-d_0 |\boldsymbol{q}|} \right)}{d_0 |\boldsymbol{q}| \tilde{\epsilon}_{\boldsymbol{q}} + 2 \epsilon_1 \epsilon_2 \left(1 - \cosh(d_0 |\boldsymbol{q}|) \right) - \epsilon_{\boldsymbol{q}}^{\mathrm{mat}} (\epsilon_1 + \epsilon_2) \sinh(d_0 |\boldsymbol{q}|)} \tag{2.24}$$

with the abbreviation

$$\tilde{\epsilon}_{\boldsymbol{q}} = \epsilon_{\boldsymbol{q}}^{\mathrm{mat}} (\epsilon_1 + \epsilon_2) \cosh(d_0 |\boldsymbol{q}|) + (\epsilon_1 \epsilon_2 + (\epsilon_{\boldsymbol{q}}^{\mathrm{mat}})^2) \sinh(d_0 |\boldsymbol{q}|) . \tag{2.25}$$

Here, the dielectric function of the material appears, which includes a non-linear wave vector dependence instead of being treated locally. It reads [98]

$$\epsilon_{\boldsymbol{q}}^{\mathrm{mat}} = 1 + \frac{1}{\frac{1}{\epsilon_{\parallel}^{mat}-1} + \alpha \frac{|\boldsymbol{q}|^2}{q_F^2} + \left(\frac{\hbar^2 \boldsymbol{q}^2}{2 m_0 E_{pl}} \right)^2} \tag{2.26}$$

and requires the in-plane susceptibility $\epsilon_{\parallel}^{\mathrm{mat}}$ of the material as well as the plasmon peak energy E_{pl} associated with the parental bulk material. Additionally, we find a dimensionless fitting parameter α. For monolayer transition-metal dichalcogenides, which are introduced in the next section as material, we use $\alpha = 1.55$ [98]. The Fermi wave number q_F in Eq. (2.26) is defined as [96]

$$q_F = \sqrt{\frac{e_0^2 m_0}{\pi^2 \epsilon_0 \hbar^2} \left(\frac{3 \pi^2 \epsilon_0 m_0 E_{pl}^2}{e_0^2 \hbar^2} \right)^{1/3}} . \tag{2.27}$$

Again, we can investigate the limiting case of ideally two-dimensional materials. We apply $d_0 \to 0$ together with the assumption of small wave vector, that $d_0 q$ can be linearized. Then the dielectric function $\epsilon_{\boldsymbol{q}}$ reduces to the well-known Rytova-Keldysh screening [92, 93]

$$\epsilon_{\boldsymbol{q}} = \frac{\epsilon_1 + \epsilon_2}{2} (1 + r_0 |\boldsymbol{q}|) \tag{2.28}$$

with screening length r_0.

In this thesis we focus mainly on the long range interaction. Long range interaction is attributed to transfer of small momenta. This simplifies the matrix element since we can use $\nu = \lambda$ and $\nu' = \lambda'$ and take $\boldsymbol{G} = 0$. We treat only carriers located in the vicinity of the relevant points in the Brillouin zone, corresponding to the high symmetry points. In this case a locally defined wave vector can be set to approximately zero. Within this low wave number

approximation, the Bloch functions can be treated perturbatively in $\boldsymbol{q}$ that the intraband cross-section are close to unity: $\langle u_{\lambda,\boldsymbol{k}+\boldsymbol{q}}|u_{\lambda,\boldsymbol{k}}\rangle \approx 1$. Consequently, the intraband Coulomb matrix element is determined solely by the statically screened quasi-two-dimensional Coulomb potential.

Carrier-phonon coupling: The last contribution to the electronic material Hamiltonian includes phonons and their interaction with electrons. The Hamiltonian reads [91]

$$H = \sum_{\alpha,\boldsymbol{K}} \hbar\Omega_{\boldsymbol{K}}^{\alpha} b_{\boldsymbol{K}}^{\dagger\alpha} b_{\boldsymbol{K}}^{\alpha} + \sum_{\lambda,\alpha,\boldsymbol{k},\boldsymbol{K}} g_{\boldsymbol{k}+\boldsymbol{K},\boldsymbol{k},\boldsymbol{K}}^{\lambda\alpha} \lambda_{\boldsymbol{k}+\boldsymbol{K}}^{\dagger} \lambda_{\boldsymbol{k}} \left(b_{\boldsymbol{K}}^{\alpha} + b_{-\boldsymbol{K}}^{\dagger\alpha} \right) \tag{2.29}$$

including the free phonon energy by the first term and the electron-phonon interaction with the second term. The operators $b_{\boldsymbol{K}}^{(\dagger)\alpha}$ denote phonon annihilation (creation) operators following bosonic commutation relations:

$$\left[b_{\boldsymbol{K}}^{\alpha}, b_{\boldsymbol{K}'}^{\dagger\alpha'} \right]_{-} = \delta_{\boldsymbol{K},\boldsymbol{K}'}^{\alpha,\alpha'}, \quad \left[b_{\boldsymbol{K}}^{(\dagger)\alpha}, b_{\boldsymbol{K}'}^{(\dagger)\alpha'} \right]_{-} = 0 \, . \tag{2.30}$$

They are characterized by the phonon mode α and a two-dimensional wave vector $\boldsymbol{K}$. The phonon dispersion of mode α is described by $\hbar\Omega_{\boldsymbol{K}}^{\alpha}$. We include two acoustic phonons, namely longitudinal acoustic (LA) and transversal acoustic (TA), and three optical modes, namely longitudinal (LO), transversal (TO) optical and the optical A_1 mode. Around the Γ-point, building the center of the Brillouin zone, the optical phonons are treated in Einstein approximation, i.e. $\hbar\Omega_{\boldsymbol{K}}^{\alpha} = \hbar\Omega^{\alpha} = \text{const}$. The acoustic phonons are treated in Debye approximation, i.e. $\hbar\Omega_{\boldsymbol{K}}^{\alpha} = \hbar c^{\alpha}|\boldsymbol{K}|$, where c^{α} denotes the velocity of sound for the given phonon mode. Zone-edge phonons are treated in Einstein approximation [103–105].

The second contribution to the Hamiltonian describes phonon-induced scattering from $(\lambda,\boldsymbol{k}+\boldsymbol{K})$ to $(\lambda,\boldsymbol{k})$ under wave vector transfer $\boldsymbol{K}$. Since the phonon energies considered in this thesis are smaller than the band gap of the materials, the phonon scattering is band conserving [103–105]. However, we have to distinguish between intravalley scattering and intervalley scattering between different high symmetry points of the Brillouin zone. The electron-phonon matrix element corresponds to a change of the self-consistent potential created from electrons and nuclei, due to a perturbation, whereby the perturbation corresponds to a phonon [106]. The electron-phonon matrix element reads

$$g_{\boldsymbol{k}+\boldsymbol{K},\boldsymbol{k},\boldsymbol{K}}^{\lambda\alpha} = \sqrt{\frac{\hbar}{2\rho\Omega_{\boldsymbol{K}}^{\alpha}A}} G_{\boldsymbol{k}+\boldsymbol{k},\boldsymbol{k},\boldsymbol{K}}^{\lambda\alpha} = \sqrt{\frac{\hbar}{2\rho\Omega_{\boldsymbol{K}}^{\alpha}A}} \langle u_{\lambda,\boldsymbol{k}+\boldsymbol{K}}|\delta V_{\boldsymbol{K}}^{\alpha}|u_{\lambda,\boldsymbol{k}}\rangle \tag{2.31}$$

with the derivative $\delta V_{\boldsymbol{K}}^{\alpha}$ of the potential between carrier and nuclei due to atomic displacements associated with a certain phonon mode. The mass density of the unit cell is denoted by ρ.

We distinguish between two kinds of electron-phonon coupling: polar and non-polar coupling. The latter is described by a deformation potential interaction. Here, the carriers interact with the local change in the crystal potential, which is associated with lattice vibrations [107]. In contrast, for polar coupling mechanisms, such as Fröhlich or piezoelectric coupling, the charged carriers couple to an internal polarization of the lattice stemming from a displacement field associated with phonons [108]. Acoustic phonons couple equally in deformation potential and piezoelectric coupling [109]. In contrast the TO and A_1 phonon mode couple mainly in deformation potential and the LO couples in Fröhlich [103]. We can split the integral as [103, 104, 108]

$$\left(G_{\boldsymbol{k}+\boldsymbol{K},\boldsymbol{k},\boldsymbol{K}}^{\lambda\alpha} \right)_{\text{ac}} = \left(G_{\boldsymbol{k}+\boldsymbol{K},\boldsymbol{k},\boldsymbol{K}}^{\lambda\alpha} \right)_{\text{ac}}^{\text{DP}} + i \left(G_{\boldsymbol{k}+\boldsymbol{K},\boldsymbol{k},\boldsymbol{K}}^{\lambda\alpha} \right)_{\text{ac}}^{\text{PE}} \tag{2.32}$$

$$\left(G_{\boldsymbol{k}+\boldsymbol{K},\boldsymbol{k},\boldsymbol{K}}^{\lambda\alpha} \right)_{\text{op}} = \left(G_{\boldsymbol{k}+\boldsymbol{K},\boldsymbol{k},\boldsymbol{K}}^{\lambda\alpha} \right)_{\text{op}}^{\text{DP}} + i \left(G_{\boldsymbol{k}+\boldsymbol{K},\boldsymbol{k},\boldsymbol{K}}^{\lambda\alpha} \right)_{\text{op}}^{\text{Fr}} \, , \tag{2.33}$$

where the imaginary unit ensures that the coupling mechanisms are out of phase and do not interfere [109]. As we will see, important for the exciton-phonon coupling are the signs of the coupling integrals. However, first-principle calculations yield only the absolute value of the scattering integrals. Therefore, a more detailed look onto the scattering mechanisms is necessary. Polar phonon coupling mechanisms, such as Fröhlich or piezoelectric, depend on the charge of the involved carrier, which is involved in the scattering event. Therefore, the signs of the integrals for valence and conduction band coincide [108]. The signs for the scattering integrals for deformation potential coupling can be extracted from the direction of band shifts occuring when the unit cell is deformed by the respective phonon mode [107]. A possible tool are strain measurements or calculations [110–112]. In the case of monolayer transition-metal dichalcogenides it is found that valence and conduction band deformation potential coupling elements have different signs. We can write

$$\left(G_{k+K,k,K}^{c/v\alpha}\right)_{\mathrm{ac}} = \pm\left|G_{k+K,k,K}^{c/v\alpha}\right|_{\mathrm{ac}}^{\mathrm{DP}} + i\left|G_{k+K,k,K}^{c/v\alpha}\right|_{\mathrm{ac}}^{\mathrm{PE}} \tag{2.34}$$

$$\left(G_{k+K,k,K}^{c/v\alpha}\right)_{\mathrm{op}} = \pm\left|G_{k+K,k,K}^{c/v\alpha}\right|_{\mathrm{op}}^{\mathrm{DP}} + i\left|G_{k+K,k,K}^{c/v\alpha}\right|_{\mathrm{op}}^{\mathrm{Fr}}. \tag{2.35}$$

The deformation potential matrix elements are treated by an analytical model described by the deformation potential approximation. Here, the matrix element is expanded in orders of the phonon wave vector, with the zeroth order (D_0) and first order ($D_1|K|$) deformation potential. Optical phonon interaction and intervalley scattering are treated in zeroth order. Interaction of acoustic phonons is evaluated in first order [113].

2.4 Photoemission Hamiltonian

So far, we formulated the Hamiltonian for crystal electrons and intrinsic material interactions such as electron-electron and electron-phonon interaction. The electronic structure within the thermal energy range around the Fermi level determines a wide range of phenomena. We can even go that far that the electronic band structure constitutes the macroscopic basis of the material's physical properties. For example, we can classify materials in semiconductor, insulators, and metals depending on their band structure. Also classical properties such as thermal conductivity or heat capacity are determined by the band structure. Or the materials optical properties such as if the material is colorful or transparent. Therefore, to understand and engineer new materials microscopic investigations of the electronic structure are necessary. When neglecting the spin, two quantities are important for the investigation: energy and wave vector. Photoelectron spectroscopy is a tool with the possibility to access these quantities.

Photoelectron spectroscopy is a collective term for all spectroscopic techniques exploiting the photoelectric effect, which was first observed by H. Hertz [114] at the end of the 1880s and later explained by A. Einstein [115]. When a material is irradiated by light and the excitation energy is larger than the ionization energy of the material, then an electron, called photoelectron, is emitted from the sample. The kinetic energy of the photoelectron is determined by the difference of the light's excitation energy and the ionization energy of the material. Therefore, photoelectron spectroscopy is an experimental technique to determine the relative energies of electrons in atoms, molecules or solids and the measured intensity is proportional to the electronic density of states [116]. Depending on the source of the ionizing radiation, photoelectron spectroscopy is divided into ultraviolet and X-ray photoelectron spectroscopy. The former probes valence, while the latter core electrons.

A highly advanced technique is angle resolved photoemission spectroscopy (ARPES) [117, 118]. When the high-energy light strikes the sample and initiates the photoemission

process, the photoelectrons leave the sample under a certain angle. The emission angle, which is measured by a hemispheric detector [26], can be traced back to the initial wave vector of the photoelectron within the sample. Using the wave vector $|\boldsymbol{k}| = \sqrt{k_x^2 + k_y^2}$ in spherical coordinates and the relation $k = \sqrt{2m_0 E}/\hbar$ for the kinetic energy of a free particle, the relation to the emission angle is

$$k = \sqrt{2m_0 E} \sin\theta/\hbar\,. \tag{2.36}$$

Besides the connection of wave vector and emission angle θ, we see from Eq. (2.36) that the magnitude of the measured wave vector depends on the kinetic energy. To access the complete Brillouin zone with ARPES, it is therefore necessary to use high energy radiation sources such as extreme ultraviolet (XUV) or X-ray. With the simultaneous measurement of kinetic energy and wave number the complete quantum state of the electron within the sample is known. Therefore, not only the electronic band structure but even fingerprints of electronic correlations are observable, which for example can constitute the basis of superconducting properties [116, 119]. Hence, ARPES is the most direct method to probe valence electrons in material systems [120–122]. The mean free path of UV photons is on the order of a few Ångström [123, 124], that ARPES is a surface sensitive method. Equation (2.36) shows also that only the in-plane momentum can be easily related to the emission angle. Thus, two-dimensional materials, where electronic states are delocalized in two directions and well localized in perpendicular direction, are ideal candidates to be investigated by ARPES.

A limitation of ARPES is that the method accesses only the occupied density of states. An extension of ARPES is time resolved ARPES (tr-ARPES), which adds a time resolution to the experiment. A common problem of many optical experiments is the indirect nature of the measurement. In pure optical experiments many possible excitation and relaxation pathways can contribute to the measured transients, which makes the identification of transfer and relaxation channels difficult [125]. Tr-ARPES can provide this information in many cases as it is capable of directly imaging the excited electron dynamics in k-space [125, 126].

To describe the photoemission process we formulate now the underlying Hamiltonian. It consists of the unperturbed vacuum Hamiltonian and the XUV-matter interaction. The free kinetic energy is described by a manifold of three-dimensional parabolas starting at the ionization energy of the material. The transition probability of the optical excitation, where a valence or conduction band electron is elevated by the XUV light to the ionization continuum is described by the matrix element $\boldsymbol{d}_{\boldsymbol{k}}^{\lambda k_\perp} = -ie\langle u_{\lambda,\boldsymbol{k}}|\nabla_{\boldsymbol{k}}|\xi_{k_\perp,\boldsymbol{k}}\rangle - ie\langle u_{\lambda,\boldsymbol{k}}|iz|\xi_{k_\perp,\boldsymbol{k}}\rangle\hat{\boldsymbol{e}}_z$ with the Cartesian unit vector $\hat{\boldsymbol{e}}_z$. Born-von Karman plane waves are an orthogonal set of functions. Since Bloch waves and tr-LEED states fulfill the Born-von Karman condition within the plane they have to be orthogonal. Since the bound states λ can by definition not equal the ionization continuum, $\boldsymbol{d}_{\boldsymbol{k}}^{\lambda k_\perp}$ is a pure interband dipole element without intraband contribution. For the photoemission we use a XUV excitation energy of 20 eV. Also for such soft XUV light the wave number is comparable small to the electronic wave vector. For example, the momentum of a zone edge electron is about 1000 times larger than that of a 20 eV photon. In the reduced zone scheme the photoemission transition is therefore wave vector conserving and can be seen as vertical [127]. Here lies also the reason for the momentum resolution of the ARPES measurement. The photoemission contribution to the Hamiltonian describing the emission process of electrons into the ionization continuum initiated by a XUV pulse, reads

$$H = \sum_{\boldsymbol{k},k_\perp} \varepsilon_{k_\perp,\boldsymbol{k}} k_{\perp,\boldsymbol{k}}^\dagger k_{\perp,\boldsymbol{k}} - \sum_{\lambda=\{c,v\},\boldsymbol{k},k_\perp} \left(\boldsymbol{d}_{\boldsymbol{k}}^{\lambda k_\perp} \cdot \boldsymbol{E}(t) \lambda_{\boldsymbol{k}}^\dagger k_{\perp,\boldsymbol{k}} + \text{H.c.} \right)\,. \tag{2.37}$$
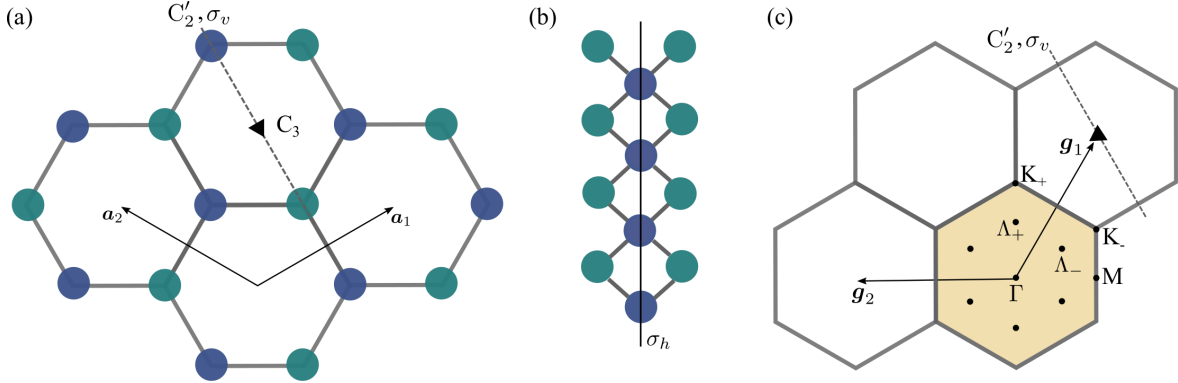
Figure 2.2: (a) A sketched top view of a monolayer TMDC with drawn symmetry axes. Blue dots denote transition-metal and green dots chalcogen atoms. (b) Side view of a monolayer TMDC displaying the σ_h symmetry. (c) Sketch of the hexagonal Brillouin zones with high symmetry points and symmetry axis. The first Brillouin zone is highlighted in gold.

We introduce the fermionic operator $k_{\perp,\boldsymbol{k}}^{(\dagger)}$, which acts as band index and perpendicular momentum and describes creation or annihilation in the three-dimensional ionization states of the vacuum.

Based on the distinct symmetry properties of the crystal bands certain bands are ruled out by the photoemission matrix element. The final state continuum wave function should be symmetric with respect to all mirror planes of the surface. The product of polarization vector and dipole operator $\boldsymbol{e} \cdot \boldsymbol{r}$ is even if the polarization is parallel to the plane but odd if the polarization is perpendicular to the plane [128]. Therefore, different polarizations probe different states. In our case, for a perpendicular irradiation the polarization vector is parallel to the plane. The material, which we are going to investigate by tr-ARPES are monolayer transition-metal dichalcogenides.

2.5   Monolayer transition-metal dichalcogenides

2.5.1   Real and reciprocal lattice

Since the exfoliation of graphene from a bulk graphite crystal, many other two-dimensional materials were identified. A very prominent family of layered two-dimensional materials are transition-metal dichalcogenides (TMDC). TMDCs are layered materials with general chemical formula MX_2, where M stands for a transition-metal and X for a chalcogen atom. Each monolayer is composed of a covalently bonded trilayer, consisting of metal atoms sandwiched by two chalcogen atom sheets. The most widely studied polytypes are the trigonal prismatic 2H-types. Here, two trilayers in a trigonal prismatic coordination (H) are required to form the bulk primitive unit cell [129]. Adjacent trilayers of the bulk crystal are held together by weak van der Waals interactions. Especially, semiconducting TMDCs are of significant interest because their band gap lies in the optical range of the electromagnetic spectrum, which is favorable for optoelectronic devices [130, 131]. The majority of attention focuses on the molybdenum- and tungsten-based constituents: MoS_2, $MoSe_2$, WS_2, and WSe_2. These four materials are also the subject of this thesis. As exemplary candidates for their class we focus on WSe_2 and $MoSe_2$.

It has been demonstrated that the band structure drastically changes, when going from bulk

to monolayer samples: The originally indirect semiconductor turns into a direct semiconductor making them even more interesting for device applications [3, 4]. Such monolayer TMDCs host many intriguing electronic and physical properties [132].

To access mono- or few-layer structures from bulk crystals an adhesive force of skotch tape is used, referred to as mechanical cleavage. This method produces large flakes of high quality with few defects. However, the production rate is low and thickness and size are hard to control [133]. Therefore, currently intense efforts to grow large-area TMDC monolayers with low-defects from chemical vapor deposition are performed. Such an industrial manufacturing is important for future implementation into technological applications [134, 135].

The investigated molybdenum- and tungsten-based TMDCs appear in a 2Hc stacking, where every transition-metal atom is situated on top of two chalcogen atoms. From a top view the composing atoms of the monolayer TMDC arrange in a hexagonal lattice, as is shown in Fig. 2.2(a) and (b). The basis vectors of the real two-dimensional lattice are

$$
\boldsymbol{a}_1 = \frac{a_0}{2} \begin{pmatrix} \sqrt{3} \\ 1 \end{pmatrix}, \quad \boldsymbol{a}_2 = \frac{a_0}{2} \begin{pmatrix} -\sqrt{3} \\ 1 \end{pmatrix} \tag{2.38}
$$

and span the planar unit cell, which contains 3 atoms. a_0 denotes the lattice constant. From a linear combination of these two vectors we can construct any translation vector $\boldsymbol{R}$. The trigonal prismatic geometry gives rise to the crystallographic point group D_{3h}. The included point symmetry operations are the 3-fold C_3 rotation, the 2-fold C_2 rotation along the monolayer plane, the horizontal reflection σ_h with its plane passing the transition-metal atom, a S_3 mirror-rotation, a σ_v vertical reflection plane, and obviously the identity. Figure 2.2 draws the symmetry axes.

The uniquely defined unit cell in reciprocal space is described by

$$
\boldsymbol{g}_1 = \frac{2\pi}{a_0} \begin{pmatrix} \frac{\sqrt{3}}{3} \\ 1 \end{pmatrix}, \quad \boldsymbol{g}_2 = \frac{2\pi}{a_0} \begin{pmatrix} -\frac{\sqrt{3}}{3} \\ 1 \end{pmatrix}, \tag{2.39}
$$

which fulfill the necessary condition: $\boldsymbol{a}_i \cdot \boldsymbol{g}_j = 2\pi\delta_{ij}$. Similar to real space, we find a hexagonal structure of the 1st Brillouin zone in momentum space, which is sketched in Fig. 2.2(c) together with the reciprocal high-symmetry points. At the center lies the Γ-point, while at the edges are the K_+ and K_- points. Monolayer TMDCs show at the zone edged K_+ and K_- points an advantageous direct band gap, forming the optical relevant points in the lattice. This situation is different compared to the classical III-V or II-IV semiconductors, such as GaAs, where the optical band gap lies at the Γ-point [136].

The K_+ and K_- points are connected by time-reversal symmetry. We can define a time-reversal operator that $\mathcal{T}\Psi(\boldsymbol{r}) = \Psi^*(\boldsymbol{r})$ holds. This action can be verified by inserting the time evolution operator for $\mathcal{T}$. Inserting a Bloch wave we obtain the identity $\mathcal{T}\Psi_{\boldsymbol{k}}(\boldsymbol{r}) = \Psi_{-\boldsymbol{k}}(\boldsymbol{r}) = \Psi_{\boldsymbol{k}}^*(\boldsymbol{r})$. Investigating the action at the K_+ point, i.e. $\boldsymbol{k} = \boldsymbol{K}_+$, we see that time-reversal symmetry ensures a valley degeneracy since $\mathcal{T}$ flips the Bloch factor as $(e^{i\boldsymbol{K}_\pm \cdot \boldsymbol{r}_\parallel})^* = e^{i\boldsymbol{K}_\mp \cdot \boldsymbol{r}_\parallel}$ and swaps therefore the eigenstates at K_+ and K_- [137]. This follows from the fact that the K_+ and K_- coordinates are related by a sign change. If we include the spin the time-reversal operator needs to be redefined as $\mathcal{T}\sigma_y$ with the Pauli spin operator σ_y to ensure time-reversal symmetry of the Hamiltonian Eq. (2.3) [138]. Now, not only $\boldsymbol{k} \to -\boldsymbol{k}$ but also the spin $s \to -s$ is exchanged under time-reversal operation, i.e. $\mathcal{T}\Psi_{\lambda,\boldsymbol{k}\uparrow}(\boldsymbol{r}) = \Psi_{\lambda,-\boldsymbol{k}\downarrow}(\boldsymbol{r})$ with time-reversal

conjugate states $E_{\lambda,\boldsymbol{k}\uparrow} = E_{\lambda,-\boldsymbol{k}\downarrow}$. We obtain at the K_+ point

$$\mathcal{T}\Psi_{\lambda,\boldsymbol{k}\uparrow} = \mathcal{T}\left(e^{i\boldsymbol{K}_+\cdot\boldsymbol{r}_\parallel}u_{\lambda,\boldsymbol{K}_+,\uparrow}\begin{pmatrix}1\\0\end{pmatrix}\right) = e^{-i\boldsymbol{K}_+\cdot\boldsymbol{r}_\parallel}\left(iu^*_{\lambda,\boldsymbol{K}_+,\uparrow}\begin{pmatrix}0\\1\end{pmatrix}\right)$$

$$= e^{i\boldsymbol{K}_-\cdot\boldsymbol{r}_\parallel}u_{\lambda,-\boldsymbol{K}\downarrow}\begin{pmatrix}0\\1\end{pmatrix}, \tag{2.40}$$

which is the Bloch state at K_- with spin $s = \downarrow$ and the corresponding energy $E_{\lambda,\boldsymbol{K}_+\uparrow} = E_{\lambda,\boldsymbol{K}_-\downarrow}$. We see that wave functions connected by conjugation have the same energy, namely the spin-up state in the K_+ valley and the corresponding spin-down in the K_- valley have the same energy. Important for this relation is the lack of inversion symmetry $E_{\lambda,\boldsymbol{k}} = E_{\lambda,-\boldsymbol{k}}$, present in monolayer TMDCs, which would restore the two-fold spin degeneracy. Therefore, the absence of the inversion symmetry in monolayer TMDCs is of essential importance for the rich coupled spin-valley physics of monolayer TMDCs [12, 138, 139]. The band splitting by the intrinsic spin-orbit coupling is lifted at the time-reversal invariant points M and Γ [140]. The M point is situated between the K_+ and K_- points and finally we introduce the $\Lambda_\pm$ points, which lie between the Γ and the $K_\pm$ points, cf. Fig. 2.2(c). It is found that the spin-orbit coupling splits the conduction band by a few tens of meV. But in contrast, the valence band splitting is about a few hundred meV [140]. This can be traced back to the orbital composition of the bands. *Ab initio* calculations reveal that the bands around the Fermi level are formed predominately by d orbitals of the heavy transition-metal atoms. Around the $K_\pm$ points the valence bands are mainly formed by the linear combination $d_{x^2-y^2} \pm id_{xy}$. The conduction band is constituted by the d_{z^2} orbital [141, 142]. At the $K_\pm$ points not all symmetries of the lattice are preserved, cf. Fig. 2.2(c). Here, only the three-fold rotational symmetry axis (C_3) and the horizontal mirror plane (σ_h) are valid symmetry operations. For the d_{z^2} orbital, constituting the conduction band, when rotated around at the lattice site no phase contribution occurs since the d_{z^2} orbital has no azimuthal phase. In contrast, for the valence band the atomic orbitals themself induce an orbital angular momentum since they exhibit an azimuthal phase winding around the transition-metal nuclei. This large, and at the nuclei localized, angular momentum originates the large spin-orbit splitting [143]. To describe the full microscopic character of the electronic wave functions and the electronic dispersion also the minor contribution of the chalcogen p orbitals needs to be included. However, their influence on the symmetry of the wave functions is negligible [143]. This rich orbital contribution to the relevant bands makes a construction of a tight binding model, valid in the whole Brillouin zone, a cumbersome task. Here, we apply an effective mass approximation and treat the band structure as parabolas around each high symmetry point. The parabolic approximation is valid up to $300\,\text{meV}$ [6, 103] and reads for the bands $\lambda = \{c, v\}$

$$E_{\lambda,\boldsymbol{k}} = \pm\frac{\hbar^2\boldsymbol{k}^2}{2m_\lambda} \pm \frac{E_G}{2}. \tag{2.41}$$

The effective masses of valence and conduction bands are denoted by m_λ and E_G corresponds to the band gap. An exemplary electronic TMDC dispersion is sketched in Fig. 2.3. Since the spin plays only a minor role in the investigated scenarios, we will focus on the spin up bands.

2.5.2   Selection rules

Now that we have defined the orbital basis functions and investigated the TMDC crystal symmetries we can revisit the previously formally formulated matrix elements. For the optical
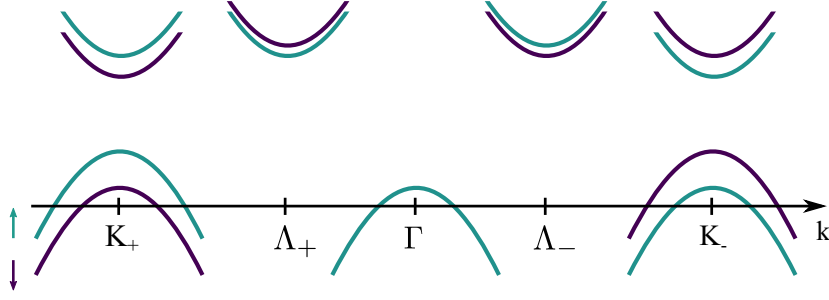
Figure 2.3: TMDC dispersion in effective mass approximation. For a complete picture of monolayer TMDCs, the spin bands are included.

valence-conduction band transition we know that the periodic Bloch factor $u_{\lambda,\boldsymbol{k}}(\boldsymbol{r})$, involving the periodic sequence of atomic orbitals, transforms according to the point group C_{3h} at the $K_\pm$ points. Thus, the Bloch functions at the Brillouin zone edges are eigenstates of the C_3 operator, which describes a $2\pi/3$ rotation with eigenvalue $\exp(i2\pi m_\lambda/3)$. For the bands hold $m_c = 0$ and $m_v = \pm 2$ due to the d_{z^2} and $d_{x^2-y^2} \pm i d_{xy}$ contribution, respectively. The dipole matrix element transforms upon two cancelling rotations as [144]

$$\langle u_{v,\boldsymbol{k}}|\boldsymbol{r}|u_{c,\boldsymbol{k}}\rangle = \langle u_{v,\boldsymbol{k}}|C_3^{-1}C_3\boldsymbol{r}C_3^{-1}C_3|u_{c,\boldsymbol{k}}\rangle = e^{-i\frac{2\pi}{3}(m_v-m_c\mp 1)}\langle u_{v,\boldsymbol{k}}|\boldsymbol{r}|u_{c,\boldsymbol{k}}\rangle . \tag{2.42}$$

We used that the C_3 operator, acting on the dipole operator, induces a phase $\exp(i2\pi m/3)$ with $m = \pm 1$ for circular polarized light $\sigma_\pm$ and $m = 0$ for linear polarized light. For a possible transition the matrix element should not change since we inserted a one. Therefore, we find the condition $(m_v - m_c \mp 1)\mathrm{mod}3 = 0$. We see immediately that the K_+ point is only excited by σ_+ light and the K_- point only by σ_-. Furthermore, we see that the transition in the respective valley does only occur if $\langle u_{v,\boldsymbol{k}}|\boldsymbol{r}|u_{c,\boldsymbol{k}}\rangle \neq 0$, i.e. the integral must be even. In other words: The product of irreducible representation $\Gamma_v^* \otimes \Gamma_r \otimes \Gamma_c$ must contain the fully symmetric representation [138]. At the $K_\pm$ points the $d_{x^2-y^2} \pm i d_{xy}$ hybridized orbital of the valence band transforms according to the irreducible representation E' and the dipole vector according to E'+A". With the help of the reduction formula for $\Gamma_v \otimes \Gamma_r$ we can check that the optical transition is allowed into final states with irreducible representation A' (and A"), having the d_{z^2} orbital as basis function. Therefore, the investigated optical transition from highest valence band into lowest conduction band is dipole allowed. A detailed derivation is given in the appendix A.1.

In a similar way, we can investigate the photoemission selection rules from the relevant high symmetry points $K_\pm$ and $\Lambda_\pm$. For the final states we know that they should be symmetric with respect to all mirror planes of the surface [145–147]. We find that the final state transforms according to A' and E'. We can then check for the perpendicular excitation geometry with in-plane parallel polarization that transitions from valence and conduction band are dipole allowed. A similar result can be obtained for the $\Lambda_\pm$, which are associated with the point group C_{1h}. The appendix A.1 shows the derivation for the TMDC photoemission selection rules.

We introduced monolayer TMDCs, their electronic dispersion and the electronic optical selections. But the low excitation properties of monolayer TMDCs are determined by excitons.

2.6   Excitons

2.6.1   Excitonic Bloch equations

The two-dimensional character of atomically-thin materials entail among others also a weak dielectric screening. Therefore, the semiconducting monolayer transition-metal dichalcogenides exhibit an enhanced Coulomb interaction, which gives rise to strongly bound electron-hole pairs or excitons [10]. These quasi-particles dominate the optical properties of monolayer TMDCs [3]. In the following we are going to investigate Coulomb-correlated electron-hole pairs in terms of the semiconductor Bloch equations. Due to the incredible importance of excitons in the linear and perturbatively nonlinear limit over quasi-free electrons or exciton plasmas an excitonic description of these two-body quasi-particles is desirable [91, 148, 149].

To investigate excitons, we start from the interband transition defined as

$$p_{\boldsymbol{k}_v, \boldsymbol{k}_c} \equiv p^{vc}_{\boldsymbol{k}_v, \boldsymbol{k}_c} = v^{\dagger}_{\boldsymbol{k}_v} c_{\boldsymbol{k}_c} \,. \tag{2.43}$$

For the interband transitions we assume near-resonant excitation conditions. Therefore, for a better readability the band indices are dropped, cf. Eq. (2.43). Within a Heisenberg equation of motion formalism we derive the semiconductor Bloch equation for the interband transition. From the Hamiltonian defined in Sec. 2.3 we obtain

$$i\hbar \frac{d}{dt} p_{\boldsymbol{k}} = (\varepsilon_{c,\boldsymbol{k}} - \varepsilon_{v,\boldsymbol{k}}) \, p_{\boldsymbol{k}} + (f_{v,\boldsymbol{k}} - f_{c,\boldsymbol{k}}) \left(\hbar \Omega^{cv}_{\boldsymbol{k}}(t) - \sum_{\boldsymbol{q}} V^{vc}_{\boldsymbol{q}} \, p_{\boldsymbol{k}+\boldsymbol{q}} \right) + i\hbar \partial_t p_{\boldsymbol{k}}|_{\text{coll}} \tag{2.44}$$

for the microscopic polarization $p_{\boldsymbol{k}} = \langle v^{\dagger}_{\boldsymbol{k}} c_{\boldsymbol{k}} \rangle$. The first term, referred to as gap dispersion, describes the oscillation of the interband transition, or microscopic polarization, and corresponds to the difference between the single-particle energies. The second term corresponds to the source term stemming from the exciting light. We see that the optical transition is driven by the valence band occupation and blocked by the conduction band occupation, which corresponds to Pauli-blocking [150]. As already discussed in Sec. 2.3 the optically induced transition is wave vector conserving. Consequently, also the valley is conserved. For monolayer TMDCs this implies that electron and hole are, depending on the polarization of the electric field, either both at the K_+ or K_- point. The Rabi-frequency is defined as $\Omega^{cv}_{\boldsymbol{k}} = \boldsymbol{d}^{cv}_{\boldsymbol{k}} \cdot \boldsymbol{E}(t)/\hbar$. Finally, we included to the derivation also Coulomb interaction. When incorporating many-body interaction to a single-particle element such as $p_{\boldsymbol{k}}$ this leads to a coupling to higher-order terms. They describe the correlation between the carriers. Troublesome is that we obtain an infinite hierarchy of equations with increasing number of carriers. To close the arising set of equations, the infinite hierarchy needs to be systematically truncated, which is achieved by the correlation expansion [151–153]. In case of Coulomb interaction the factorization of the obtained 4-operator quantity is called Hartree-Fock factorization. The energy renormalizing terms are absorbed into the single-particle energies $\varepsilon_{\lambda, \boldsymbol{k}}$. Additionally, we find the last term of Eq. (2.44), which describes a Coulomb-induced renormalization of the Rabi-frequency. It can be interpreted as local field contribution and gives rise to the formation of excitons. The correlated part of the factorization gives rise to many-body interaction [154] and scattering-induced dephasing [155], and is schematically included in $\partial_t p_{\boldsymbol{k}}|_{\text{coll}}$. At this point electron-phonon interaction is neglected. Note, that the wave vector $\boldsymbol{k}$ is defined throughout the Brillouin zone and addresses implicitly the different valleys.

So far the equation of motion is expressed in the electron-hole pair picture. We see that the Coulomb interaction couples every wave vector to all other wave vectors making a numerical treatment fairly difficult. To circumvent this problem we transform from the electron-hole
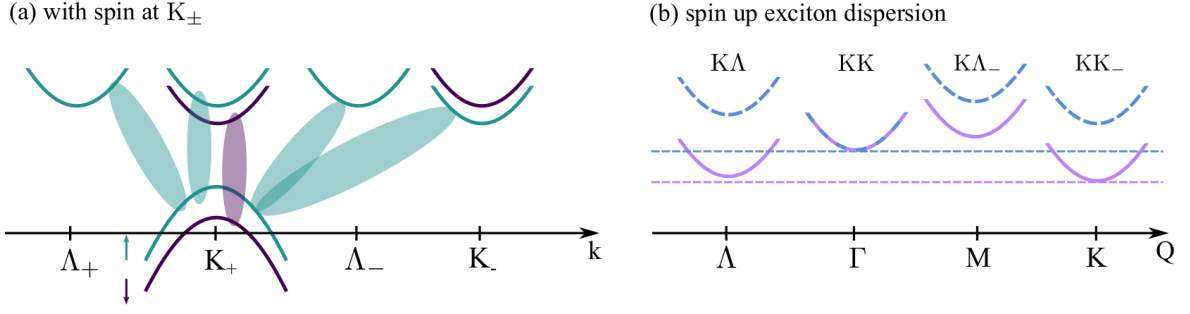
(a) with spin at $K_\pm$

(b) spin up exciton dispersion

Figure 2.4: (a) Electron-hole band structure with spin up and down at the $K_\pm$ points and the possible electron-hole pairs. (b) Corresponding exciton band structure. Blue dashed denotes the molybdenum-based TMDCs and violet solid tungsten-based TMDCs. In the former materials the Γ-exciton forms the global minimum and in the latter the momentum-indirect states are energetically more favorable.

pair into the exciton picture. The transformation is achieved by performing a coordinate transformation. Since we need to treat a two-body system, we define

$$\boldsymbol{q} = \alpha \boldsymbol{k}_v + \beta \boldsymbol{k}_c, \quad \text{and} \quad \boldsymbol{Q} = \boldsymbol{k}_c - \boldsymbol{k}_v \tag{2.45}$$

as relative $\boldsymbol{q}$ and center-of-mass momentum $\boldsymbol{Q}$. The mass factors are defined as ratios of electron or hole mass to the excitonic mass according to

$$\alpha = \frac{m_c}{m_v + m_c}, \quad \text{and} \quad \beta = \frac{m_v}{m_v + m_c} . \tag{2.46}$$

With the transformation, the pair operators carry relative and center-of-mass momentum. By projecting the pair operators onto a complete basis relative and center-of-mass motion can be separated. Denoting the pair operator in exciton basis by $P_{\boldsymbol{q},\boldsymbol{Q}}$ we can write

$$P_{\boldsymbol{q},\boldsymbol{Q}} = \sum_\mu \varphi_{\mu,\boldsymbol{q}} P_{\mu,\boldsymbol{Q}} . \tag{2.47}$$

By these means, the exciton depends solely on the center-of-mass momentum. As basis function we choose the exciton wave function $\varphi_{\mu,\boldsymbol{q}}$, which determines the relative motion of the exciton of state μ. They are obtained as solution of the Wannier equation. In the linear limit, i.e. neglecting Pauli blocking, it reads [91, 156, 157]

$$\frac{\hbar^2 \boldsymbol{q}^2}{2m} \varphi_{\mu,\boldsymbol{q}} - \sum_{\boldsymbol{k}} V_{\boldsymbol{k}}^{vc} \varphi_{\mu,\boldsymbol{q}+\boldsymbol{k}} = E_B^\mu \varphi_{\mu,\boldsymbol{q}} . \tag{2.48}$$

The first term describes the kinetic energy with reduced exciton mass m. The second term takes into account the electron-hole intraband Coulomb interaction, which gives rise to the exciton binding. Besides the exciton wave function as eigenfunction we obtain also the corresponding exciton binding energy E_B^μ with exciton quantum number μ as eigenvalue. The Wannier equation depends on the electron and hole valleys and can be applied to all kinds of excitons possible in a complex multivalley band structure. We can transform the electronic dispersion with electron-hole pairs into an excitonic dispersion as is sketched in Fig. 2.4. Excitons with electron and hole at the K_+ (or K_-) points form the excitonic Γ point since

it includes the vanishing center-of-mass momentum $\boldsymbol{Q}$. Γ excitons with electron and hole of spin up form the A exciton. The spin down exciton is referred to as B exciton. Since we focus on spin up (A exciton is the energetically lowest lying), and if not other stated, we drop the A and just write exciton. Additionally, also momentum indirect excitons are possible such as $\Lambda_\pm$ excitons, where the hole is at the K_+ point and the electron at the $\Lambda_\pm$ point or K excitons with hole at the K_+ and electron at the K_- point. An alternative labeling of excitons is K_+K_+, $K_+\Lambda_+$, or K_+K_- depending where the electron is situated. Generally, the K_+ is exchangeable by K_-, which yields the same excitonic configurations. To reduce the clumsy notation we drop the plus sign $K_+ \to K$ when addressing the excitonic states. Interestingly, when numerically solving the Wannier equation, we find that Γ excitons form the global minimum for molybdenum-based TMDCs but momentum-indirect Λ and K excitons are energetically more favorable in tungsten-based TMDCs, cf. Fig. 2.4(b). The equation of motion for the exciton in the limit of negligible Pauli blocking reads

$$i\hbar\frac{d}{dt}P_{\mu,\boldsymbol{Q}} = E_{\mu,\boldsymbol{Q}}P_{\mu,\boldsymbol{Q}} + \hbar\Omega_\mu(t)\ \delta_{\boldsymbol{Q},0} + i\hbar\partial_t P_{\mu,\boldsymbol{Q}}|_{\text{coll}}\,. \tag{2.49}$$

Compared to Eq. (2.44), the equation of motion is now in a diagonal form and corresponds to a simple driven harmonic oscillator with the exciton kinetic energy $E_{\mu,\boldsymbol{Q}} = \hbar^2\boldsymbol{Q}^2/2M + E_\mu$, where $M = m_h + m_e$ denotes the exciton mass and $E_\mu = E_G + E_B^\mu$ the exciton energy. The driving term is the excitonic Rabi frequency $\Omega_\mu(t) = \sum_{\boldsymbol{q}}\varphi_{\mu,\boldsymbol{q}}^*\Omega_{\boldsymbol{q}}^{cv}$. We see that only excitons with vanishing center-of-mass momentum can be excited, which corresponds to vertical transitions at the $K_\pm$ points in the electronic picture.

We have discussed the complex quasi-particle band structure. But, because of the optical selection rules, the excitons in Eq. (2.49) are restricted to the optically active Γ excitons within the light cone. The possibility for the formation of momentum-indirect excitons is given by exciton-phonon interaction, which is included in Eq. (2.49) only schematically by $\partial_t P_{\mu,\boldsymbol{Q}}|_{\text{coll}}$. In the following, exciton-phonon interaction is briefly investigated. Therefore, we include electron-phonon interaction to the semiconductor Bloch equation Eq. (2.44) and transform the additional contribution into the exciton picture. The exciton-phonon contribution to the excitonic Bloch equation reads

$$i\hbar\frac{d}{dt}P_{\mu,\boldsymbol{Q}}|_{\text{phon}} = \sum_{\alpha,\boldsymbol{K}} g_{\mu\mu',\boldsymbol{K}}^\alpha \left(S_{\mu',\boldsymbol{Q}-\boldsymbol{K},\boldsymbol{K}}^\alpha + \tilde{S}_{\mu',\boldsymbol{Q}-\boldsymbol{K},-\boldsymbol{K}}^\alpha \right)\,. \tag{2.50}$$

We find that the exciton transition couples to the phonon-assisted transitions $\overset{(\sim)}{S}{}_{\mu,\boldsymbol{Q}-\boldsymbol{K},\boldsymbol{K}}^\alpha = \langle P_{\mu,\boldsymbol{Q}-\boldsymbol{K}}b_{\boldsymbol{K}}^{(\dagger)\alpha}\rangle$. The sum over the phonon quantum numbers include not only intra- but also intervalley scattering of excitons. Important is that the hole scattering can be neglected due to a large energetic separation of excitonic states, which are addressable by intervalley scattering of holes. The exciton-phonon matrix element is defined as

$$g_{\mu\mu',\boldsymbol{K}}^\alpha = \sum_{\boldsymbol{q}} \left(\varphi_{\mu,\boldsymbol{q}}^* g_{\boldsymbol{K}}^{c\alpha} \varphi_{\mu',\boldsymbol{q}+\beta\boldsymbol{K}} - \varphi_{\mu,\boldsymbol{q}}^* g_{\boldsymbol{K}}^{v\alpha} \varphi_{\mu',\boldsymbol{q}-\alpha\boldsymbol{K}} \right)\,. \tag{2.51}$$

Here, we see the earlier claimed substraction of conduction and valence band electron-phonon matrix element. For electrons and holes with similar effective mass the form factors, constituting of the product of the exciton wave functions, are comparable. As consequence, the exciton-phonon interaction vanishes if the electronic matrix elements have equivalent sign and add up for opposite sign. The phonon-assisted transitions are coupling back to the exciton

transition via the phonon population $n_{\boldsymbol{K}}^{\alpha}$, which is treated in bath approximation:

$$i\hbar\frac{d}{dt}S_{\mu,\boldsymbol{Q},\boldsymbol{K}}^{\alpha} = \left(E_{\mu,\boldsymbol{Q}} + \hbar\Omega_{\boldsymbol{K}}^{\alpha}\right)S_{\mu,\boldsymbol{Q},\boldsymbol{K}}^{\alpha} + \sum_{\mu'}\left(g_{\mu\mu',-\boldsymbol{K}}^{\alpha}P_{\mu',\boldsymbol{Q}+\boldsymbol{K}}\right)\left(1 + n_{\boldsymbol{K}}^{\alpha}\right) + i\hbar\partial_t S_{\mu,\boldsymbol{Q},\boldsymbol{K}}^{\alpha}|_{\text{coll}},$$

(2.52)

$$i\hbar\frac{d}{dt}\tilde{S}_{\mu,\boldsymbol{Q},\boldsymbol{K}}^{\alpha} = \left(E_{\mu,\boldsymbol{Q}} - \hbar\Omega_{\boldsymbol{K}}^{\alpha}\right)\tilde{S}_{\mu,\boldsymbol{Q},\boldsymbol{K}}^{\alpha} + \sum_{\mu'}\left(g_{\mu\mu',-\boldsymbol{K}}^{\alpha}P_{\mu',\boldsymbol{Q}+\boldsymbol{K}}\right)n_{\boldsymbol{K}}^{\alpha} + i\hbar\partial_t\tilde{S}_{\mu,\boldsymbol{Q},\boldsymbol{K}}^{\alpha}|_{\text{coll}}. \quad (2.53)$$

The first equation describes phonon emission while the second equation describes phonon absorption. The phonon-assisted transitions can be solved in a Markov approximation. As consequence we find a self-consistent expression for the non-radiative phonon-induced dephasing, determining the exciton coherence lifetime [158]. In contrast, solving the phonon-assisted transitions by Fourier transformation leads to a complex and frequency-dependent self-energy of the excitonic transition. The real part describes a red-shift of the exciton resonance, referred to as polaron shift. The frequency-dependent imaginary part of the self-energy leads to an asymmetric lineshape of the absorption line, which can be attributed to phonon sidebands [159–162].

By investigating only the optically prepared exciton transition with vanishing center-of-mass momentum we considered only the coherent limit. The quantity $|P_{\mu,\boldsymbol{Q}=0}|^2$ is called coherent exciton. Due to exciton-phonon interaction the coherent excitons decay and form the source of incoherent excitons $N_{\mu,\boldsymbol{Q}} = \delta\langle P_{\mu,\boldsymbol{Q}}^{\dagger}P_{\mu,\boldsymbol{Q}}\rangle$, where the δ denotes the correlated quantity. The equation of motion reads

$$i\hbar\frac{d}{dt}N_{\mu,\boldsymbol{Q}} = 2i\sum_{\mu',\alpha,\boldsymbol{K}}g_{\mu\mu',\boldsymbol{K}}^{\alpha}\Im\mathfrak{m}\left[\left(S_{\mu,\boldsymbol{Q},\boldsymbol{K}}^{*\alpha}P_{\mu',\boldsymbol{Q}-\boldsymbol{K}} + \tilde{S}_{\mu,\boldsymbol{Q},-\boldsymbol{K}}^{*\alpha}P_{\mu',\boldsymbol{Q}-\boldsymbol{K}}\right)\right]$$

$$+ 2i\sum_{\mu',\alpha,\boldsymbol{K}}g_{\mu\mu',\boldsymbol{K}}^{\alpha}\Im\mathfrak{m}\left[\left(O_{\mu\mu',\boldsymbol{Q},\boldsymbol{Q}-\boldsymbol{K},\boldsymbol{K}}^{\alpha} + \tilde{O}_{\mu\mu',\boldsymbol{Q},\boldsymbol{Q}-\boldsymbol{K},-\boldsymbol{K}}^{\alpha}\right)\right]. \quad (2.54)$$

We see that the phonon-assisted decay of the coherent excitons (first line) are the source of the incoherent excitons with finite center-of-mass momentum. The formed incoherent excitons can then scatter with phonons. The second line describes exactly the process of exciton relaxation and thermalization. The mediating quantities are the phonon-assisted densities $\overset{(\sim)}{O}_{\mu\mu',\boldsymbol{Q},\boldsymbol{Q}-\boldsymbol{K},\boldsymbol{K}}^{\alpha} = \delta\langle P_{\mu,\boldsymbol{Q}}^{\dagger}P_{\mu',\boldsymbol{Q}-\boldsymbol{K}}b_{\boldsymbol{K}}^{(\dagger)\alpha}\rangle$. Deriving equations of motions for the phonon-assisted densities and by inserting their Born-Markov solutions together with the Born-Markov solutions for the phonon-assisted polarizations we obtain an excitonic Boltzmann equation. The numerical solution was performed by Malte Selig and published in reference [163].

The incoherent excitons are also the source of photoluminescence – excitonic recombination under photon emission. In the coherent limit we briefly discussed that the coupling of exciton coherence to the phonon-assisted coherence gives rise to phonon sidebands in linear absorption. In comparable matter, the coupling of exciton density to the phonon-assisted density via an exciton-phonon-photon correlation gives rise to phonon sidepeaks in the luminescence spectra, which are discussed in detail in reference [164].

2.6.2 Self-consistent Maxwell-excitonic Bloch equations

The easiest method to investigate excitons is a linear absorption measurement. The absorption of a material is determined by its reflection and transmission regarding the irradiating light. Obviously, the excitation triggers a response of the material, which influences the light

waves [156]. To obtain a self-consistent coupling between light and material, we need to couple the excitonic Bloch equations with the Maxwell equations. From the coupling, we can derive an expression for the absorption coefficient and identify the radiative dephasing of the exciton. For a normal incidence of the exciting light, the field varies only in propagation direction and the polarization is orthogonal to the z-axis. As consequence, the in-plane divergence of the electric field vanishes and we can use the one-dimensional wave equation [156, 165]

$$\frac{\partial^2}{\partial z^2}E(z,t) - \frac{n^2}{c^2}E(z,t) = -\mu_0\frac{\partial^2}{\partial t^2}P(z,t)\,. \tag{2.55}$$

We assume a constant uniform background refraction index n. The vacuum speed of light and the vacuum magnetic permeability are denoted by c and μ_0, respectively. The source of the wave equation corresponds to the macroscopic polarization $P(z,t)$. The solution of the wave equation reads [65, 166, 167]

$$E(z,t) = E_0(z,t) - \mu_0\frac{c}{2n}\frac{\partial}{\partial u}P(u)\Big|_{u=t-|nz|/c}\,. \tag{2.56}$$

The incoming light is divided into reflected and transmitted part

$$E_R(z,t) = -\mu_0\frac{c}{2n}\frac{\partial}{\partial u}P(u)\Big|_{u=t-|nz|/c} \qquad z \leq 0\,, \tag{2.57}$$

$$E_T(z,t) = E_0(z,t) - \mu_0\frac{c}{2n}\frac{\partial}{\partial u}P(u)\Big|_{u=t-|nz|/c} \qquad z \geq 0\,. \tag{2.58}$$

The excitation geometry is sketched in Fig. 2.5(a). Already at this level, we see that the reflected and transmitted light are influenced by the material response. The equations can be solved by Fourier transformation. Assuming an infinite thin sample at $z = 0$ the electric fields read

$$E_R(\omega) = i\mu_0\frac{c}{2n}\omega P(\omega)\,, \tag{2.59}$$

$$E_T(\omega) = E_0(\omega) + i\mu_0\frac{c}{2n}\omega P(\omega)\,. \tag{2.60}$$

The derived expressions hold for linear and nonlinear excitation conditions. In linear optics the field is directly proportional to the electric field at the materials position: $P(\omega) = \epsilon_0\chi(\omega)E_T(\omega)$ with the scalar susceptibility $\chi(\omega)$. Combining the definition of the linear polarization with the calculated electric fields we can derive the self-consistent reflected and transmitted fields

$$E_R(\omega) = \frac{i\frac{\omega}{2nc}\chi(\omega)}{1 - i\frac{\omega}{2nc}\chi(\omega)}E_0(\omega)\,, \tag{2.61}$$

$$E_T(\omega) = \frac{1}{1 - i\frac{\omega}{2nc}\chi(\omega)}E_0(\omega)\,. \tag{2.62}$$

The transmission and reflection coefficients can now easily be calculated from the definitions $t(\omega) = |E_T(\omega)/E_0(\omega)|^2$ and $r(\omega) = |E_R(\omega)/E_0(\omega)|^2$, respectively [65]. On the other side, we can also calculate the frequency-dependent self-consistent absorption coefficient [166], which reads

$$\alpha(\omega) = 1 - r(\omega) - t(\omega) = \frac{\frac{\omega}{nc}\Im\mathrm{m}(\chi(\omega))}{|1 - i\frac{\omega}{2nc}\chi(\omega)|^2}\,. \tag{2.63}$$
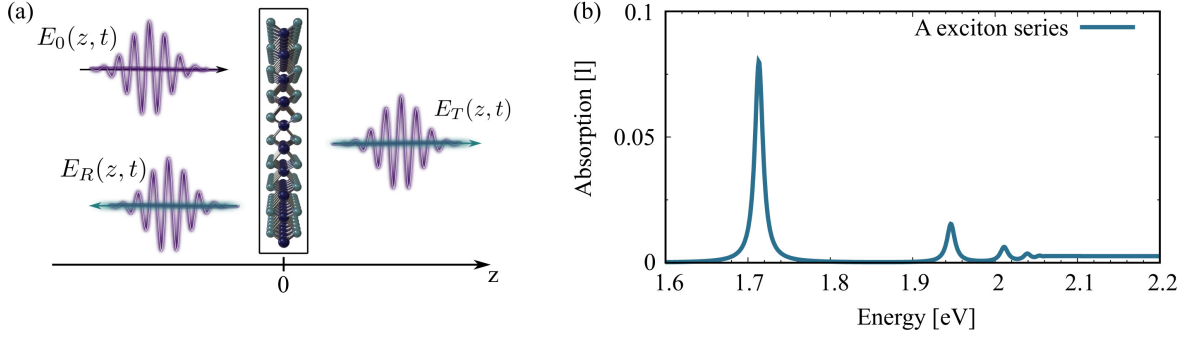
Figure 2.5: (a) Perpendicular irradiation of a sample with the electric field $E_0(z,t)$. The light is reflected ($E_R(z,t)$) and transmitted ($E_T(z,t)$) alternated by the response of the material. (b) A exciton series of the WSe$_2$ exciton. Clearly observable is the $1s$ to $3s$ exciton and the continuum starting at the band gap.

The absorption coefficient is determined by the imaginary part of the susceptibility. The denominator is renormalizing the absorption due to the radiation coupling in the sample. The denominator gains importance with increasing radiation coupling [166].

A second quantity, which we obtain from the coupling of Maxwell's equations and the excitonic Bloch equations is the radiative lifetime of the exciton. As discussed, the source of the wave equation is the macroscopic polarization, which is determined by the microscopic polarization $P(\omega) = \sum_\mu d_\mu P_\mu(\omega)$ with excitonic dipole element d_μ. On this level, we can combine the Maxwell equations and the excitonic Bloch equations. By plugging the electric field together with the definition of the macroscopic polarization into the Fourier transformed excitonic Bloch equation Eq. (2.49) for a fixed exciton number μ we obtain

$$\hbar\omega P_\mu(\omega) = E_\mu P_\mu(\omega) + d_\mu \cdot \left(E_0(\omega) + i\frac{\omega}{2nc\epsilon_0} d_\mu P_\mu(\omega) \right) . \tag{2.64}$$

From the above equation we can identify the radiative dephasing [158]

$$\gamma_{\text{rad}} = \frac{\omega}{2nc\epsilon_0}|d_\mu|^2 , \tag{2.65}$$

which is determined by the square of the excitonic dipole matrix element satisfying Fermi's golden rule.

Figure 2.5(b) displays the absorption spectrum of WSe$_2$ for the A excitons broadened by a radiativ and non-radiative dephasing [158]. We observe a s-like Rydberg series. The strongest bound $1s$ exciton exhibits also the highest oscillator strength, which is decreasing with increasing exciton number. At last, the spectrum enters the continuum. The energy difference between $1s$ peak and the start of the continuum marks the band gap.

2.7 Excitons in tr-ARPES

2.7.1 Excitonic tr-ARPES theory

As already introduced, photoemission spectroscopy accesses only the occupied density of states. To access excited states and add a time resolution, a pump process is preceding the photoemitting XUV pulse. Typically, in tr-ARPES, the excitation energy of the pump pulse

corresponds to the band gap energy or slightly larger. This injects a non-equilibrium carrier distribution in the unoccupied conduction band, which then can be accessed by the probe pulse. By varying the time delay between pump and probe pulse the dynamics of the excited carriers can be traced directly in momentum space [126]. Two-dimensional semiconductors, such as monolayer transition-metal dichalcogenides, exhibit strongly bound excitons, which dominate the optical properties of these materials. Consequently, we want to address the question, whether excitons do appear in time-resolved ARPES. In this case, the power of tr-ARPES would even increase, since it could not only access quasi-free electrons but also correlated two-particle states and image directly the excitonic Brillouin zone.

The time-resolved photoemission signal is proportional to the total number of electrons per solid angle and energy interval [168, 169]

$$I_{\boldsymbol{k}}(E, \tau) = \frac{dN_{\boldsymbol{k}}(E, \tau)}{d\Omega_{\boldsymbol{k}} dE} \, , \tag{2.66}$$

where τ denotes the time delay between pump and probe pulse. J. K. Freericks and coworkers derived an expression for the photoemission signal solely exploiting the sudden approximation [170]. This approximation assumes that the photoelectrons do not interact with the sample anymore. J. K. Freericks *et al.* find that the signal depends on the matrix element and the one-particle lesser Green's function of the photoelectrons. Therefore, we use the Heisenberg equation of motion to develop a microscopic description of the time and momentum resolved photoemitted vacuum electron distribution $f_{k_\perp, \boldsymbol{k}} = \langle k_{\perp, \boldsymbol{k}}^\dagger k_{\perp, \boldsymbol{k}} \rangle$ [171, 172]. Assuming that the photodetector collects all emitted photoelectrons, we define the tr-ARPES signal as

$$I_{\boldsymbol{k}, \varepsilon_{\boldsymbol{k}, k_\perp}} (\tau) = \lim_{t \to \infty} \int_{-\infty}^{t} dt' \, \partial_{t'} f_{k_\perp, \boldsymbol{k}}(t', \tau) \, . \tag{2.67}$$

The equation of motion of the vacuum electron occupation reads

$$\frac{d}{dt} f_{k_\perp, \boldsymbol{k}} = -2\Im\mathrm{m} \left(\Omega_{\boldsymbol{k}}^{vk_\perp \xi_v} P_{\boldsymbol{k}}^{vk_\perp \xi_v} + \Omega_{\boldsymbol{k}}^{ck_\perp \xi_c} P_{\boldsymbol{k}}^{ck_\perp \xi_c} \right) \, . \tag{2.68}$$

We find that the sources of the vacuum electrons are the photoemission amplitudes of valence and conduction band with the corresponding Rabi frequencies $\Omega_{\boldsymbol{k}}^{vk_\perp \xi_v} = \boldsymbol{d}_{\boldsymbol{k}}^{vk_\perp \xi_v} \cdot \boldsymbol{E}(t)/\hbar$ and $\Omega_{\boldsymbol{k}}^{ck_\perp \xi_c} = \boldsymbol{d}_{\boldsymbol{k}}^{ck_\perp \xi_c} \cdot \boldsymbol{E}(t)/\hbar$, respectively. The photoemission amplitudes are defined as $P_{\boldsymbol{k}}^{vk_\perp \xi_v} = \langle v_{\boldsymbol{k}}^{\dagger \xi_v} k_{\perp, \boldsymbol{k}} \rangle$ and $P_{\boldsymbol{k}}^{ck_\perp \xi_c} = \langle c_{\boldsymbol{k}}^{\dagger \xi_c} k_{\perp, \boldsymbol{k}} \rangle$. For easier insights into the equations with respect to the complex quasi-particle band structure of monolayer TMDCs and the origin of the photoemission, we include at this point a valley index ξ_λ to the fermionic operators. This quantum number indicates the valley location of the electron and $\boldsymbol{k}$ is then defined locally around the corresponding valley. The total wave vector is given by $\boldsymbol{\xi}_\lambda + \boldsymbol{k}$.

Because of the sharp excitation pulse, we can perform a rotating wave approximation for the photoemission amplitudes

$$P_{\boldsymbol{k}}^{\lambda k_\perp}(t) = \tilde{P}_{\boldsymbol{k}}^{\lambda k_\perp}(t) e^{-i\omega_{xuv} t} \tag{2.69}$$

and split off the the rapid carrier frequency pulse oscillation from the XUV pulse. The quantity $\tilde{P}_{\boldsymbol{k}}^{\lambda k_\perp}$ is now a slowly varying envelope. In the following all equations are presented in rotating wave approximation and for the sake of readability the tilde is dropped.

In Eq. (2.68) the vacuum population is determined by the photoemission of uncorrelated valence and conduction band electrons. The procedure to take into account the electron-hole Coulomb coupling for the electrons is based on the unit operator method. This formalism was

originally introduced by A. L. Ivanov and H. Haug to describe exciton-exciton scattering. They suggested a transcription to transfer electron operators to electron-hole pair operators [149,173]. Exploiting the completeness relation of the Fock space [149,173–175] we define a unit operator

$$
\mathbb{1} = |0\rangle\langle 0| + \sum_{\xi_v, \boldsymbol{k}_v} v_{\boldsymbol{k}_v}^{\xi_v} v_{\boldsymbol{k}_v}^{\dagger \xi_v} + \sum_{\xi_c, \boldsymbol{k}_c} c_{\boldsymbol{k}_c}^{\dagger \xi_c} c_{\boldsymbol{k}_c}^{\xi_c} + \sum_{\xi_c, \xi_v, \boldsymbol{k}_c, \boldsymbol{k}_v} c_{\boldsymbol{k}_c}^{\dagger \xi_c} v_{\boldsymbol{k}_v}^{\xi_v} |0\rangle\langle 0| v_{\boldsymbol{k}_v}^{\dagger \xi_v} c_{\boldsymbol{k}_c}^{\xi_c}
$$

$$
+ \sum_{\xi_{c_1}, \xi_{c_2}, \boldsymbol{k}_{c_1}, \boldsymbol{k}_{c_2}} c_{\boldsymbol{k}_{c_1}}^{\dagger \xi_{c_1}} c_{\boldsymbol{k}_{c_2}}^{\dagger \xi_{c_2}} |0\rangle\langle 0| c_{\boldsymbol{k}_{c_2}}^{\xi_{c_2}} c_{\boldsymbol{k}_{c_1}}^{\xi_{c_1}} + \sum_{\xi_{v_1}, \xi_{v_2}, \boldsymbol{k}_{v_1}, \boldsymbol{k}_{v_2}} v_{\boldsymbol{k}_{v_1}}^{\xi_{v_1}} v_{\boldsymbol{k}_{v_2}}^{\xi_{v_2}} |0\rangle\langle 0| v_{\boldsymbol{k}_{v_2}}^{\dagger \xi_{v_2}} v_{\boldsymbol{k}_{v_1}}^{\dagger \xi_{v_1}}
$$

$$
+ \frac{1}{2} \sum_{\xi_{c_1}, \xi_{c_2}, \xi_v, \boldsymbol{k}_{c_1}, \boldsymbol{k}_{c_2}, \boldsymbol{k}_v} c_{\boldsymbol{k}_{c_1}}^{\dagger \xi_{c_1}} v_{\boldsymbol{k}_v}^{\xi_v} c_{\boldsymbol{k}_{c_2}}^{\dagger \xi_{c_2}} |0\rangle\langle 0| c_{\boldsymbol{k}_{c_2}}^{\xi_{c_2}} v_{\boldsymbol{k}_v}^{\dagger \xi_v} c_{\boldsymbol{k}_{c_1}}^{\xi_{c_1}}
$$

$$
+ \frac{1}{2} \sum_{\xi_{v_1}, \xi_{v_2}, \xi_c, \boldsymbol{k}_{v_1}, \boldsymbol{k}_{v_2}, \boldsymbol{k}_c} v_{\boldsymbol{k}_{v_1}}^{\xi_{v_1}} c_{\boldsymbol{k}_c}^{\dagger \xi_c} v_{\boldsymbol{k}_{v_2}}^{\xi_{v_2}} |0\rangle\langle 0| v_{\boldsymbol{k}_{v_2}}^{\dagger \xi_{v_2}} c_{\boldsymbol{k}_c}^{\xi_c} v_{\boldsymbol{k}_{v_1}}^{\dagger \xi_{v_1}} + \mathcal{O}(n_X a_X^2)^2 \tag{2.70}
$$

where n_X denotes the pair (surface) density and a_X the exciton Bohr radius. The conventional semiconductor ground state $|0\rangle$ consists of a completely filled valence and empty conduction band. The expansion of $c_{\boldsymbol{k}}^{\dagger \xi_c} k_{\perp, \boldsymbol{k}}$ in Eq. (2.68) yields

$$
c_{\boldsymbol{k}}^{\dagger \xi_c} k_{\perp, \boldsymbol{k}} = \sum_{\xi_v, \boldsymbol{k}_v} c_{\boldsymbol{k}}^{\dagger \xi_c} v_{\boldsymbol{k}_v}^{\xi_v} |0\rangle\langle 0| v_{\boldsymbol{k}_v}^{\dagger \xi_v} k_{\perp, \boldsymbol{k}}
$$

$$
+ \frac{1}{2} \sum_{\xi_{v_1}, \xi_{v_2}, \xi_{c_2}, \boldsymbol{k}_{v_1}, \boldsymbol{k}_{v_2}, \boldsymbol{k}_{c_2}} c_{\boldsymbol{k}}^{\dagger \xi_c} v_{\boldsymbol{k}_{v_1}}^{\xi_{v_1}} c_{\boldsymbol{k}_{c_2}}^{\dagger \xi_{c_2}} v_{\boldsymbol{k}_{v_2}}^{\xi_{v_2}} |0\rangle\langle 0| v_{\boldsymbol{k}_{v_2}}^{\dagger \xi_{v_2}} c_{\boldsymbol{k}_{c_2}}^{\xi_{c_2}} v_{\boldsymbol{k}_{v_1}}^{\dagger \xi_{v_1}} k_{\perp, \boldsymbol{k}} + \mathcal{O}(n a_X^2)^3 . \tag{2.71}
$$

Note that the expansion has to be performed on the operator level before taking the expectation values. From this procedure the conduction band electron operators are expressed uniquely by electron-hole pair operators. Since we consider a weak optical excitation below the free-particle band gap of an undoped semiconductor only the second contributions to the unit operator needs to be taken into account, which yields the first term of Eq. (2.71). However, to illustrate the method and its power we display also the second order, which stems from the eighth term in Eq. (2.70). In the next step, we need to replace the projection operator. From Eq. (2.70) we obtain $|0\rangle\langle 0| = \mathbb{1} - \sum_{\xi_v, \xi_c, \boldsymbol{k}_v, \boldsymbol{k}_c} c_{\boldsymbol{k}_c}^{\dagger \xi_c} v_{\boldsymbol{k}_v}^{\xi_v} |0\rangle\langle 0| v_{\boldsymbol{k}_v}^{\dagger \xi_v} c_{\boldsymbol{k}_c}^{\xi_c} + \mathcal{O}(n a_x^2)^2$. At this point, the projection operator still depends on itself. Therefore, we insert the expression infinitely often into itself and obtain

$$
|0\rangle\langle 0| = \mathbb{1} - \sum_{\xi_v, \xi_c, \boldsymbol{k}_v, \boldsymbol{k}_c} c_{\boldsymbol{k}_c}^{\dagger \xi_c} v_{\boldsymbol{k}_v}^{\xi_v} \left(\mathbb{1} + \mathcal{O}(n a_X^2) \right) v_{\boldsymbol{k}_v}^{\dagger \xi_v} c_{\boldsymbol{k}_c}^{\xi_c} . \tag{2.72}
$$

By combining Eq. (2.71) and Eq. (2.72), we find the final expression of the electron photoemission amplitude in terms of electron-hole pairs:

$$
c_{\boldsymbol{k}}^{\dagger \xi_c} k_{\perp, \boldsymbol{k}} = \sum_{\xi_v, \boldsymbol{k}_v} c_{\boldsymbol{k}}^{\dagger \xi_c} v_{\boldsymbol{k}_v}^{\xi_v} v_{\boldsymbol{k}_v}^{\dagger \xi_v} k_{\perp, \boldsymbol{k}}
$$

$$
- \frac{1}{2} \sum_{\xi_{v_1}, \xi_{v_2}, \xi_{c_2}, \boldsymbol{k}_{v_1}, \boldsymbol{k}_{v_2}, \boldsymbol{k}_{c_2}} c_{\boldsymbol{k}}^{\dagger \xi_c} v_{\boldsymbol{k}_{v_1}}^{\xi_{v_1}} c_{\boldsymbol{k}_{c_2}}^{\dagger \xi_{c_2}} v_{\boldsymbol{k}_{v_2}}^{\xi_{v_2}} v_{\boldsymbol{k}_{v_2}}^{\dagger \xi_{v_2}} c_{\boldsymbol{k}_{c_2}}^{\xi_{c_2}} v_{\boldsymbol{k}_{v_1}}^{\dagger \xi_{v_1}} k_{\perp, \boldsymbol{k}} + \mathcal{O}(n a_X^2)^3 . \tag{2.73}
$$

Since we restrict ourself to the low excitation regime only the first term is relevant and the second contribution neglected from now on. In a similar way we expand the valence band electrons in $v_{\boldsymbol{k}}^{\dagger \xi_v} k_{\perp, \boldsymbol{k}}$ of Eq. (2.68), which yields in lowest order

$$
v_{\boldsymbol{k}}^{\dagger \xi_v} k_{\perp, \boldsymbol{k}} = \sum_{\xi_c, \boldsymbol{k}_c} v_{\boldsymbol{k}}^{\dagger \xi_v} c_{\boldsymbol{k}_c}^{\dagger \xi_c} c_{\boldsymbol{k}_c}^{\xi_c} k_{\perp, \boldsymbol{k}} = v_{\boldsymbol{k}}^{\dagger \xi_v} k_{\perp, \boldsymbol{k}} - \sum_{\xi_c, \boldsymbol{k}_c} v_{\boldsymbol{k}}^{\dagger \xi_v} c_{\boldsymbol{k}_c}^{\xi_c} c_{\boldsymbol{k}_c}^{\dagger \xi_c} k_{\perp, \boldsymbol{k}} . \tag{2.74}
$$

Here, the situation is different. We find that the electron-hole Coulomb interaction leads to corrections of $v_{\boldsymbol{k}}^{\dagger \xi_v} k_{\perp,\boldsymbol{k}}$. Due to the weak excitation the valence band occupation satisfies $f_{v,\boldsymbol{k}}^{\xi_v} \approx 1$ for all investigated scenarios. As consequence the term $v_{\boldsymbol{k}}^{\dagger \xi_v} k_{\perp,\boldsymbol{k}}$ is dominating compared to the many-body correction justifying the neglect of the Coulomb correction to the valence band electrons. To treat the quantum mechanical hierarchy problem arising from the many-particle interaction we exploit the cluster expansion scheme [151–153].

In the lowest order the equation of motion Eq. (2.68) becomes

$$\frac{d}{dt} f_{k_\perp,\boldsymbol{k}} = -2\Im\mathrm{m} \left(\Omega_{\boldsymbol{k}}^{vk_\perp \xi_v} P_{\boldsymbol{k}}^{vk_\perp \xi_v} + \Omega_{\boldsymbol{k}}^{ck_\perp \xi_c} p_{\boldsymbol{k}}^{*\xi_v \xi_c} P_{\boldsymbol{k}}^{vk_\perp \xi_v} e^{-\frac{1}{i\hbar}\varepsilon_{vis}t} + \sum_{\xi_v,\boldsymbol{k}_v} \Omega_{\boldsymbol{k}}^{ck_\perp \xi_c} \delta\langle p_{\boldsymbol{k}_v,\boldsymbol{k}}^{\dagger \xi_v \xi_c} P_{\boldsymbol{k}_v}^{vk_\perp \xi_v}\rangle \right) .$$

$$(2.75)$$

The first term describes photoemission of the filled valence band. The second and third term stems from the photoemission amplitude of the conduction band electrons. In the former we identify the interband transition $p_{\boldsymbol{k}}^{*\xi_v \xi_c}$, which couples to the photoemission amplitude of valence band electrons. The interband transition is driven by the VIS pump laser and strongly off-resonant to the XUV pulse. Therefore, the valence-conduction band transition is written in rotating wave approximation with decoupled fast oscillation with frequency of the exciting pump laser pulse $\varepsilon_{vis}/\hbar$. The last term corresponds to the Coulomb-correlated photoemission.

First we turn our attention to the kinetics of the photoemission amplitude of valence band electrons:

$$i\hbar\frac{d}{dt} P_{\boldsymbol{k}}^{vk_\perp \xi_v} = \left(\varepsilon_{k_\perp,\boldsymbol{k}} - \varepsilon_{v,\boldsymbol{k}}^{\xi_v} - \varepsilon_{xuv} \right) P_{\boldsymbol{k}}^{vk_\perp \xi_v} + i\hbar\partial_t P_{\boldsymbol{k}}^{vk_\perp \xi_v}|_{\mathrm{coll}}$$
$$+ \hbar\Omega_{\boldsymbol{k}}^{k_\perp v\xi_v} f_{v,\boldsymbol{k}}^{\xi_v} + \hbar\Omega_{\boldsymbol{k}}^{k_\perp c\xi_c} p_{\boldsymbol{k}}^{\xi_v \xi_c} \; e^{\frac{1}{i\hbar}\varepsilon_{vis}t} .$$

$$(2.76)$$

The free oscillation carries the kinetic energy of the photoelectron, the valence band dispersion and the excitation energy of the XUV pulse. The second term summarizes higher-order correlations from electron-electron and electron-phonon interaction, which lead to a dephasing of the transition. The last two terms are the sources. First of all, the transition is driven by the valence band occupation but couples also to the interband transition both mediated by the XUV pulse.

The correlated photoemission reads

$$i\hbar\frac{d}{dt}\delta\langle p_{\boldsymbol{k}_v,\boldsymbol{k}}^{\dagger \xi_v \xi_c} P_{\boldsymbol{k}_v}^{vk_\perp \xi_v}\rangle = \left(\varepsilon_{k_\perp,\boldsymbol{k}} + \varepsilon_{v,\boldsymbol{k}_v}^{\xi_v} - \varepsilon_{v,\boldsymbol{k}_v}^{\xi_v} - \varepsilon_{c,\boldsymbol{k}}^{\xi_c} - \varepsilon_{xuv} \right) \delta\langle p_{\boldsymbol{k}_v,\boldsymbol{k}}^{\dagger \xi_v \xi_c} P_{\boldsymbol{k}_v}^{vk_\perp \xi_v}\rangle$$
$$+ i\hbar\partial_t \delta\langle p_{\boldsymbol{k}_v,\boldsymbol{k}}^{\dagger \xi_v \xi_c} P_{\boldsymbol{k}_v}^{vk_\perp \xi_v}\rangle|_{\mathrm{coll}}$$
$$+ \sum_{\boldsymbol{q}} V_{\boldsymbol{q}}^{cv\xi_c \xi_v} \; \left(f_{v,\boldsymbol{k}_v+\boldsymbol{q}}^{\xi_v} - f_{c,\boldsymbol{k}+\boldsymbol{q}}^{\xi_c} \right) \delta\langle p_{\boldsymbol{k}_v+\boldsymbol{q},\boldsymbol{k}+\boldsymbol{q}}^{\dagger \xi_v \xi_c} P_{\boldsymbol{k}_v}^{vk_\perp \xi_v}\rangle$$
$$+ \hbar\Omega_{\boldsymbol{k}}^{k_\perp c\xi_c} \; \delta\langle p_{\boldsymbol{k}_v,\boldsymbol{k}}^{\dagger \xi_v \xi_c} p_{\boldsymbol{k}_v,\boldsymbol{k}}^{\xi_v \xi_c}\rangle .$$

$$(2.77)$$

Again, we find a free oscillation with the single-particle energies and a collision term simulating a dephasing. The attractive Coulomb interaction attacks the electron-hole pair constituting the photoemission transition (third line), which is optically driven by the interband Coulomb correlations (last line). Generally, the vacuum occupation is assumed to be small compared to the valence band and electron-hole occupations and therefore neglected as Pauli-blocking factor, which was also done in Eq. (2.76).
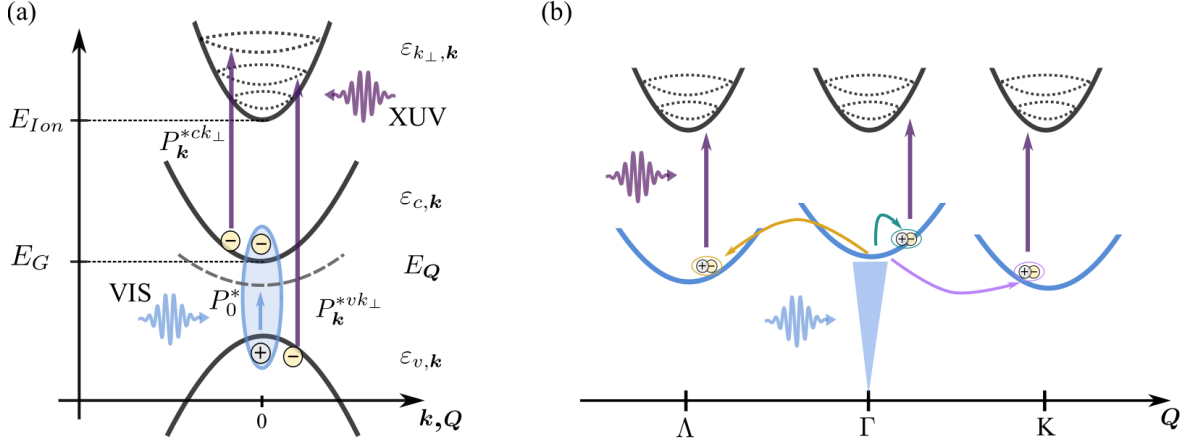
Figure 2.6: (a) Sketch of the possible transitions in tr-ARPES for a two-band semiconductor with an excitonic state (grey dashed). The VIS pump pulse excites an excitonic transition and the XUV probe pulse can photoemit either valence or conduction band electrons. (b) Photoemission sketch from a complex excitonic band structure. The optically excited excitonic transition in the light cone decay into incoherent Γ excitons due to intravalley phonon scattering. Additionally, also intervalley phonon scattering is possible leading to momentum indirect excitons with electron and hole at different high symmetry points. The XUV pulse can photoemit electrons, which are bound into Γ excitons but also electrons, which form the momentum-indirect intervalley excitons. Figure is similarly published in Ref. [125]

Transforming to the exciton picture, we find an expression for the photoemission signal Eq. (2.75)

$$\frac{d}{dt}f_{k_\perp,\boldsymbol{k}} = -2\Im\mathrm{m}\left(\Omega_{\boldsymbol{k}}^{vk_\perp\xi_v}P_{\boldsymbol{k}}^{vk_\perp\xi_v} + \sum_\mu \Omega_{\mu,\boldsymbol{k}}^{ck_\perp\xi_c-}P_{\mu,0}^{*\xi_v\xi_c}P_{\boldsymbol{k}}^{vk_\perp\xi_v} + \sum_{\mu,\xi_v,\boldsymbol{Q}}\Omega_{\mu,\boldsymbol{k},\boldsymbol{Q}}^{ck_\perp\xi_c}\delta\langle P_{\mu,\boldsymbol{Q}}^{\dagger\xi_v\xi_c}P_{\boldsymbol{k}-\boldsymbol{Q}}^{vk_\perp\xi_v}\rangle\right)$$

$$(2.78)$$

with the coupling elements $\Omega_{\mu,\boldsymbol{k}}^{ck_\perp\xi_c-} = \Omega_{\boldsymbol{k}}^{ck_\perp\xi_c}\varphi_{\mu,\boldsymbol{k}}^{*\xi_v\xi_c}e^{-\frac{1}{i\hbar}\varepsilon_{vis}t}$ and $\Omega_{\mu,\boldsymbol{k},\boldsymbol{Q}}^{ck_\perp\xi_c} = \Omega_{\boldsymbol{k}}^{ck_\perp\xi_c}\varphi_{\mu,\boldsymbol{k}-\alpha_{\xi_v}^{\xi_c}\boldsymbol{Q}}^{*\xi_v\xi_c}$. Within the low excitation limit, we find three different sources for the photoemission signal.

Obviously, we find the photoemission of valence band electrons contributing to the photoemission signal. It will lead to an image of the occupied valence band. In term two we identify the exciton transition with vanishing center-of-mass momentum, described by Eq. (2.49), which couples to the photoemission amplitude of valence band electrons. Since the exciton transition is restricted to the $K_\pm$ points, the second term will only contribute at these high symmetry points to the tr-ARPES signal. The corresponding matrix element is determined by the exciton wave function and carries a rapidly oscillating phase stemming from the pump-driven transition. And finally, the last term can be identified as exciton-assisted photoemission including a finite center-of-mass momentum. The latter is described by

$$i\hbar\frac{d}{dt}\delta\langle P_{\mu,\boldsymbol{Q}}^{\dagger\xi_v\xi_c}P_{\boldsymbol{k}-\boldsymbol{Q}}^{vk_\perp\xi_v}\rangle = \left(\varepsilon_{k_\perp,\boldsymbol{k}} - \varepsilon_{v,\boldsymbol{k}-\boldsymbol{Q}}^{\xi_v} - E_{\mu,\boldsymbol{Q}}^{\xi_v\xi_c} - \varepsilon_{xuv}\right)\delta\langle P_{\mu,\boldsymbol{Q}}^{\dagger\xi_v\xi_c}P_{\boldsymbol{k}-\boldsymbol{Q}}^{vk_\perp\xi_v}\rangle$$

$$+ i\hbar\partial_t\delta\langle P_{\mu,\boldsymbol{Q}}^{\dagger\xi_v\xi_c}P_{\boldsymbol{k}-\boldsymbol{Q}}^{vk_\perp\xi_v}\rangle|_{\mathrm{coll}} + \hbar\sum_\lambda \tilde{\Omega}_{\mu,\lambda,\boldsymbol{k},\boldsymbol{Q}}^{k_\perp c\xi_v\xi_c}N_{\lambda,\boldsymbol{Q}}^{\xi_v\xi_c} \qquad (2.79)$$

with $\tilde{\Omega}^{k_\perp c \xi_v \xi_c}_{\mu,\lambda,\boldsymbol{k},\boldsymbol{Q}} = \Omega^{k_\perp c \xi_c}_{\boldsymbol{k}} |\varphi^{\xi_v \xi_c}_{\lambda,\boldsymbol{k}-\alpha^{\xi_c}_{\xi_v}\boldsymbol{Q}}|^2 \varphi^{\xi_v \xi_c}_{\mu,\boldsymbol{k}-\alpha^{\xi_c}_{\xi_v}\boldsymbol{Q}}$. We see that in the gap dispersion the exciton energy explicitly appears. Further, the exciton-assisted photoemission is directly driven by incoherent excitons. We can therefore expect that the information on the bound TMDC excitons and their incoherent scattering dynamics is encoded in this quantity. Finally, we give also the photoemission amplitude for valence band electrons in exciton basis:

$$
i\hbar \frac{d}{dt} P^{vk_\perp \xi_v}_{\boldsymbol{k}} = \left(\varepsilon_{k_\perp,\boldsymbol{k}} - \varepsilon^{\xi_v}_{v,\boldsymbol{k}} - \varepsilon_{xuv} \right) P^{vk_\perp \xi_v}_{\boldsymbol{k}} + i\hbar \partial_t P^{vk_\perp \xi_v}_{\boldsymbol{k}}|_{\text{coll}}
$$
$$
+ \hbar \Omega^{k_\perp v \xi_v}_{\boldsymbol{k}} f^{\xi_v}_{v,\boldsymbol{k}} + \hbar \sum_{\mu,\xi_c} \Omega^{k_\perp c \xi_c +}_{\mu,\boldsymbol{k}} P^{\xi_v \xi_c}_{\mu,0} \delta_{\xi_c,\text{K}_\pm} \tag{2.80}
$$

with $\Omega^{k_\perp c \xi_c +}_{\mu,\boldsymbol{k}} = \Omega^{k_\perp c \xi_c}_{\boldsymbol{k}} \varphi^{\xi_v \xi_c}_{\mu,\boldsymbol{k}} \, e^{\frac{1}{i\hbar} \varepsilon_{vis} t}$. We see that the second source with appearing exciton transition is counter-rotating to the second contribution of the tr-ARPES signal Eq. (2.78). Consequently, source two of the tr-ARPES signal is slowly oscillating and contributes to the signal. Figure 2.6 (a) displays a sketch of the tr-ARPES transitions for a two-band semiconductor, for example by restricting the Brillouin zone to the K_+ point. The sketch shows the possible induced optical transitions namely the below band gap interband transition and the photoemission amplitudes from two-dimensional electronic states into the three-dimensional ionization continuum. Figure 2.6(b) transforms into the excitonic picture and extends to a multivalley situation. Excitons are optically injected in the light cone. Subsequent exciton-phonon interaction leads to a transfer to incoherent excitons with finite center-of-mass momentum, which form the source of the correlated photoemission amplitude Eq. (2.79).

2.7.2   Exciton dynamics in tr-ARPES

In the following, we investigate in detail the material WSe_2 as exemplary material for tungsten-based TMDCs. Afterwards, we compare with MoSe_2 representing the molybdenum-based TMDCs. We focus on the $1s$ exciton justified by the large energetic $1s$-$2s$ separation compared to the thermal energy. In terms of equations, the exciton number can be dropped. While the pump pulse is chosen to excite resonantly the exciton, i.e. $\varepsilon_{vis} = E_{1s}$, the XUV probe pulse has an excitation energy of 20 eV. The pulses are assumed to be Gaussians with intensity widths of 35 fs and 20 fs for VIS and XUV, respectively. The temperature is fixed to 77 K. At room temperature we can expect a similar behavior but with more efficient exciton-phonon scattering.

We start with a pump-probe delay of 25 fs corresponding to the coherent limit with slightly overlapping pump and probe pulses. Figure 2.7(a) displays the calculated tr-ARPES signal. Note that the k-axis lies at the K point. At 0 eV we obtain a direct image of the valence band, which curvature is determined by its effective mass, and is described by the first term in Eq. (2.78). In principle, a reduced intensity at the maximum could reflect the excited hole occupation. However, since in the low-excitation limit this contribution is vanishing small, a fingerprint of the holes is not observed. Second, we observe a strong signal at the exciton energy clearly lying below the free-particle band gap shown as grey dashed line. The excitonic signal has two contributions: from coherent and incoherent excitons described by source two and three of Eq. (2.78), respectively. Figure 2.7(b) and (c) display the tr-ARPES signal in case of artificially turned off incoherent (b) or coherent (c) excitons. Comparing to the full signal we recognize that the tr-ARPES signal at such short time delays is mainly dominated by the coherent exciton, described by the second term in Eq. (2.78). Since it consists of a product of exciton coherence and photoemission of valence band electrons, it contributes only as long as the exciton transition does not vanish. Consequently, this signal directly reflects
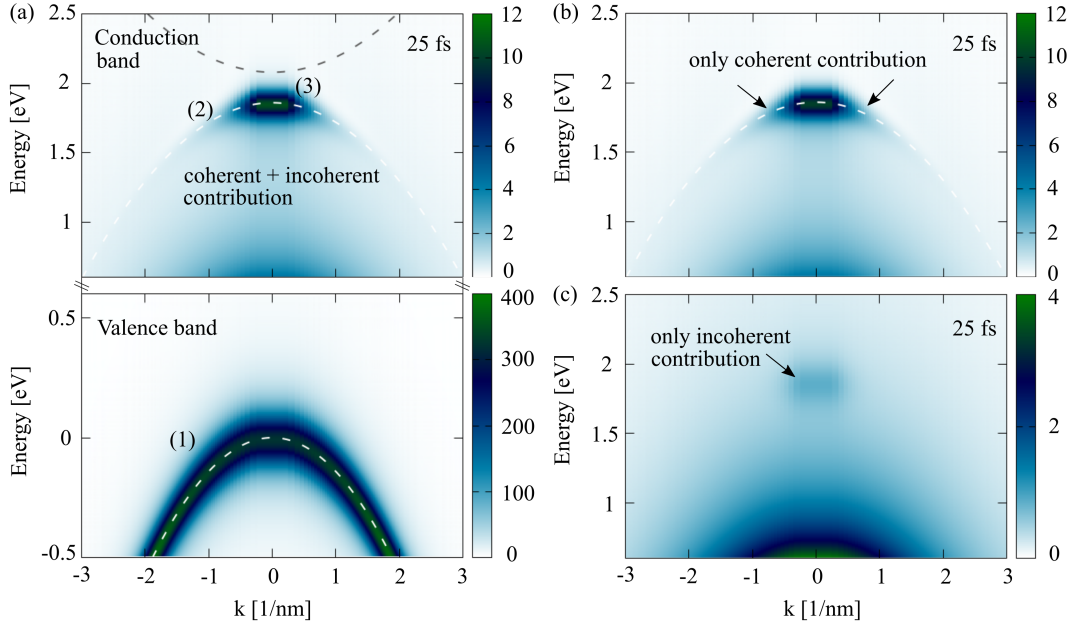
Figure 2.7: (a) Calculated tr-ARPES signal at 25 fs delay time imaging the completely filled valence band and a signal at the exciton energy below the free-particle band gap (grey dashed). The excitonic signal displays a shadow of the valence band (white dashed). (b) Tr-ARPES signal from the coherent source. (c) Tr-ARPES signal from the incoherent source. Figure is similarly published in Ref. [125]

the coherence lifetime of the exciton, sometimes referred to as T_2-time. Interestingly, we see that the excitonic signal at $k = 0$ exhibits a shadow of the valence band. To clarify this, we plot the valence band dispersion as white dashed line and see a perfect match between signal and dispersion. This intriguing signal stems from the fact that the photoemission amplitude of valence band electrons couples to the exciton transition, which has vanishing center-of-mass momentum. In terms of an assisted-transition picture, we can regard the photoemission process of excitons as a recombination of an exciton with immediate photoemission of the created valence band electron. This picturesquely describes, why we see a signal at the exciton energy, which was gained during the annihilation, and which exhibits a valence band shape. However, this picture suggests a two-step process, which is not necessary. Since the signal is driven by the exciton transition, which is bound to the $K_\pm$ points, it exists only at these high symmetry points. Further, we see that the signal's intensity decreases for increasing wave number.

To obtain more analytical insights into the coherent tr-ARPES signal, we can formally integrate the equations Eq. (2.78), (2.80), and (2.49), assuming exponentially shaped pulses of the form $\exp(-|t - \tau|/\sigma)$ with width σ. In the limit of $\sigma \to 0$ we find for the coherent tr-ARPES signal

$$I_{\boldsymbol{k}}(\varepsilon_{k_\perp,\boldsymbol{k}}) \propto |\varphi_{\boldsymbol{k}}|^2 \delta\left(\varepsilon_{k_\perp,\boldsymbol{k}} - \varepsilon_{xuv} - E_{1s} - \varepsilon_{v,\boldsymbol{k}}\right) . \tag{2.81}$$

From the delta-function, we clearly see that the signal lies at the exciton energy with a valence band dispersion contribution stemming from the hole left in the sample during the photoemission of the Coulomb-bound electron to ensure energy conservation. In experiments it is now possible to first pump strongly far above the band gap to excite a non-equilibrium

electron distribution and in a second experiment pump around the exciton energy. From the energy difference between the tr-ARPES signals the exciton binding energy can be measured [176]. Additionally, we see in Eq. (2.81) that the signal is directly proportional to the exciton wave function squared. This suggests that the decrease of the intensity along the valence band shadow could be related to the exciton wave function. To gain more insights, we plot in Fig. 2.8(a) the tr-ARPES signal with artificially turned off valence band and vanishing incoherent excitons $N_{\bm{Q}}^{\xi_v \xi_c} = 0$. Here, the valence band artifact can be observed even better since the contribution of the strongly overshining valence band is absent. From this signal, we plot in Fig. 2.8(a) the momentum distribution curve (MDC), which is defined as

$$I_{\bm{k}}(\tau) = \int_{-\infty}^{\infty} d\varepsilon_{k_z} \ I_{\bm{k}, \varepsilon_{\bm{k}, k_z}}(\tau) \tag{2.82}$$

and integrates over the energy axis. We clearly see in the inset of Fig. 2.8(a), how the MDC is overlapping with the exciton wave function squared obtained as solution of the Wannier equation. Therefore, we conclude that in the ultrafast coherent limit tr-ARPES is a technique to image the exciton wave function and measure the exciton Bohr radius in momentum space [125, 177]. Via a two-dimensional Fourier transform of the MDC it is even possible to visualize the electron-hole distribution in real space [176, 178]. Important is that the square root of the MDC is Fourier transformed since the tr-ARPES signal is proportional to the wave function squared. A direct Fourier transformation of the MDC would correspond to a convolution of the real space wave function with itself. In Fig. 2.8(b) we show the Fourier transform of the MDC, the real space exciton wave function, and the obtained radial distribution, which forms the traditional definition of the Bohr radius of a two-dimensional hydrogen model. Because of the non-hydrogenic character of the TMDC excitons we define the spatial extension of an exciton via the root mean square defined as $\sqrt{\langle \varphi_{1s} | r^2 | \varphi_{1s} \rangle}$ [179]. We find a root mean square of 1.6 nm, which differs from the peak of the radial distribution and extents over multiple unit cells.

Finally, we discuss the weak incoherent contribution to the signal, cf. Fig. 2.7(c). It stems from incoherent KK excitons localized at the exciton energy. Since they form due to exciton-phonon scattering of optically excited coherent excitons, a certain built up time is necessary. Therefore, at 25 fs the number of formed incoherent excitons is low compared to coherent excitons and contributes only weakly to the signal. Compared to the coherent signal, the incoherent signal is blurred out and does not show the clear valence band shadow anymore. The reason is that in the incoherent limit thermally distributed excitons are present with finite center-of-mass momentum. The signal is now determined by a convolution of the valence band with the exciton dispersion, distribution and exciton wave function, cf. Eq. (2.78) last term and Eq. (2.79).

After having investigated the tr-ARPES signal at short delay times around the K point, we extent the study to large delay times including all high symmetry points of the hexagonal Brillouin zone. First, we choose a pump-probe delay time of 400 fs being much larger than the typical exciton-phonon scattering times in monolayer TMDCs [163]. In Fig. 2.9(a) we recognize a strong signal at the Λ valley, which stems from momentum-indirect KΛ excitons with hole at the K and electron at the Λ valley. As already discussed for the coherent limit, one could expect also at the Λ valley an artifact of the hole. Since it remained at the K point the curvature would correspond to the effective hole mass at the K instead of the Λ valley. However, since the signal is convoluted with the thermally distributed excitons it not observable anymore and difficult to extract as already discussed at the K point. In Fig. 2.9(a), a weaker intensity remains at the K point, which has its origin in momentum-indirect KK$_-$
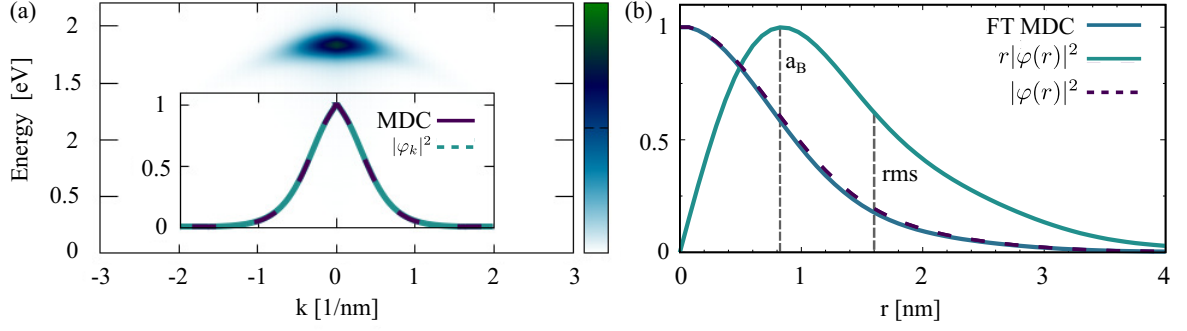
Figure 2.8: (a) Excitonic tr-ARPES signal with artificially turned off valence band. The inset shows the MDC of the tr-ARPES signal and the squared exciton wave function in momentum space. We see that both quantities perfectly coincide. (b) Also in real space, the Fourier transformed tr-ARPES signal and the squared exciton wave function perfectly match. Additionally, we show an analogue of the radial distribution function defined as $r|I(r)|^2$, which forms the traditional Bohr radius definition. The peak and the root mean square value differ by about a factor of two.

excitons. Note, that we show the tr-ARPES signal as function of absolute value of the in-plane wave vector. Therefore, all three Λ valleys contribute equally to the observed signal at the Λ point in Fig. 2.9(a). Additionally, since KK_- excitons have a center-of-mass momentum of $Q = K$ they are refolded to the K-point. Comparing the intensities suggests that the KK excitons scatter about equally into $K\Lambda$ and KK_- excitons, where they thermalize. The reason is that these momentum-indirect excitons lie energetically below the optically excited KK excitons. At last, we want to stress that if the tr-ARPES signal is investigated as cut through the Brillouin zone along the high symmetry traces all valleys and corresponding excitons could be resolved individually.

To trace the exciton dynamics, we show in Fig. 2.9(b)-(e) the energy distribution curves (EDC) for different time delays. The EDC is defined as cut of the tr-ARPES signal at a constant wave number. Generally, the first peak stems from the valence band at the K-point and is independent of the delay time. Since the valence band at the Λ valley lies energetically far away and plays no role for the exciton dynamics it is neglected. The peaks around $1.8\,\text{eV}$ can be related to the excitons. We can nicely see, for increasing delay time, the relaxation into the momentum-indirect exciton states. Only recently, it has been successful to access excitons in tr-ARPES experimentally and resolve the predicted momentum-indirect excitons [176, 180].

At the end, we briefly discuss the influence of the Coulomb corrections to the valence band electrons, which has been neglected. The excitonic correction reads

$$P_{\boldsymbol{k}}^{vk\perp\xi_v} = P_{\boldsymbol{k}}^{vk\perp\xi_v} - \sum_{\mu,\xi_c} \varphi_{\mu,\boldsymbol{k}}^{\xi_v\xi_c} P_{\mu,0}^{\xi_v\xi_c} P_{\boldsymbol{k}}^{ck\perp\xi_c} - \sum_{\mu,\xi_c,\mathbf{Q}} \varphi_{\mu,\boldsymbol{k}+\beta_{\xi_v}^{\xi_c}\mathbf{Q}}^{\xi_v\xi_c} \delta \langle P_{\mu,\mathbf{Q}}^{\xi_v\xi_c} P_{\boldsymbol{k}+\boldsymbol{Q}}^{ck\perp\xi_c} \rangle . \tag{2.83}$$

The correlated two-particle quantity is driven by the incoherent bound excitons and would lead to an excitonic satellite at the exciton binding energy above the valence band. The second term couples the excitonic transition with an unbound electron-hole plasma. This contribution would lead to a shadow of the conduction band above the valence band at the exciton binding energy [181]. However, these signals should be rather small compared to the dominant signal from the valence band, especially in the case of low excitation density.
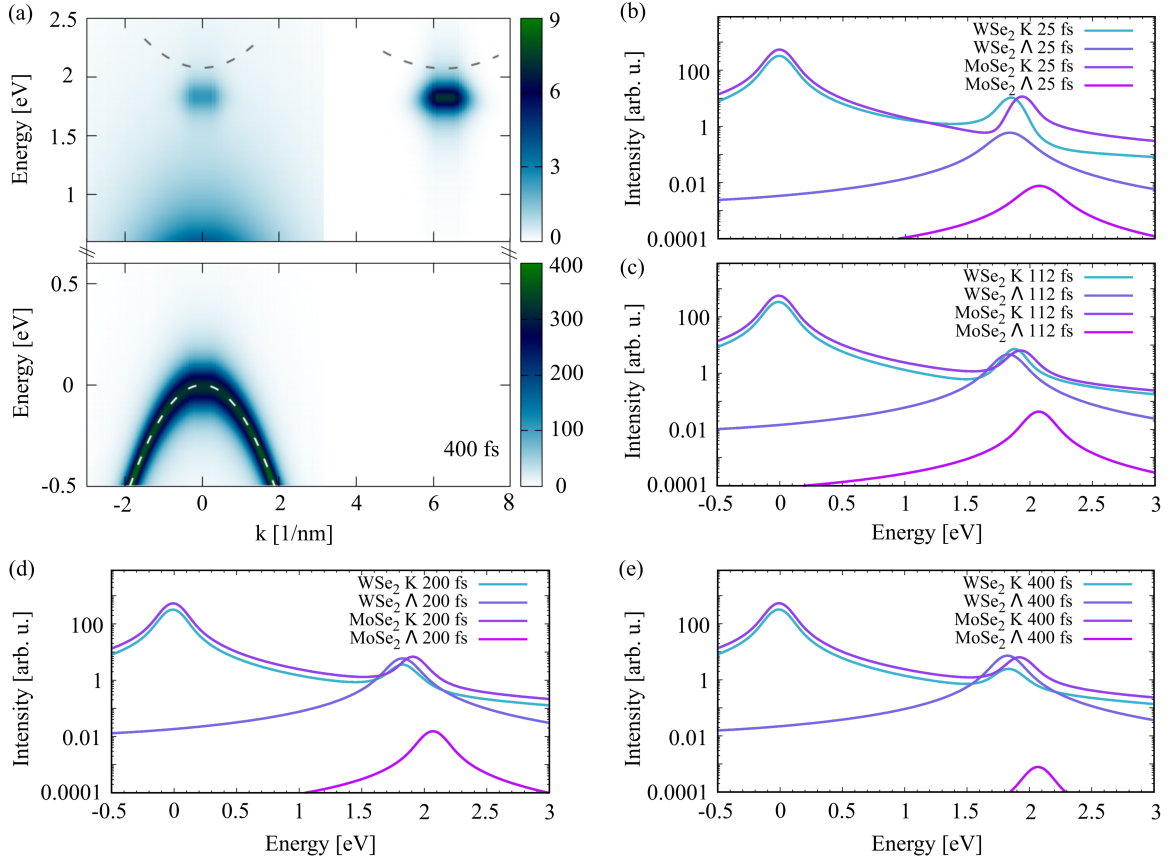
Figure 2.9: (a) Calculated WSe$_2$ tr-ARPES signal at 400 fs pump-probe delay. The momentum-indirect KΛ excitons are directly resolved. The remaining signal at the K point stems from momentum-indirect KK$_-$. (b)-(e) EDCs of WSe$_2$ and MoSe$_2$ at the K and Λ point for different delay times resolving the phonon-induced exciton scattering. WSe$_2$ is characterized by exciton-phonon scattering into momentum-indirect states. Note the logarithmic scale.

So far, we investigated in detail the tr-ARPES signal of WSe$_2$ after resonant exciton excitation. Now, we compare the EDCs of the tr-ARPES signal at different time delays between WSe$_2$ and MoSe$_2$, shown in Fig. 2.9(b)-(e). Based on the exciton relaxation dynamics, which we resolve by tr-ARPES, we find a crucial difference in the excitonic band structure between both materials. For tungsten-based TMDCs, the KΛ and KK$_-$ excitons lie energetically below the optically excited KK exciton. In contrast, for molybdenum-based TMDCs the KK excitons form the global minimum. While for WSe$_2$ the relaxation and thermalization is mediated by intervalley phonons providing the necessary momentum to access the lower lying momentum-indirect exciton states, the scattering dynamics in MoSe$_2$ is determined by intravalley scattering. Optical excitation, phonon-mediated formation, and subsequent relaxation and thermalization is restricted mainly to the K valley.

2.7.3 Non-resonant exciton excitation

So far, we excited the 1s exciton perfectly resonant. Next, we investigate the EDCs when the pump excitation energy is slightly detuned to the 1s exciton resonance. The first consequence

Figure 2.10: (a) Energy distribution curve of coherent tr-ARPES at 25 fs pump-probe delay for detuned excitation. We observe an energetic shift of the EDC corresponding to the detuning. (b) Energy distribution curve at 25 fs pump-probe delay for detuned excitation solely taking incoherent excitons into account. The signal is energetically independent of the excitation condition.

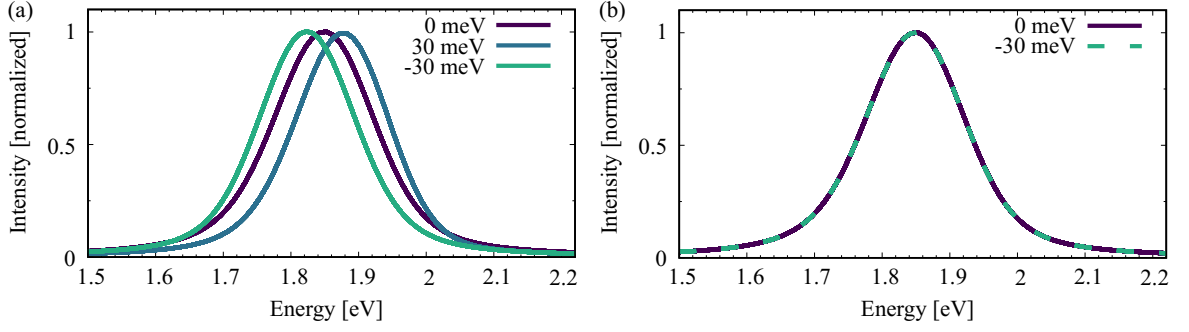is, that the phonon-assisted transitions can not be solved in a Born-Markov approximation anymore. Instead they have to be solved dynamically together with the exciton formation and relaxation. Generally, the detuned excitation leads to smaller injection of excitons in the sample.

For the investigation of the tr-ARPES signal, we split the signal into its coherent and incoherent contribution. Figure 2.10(a) displays the obtained EDCs. Generally, from Fig. 2.10 we can see that the coherent signal shifts energetically depending on the excitation energy of the pump pulse. The reason is that the exciton transition P_0 oscillates with the pump excitation energy. Comparing with Eq. (2.78), we see that this determines the energetic position of the tr-ARPES signal. In contrast, the incoherent signal is independent of the excitation condition. Therefore, the signal lies always at the exciton energy. We can conclude, when exciting the exciton slightly detuned, the tr-ARPES signal lies first at the pump energy and shifts energetically with time to the real exciton energy.

2.8 Coherent-pump Fourier transform ARPES

We developed an excitonic tr-ARPES theory, which shows that the tightly bound excitons contribute to the photoemission signal and that their dynamics can be resolved over the Brillouin zone. In principle, the coherent signal, which leads to a weak valence band signal at the exciton energy reflects the coherence lifetime of the exciton. The coherence lifetime is directly related to the exciton linewidth measured in absorption experiments. However, since the simultaneous formation of incoherent excitons contributes to the same signal, it is difficult to extract directly the coherence lifetime from tr-ARPES. We suggest, together with Michele Puppin from the École polytechnique fédérale de Lausanne, a slightly different setup by combining a coherent tr-ARPES experiment with a second VIS pulse. The interference of both pump pulses should enable the extraction of the coherence lifetime. Figure 2.11(a) sketches the setup. The coherent tr-ARPES consists of a simultaneuous VIS and XUV pulse ($\tau = 0$) at a fixed time. A second VIS pulse irradiates the sample at time delay T with respect to the coherent tr-ARPES. The tr-ARPES signal is then investigated as function of time delay T. For $T > 0$ the second VIS pulse arrives before the tr-ARPES pulses, while for $T < 0$ the second VIS pulses arrives afterwards.

The equation of motion for the excitonic transition in rotating wave approximation and driven by two exciton resonant pump pulses reads

$$i\hbar \frac{d}{dt} P_0(t,T) = -i\gamma P_0(t,T) + \hbar\Omega(t) + \hbar\Omega(t-T)e^{i\omega_X T} \qquad (2.84)$$

where the second pump pulse arrives at $t-T$ compared to the first one. The pulse width and intensity of both pumps are identical. The exciton frequency corresponds to $E_{1s}/\hbar \equiv E_X/\hbar = \omega_X$. From the developed tr-ARPES theory, we know that the excitonic transition enters the coherent tr-ARPES signal and drives the photoemission amplitude of valence band electrons. Since we are only interested in coherent processes and we have previously seen that the amount of incoherent excitons is very low for small VIS-XUV delays, we neglect the incoherent contribution. Additionally, we take the tr-ARPES signal at $k=0$. To obtain first insights, we can formally integrate all equations and obtain

$$f(T) = \int_{-\infty}^{\infty} dt \; \partial_t f(t,T) \qquad (2.85)$$

$$\frac{d}{dt} f(t,T) = -2\Im\mathrm{m} \left[i|\Omega|^2 |\Omega_{xuv}|^2 E_{xuv}(t)e^{(iE_X - i\Delta\varepsilon - \gamma)t/\hbar} \right.$$

$$\times \left(\int_{-\infty}^{t} dt' \; e^{\gamma t'/\hbar} E(t') + e^{i\omega_X T} \int_{-\infty}^{t} dt' \; e^{\gamma t'/\hbar} E(t'-T) \right)$$

$$\times \int_{-\infty}^{t} dt' \; e^{(i\Delta\varepsilon - iE_X + \gamma)t'/\hbar} E_{xuv}(t') \left. \left(\int_{-\infty}^{t'} dt'' \; e^{-\gamma t''/\hbar} E(t'') + e^{i\omega_X T} \int_{-\infty}^{t'} dt'' \; e^{\gamma t''/\hbar} E(t''-T) \right) \right].$$

$$(2.86)$$

We define the Rabi-frequencies Ω and Ω_{xuv} now as the dot product of dipole element and polarization vector and $E(t)$ and $E_{xuv}(t)$ denote the pulse envelopes. E_X denotes the exciton energy and $\Delta\varepsilon = \varepsilon_{k_\perp} - \varepsilon_v - \varepsilon_{xuv}$. The tr-ARPES signal in time domain is a difficult expression consisting of multiple convolutions of pulse envelops and exponential functions carrying the exciton dephasing γ. For Gaussian pulses the integral has no analytical solution. Therefore, as first attack, we assume delta-sharp pulses for pump and probe. Then, we can solve the above integrals and obtain for the tr-ARPES signal

$$f(T) = -4|\Omega|^2 |\Omega_{xuv}|^2 \cos(\omega_X T)e^{-\gamma T/\hbar}\Theta(T) \,. \qquad (2.87)$$

First of all, we see that the signal exhibits a fast oscillation with the exciton frequency, which stems from the interference of the two time delayed pump pulses. For $T > 0$ the envelope corresponds to an exponential decay determined by the exciton dephasing constant. We can expect that the suggested method indeed might be able to directly extract the T_2-time, at least for short enough pulses compared to the lifetime. For $T < 0$ the signal drops to zero. Figure 2.11(b) displays the numerical result with a VIS pulse width of 5 fs. As the analytical solution suggests, for $T > 0$ the envelope of the tr-ARPES signal follows an exponential decay with the dephasing constant γ. For $T < 0$, as we expect from Eq. (2.87), the signal rapidly decreases to zero. Since we have no infinite thin pulse, but a finite width of 5 fs, the tr-ARPES signal follows the pulse, which is drawn in grey dashed. For the resonant excitation, the underlying fast oscillation corresponds to the exciton frequency.

After having discussed the underlying equations and investigated the limiting case of infinite short pulses, we present the numerical results for Gaussian pulses with realistic widths. We choose an intensity pulse width of 40 fs for the two VIS pulses and 20 fs for the XUV pulse. Figure 2.12 presents the results for three different dephasing constants. Figure 2.12(a) shows
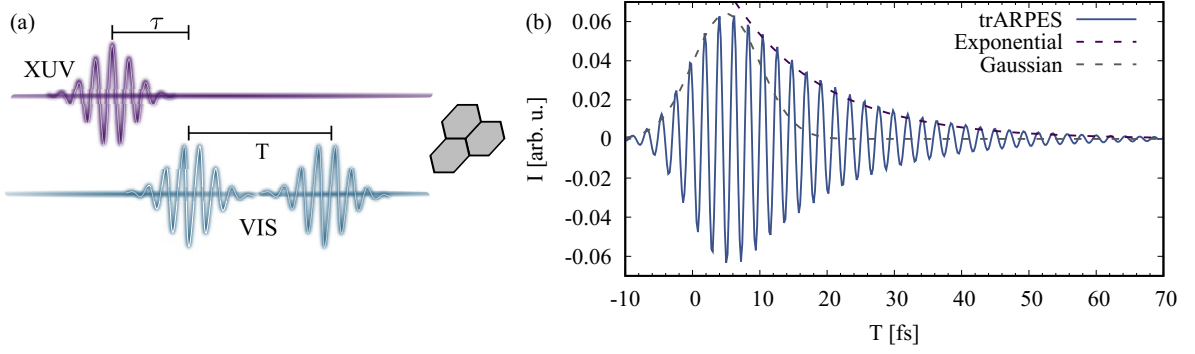
Figure 2.11: (a) Sketch of the coherent pump Fourier transform ARPES. Two VIS pump pulses with delay T are combined with a photoemitting XUV probe pulse with time delay τ to one of the VIS pulses. We choose as convention $\tau = 0$ and vary T with respect to the coherent tr-ARPES experiment. (b) Tr-ARPES signal as function of delay T for 5 fs short pump pulses. The left tail quickly decreases to zero, while the right tail decreases exponentially with $\exp(-\gamma T/\hbar)$ shown by the fit. Additionally, we display the Gaussian pump pulse as grey dashed.

the result with the microscopically calculated dephasing of $\gamma = 22\,\text{meV}$ at room temperature. Figure 2.12(b) and (c) display the results for a twice and four times larger dephasing constant at unchanged pulse widths. By artificially tuning the dephasing we can check the limits of the suggested method.

Generally, looking at Fig. 2.12(a)-(c), we conclude that their is no strong difference in the time domain. We add in red dashed the exponential decay around $T = 0$. We find no matching for any γ. In violet dash we try to fit the exponential decay away from $T = 0$. Also here the agreement is generally bad but becomes better with smaller γ. For completeness we add also the Gaussian pulse to the plots.

To further analyze the results we transform the signal from time domain to frequency space by Fourier transformation. Figure 2.12(d)-(f) show the obtained results. The fast oscillation yields a signal at the exciton energy. Since the fast oscillation is determined by the laser excitation frequency the peak shifts depending on the detuning to the exciton. As already discussed in the previous section, a detuned excitation would also lead to an energetic shift of the curve related to the detuning. We see that for pulses short enough or in comparable magnitude to the dephasing time, the Fourier transformed spectra accurately yield the dephasing constant. For $\gamma = 22\,\text{meV}$ a Lorentzian almost perfectly fits and yields the dephasing constant from its full width half maximum. When the pulse width is comparable to the dephasing time (Fig. 2.12(d)), the curve is best described by a Voigt profile corresponding to a convolution of Gaussian and Lorentzian, as has already been discussed from Eq. (2.86). Also here, the dephasing is obtained in convincing accuracy. When the pulse is long compared to the lifetime, the Fourier transformed spectrum simply corresponds to the Gaussian pump pulses. We conclude that a growing γ leads to the fact that the pulse becomes spectral short compared to γ, which is unfavorable for the method. However, as long as the dephasing and the spectral pulse broadening are comparable the method yields the exciton T_2-time with great accuracy.
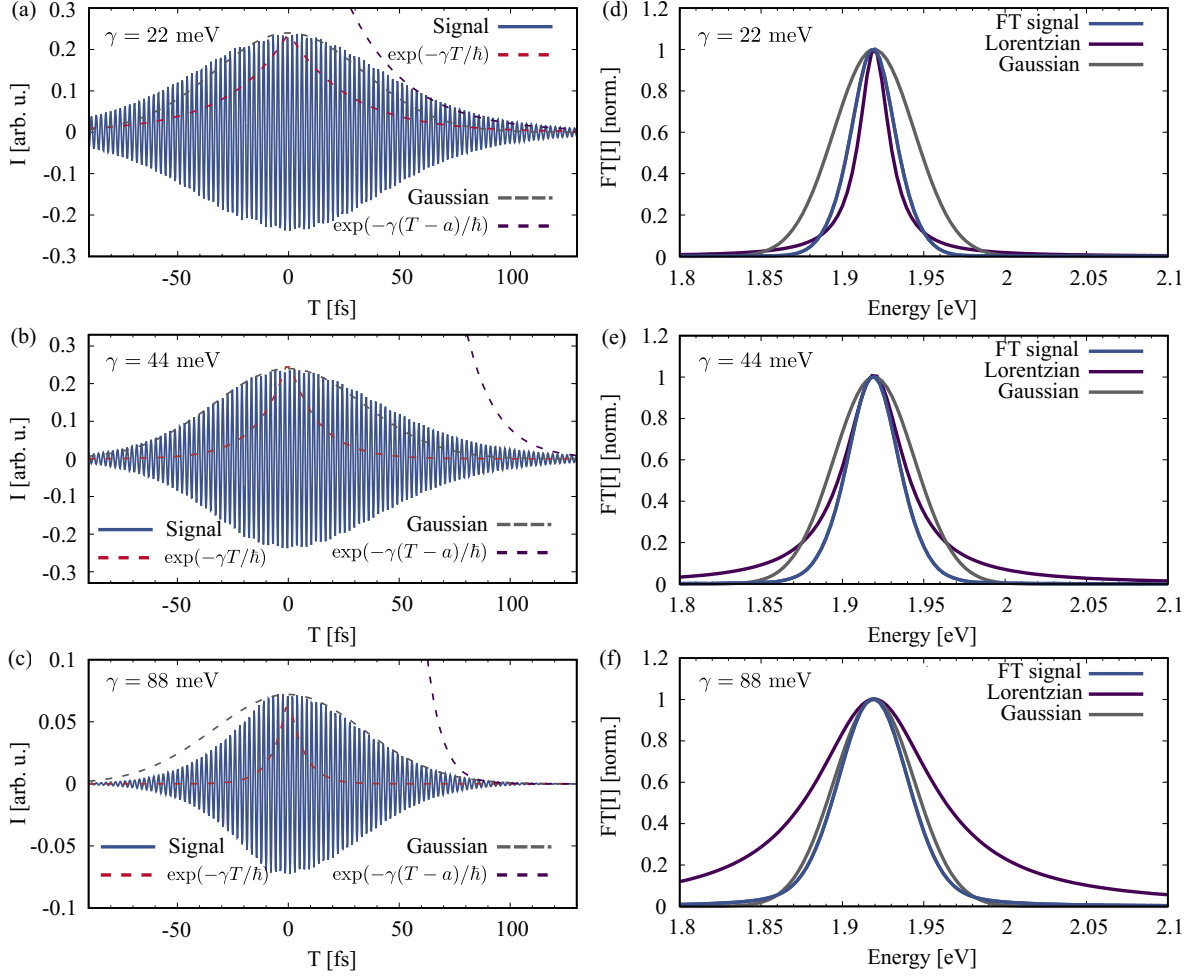
Figure 2.12: (a)-(c) Tr-ARPES signal in time domain for three different dephasings. Added are exponential functions around $T = 0$ and shifted to the signal's tail with $a = 34\,\text{fs}$, $a = 85\,\text{fs}$, and $a = 65\,\text{fs}$, respectively, with $\exp(-\gamma(T - a)/\hbar)$. The grey solid line displays a Gaussian with $40\,\text{fs}$ width. (d)-(f) Corresponding Fourier transformed tr-ARPES signals together with Gaussian and Lorentzian with corresponding width σ and γ, respectively. As long as the dephasing is comparable to the spectral pulse width the Fourier transform yields accurately the exciton linewidth.

2.9   Conclusion

This chapter introduced monolayer transition-metal dichalcogenides as material system, whose optical properties are dominated by tightly bound excitons. The optically excited interband transition exhibits a renormalization of the Rabi-frequency, due to Coulomb interaction, which is identified as the formation of excitons. The many-body problem is circumvented by introducing the exciton basis. Optically excited are exciton transitions with vanishing center-of-mass momentum. Subsequently, exciton-phonon interaction induces a transfer from coherent to thermally distributed incoherent excitons with finite center-of-mass momentum. We addressed the question if excitons do appear in time and angle resolved photoemission spectroscopy, which naively seen corresponds to a one-particle experiment. To answer the question, we derived an excitonic description of tr-ARPES by exploiting the unit-operator method and

expanding the photoemitted valence and conduction band electrons after electron-hole pairs. We find indeed, that strongly bound excitons, although being two-particle complexes, can be resolved by photoemission spectroscopy [125, 177, 182]. The momentum resolution of tr-ARPES enables access to relaxation and thermalization of excitons throughout the Brillouin zone. We find that excitons in tungsten-based TMDCs relaxe in momentum-indirect excitons, where the hole remains at the K point but the electron is either at the Λ or K_- point due to their energetic favorable position compared to Γ excitons. In contrast, the Γ exciton in molybdenum-based TMDCs forms the global minimum. Therefore, the exciton dynamics is restricted to intravalley scattering. The possibility to access excitons by tr-ARPES might open new perspectives in exciton physics [183–187].

For short time delays between pump and probe pulse the tr-ARPES signal shows at the exciton energy a shadow of the valence band reflecting the hole left in the material. Interestingly, the intensity along this intriguing signal reflects the exciton wave function squared in momentum space. We conclude that tr-ARPES is a method to directly image the envelop of the exciton wave function. A Fourier transformation of the signal enables a transcription to real space and direct access to the electron-hole separation. This signal is only present as long as the exciton transition is finite. Since the exciton transition oscillates with the excitation energy of the laser pulse a detuned excitation first yields a tr-ARPES signal differing by the detuning from the exciton energy. With ongoing time incoherent excitons form, which lie at the exciton energy. Therefore, when investigating the EDC over time of a detuned excitation the tr-ARPES signal shifts in time to the real exciton energy.

Since coherent and incoherent excitons contribute to the same signal it is rather complicated to extract the exciton lifetime (T_2-time) from tr-ARPES. We suggest coherent-pump Fourier transform ARPES as method to access the lifetime. We combine a coherent tr-ARPES experiment of simultaneous pump and probe pulse with a second VIS pulse. The tr-ARPES signal is investigated as function of time delay between the second VIS and the coherent tr-ARPES. A Fourier transformation of the obtained interference spectrum yields a Voigt-profile from which the dephasing constant can be obtained. The method depends strongly on the relation of the exciton lifetime to the pulse width. For short or comparably pulse width compared to the exciton lifetime the method yields accurately the T_2-time.

Chapter 3

WSe$_2$-graphene energy and charge transfer in tr-ARPES

In the last chapter we focused on monolayers of atomically-thin materials. We turn now our attention to van der Waals heterostructures. Since the exfoliation of graphene the number of atomically-thin materials with different intriguing properties is constantly growing. Van der Waals heterostructures are synthetic quantum materials composed of stacks of different two-dimensional layered materials [27, 28]. The idea is to design materials based on the desired properties. Since the heterostructure electrons are exposed to interlayer coupling, the material properties are not only defined by the monolayers but also by interactions between them [29, 30]. In the last chapter, we have seen that the properties of monolayer TMDCs in the low excitation regime are dominated by exceptionally strongly bound excitons. In contrast, the prototype two-dimensional material graphene exhibits totally different properties. Graphene is composed of an atomically-thin honeycomb sheet of carbon atoms and is a semi-metal. As for semiconductors the valence band is completely filled and the conduction band empty but the band gap is vanishing, that the two bands touche at the so called Dirac point, situated at the K points. For low energies around the K point, which is the most relevant region for many optical and electronic properties of graphene, the electronic dispersion is linear. Therefore, electrons at the Dirac point have zero effective mass and are referred to as Dirac electrons [188]. A comparison of graphene with conventional materials as silicon or copper shows graphene's exceptional standing: The carrier mobility is hundred times larger, than in silicon, the electrical conductivity is 13 times better than in copper, and also the heat conductivity is twice as large as copper's [189, 190]. Therefore, there is at the moment great interest in combining the properties by building a TMDC-graphene heterostructure and studying the coupling mechanisms [191–195]. In the following, we will investigate different energy and charge transfer mechanisms in a WSe$_2$-graphene stack.

3.1 Förster coupling

A prominent energy transfer mechanism is Förster transfer [196, 197]. A detailed analysis of Förster transfer in a WSe$_2$-graphene stack was given by Malte Selig in reference [198]. To have a complete overview of the different possible energy and charge transfer mechanisms, we give in the following a brief summary of the derived Förster results.

To investigate the Förster coupling, we start from the Hamiltonian

$$H = \sum_{\substack{\lambda,\lambda',\nu,\nu' \\ \boldsymbol{k},\boldsymbol{q},\boldsymbol{k}',\boldsymbol{q}'}} V_{\boldsymbol{k},\boldsymbol{q},\boldsymbol{q}',\boldsymbol{k}'}^{\lambda\nu\nu'\lambda'} \lambda_{\boldsymbol{k}}^\dagger \nu_{\boldsymbol{q}}^\dagger \nu'_{\boldsymbol{q}'} \lambda'_{\boldsymbol{k}'} \,. \tag{3.1}$$

To dispense a layer index, we use as convention $(\lambda^{(')}, \boldsymbol{k}^{(')})$ for WSe$_2$ quantum numbers and $(\nu^{(')}, \boldsymbol{q}^{(')})$ denote the graphene band and wave vector. The matrix element reads

$$V_{\boldsymbol{k},\boldsymbol{q},\boldsymbol{q}',\boldsymbol{k}'}^{\lambda\nu\nu'\lambda'} = \int_{\mathbb{R}^3} d^3r \int_{\mathbb{R}^3} d^3r' \; \Psi^*_{\lambda,\boldsymbol{k}}(\boldsymbol{r}) \Psi^*_{\nu,\boldsymbol{q}}(\boldsymbol{r}') V(\boldsymbol{r},\boldsymbol{r}') \Psi_{\nu',\boldsymbol{q}'}(\boldsymbol{r}') \Psi_{\lambda',\boldsymbol{k}'}(\boldsymbol{r}) \tag{3.2}$$

with electronic Bloch waves $\Psi_{\lambda/\nu,\boldsymbol{k}/\boldsymbol{q}}$ in WSe$_2$ and graphene integrated over the complete space. The Coulomb potential takes into account the dielectric environment of the heterostructure. Both materials are separated by a distance z with a dielectric constant ϵ. The interlayer potential can be derived by solving the Poisson equation for a five layer model: substrate, TMDC, spacing, graphene, and supstrate with appropriate boundary conditions [199]. If the spacing is sent to zero, the used interlayer Coulomb potential, displayed in the appendix A.3.1, recovers the well-known Rytova-Keldysh potential with summed layer thicknesses [199]. By Fourier transformation of the Coulomb potential and $\boldsymbol{k} \cdot \boldsymbol{p}$ expansion [154] of the integral the matrix element can be evaluated [198]. Together with an exciton basis we find

$$H = \sum_{\mu,\boldsymbol{Q},\boldsymbol{q}} F_{\mu,\boldsymbol{Q}}(z) P_{\mu,\boldsymbol{Q}}^\dagger R_{\boldsymbol{Q}}^{\boldsymbol{q}} + \text{H.c.} \,, \tag{3.3}$$

where $P_{\mu,\boldsymbol{Q}}^\dagger$ denotes the exciton transition in WSe$_2$ and $R_{\boldsymbol{Q}}^{\boldsymbol{q}} = c_{\boldsymbol{q}+\frac{1}{2}\boldsymbol{Q}}^\dagger v_{\boldsymbol{q}-\frac{1}{2}\boldsymbol{Q}}$ stands for a pair operator in graphene. For Förster coupling an excitonic transition couples to an inverse interband transition in graphene, as sketched in Fig. 3.1(a). The matrix element reads [150]

$$F_{\mu,\boldsymbol{Q}}(z) = \frac{1}{e^2\sqrt{A}} V_{\boldsymbol{Q}}(z) \varphi_\mu(\boldsymbol{r}=0) \boldsymbol{Q} \cdot \boldsymbol{d}_W^* \boldsymbol{Q} \cdot \boldsymbol{d}_G \,. \tag{3.4}$$

The matrix element is characterized by the dot product of the dipole elements $\boldsymbol{d}_{W/G}$ of both materials (W for WSe$_2$ and G for graphene), which shows that Förster coupling is a dipole-dipole interaction. Besides finite dipole elements, the coupling mechanism requires a non-vanishing center-of-mass momentum of the exciton. Otherwise, for $\boldsymbol{Q} = 0$ the coupling mechanism directly vanishes. From the Hamiltonian Eq. (3.3) and the Heisenberg equation of motion formalism we can derive equations of motion for exciton transition $P_{\boldsymbol{Q}}$ and $R_{\boldsymbol{Q}}^{\boldsymbol{q}}$. Restricting the discussion to $1s$ excitons, the exciton number μ is dropped:

$$i\hbar \frac{d}{dt} P_{\boldsymbol{Q}} = E_{\boldsymbol{Q}} P_{\boldsymbol{Q}} + \sum_{\boldsymbol{q}} F_{\boldsymbol{Q}} R_{\boldsymbol{Q}}^{\boldsymbol{q}} \,, \tag{3.5}$$

$$i\hbar \frac{d}{dt} R_{\boldsymbol{Q}} = E_{\boldsymbol{Q}}^{\boldsymbol{q}} R_{\boldsymbol{Q}}^{\boldsymbol{q}} + F_{\boldsymbol{Q}} P_{\boldsymbol{Q}} \,. \tag{3.6}$$

The first term describes the free energy of the transition amplitude and the second term the Förster coupling. The formal solution of the graphene transition reads

$$R_{\boldsymbol{Q}}^{\boldsymbol{q}} = \frac{1}{i\hbar} F_{\boldsymbol{Q}} \int_{-\infty}^t dt' \; e^{\frac{1}{i\hbar} E_{\boldsymbol{Q}}^{\boldsymbol{q}}(t-t')} P_{\boldsymbol{Q}}(t') = \frac{1}{i\hbar} F_{\boldsymbol{Q}} \int_{-\infty}^t dt' \; e^{\frac{1}{i\hbar} E_{\boldsymbol{Q}}^{\boldsymbol{q}}(t-t')} e^{\frac{1}{i\hbar} E_{\boldsymbol{q}} t'} \tilde{P}_{\boldsymbol{Q}}(t') \,, \tag{3.7}$$

where the tilde index denotes a slow oscillating amplitude. The graphene transition can be solved within a Markov approximation and plugged back into the equation of motion for
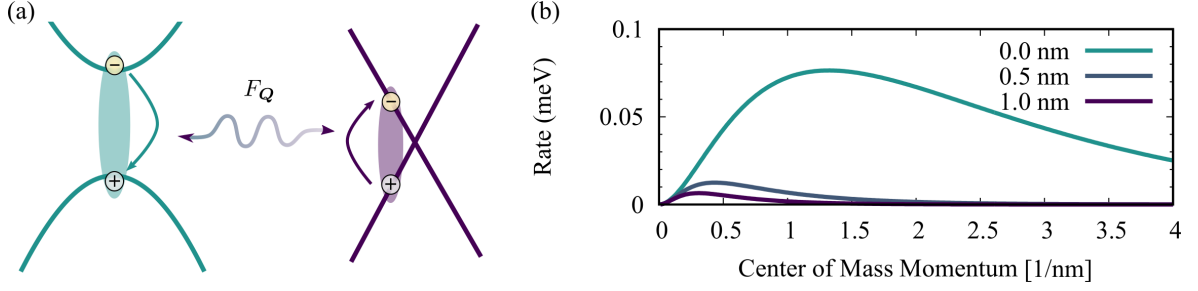
Figure 3.1: (a) Förster coupling between TMDC and graphene. (b) Förster transfer rate for different interlayer distances. A close stacking of $0\,\mathrm{nm}$ yields the highest transfer rate. Figure is similarly published in Ref. [200].

the exciton transition. The Markov approximation is good as long as the Förster interlayer coupling is smaller than the spectral bandwidth provided by the broad electronic energy distribution in graphene. We substitute $t - t' = s$ and obtain

$$R_{\boldsymbol{Q}}^{\boldsymbol{q}} = \frac{1}{i\hbar} F_{\boldsymbol{Q}} \int_0^\infty ds \ e^{\frac{1}{i\hbar}(E_{\boldsymbol{Q}}^{\boldsymbol{q}} - E_{\boldsymbol{Q}})s} e^{\frac{1}{i\hbar} E_{\boldsymbol{Q}} t} \tilde{P}_{\boldsymbol{Q}}(t-s) = \frac{1}{i\hbar} F_{\boldsymbol{Q}} P_{\boldsymbol{Q}}(t) \int_0^\infty ds \ e^{\frac{1}{i\hbar}(E_{\boldsymbol{Q}}^{\boldsymbol{q}} - E_{\boldsymbol{Q}})s} \ , \quad (3.8)$$

where in the second step we performed the Markov approximation and assumed that the envelope of the amplitude does depend only weakly on s and can be taken out of the integral. Performing the integration yields

$$R_{\boldsymbol{Q}}^{\boldsymbol{q}} = -i\pi F_{\boldsymbol{Q}} \delta(E_{\boldsymbol{Q}}^{\boldsymbol{q}} - E_{\boldsymbol{Q}}) P_{\boldsymbol{Q}} \ , \quad (3.9)$$

which can be inserted in Eq. (3.5). Then it is possible to read off the Förster induced transition rate

$$\Gamma_{\boldsymbol{Q}}(z) = 4\pi \sum_{\boldsymbol{q}} |F_{\boldsymbol{Q}}(z)|^2 \delta\left(E_{\boldsymbol{Q}}^{\boldsymbol{q}} - E_{\boldsymbol{Q}}^{1s}\right) \ , \quad (3.10)$$

where we included a factor 4 to account for the electron spin and valley in graphene. The graphene dispersion is linear in the investigated $\boldsymbol{q}$ region for coherent or even thermalized TMDC excitons. Paired with the assumption that typically $|\boldsymbol{q}| \ll |\boldsymbol{Q}|$ we can assume that the graphene electron energy is independent of the center-of-mass momentum $E_{\boldsymbol{Q}}^{\boldsymbol{q}} = \hbar v_F(|\boldsymbol{q} + \boldsymbol{Q}/2| + |\boldsymbol{q} - \boldsymbol{Q}/2|) \approx 2\hbar v_F |\boldsymbol{q}|$, with the Fermi velocity v_F. The summation over the delta function can be treated analytically. Together with an average over the angle dependence of $|F_{\boldsymbol{Q}}(z)|^2$ we finally find [198]

$$\Gamma_{\boldsymbol{Q}}(z) = \frac{|V_{\boldsymbol{Q}}(z)|^2 |\varphi_{1s}(\boldsymbol{r} = 0)|^2 d_T^2 d_G^2 E_{\boldsymbol{Q}}^{1s} Q^4}{8\hbar^2 v_F^2 e^2} \ . \quad (3.11)$$

Figure 3.1(b) displays the Förster rate as function of center-of-mass momentum for different layer distances. Since the Förster coupling is directly proportional to the center-of-mass momentum it vanishes at the origin. Therefore, Förster coupling has no influence on the linewidth of the exciton transition [198]. For increasing momentum we observe a monotonous increase followed by an exponential decay. The behavior results from an interplay of the Q^4 dependence and the momentum dependence of the Coulomb potential. Because the Coulomb potential enters the scattering rate we can also expect a strong influence of the dielectric

environment to the transfer rate. For a silicon carbide substrate we find that the transition rate peaks at 0.08 meV even for a close stacking of $z = 0$. Since for close stackings the Förster rate drops with distance as $\exp(-z)$ the transfer rate quickly decreases for larger layer distances [198]. We conclude that Förster coupling is a slow coupling mechanism on a picosecond time scale.

3.2 Dexter coupling

Besides Förster transfer, a second prominent energy transfer mechanism is Dexter transfer. In contrast to Förster transfer, which is a dipole-dipole interaction, Dexter relys on a wave function overlap of the involved states [201, 202]. The Dexter transfer is described by the following Hamiltonian with matrix element

$$H = \sum_{\boldsymbol{k},\boldsymbol{q},\boldsymbol{k}',\boldsymbol{q}'} V^{cvvc}_{\boldsymbol{k},\boldsymbol{q},\boldsymbol{k}',\boldsymbol{q}'} c^\dagger_{\boldsymbol{k}} v^\dagger_{\boldsymbol{q}} v_{\boldsymbol{k}'} c_{\boldsymbol{q}'} + \text{H.c.} \tag{3.12}$$

$$V^{cvvc}_{\boldsymbol{k},\boldsymbol{q},\boldsymbol{k}',\boldsymbol{q}'} = \int_{\mathbb{R}^3} d^3r \int_{\mathbb{R}^3} d^3r' \ \Psi^*_{c,\boldsymbol{k}}(\boldsymbol{r})\Psi^*_{v,\boldsymbol{q}}(\boldsymbol{r}')V(\boldsymbol{r},\boldsymbol{r}')\Psi_{v,\boldsymbol{k}'}(\boldsymbol{r}')\Psi_{c,\boldsymbol{q}'}(\boldsymbol{r}) \tag{3.13}$$

and sketched in Fig. 3.2(a). While for a Förster transfer the carriers stay in their respective layer, Dexter coupling is characterized by a layer exchange of valence and conduction band electrons. The notation is equivalent to the previously discussed Förster transfer. Because of the in-plane translation invariance of the Coulomb potential, we can Fourier transform the Coulomb potential with respect to the in-plane component. Inserting the Bloch waves and by shifting the integral into the first common unit cell $\boldsymbol{r}_\parallel \to \boldsymbol{r}_\parallel + \boldsymbol{R}_n$, we can decompose the spatial integrals to obtain

$$V^{cvvc}_{\boldsymbol{k},\boldsymbol{q},\boldsymbol{k}',\boldsymbol{q}'} = \frac{1}{A} \sum_{\boldsymbol{K}} \int_{UC} dz \int_{UC} dz' \ \chi_c(z)\chi_v(z')V_{\boldsymbol{K}}(z,z')\delta_{\boldsymbol{k},\boldsymbol{q}'+\boldsymbol{K}}\delta_{\boldsymbol{q},\boldsymbol{k}'-\boldsymbol{K}} \ . \tag{3.14}$$

We introduced the abbreviation $\chi_\lambda(z) = \langle u_{\lambda,W}|u_{\lambda,G}\rangle/V_{UC}$, where the dependence on the orbital overlap becomes apparent. The indices W and G are layer indices denoting WSe$_2$ and graphene. In the following, we assume a close stack with zero interlayer distance. The z-integrals can be decomposed into two integrals, one over WSe$_2$ and one over graphene. For an atomically-thin material we can assume that the Coulomb potential varies only weakly with each layer, that the z/z'-dependence of the Coulomb potential can be replaced by the positions of the layers. Additionally, we assume that the integration in both layers contribute equally to the wave function overlap between WSe$_2$ and graphene in conduction and valence band, that we can write $\chi_{\lambda,W} = \chi_{\lambda,G} = \chi_\lambda/2$ [200]. After a projection onto the excitonic wave function, we obtain the Dexter Hamiltonian

$$H = -\sum_{\mu,\boldsymbol{K},\boldsymbol{q}} D_{\mu,\boldsymbol{K}} P^\dagger_{\mu,\boldsymbol{K}} R^{\boldsymbol{K}_G+\boldsymbol{q}}_{\boldsymbol{K}} + \text{H.c.} \tag{3.15}$$

with

$$D_{\mu,\boldsymbol{K}} = \frac{1}{4\sqrt{A}}\chi_c\chi_v\varphi^*_\mu(\boldsymbol{r}=0)V^{\text{Dex}}_{\boldsymbol{K}_W-\boldsymbol{K}_G} \ , \tag{3.16}$$

where $V^{\text{Dex}}_{\boldsymbol{K}}$ corresponds to the sum of the Coulomb potentials at each material position, cf. App. A.3.1. We observe that the Dexter coupling element depends on the momentum distance between the K points in TMDC and graphene, which originates from the different
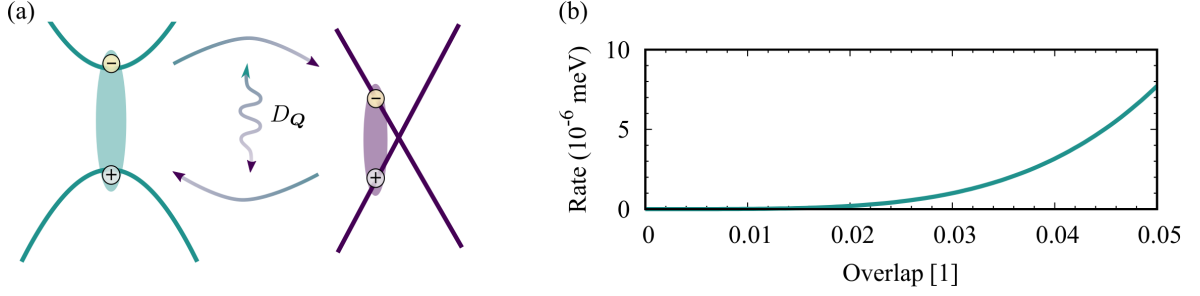
Figure 3.2: (a) Dexter coupling between TMDC and graphene. (b) The Dexter transfer rate is increasing with increasing orbital overlap but remains exceedingly small. Figure is similarly published in Ref. [200].

lattice constants. The distance is about $|K_G - K_W| \approx 3.6 \, \text{nm}^{-1}$, which is large compared to the valley local relative and center-of-mass momenta. Therefore, we neglected the relative and center-of-mass momentum in the Coulomb potential as a first approximation. A more detailed derivation of the Dexter coupling element is given in the appendix A.3.1.

Analogously to the Förster case, we calculate the Dexter-induced scattering of WSe$_2$ excitons to graphene, which reads

$$\Gamma_{\boldsymbol{Q}} = 2\pi \sum_{\boldsymbol{q}} |D_{\boldsymbol{Q}}|^2 \delta(E_{\boldsymbol{Q}}^{\boldsymbol{q}} - E_{\boldsymbol{Q}}^{1s}) = \frac{|D_{\boldsymbol{Q}}|^2 A E_{\boldsymbol{Q}}^{1s}}{4\hbar^2 v_F^2} \,, \tag{3.17}$$

where we evaluated the momentum sum. As long as the center-of-mass momentum $\boldsymbol{Q}$ is much smaller than the K point distance of both materials, the Dexter rate is independent of the center-of-mass momentum. Figure 3.2(b) displays the Dexter rate as function of wave function overlap. We see that for reasonable overlap, the transfer rate is in the magnitude of a millionth meV. Therefore, Dexter energy transfer can be ruled out for a WSe$_2$-graphene heterostructure.

3.3 Phonon-assisted tunneling

So far, we discussed the transfer rates for two energy transfer processes. Apart from energy also charge transfer mechanisms can occur. We present now a microscopic calculation of the interlayer phonon-assisted tunneling process. Due to the strongly different dispersions of WSe$_2$ and graphene, the phonons are indispensable to ensure energy and momentum conservation during the tunneling process. We keep the derivation as general as possible, such that it can be applied also to different processes as phonon-assisted Dexter transfer for example. Additionally, we will see that the derivation does not distinguish between fermionic and bosonic operators. The presented formalism can therefore also be used to an excitonic Hamiltonian [149]. We introduce the compound indices a, b accounting for layer, band, and momentum of carriers and c carrying the phonon quantum numbers. The Hamiltonian reads

$$H = \sum_a \varepsilon_a a_a^\dagger a_a + \sum_c \hbar \Omega_c b_c^\dagger b_c + \sum_{a,b} t_{ab} a_a^\dagger a_b + \sum_{a,b,c} g_{abc} a_a^\dagger a_b \left(b_c + b_{-c}^\dagger \right) = H_0 + H_1 \,. \tag{3.18}$$

The first two terms correspond to the dispersion of carriers and phonons and are abbreviated as the free Hamiltonian H_0. The third and fourth term constitute the interaction Hamiltonian

H_1. The third term describes tunneling from state a to b and the last term represents phonon-assisted scattering of carriers. After specifying the necessary Hamiltonian for the investigated process, we apply a canonical transformation [108]

$$H' = e^{-S}He^S = H_0 + (H_1 + [H_0, S]) + \frac{1}{2}[H_1, S]. \tag{3.19}$$

The collected terms in the middle constitute the first order and the last term corresponds to second order contributions. Since we are interested in the second order process of phonon-assisted tunneling we claim that the first order in the interaction vanishes [108]. Therefore, we choose

$$S = \sum_{a,b} \alpha_{ab} t_{ab} a_a^\dagger a_b + \sum_{a,b,c} g_{abc} a_a^\dagger a_b (\beta_{abc} b_c + \gamma_{abc} b_{-c}^\dagger), \tag{3.20}$$

with the coefficients

$$\alpha_{ab} = \frac{1}{\epsilon_b - \epsilon_a}, \quad \beta_{abc} = \frac{1}{\epsilon_b - \epsilon_a + \hbar\omega_c}, \quad \gamma_{abc} = \frac{1}{\epsilon_b - \epsilon_a - \hbar\omega_c}. \tag{3.21}$$

The notation $-c$ denotes that the phonon wave vector is negative. By inserting the operator S into Eq. (3.19) we can verify that the first order cancels with H_0. The transformed Hamiltonian reads

$$H' = \frac{1}{2}[H_1, S] \tag{3.22}$$

carrying only second order processes. The Hamiltonian includes higher-order tunneling terms, two-phonon processes, phonon-mediated attractive electron-electron interaction but also the desired phonon-assisted tunneling. Restricting ourself only to the last contribution of the Hamiltonian we obtain

$$H' = \frac{1}{2} \sum_{a,b,c,d} t_{db} g_{adc} a_a^\dagger a_b ((\frac{1}{\epsilon_b - \epsilon_d} - \frac{1}{\epsilon_d - \epsilon_a + \hbar\omega_c})b_c + (\frac{1}{\epsilon_b - \epsilon_d} - \frac{1}{\epsilon_d - \epsilon_a - \hbar\omega_{-c}})b_{-c}^\dagger)$$

$$- \frac{1}{2} \sum_{a,b,c,d} t_{ad} g_{dbc} a_a^\dagger a_b ((\frac{1}{\epsilon_d - \epsilon_a} - \frac{1}{\epsilon_b - \epsilon_d + \hbar\omega_c})b_c + (\frac{1}{\epsilon_d - \epsilon_a} - \frac{1}{\epsilon_b - \epsilon_d - \hbar\omega_{-c}})b_{-c}^\dagger). \tag{3.23}$$

Up to this point, we derived a general and exact expression for the phonon-assisted tunneling process. As a next step we can insert the compound indices for electrons $a/b = (\lambda_{a/b}, \boldsymbol{k}_{a/b}, l_{a/b})$, where l stands for the layer, and for the phonons $c = (\boldsymbol{K}_c, l_c, \alpha_c)$ with α denoting the phonon mode as introduced in Sec. 2.3. Then, we can apply the selection rules from the matrix elements and use material specific approximations. For the tunneling we apply that the process changes the layer index but band and momentum are conserved. For the phonon scattering the layer and band index are conserved but the momentum changes. Then, we explicitly see that the first line of Eq. (3.23) describes the process of tunneling followed by phonon scattering, while the second line includes phonon scattering proceeded by tunneling. The processes are sketched in Fig. 3.3(a). The energy window is opened by phonons. Executing the sum over the layers, we can divide the Hamiltonian into one part involving WSe$_2$ phonons and a second part with graphene phonons. Additionally, we evaluate the coefficients. For this purpose, we fix the momenta in WSe$_2$ to the vicinity of the K$_+$ point. Together with energy conserving scattering processes, this fixes the energy and momentum range of the involved carriers. Since we restrict the analysis to the K$_+$ point, we obtain $\alpha_{c,\boldsymbol{k}\approx K_W}^{G-W} = 1/\text{eV}$ and $\alpha_{c,\boldsymbol{k}\approx K_G}^{W-G} = \frac{1}{250\text{meV}}$

read out from DFT calculations [200]. For the other two coefficients $\beta_{\lambda,\boldsymbol{k},\boldsymbol{K}}^{l\alpha}$ and $\gamma_{\lambda,\boldsymbol{k},\boldsymbol{K}}^{l\alpha}$, which involve the phonon energies of the materials, we find that the single-particle energy difference is always extensively larger than the phonon energy. Consequently, we can neglect the phonon energy and obtain the Hamiltonian

$$
\begin{aligned}
H &= \sum_{\boldsymbol{k},\boldsymbol{K},\lambda,\alpha} \left[\frac{t_\lambda^{G-W} g_{\lambda,\boldsymbol{K}}^{W\alpha}}{\varepsilon_{K_G}^W - \varepsilon_{K_G}^G} \left(b_{\boldsymbol{K}}^{W\alpha} + b_{-\boldsymbol{K}}^{\dagger W\alpha} \right) + \frac{t_\lambda^{W-G} g_{\lambda,\boldsymbol{K}}^{G\alpha}}{\varepsilon_{K_W}^G - \varepsilon_{K_W}^T} \left(b_{\boldsymbol{K}}^{G\alpha} + b_{-\boldsymbol{K}}^{\dagger G\alpha} \right) \right] \lambda_{\boldsymbol{k}+\boldsymbol{K}}^{\dagger W} \lambda_{\boldsymbol{k}}^G + \text{H.c.} \\
&= \sum_{\boldsymbol{k},\boldsymbol{K},\lambda,\alpha} h_{\boldsymbol{K}}^{W\alpha} \lambda_{\boldsymbol{k}+\boldsymbol{K}}^{\dagger W} \lambda_{\boldsymbol{k}}^G \left(b_{\boldsymbol{K}}^{W\alpha} + b_{-\boldsymbol{K}}^{\dagger W\alpha} \right) + \sum_{\boldsymbol{k},\boldsymbol{K},\lambda,\alpha} h_{\boldsymbol{K}}^{G\alpha} \lambda_{\boldsymbol{k}+\boldsymbol{K}}^{\dagger W} \lambda_{\boldsymbol{k}}^G \left(b_{\boldsymbol{K}}^{G\alpha} + b_{-\boldsymbol{K}}^{\dagger G\alpha} \right) + \text{H.c.}, \quad (3.24)
\end{aligned}
$$

where we abbreviated in the second step the matrix elements as $h_{\boldsymbol{K}}^{l\alpha}$. Assuming that the electron-phonon matrix element changes only weakly with $\boldsymbol{K}$ close to the K_+ point we can approximate the functions $h_{\boldsymbol{K}}^{l\alpha}$ as constants. A detailed derivation of the phonon-assisted tunneling matrix element can be found in the appendix A.3.2. From the Hamiltonian we can derive the relaxation rate of graphene carriers to WSe$_2$

$$
\begin{aligned}
\Gamma_{\boldsymbol{k}}^G &= 2\pi \sum_{\pm,\boldsymbol{K},\alpha,l} |h_{\boldsymbol{K}}^{l\alpha}|^2 \left(\frac{1}{2} \pm \frac{1}{2} + n_{\boldsymbol{K}}^{l\alpha} \right) \delta(\varepsilon_{\boldsymbol{k}}^G - \varepsilon_{\boldsymbol{k}+\boldsymbol{K}}^W \mp \hbar\omega_{\boldsymbol{K}}^{l\alpha}) \\
&= A \sum_{l,\alpha,\pm} \frac{m^W}{\hbar^2} |h^l|^2 \left(\frac{1}{2} \pm \frac{1}{2} + n^{l\alpha} \right) 1_{\varepsilon_{\boldsymbol{k}}^G \mp \hbar\omega^{l\alpha} - \varepsilon_{\boldsymbol{0}}^W > 0}, \quad (3.25)
\end{aligned}
$$

where we approximated $h_{\boldsymbol{K}}^{l\alpha} \approx h^{l\alpha}$ and $\hbar\omega_{\boldsymbol{K}}^{l\alpha} \approx \hbar\omega^{l\alpha}$. We recognize that the rate is constant for graphene electrons with minimum conduction band energy plus phonon energy. This results from the constant density of states in WSe$_2$. As the carriers can tunnel from graphene to WSe$_2$, also the inverse process is possible. We obtain

$$
\Gamma_{\boldsymbol{k}}^W = 2\pi \sum_{\pm,\boldsymbol{K},\alpha,l} |h_{\boldsymbol{K}}^{l\alpha}|^2 \left(\frac{1}{2} \pm \frac{1}{2} + n_{\boldsymbol{K}}^{l\alpha} \right) \delta(\varepsilon_{\boldsymbol{k}}^W - \varepsilon_{\boldsymbol{k}+\boldsymbol{K}}^G \mp \hbar\omega_{\boldsymbol{K}}^{l\alpha}) \quad (3.26)
$$

$$
= A \sum_{l,\alpha,\pm} \frac{\varepsilon_{\boldsymbol{k}} \mp \hbar\omega^{l\alpha}}{\hbar^2 v_F^2} |h^l|^2 \left(\frac{1}{2} \pm \frac{1}{2} + n^{l\alpha} \right). \quad (3.27)
$$

For the tunneling, we take the ionization energy of WSe$_2$ as potential barrier and approximate the tunneling element as $t = \chi E_{Ion}$ [199], with χ being the wave function overlap and E_{Ion} the ionization energy of the material. For the numerical evaluation, we include two optical phonon modes for both materials. For graphene the phonon energy is $200\,\text{meV}$ with a coupling strength of $g = 200\,\text{meV}$ [203]. For WSe$_2$ we use $30\,\text{meV}$ and a coupling strength of $10\,\text{meV}$ [105]. Figure 3.3(b) displays the electron scattering rates as function of wave function overlap. We find a quadratic behavior. The difference between both scattering rates stems from the different final density of states of the two materials.

Similar to the conduction electrons also the valence electrons can tunnel between the materials. The phonon energies and coupling strength are similar but we have to take into account the different dispersion of the valence band. Figure 3.3(c) displays the results for the valence band electron tunneling, where we find a qualitative similar behavior and strength. However, the tunneling of holes from WSe$_2$ to graphene is more likely compared to the electrons. The reason is the larger density of states of graphene for the involved final states. This originates from the fact that the Fermi energy is closer to the conduction band minimum compared to the valence band maximum of WSe$_2$.
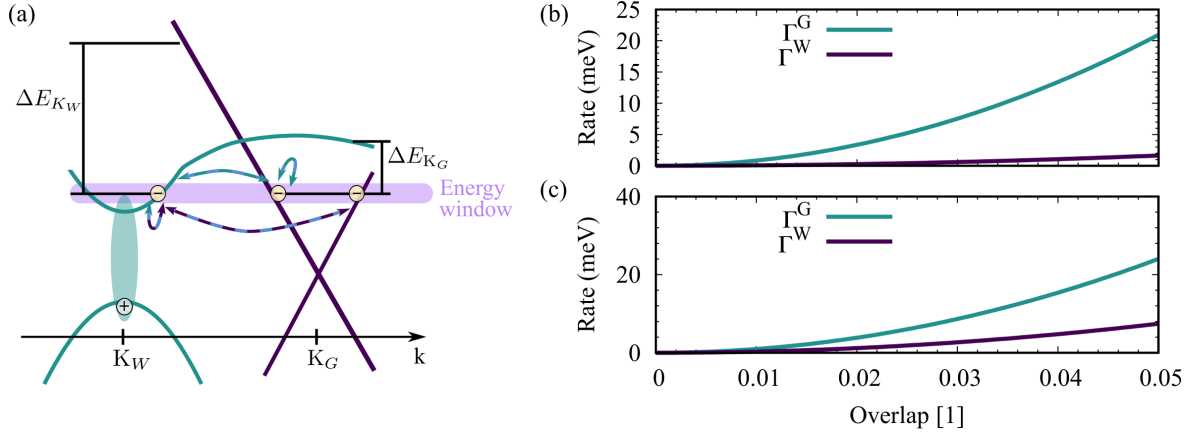
Figure 3.3: (a) Phonon-assisted electron tunneling. TMDC and graphene phonons open a window for tunneling between the TMDC and graphene necessary because of the different material dispersions. (b) Tunneling rate for WSe₂ and graphene conduction band electrons is increasing with wave function overlap. (c) Analogously, the tunneling rate for WSe₂ and graphene valence band electrons is increasing with wave function overlap. Figure is similarly published in Ref. [200].

3.4 Meitner-Auger-like energy transfer

At last, we discuss a very interesting and unusual coupling mechanism, which we will refer to as Meitner-Auger-like interlayer transfer. A schematic illustration is shown in Fig. 3.4(a): A TMDC exciton recombines non-radiatively and excites graphene electrons deep in the valence band to valence band states close to the Dirac point. From a Pauli-blocking argument, this works only if the excited valence band states are vacant for example due to p-doping or during laser excitation. We can therefore see this coupling mechanism as a conversion of optically excited TMDC excitons into graphene plasmons.

Starting point for the investigation of this coupling mechanism is the Coulomb Hamiltonian

$$H = \sum_{\substack{\lambda,\lambda',\nu,\nu' \\ \boldsymbol{k},\boldsymbol{q},\boldsymbol{k}',\boldsymbol{q}'}} V_{\boldsymbol{k},\boldsymbol{q},\boldsymbol{q}',\boldsymbol{k}'}^{\lambda\nu\nu'\lambda'} \; \lambda_{\boldsymbol{k}}^\dagger \nu_{\boldsymbol{q}}^\dagger \nu_{\boldsymbol{q}'}' \lambda_{\boldsymbol{k}'}' \,. \tag{3.28}$$

As for the description of the Förster and Dexter processes we use as convention $(\lambda^{(')}, \boldsymbol{k}^{(')})$ for WSe₂ quantum numbers and $(\nu^{(')}, \boldsymbol{q}^{(')})$ for graphene band and wave vector to dispense a layer index. The matrix element reads

$$V_{\boldsymbol{k},\boldsymbol{q},\boldsymbol{q}',\boldsymbol{k}'}^{\lambda\nu\nu'\lambda'} = \int_{\mathbb{R}^3} d^3r \int_{\mathbb{R}^3} d^3r' \; \Psi_{\lambda,\boldsymbol{k}}^*(\boldsymbol{r})\Psi_{\nu,\boldsymbol{q}}^*(\boldsymbol{r}')V(\boldsymbol{r},\boldsymbol{r}')\Psi_{\nu',\boldsymbol{q}'}(\boldsymbol{r}')\Psi_{\lambda',\boldsymbol{k}'}(\boldsymbol{r}) \,. \tag{3.29}$$

To describe the sketched mechanism, we restrict the graphene bands to the valence band $\nu = \nu' = v$ and the TMDC bands to an interband transition $\lambda \neq \lambda'$. The integral can be evaluated within a $\boldsymbol{k} \cdot \boldsymbol{p}$ expansion as shown in the appendix A.3.3. Transforming the TMDC interband transition into the exciton picture we obtain

$$H = \sum_{\mu,\boldsymbol{k},\boldsymbol{Q}} W_{\mu,\boldsymbol{Q}} \; P_{\mu,\boldsymbol{Q}}^\dagger v_{\boldsymbol{k}-\boldsymbol{Q}}^\dagger v_{\boldsymbol{k}} + \text{H.c.} \tag{3.30}$$
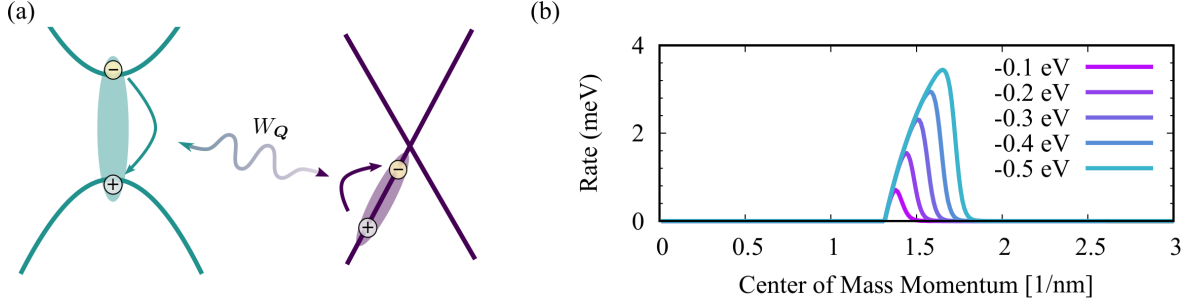
Figure 3.4: (a) Meitner-Auger energy transfer couples a TMDC interband transition with a graphene intraband transition. (b) Meitner-Auger energy transfer as function of center-of-mass momentum for different transient chemical potentials. An increasing chemical potential leads to an increased transfer rate but requires also higher center-of-mass momentum to ensure momentum conservation. Figure is similarly published in Ref. [200].

with the coupling element

$$W_{\mu,\boldsymbol{Q}} = \frac{1}{e} V_{\boldsymbol{Q}} \boldsymbol{d} \cdot \boldsymbol{Q} \varphi_\mu^*(\boldsymbol{r} = 0) \,. \tag{3.31}$$

Since we assume a resonant exciton excitation the exciton number is restricted to the lowest $1s$ exciton and the corresponding index can be dropped. The matrix element is determined by the excitonic dipole matrix element, the interlayer Coulomb potential, and scales directly with the center-of-mass momentum. Therefore, this coupling mechanism corresponds to a dipole-monopole type. At this point we can already state that coherent excitons, which exhibit a zero center-of-mass momentum, do not contribute to this kind of energy transfer mechanism. From Heisenbergs equation of motion we can derive the equations of motion for TMDC exciton occupation $N_{\boldsymbol{Q}}$ and graphene valence band electron occupation $f_{\boldsymbol{k}} = \langle v_{\boldsymbol{k}}^\dagger v_{\boldsymbol{k}} \rangle$:

$$\frac{d}{dt} N_{\boldsymbol{Q}} = \frac{2\pi}{\hbar} \sum_{\boldsymbol{k}} |W_{\boldsymbol{Q}}|^2 \left(f_{\boldsymbol{k}}(1 - f_{\boldsymbol{k}-\boldsymbol{Q}}) - N_{\boldsymbol{Q}}(f_{\boldsymbol{k}-\boldsymbol{Q}} - f_{\boldsymbol{k}}) \right) \delta(\varepsilon_{\boldsymbol{k}} - \varepsilon_{\boldsymbol{k}-\boldsymbol{Q}} - E_{\boldsymbol{Q}}) \tag{3.32}$$

$$\frac{d}{dt} f_{\boldsymbol{k}} = \frac{2\pi}{\hbar} \sum_{\boldsymbol{Q}} |W_{\boldsymbol{Q}}|^2 \left(f_{\boldsymbol{k}-\boldsymbol{Q}}(1 - f_{\boldsymbol{k}}) - N_{\boldsymbol{Q}}(f_{\boldsymbol{k}} - f_{\boldsymbol{k}-\boldsymbol{Q}}) \right) \delta(\varepsilon_{\boldsymbol{k}-\boldsymbol{Q}} - \varepsilon_{\boldsymbol{k}} - E_{\boldsymbol{Q}})$$

$$+ \frac{2\pi}{\hbar} \sum_{\boldsymbol{Q}} |W_{\boldsymbol{Q}}|^2 \left(N_{\boldsymbol{Q}}(f_{\boldsymbol{k}-\boldsymbol{Q}} - f_{\boldsymbol{k}}) - f_{\boldsymbol{k}}(1 - f_{\boldsymbol{k}-\boldsymbol{Q}}) \right) \delta(\varepsilon_{\boldsymbol{k}} - \varepsilon_{\boldsymbol{k}-\boldsymbol{Q}} - E_{\boldsymbol{Q}}) \,. \tag{3.33}$$

In the Boltzmann equation Eq. (3.32) we find first an in-scattering rate, which is proportional to the graphene electron occupation and checks, whether the state $\boldsymbol{k} - \boldsymbol{Q}$ is empty. Secondly, we can identify a decay rate of WSe$_2$ excitons, which we express by

$$\Gamma_{\boldsymbol{Q}} = 8\pi \sum_{\boldsymbol{k}} (f_{\boldsymbol{k}-\boldsymbol{Q}} - f_{\boldsymbol{k}}) \delta(\epsilon_{\boldsymbol{k}} - \epsilon_{\boldsymbol{k}-\boldsymbol{Q}} - E_{\boldsymbol{Q}}) \,. \tag{3.34}$$

The additional factor of 4 takes into account the valley and spin degree of freedom in graphene. The linear graphene valence band is described by $\varepsilon_{\boldsymbol{k}} = -\hbar v_F k$. Consequently, we can identify the state at $\boldsymbol{k}$ as close lying to the Dirac point. Electrons with $\boldsymbol{k} - \boldsymbol{Q}$ are located deep in the valence band. We can exploit this observation by assuming that electrons close to the Dirac point have much smaller momentum, i.e $\boldsymbol{Q} \ll \boldsymbol{k}$, than electrons deep in the valence
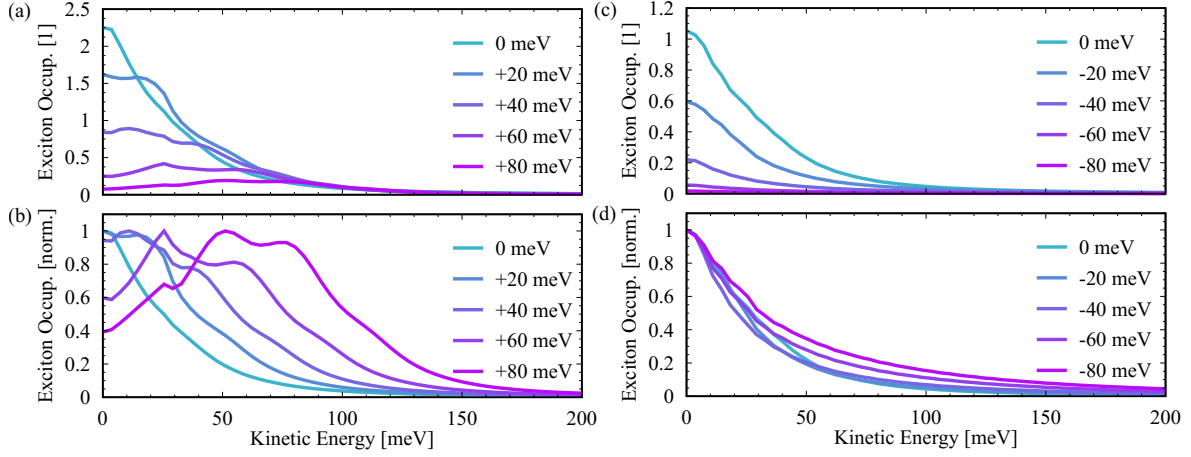
Figure 3.5: (a) Γ exciton occupation as function of kinetic energy for above exciton energy pumping. Larger detuning leads to a smaller exciton injection. (b) Exciton occupations normalized to one value. With larger detuning the excitons populate higher energy states. (c) Also below resonance pumping leads to a smaller amount of excitons. (d) Also below resonance pumping leads to a substantial hot exciton distribution. Figure is similarly published in Ref. [200].

band, where $\boldsymbol{k} + \boldsymbol{Q} \approx \boldsymbol{k}$ should hold in that case. This greatly simplifies the expression of the decay rate since we can evaluate the momentum sum with the Dirac function. We obtain analytically for the exciton decay

$$\Gamma_{\boldsymbol{Q}} = |W_{\boldsymbol{Q}}|^2 \frac{4}{\hbar v_F} \left(Q - \frac{E_{\boldsymbol{Q}}}{\hbar v_F} \right) \left(f_{\boldsymbol{Q}} - f_{Q - \frac{E_{\boldsymbol{Q}}}{\hbar v_F}} \right) \theta \left(Q - \frac{E_{\boldsymbol{Q}}}{\hbar v_F} \right) . \tag{3.35}$$

We see that the strength of the rate depends on the Meitner-Auger matrix element and the density of states of graphene. The occupation difference in graphene between the involved states describes Pauli blocking. The Heaviside function accounts for the fact that a certain minimal momentum is necessary to fulfill the momentum and energy conservation of the interlayer transfer. With an exciton energy of about 1.6 eV, this mechanisms leads to hot hole distributions deep in the graphene valence band. In more detail, the simultaneous photoexcitation of both materials leads to a resonant WSe$_2$ exciton excitation and prepares the required hole vacancies in graphene below the Dirac point. In order to allow this transition a certain center-of-mass momentum is necessary, which stems from exciton-phonon interaction leading to the formation of incoherent excitons $N_{\boldsymbol{Q}}$. Figure 3.4(b) displays the Meitner-Auger interfacial energy transfer rate as function of center-of-mass momentum for different scenarios of transient photoinduced chemical potential. We observe that the transfer time, inversely determined by the decay rate, depends on the chemical potential and requires a momentum of about 1.3 nm^{-1}. The obtained transfer rates lie in the range of 270 fs ($\mu = -0.3$ eV) to 175 fs ($\mu = -0.5$ eV) and therefore could dominate over the previously discussed energy and charge transfer mechanisms. However, a necessary center-of-mass momentum of ~ 1.3 nm^{-1} corresponds to a kinetic energy of 100 meV, which is fairly large. Even the mean exciton kinetic energy of 25.6 meV at room temperature is not enough to explain the required energy. Therefore, we investigate the energy- and momentum resolved exciton occupation for detuned excitation. To have an increased excess energy of the excitons, the pump photon energy is

chosen above the excitonic transition energy. The equation of motion for the detuned excitonic transition in the rotating frame reads

$$i\hbar \frac{d}{dt} P_0 = (E_{1s} - \varepsilon_{vis} - i\gamma)P_0 + \hbar\Omega(t). \qquad (3.36)$$

The first term describes the detuning between the exciton energy and the light excitation energy ε_{vis}. The dephasing constant γ includes radiative and non-radiative decay. The second term describes the optical excitation. The incoherent exciton occupation follows

$$\frac{d}{dt} N_{\boldsymbol{Q}} = \Gamma_{\boldsymbol{Q}}^{\text{Form}} |P_0|^2 + \sum_{\boldsymbol{K}} \Gamma_{\boldsymbol{Q},\boldsymbol{K}}^{\text{in}} N_{\boldsymbol{K}} - \sum_{\boldsymbol{K}} \Gamma_{\boldsymbol{Q},\boldsymbol{K}}^{\text{out}} N_{\boldsymbol{Q}} \qquad (3.37)$$

with a formation rate of incoherent excitons due to phonon-induced dephasing of coherent excitons. The last two terms with in- and out-scattering rates $\Gamma_{\boldsymbol{Q},\boldsymbol{K}}$ describe the thermalization of incoherent excitons. To investigate an analytical formula for a better understanding, we solve the phonon-assisted transitions adiabatically, that we can write the formation coupling element as

$$\Gamma_{\boldsymbol{Q}}^{\text{Form}} = \frac{2}{\hbar} \sum_{\pm,\alpha} |g_{\boldsymbol{Q}}^{\alpha}|^2 \left(\frac{1}{2} \pm \frac{1}{2} + n_{\boldsymbol{Q}}^{\alpha} \right) \frac{\gamma}{(E_{\boldsymbol{Q}} - \varepsilon_{vis} \mp \hbar\Omega_{\boldsymbol{Q}}^{\alpha})^2 + \gamma^2}. \qquad (3.38)$$

The phonon energy and occupation are described by $\hbar\Omega_{\boldsymbol{Q}}^{\alpha}$ and $n_{\boldsymbol{Q}}^{\alpha}$, respectively. The $\pm$ summation takes into account phonon emission and absorption processes.

Figure 3.5(a) displays the room temperature exciton occupation as function of kinetic energy at the time of the pump pulse maximum for different excitation energies. Obviously, the number of injected excitons decreases with increasingly non-resonant pumping but the excitons occupy larger energies due to the pump excess energy paired with acoustic and optical phonon scattering. A closer look at the occupations at larger detuning reveals two peaks. The higher lying peak stems from exciton formation supported by acoustic phonons. The lower maximum originates from the exciton formation with optical phonons and exciton relaxation from the higher lying maximum via optical phonon emission [200]. This becomes even more apparent, when investigating the normalized exciton occupation as shown in Fig. 3.5(b).

The second scenario, which we investigate is pumping below the exciton resonance. Again, the number of injected exciton decreases with increased detuning, cf. Fig. 3.5(c). But interestingly, the formed excitons broaden over the dispersion, that we find a substantial amount of excitons at high kinetic energy. The reason is that the imaginary part of the exiton-phonon self-energy, which enters the formation rate Eq. (3.38), broadens with increasing detuning and therefore enables occupations of hot excitons at large kinetic energy [200].

In summary, near-resonant excitation leads to a hot exciton formation at large kinetic energy, even above 100 meV. Therefore, under the right excitation conditions the interlayer Meitner-Auger interfacial energy transfer can occur and majorly determine the transfer rate in WSe$_2$-graphene stacks.

3.5 Tr-ARPES signatures in experiment

A tr-ARPES experiment, which investigated the interlayer energy and charge transfer processes in a WSe$_2$-graphene stack was performed by Shuo Dong from the Fritz-Haber Institut of the Max Planck society and published in Ref. [200]. Their experiment measured the four-dimensional photoemission intensity $I(E, k_x, k_y, \tau)$ from the heterostructure. The in-plane
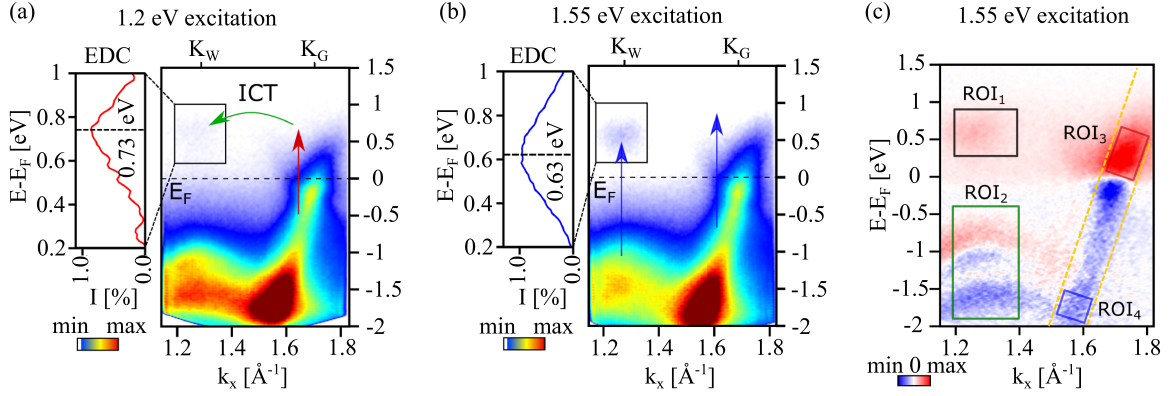
Figure 3.6: (a) Experimental tr-ARPES signal at the K points of graphene and WSe$_2$ under photoexcitation of 1.2 eV. Only the graphene component is excited and a subsequent interlayer charge transfer (ICT) from the excited graphene electrons to the WSe$_2$ layer is observed. The EDC shows that the WSe$_2$ final state lies almost 0.7 eV above the Fermi level. (b) Experimental tr-ARPES signal at the K points of graphene and WSe$_2$ under photoexcitation of 1.55 eV. Here, both materials are excited. The WSe$_2$ signal lies about 100 meV below the signal obtained from the ICT (see EDC) emphasizing the excitonic nature of the signal. (c) Differential spectrum of (b) and a spectrum for negative pump-pulse delay. We find strong signals at the WSe$_2$ valence bands (ROI$_2$), WSe$_2$ exciton (ROI$_1$), graphene excited electrons (ROI$_3$) and hot holes in graphene (ROI$_4$). Figure is similarly published in Ref. [200].

wave vector components are k_x and k_y. The tr-ARPES experiment investigates two scenarios: 1) A pump excitation energy of 1.2 eV corresponding to an excitation below the optical band gap of WSe$_2$ and 2) an excitation close to resonance of the exciton with 1.55 eV.

For a 1.2 eV pump solely the graphene component of the heterostructure at the K point K_G is excited. Time delayed to the hot carrier population in graphene a population of the K and Λ valleys in WSe$_2$ is observable, cf. Fig. 3.6(a), due to a charge transfer. As shown previously, to ensure momentum and energy conservation the carrier tunneling is accompanied by phonon scattering. The excited WSe$_2$ electrons may scatter back to graphene and relax towards the Fermi level. From the measured scattering rate of about 50 fs ($\Gamma = \hbar/50\,\mathrm{fs}$), we can estimate the wave function overlap to lie around 4%, cf. Fig. 3.3(b).

The second excitation condition is in close resonance to the WS$_2$ exciton, which entails a simultaneous excitation of both materials. First, the tr-ARPES measurement Fig. 3.6(b) shows a signal at the WSe$_2$ K point, which lies about 100 meV below the signal, which is obtained exclusively from the charge transfer from graphene. This emphasize that the signal corresponds to an excitonic signature. The differential spectrum, which is shown in Fig. 3.6(c) is obtained by substracting the spectrum for negative pump-probe delay. At the WSe$_2$ K point the figure shows the TMDC valence band (region of interest ROI$_2$) and the TMDC exciton (ROI$_1$). Additionally, it shows besides an electronic modification around the Fermi level (ROI$_3$), also a strong peak at -1.8 eV (ROI$_4$) in the graphene layer. The photoexcitation and phonon-assisted tunneling can be ruled out as origin for the signature as the energetically gap is to deep. However, the energy difference between the deep lying valence states at -1.8 eV and the states close to the Fermi level at -0.2 eV corresponds well to the exciton energy (1.6 eV). Consequently, this feature is explainable by the interlayer Meitner-Auger recombination, which was previously introduced.

3.6 Conclusion

In this chapter, we investigated different interfacial energy and charge transfer mechanisms in a WSe$_2$-graphene heterostructure. We started by investigating the Förster coupling, which is a dipole-dipole coupling. We find that the Förster transfer rate follows first a Q^4 behavior before decaying exponentially with Q. For coherent excitons with vanishing center-of-mass momentum the Förster transfer does not occur. Additionally, the transfer rate decays exponentially with the layer distance [198]. For a close stacked WSe$_2$-graphene heterostrocture on a silicon carbide substrate we find a maximum transfer rate of 0.08 meV.

As second energy transfer process we studied Dexter coupling, which depends of the wave function overlap of the different layers. Due to a small overlap, the process is extremely unlikely in a WSe$_2$-graphene heterostructure.

Then we investigated phonon-assisted tunneling as possible charge transfer mechanism. Due to the different dispersions of the materials phonons are necessary to enable energy and momentum conservation. Both processes, tunneling and phonon scattering, were simultaneously included by a canonical transformation. We find transfer rates for electrons and holes in the range of 20 meV. Therefore, phonon-assisted tunneling is a rather likely and fast process.

At last, we introduced interlayer Meitner-Auger energy transfer as new excitation transfer mechanism. Here, an exciton decays non-radiatively and excites graphene intraband transitions. The transfer rate lies around 3 meV. We conclude that tunneling and Meitner-Auger energy transfer are two possible coupling mechanisms on comparable time scales. However, Meitner-Auger energy transfer requires hot exciton distributions, for example achievable by non-resonant exciton pumping. Second, Meinter-Auger energy transfer creates hot hole distributions deep in the valence band, which are observable in tr-ARPES or optical pump-probe spectroscopy. Consequently, Meitner-Auger energy transfer has a unique spectroscopic signature, which allows to distinguish it from phonon-assisted tunneling.

Chapter 4

THz spectroscopy of excitonic phases in HIOS

Solid state materials are classified based on their band structure. Every text book distinguishes between metal or semi-metal, semiconductor and insulator. Defined by the parameter of band gap, metals have a negative band gap, meaning an overlap of valence and conduction band. Consequently, an energy band in a metal is partially filled with electrons, which leads to a high conductance. Metals are often described by the Drude model of a free electron gas [204]. For semi-metals the valence band is completely filled, however the band gap is zero that valence and conduction band touche. Therefore, they are conductive but with slightly higher resistance than metals. An archetype of semi-metals is graphene. Semiconductors have filled valence and empty conduction bands, both separated by a band gap. The energetic width of the band gap is of a magnitude that electrons can be lifted from valence to conduction band by thermal or optical excitation. The optical response is given by a Lorentz response. The insulator has a similar band structure as semiconductors but with larger band gap. Insulators have therefore high resistances. The insulator family has many different members. Besides the trivial band gap insulator, insulating states can also rise due to electron-electron interaction or due to disorder coupled with quantum interference. For example in Anderson insulators the electrons are localized by quantum interference [205]. P. W. Anderson suggested that strong electron localization is possible if the degree of disorder in a lattice exceeds a certain limit, which leads to a suppression of diffusion. As a result of Anderson localization one talks also of a metal-to-insulator transition. In contrast, the Mott localization describes a transition from metallic to insulating behavior due to strong mutual Coulomb repulsion of electrons [206]. Another example for an unconventional insulator are topological insulators. These materials are insulators in the bulk but have metallic states at their surface, due to the topological order [207].

In the 1960s, an exotic state was predicted named excitonic insulator (EI). The EI is a charge neutral and strongly interacting phase that arises from spontaneous formation of excitons. For semiconductors in thermodynamic equilibrium it is expected to appear when the exciton binding energy naively exceeds the band gap. Among others, this concept was launched by R. S. Knox, who expected this phase in indirect semi-metals [37]. Therefore, the excitonic insulator separates the semi-metal from the semiconducting phase. A few years later L. V. Keldysh and W. Kohn discussed the formation of an EI from a semiconductor [208, 209]. This new phase exhibits a correlated ground state of excitons, which shows formal analogy to the BCS ground state of superconductivity. Since this new phase is expected to host many novel properties such as superfluidity [210, 211] or high-temperature excitonic superconductivity [212, 213]
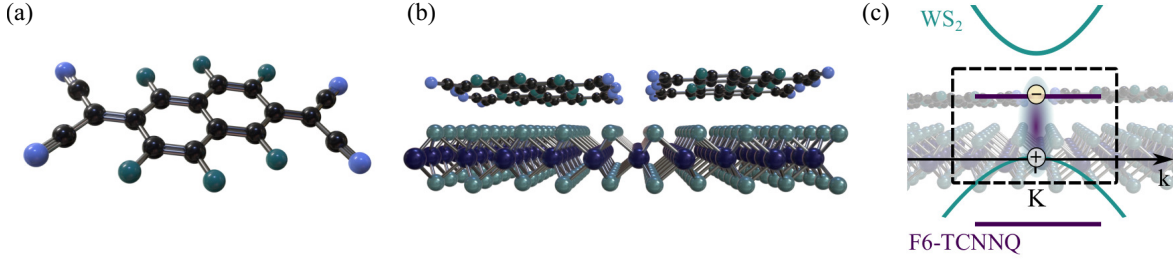
(a) (b) (c)

Figure 4.1: (a) Molecule structure of F6TCNNQ. The molecule is a naphtoquinon derivative with two dicyano compounds (nitrogen atoms in blue) and six fluorine (green) components. (b) Freestanding HIOS constituting of a monolayer of WS_2 and a thin film of periodically arranged F6TCNNQ molecules. (c) HIOS dispersion close to the K_+ point with direct band gap. The excitonic ground state is built from interlayer excitons with hole in WS_2 and electron in the molecules. Figure appears similarly in Ref. [230].

this new class of insulators has attracted great attention over the last decades. However, as the EI itself also its exotic properties are still under debate. Concerning the experimental realization, although spectroscopic signatures of EIs have been reported, conclusive evidence is still missing. There are a few materials, which are suspected to have excitonic insulator ground states in a solid state, namely 1T-TiSe$_2$, Ta$_2$NiSe$_5$ or TmSe$_{0.45}$Te$_{0.55}$ [214–221]. However, in a solid state context it has been difficult to determine if the excitonic ground state has been realized [222–225]. At the beginning, a lot of attention has focused on the realization of the EI from the original idea of an indirect semi-metal, such as 1T-TiSe$_2$. However, because of the finite momentum transfer, the formation of a momentum-indirect exciton is accompanied by charge density waves [224]. This makes it difficult to distinguish between excitonic insulator phase transition or Peierls phase transition. Unfortunately, for direct materials, the competing effect of band gap renormalization and exciton binding energy is present. A decreasing band gap entails also a decreasing exciton binding energy. Therefore, simply diminishing the band gap of a direct semiconductor is not doing the trick either.

In this chapter, we discuss the possibility of realizing the excitonic insulator in hybrids of two-dimensional semiconductors and organic molecules exploiting spatial-indirect interlayer excitons. The study of hybrid inorganic/organic systems (HIOS) is a growing field with gaining technological importance since it combines the best of two worlds: Strong light-matter interaction and easy tunability of the electronic orbitals of organic molecules with high carrier mobility of inorganic semiconductors [226–228]. In the case of excitonic insulators, the low dielectric constant of organic molecules [229] and the strong localization of their electrons are ideal conditions for a large interlayer exciton binding energy. The plethora of organic molecules allows to choose material combinations with appropriate level alignments and band gap. The easy tunability of the molecular orbitals enables a comparably easy change between the excitonic phases in contrast to TMDC heterostructures. With a direct heterostructure dispersion we circumvent the problematic of possible rising Peierls charge density waves. Moreover, the spatial separation of electrons and holes yields an exciton condensation that may produce a dipolar superfluid [41].

4.1 Hamiltonian

The expected heterostructure, which exhibits an excitonic ground state is a self-assemble layer of F6TCNNQ molecules placed on top of a WS_2 monolayer. The 1,3,4,5,7,8-hexafluoro-tetra-cyano-naphthoquinodimethane (F6TCNNQ) molecule is a powerful electron acceptor [231], which is known for strong interaction with various materials [91, 232, 233]. Experiments observe mostly charge transfer from the host material to the acceptor molecules [234]. A large number of F6TCNNQ molecules form a flat, quasi two-dimensional, film, which is weakly, non-covalently, bound to the WS_2 layer. Figure 4.1(a) and (b) display the molecule and the investigated heterostructure. Figure 4.1(b) shows a free-standing heterostructure. In order to built the EI and tune the excitonic phases we imagine a structure of the following form: F6TCNNQ-WS_2 stack encapsulated by hBN to separate the heterostructure from the two outside situated graphene layers acting as electrodes. We use a TMDC-molecule distance of $0.5\,nm$. Monolayer TMDCs exhibit a strong exciton binding energy due to their two-dimensionality leading to a low dielectric environment screening. We combine the TMDC monolayer with a F6TCNNQ film, which exihibts a low dielectric constant of $\epsilon = 3$ [235]. Further, density functional theory (DFT) calculations reveal that the electronic dispersion of a F6TCNNQ lattice corresponds to flat bands. Both properties favor large exciton binding energies. Figure 4.1(c) displays the heterostructure dispersion at the K_+ point. The valence and conduction band of WS_2 are described by parabolic dispersions. In contrast, the molecular layer exhibits flat bands for highest occupied molecular orbital (HOMO) and lowest unoccupied molecular orbital (LUMO). Later, we will see that the naively calculated interlayer exciton binding energy exceeds the heterostructure band gap. Therefore, the WS_2 valence band and the molecular LUMO will form the region of interest. First, we need to formulate the underlying Hamiltonian, which reads

$$H = \sum_{\lambda,\boldsymbol{k}} \varepsilon_{\lambda,\boldsymbol{k}} \lambda_{\boldsymbol{k}}^{\dagger} \lambda_{\boldsymbol{k}} + \sum_{\lambda,\lambda',\boldsymbol{k},\boldsymbol{k}',\boldsymbol{q}} V_{\boldsymbol{q}}^{W} \lambda_{\boldsymbol{k}+\boldsymbol{q}}^{\dagger} \lambda_{\boldsymbol{k}'-\boldsymbol{q}}'^{\dagger} \lambda_{\boldsymbol{k}'}' \lambda_{\boldsymbol{k}} + \sum_{\nu,n} \varepsilon_{\nu,n} a_{\nu,n}^{\dagger} a_{\nu,n}$$

$$+ \sum_{n_a,n_b,\nu_a,\nu_b} V_{n_a,n_b,\nu_a,\nu_b}^{\mathrm{m}} a_{n_a,\nu_a}^{\dagger} a_{n_b,\nu_b}^{\dagger} a_{n_b,\nu_b} a_{n_a,\nu_a} + \sum_{n,\nu,\boldsymbol{k}} V_{n,\lambda,\nu,\boldsymbol{k}} \lambda_{\boldsymbol{k}}^{\dagger} a_{n,\nu}^{\dagger} a_{\bar{n},\nu} \bar{\lambda}_{\boldsymbol{k}}. \qquad (4.1)$$

The first two terms describe the single-particle energies and intraband Coulomb interaction of TMDC electrons already defined in Sec. 2.3. The third term describes the single-particle energies $\varepsilon_{\nu,n}$ of the electrons in the molecule bands. The index $n = \{H, L\}$ denotes the HOMO (H) and LUMO (L) of the ν-th molecule. In the second line we find the intermolecular Coulomb coupling between molecule ν_a with electronic state $n_a \in \{H, L\}$ and molecule ν_b in state $n_b \in \{H, L\}$. The last term denotes interlayer Coulomb coupling $V_{n,\lambda,\nu,\boldsymbol{k}}$ between molecule ν and the TMDC.

The presented Hamiltonian treats the TMDC electrons in a lattice-periodic Bloch basis. In contrast, the basis of the molecule electrons is localized and non-periodic. Since the molecules form a periodic lattice it is possible to express both layers in a consistent description. The TMDC unit cells are assumed to match the molecular unit cell, that the molecular lattice vectors are integer multiples of the TMDC lattice vectors [236]. DFT calculation suggest that the structure relaxes in the way that one molecule matches 16 WS_2 unit cells. The interlayer band gap between WS_2 valence band and LUMO corresponds to $E_G = 0.12\,eV$. The Kohn-Sham energy levels of F6TCNNQ and WS_2 are obtained with the range-separated HSE06 hybrid functional [237], as implemented in the FHI-aims program [238–240] and using standard „intermediate" settings [241, 242]. Perturbative spin-orbit interaction is considered. The DFT calculations were performed by Mariana Rossi from the Max Planck Institute for

the structure and dynamics of matter. Within a Bloch basis the electronic operators are expanded that

$$a_{\nu,n} = \frac{1}{\sqrt{N_{\mathrm{m}}}} \sum_{\boldsymbol{k}} e^{-i\boldsymbol{k}\cdot\boldsymbol{R}_\nu} a_{n,\boldsymbol{k}}, \quad \text{and} \quad a_{n,\boldsymbol{k}} = \frac{1}{\sqrt{N_{\mathrm{m}}}} \sum_{\nu=1}^{N_{\mathrm{m}}} e^{i\boldsymbol{k}\cdot\boldsymbol{R}_\nu} a_{\nu,n} \tag{4.2}$$

with two-dimensional wave vector $\boldsymbol{k}$ and the number of molecular unit cells N_{m}. The normalization condition is chosen such that the fermionic commutation relation of the molecular creation and annihilation operators are conserved. The introduced transformation corresponds to the case of a tight-binding approach for the molecular field operators. The Hamiltonian in Bloch basis reads

$$H = \sum_{\lambda,\boldsymbol{k}} \varepsilon_{\lambda,\boldsymbol{k}} \lambda_{\boldsymbol{k}}^\dagger \lambda_{\boldsymbol{k}} + \sum_{n,\boldsymbol{k}} \varepsilon_{n,\boldsymbol{k}} a_{n,\boldsymbol{k}}^\dagger a_{n,\boldsymbol{k}} + \sum_{\lambda,\lambda',\boldsymbol{k},\boldsymbol{k}',\boldsymbol{q}} V_{\boldsymbol{q}}^W \, \lambda_{\boldsymbol{k}+\boldsymbol{q}}^\dagger \lambda_{\boldsymbol{k}'-\boldsymbol{q}}'^\dagger \lambda_{\boldsymbol{k}'}' \lambda_{\boldsymbol{k}}$$

$$+ \sum_{n,n',\boldsymbol{k},\boldsymbol{k}',\boldsymbol{q}} V_{\boldsymbol{q}}^{\mathrm{m}} \, a_{n,\boldsymbol{k}+\boldsymbol{q}}^\dagger a_{n',\boldsymbol{k}-\boldsymbol{q}}^\dagger a_{n',\boldsymbol{k}'} a_{n,\boldsymbol{k}} + \sum_{n,\lambda,\boldsymbol{k},\boldsymbol{k}',\boldsymbol{q}} V_{\boldsymbol{q}} \, \lambda_{\boldsymbol{k}+\boldsymbol{q}}^\dagger a_{n,\boldsymbol{k}'-\boldsymbol{q}}^\dagger a_{\bar{n},\boldsymbol{k}'} \bar{\lambda}_{\boldsymbol{k}} \,. \tag{4.3}$$

Since the molecules form a periodic crystal with possible momentum transformation the discrete molecular energy levels form bands. From this point on, we refer to HOMO and LUMO as valence and conduction band. Generally, the wave vectors of TMDC and molecular crystal life in different spaces. Because of the large extent of the molecules compared to the TMDC unit cells, the molecular Brillouin zone is much smaller than the TMDC's Brillouin zone. However, the Brillouin zones overlap at the K_+ points, where the wave vector in both materials per definition coincide. Moving away from the K_+ point, for example by including also the Λ valleys, Umklapp processes need to be considered, to map the TMDC wave vector back into the shared Brillouin zone. However, since we focus at the K_+ point the wave vector is well-defined and exchangeable. The Hamiltonian considers Coulomb interaction with valence and conduction band electrons within the individual layers but also interlayer Coulomb interaction. The Coulomb potentials $V_{\boldsymbol{q}}^W$, $V_{\boldsymbol{q}}^{\mathrm{m}}$, and $V_{\boldsymbol{q}}$ are the intralayer potentials of the TMDC, molecular crystal and the interlayer potential, respectively.

The heterostructure exhibits four different excitonic configurations: WS_2 intralayer excitons, F6TCNNQ intralayer excitons, and interlayer excitons. The latter can have either an electron in WS_2 and a hole in F6-TCNNQ, or a hole in WS_2 and an electron in the molecules. When naively solving the Wannier equation with full valence bands as ground states we find that the interlayer excitons with electron in the TMDC and hole in F6-TCNNQ lie energetically far away from all other states. In contrast, the binding energy of the exciton with hole in WS_2 and electron in the molecule exceeds the heterostructure band gap. This suggests that this specific interlayer exciton forms a new ground state.

4.2   Excitonic ground state

Since the excitonic ground state is formed by an interlayer exciton we concentrate on the region of interest highlighted in Fig. 4.1(c) by the dashed box. This means that the valence band index v simultaneously refers to the TMDC layer and the conduction band index c indicates concurrently the molecule layer. Since we focus on interlayer processes we neglected in foresight Meitner-Auger or Dexter-like exchange processes in the Hamiltonian Eq. (4.3). The reason is that their matrix elements require a wave function overlap, which is, due to the spatial separation of electrons and holes, negligible small.

To derive the new ground state, we start from the spatially homogeneous mean-field Hamiltonian obtained from Eq. (4.3)

$$H = \sum_{\lambda,\boldsymbol{k}} \tilde{\varepsilon}_{\lambda,\boldsymbol{k}} \lambda_{\boldsymbol{k}}^\dagger \lambda_{\boldsymbol{k}} - \sum_{\boldsymbol{k}} \Delta_{\boldsymbol{k}} \left(v_{\boldsymbol{k}}^\dagger c_{\boldsymbol{k}} + c_{\boldsymbol{k}}^\dagger v_{\boldsymbol{k}} \right)$$
$$+ ie \sum_{\lambda,\boldsymbol{k}} \mathbf{E}(t) \cdot (\nabla_{\boldsymbol{k}} \lambda_{\boldsymbol{k}}^\dagger) \lambda_{\boldsymbol{k}} + \hbar \sum_{\boldsymbol{k}} \Omega_{\boldsymbol{k}}(t) \left(v_{\boldsymbol{k}}^\dagger c_{\boldsymbol{k}} + c_{\boldsymbol{k}}^\dagger v_{\boldsymbol{k}} \right) , \tag{4.4}$$

which reproduces the semiconductor Bloch equations in Hartree-Fock limit. The single-particle energies $\tilde{\varepsilon}_{\lambda,\boldsymbol{k}}$ are renormalized by electron-electron, hole-hole, and electron-hole Coulomb interaction and read

$$\tilde{\varepsilon}_{v,\boldsymbol{k}} = \varepsilon_{v,\boldsymbol{k}} + \sum_{\boldsymbol{k}'} V_{\boldsymbol{0}}^W f_{v,\boldsymbol{k}'} + \sum_{\boldsymbol{k}'} V_{\boldsymbol{0}} f_{c,\boldsymbol{k}'} - \sum_{\boldsymbol{k}'} V_{\boldsymbol{k}-\boldsymbol{k}'}^W f_{v,\boldsymbol{k}'} - \sum_{\boldsymbol{k}'} V_{\boldsymbol{k}-\boldsymbol{k}'} f_{c,\boldsymbol{k}'} \tag{4.5}$$

$$\tilde{\varepsilon}_{c,\boldsymbol{k}} = \varepsilon_{c,\boldsymbol{k}} + \sum_{\boldsymbol{k}'} V_{\boldsymbol{0}}^{\mathrm{m}} f_{c,\boldsymbol{k}'} + \sum_{\boldsymbol{k}'} V_{\boldsymbol{0}} f_{v,\boldsymbol{k}'} - \sum_{\boldsymbol{k}'} V_{\boldsymbol{k}-\boldsymbol{k}'}^{\mathrm{m}} f_{c,\boldsymbol{k}'} - \sum_{\boldsymbol{k}'} V_{\boldsymbol{k}-\boldsymbol{k}'} f_{v,\boldsymbol{k}'} . \tag{4.6}$$

They carry the valence and conduction band electron occupations $f_{\lambda,\boldsymbol{k}} = \langle \lambda_{\boldsymbol{k}}^\dagger \lambda_{\boldsymbol{k}} \rangle$ in TMDC and molecular layer. The quantity $\Delta_{\boldsymbol{k}} = \sum_{\boldsymbol{k}'} V_{\boldsymbol{k}-\boldsymbol{k}'} p_{\boldsymbol{k}'}$ takes into account the binding of excitons. Additionally, we include light-matter interaction consisting of interband transitions described by the Rabi-frequency $\Omega_{\boldsymbol{k}} = \boldsymbol{d}_{\boldsymbol{k}} \cdot \boldsymbol{E}(t)/\hbar$ and intraband transitions. The former includes interband transitions between the layers, which are therefore negligible small [243, 244]. For the latter the gradient acts onto the creation operator. Since the EI forms without any external excitation, in the following only the field-independent part of the Hamiltonian Eq. (4.4) is considered. It can be convenient to express the Hamiltonian in Nambu-Gor'kov basis [245, 246]. It yields

$$H = \sum_{\boldsymbol{k}} \Psi_{\boldsymbol{k}}^\dagger \begin{pmatrix} \tilde{\varepsilon}_{c,\boldsymbol{k}} & -\Delta_{\boldsymbol{k}} \\ -\Delta_{\boldsymbol{k}}^* & \tilde{\varepsilon}_{v,\boldsymbol{k}} \end{pmatrix} \Psi_{\boldsymbol{k}} , \tag{4.7}$$

where we cast the creation and annihilation operators into the Nambu-Gor'kov spinors

$$\Psi_{\boldsymbol{k}}^\dagger = (c_{\boldsymbol{k}}^\dagger,\ v_{\boldsymbol{k}}^\dagger), \quad \text{and} \quad \Psi_{\boldsymbol{k}} = \begin{pmatrix} c_{\boldsymbol{k}} \\ v_{\boldsymbol{k}} \end{pmatrix} . \tag{4.8}$$

So far, the Hamiltonian is non-diagonal, which means that the fundamental excitations of the system are not just electrons or holes. The goal is to find a proper basis, which makes the Hamiltonian diagonal. Finding a proper basis transformation corresponds to finding a suitable combination of electrons and holes, which is a fundamental excitation of the system. A hermitian matrix can be diagonalized by a unitary matrix, i.e. a matrix U such that $UU^\dagger = \mathbb{1} = U^\dagger U$. We insert the unitary operator as

$$H = \sum_{\boldsymbol{k}} \Psi_{\boldsymbol{k}}^\dagger U_{\boldsymbol{k}} U_{\boldsymbol{k}}^\dagger \begin{pmatrix} \tilde{\varepsilon}_{c,\boldsymbol{k}} & -\Delta_{\boldsymbol{k}} \\ -\Delta_{\boldsymbol{k}}^* & \tilde{\varepsilon}_{v,\boldsymbol{k}} \end{pmatrix} U_{\boldsymbol{k}} U_{\boldsymbol{k}}^\dagger \Psi_{\boldsymbol{k}} . \tag{4.9}$$

Every 2×2 hermitian matrices can be parametrized by two complex parameters u and w with the condition $|u^2| + |w^2| = 1$. The Hamiltonian Eq. (4.9) can be diagonalized in terms of new Bogoliubov fields. We choose a representation of the unitary matrix such that the new quasi-particle operators are defined as

$$\begin{pmatrix} \alpha_{\boldsymbol{k}} \\ \beta_{\boldsymbol{k}} \end{pmatrix} = U_{\boldsymbol{k}}^\dagger \Psi_{\boldsymbol{k}} = \begin{pmatrix} -w_{\boldsymbol{k}} & u_{\boldsymbol{k}} \\ u_{\boldsymbol{k}}^* & w_{\boldsymbol{k}}^* \end{pmatrix} \begin{pmatrix} c_{\boldsymbol{k}} \\ v_{\boldsymbol{k}} \end{pmatrix} . \tag{4.10}$$
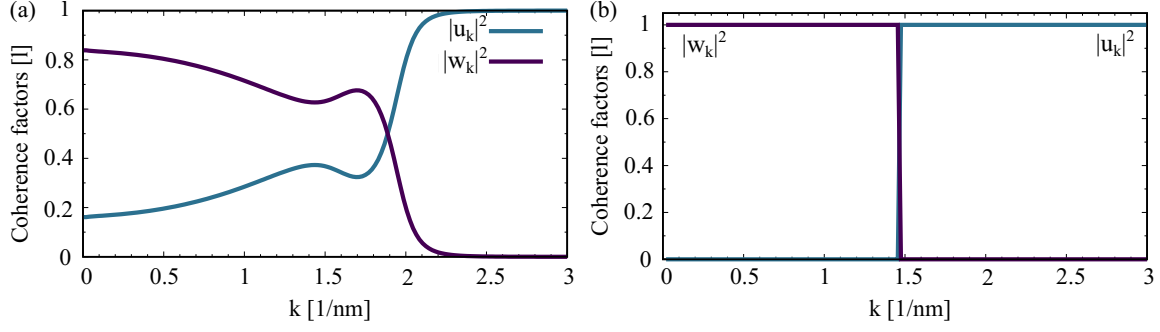
Figure 4.2: (a) Coherence factors in the EI phase. We find a mixing of electron and hole pair states. (b) Coherence factors in the semiconducting limit recovering the anticipated step function.

Since the coefficients fulfill $|u_{\boldsymbol{k}}|^2 + |w_{\boldsymbol{k}}|^2 = 1$ the commutation relation is conserved and the new operators satisfy the standard fermionic commutation relation. The complex parameters can be taken as real without the loss of generality. A possible explanation yield the semiconductor Bloch equations for microscopic transition $p_{\boldsymbol{k}}$ and occupation $f_{\lambda,\boldsymbol{k}}$. Since we are interested in the systems ground state, their dynamics vanishes. From the stationary limit we see immediately that $p_{\boldsymbol{k}}$, and therefore also $\Delta_{\boldsymbol{k}}$, is real. We find for the Hamiltonian

$$H = \sum_{\boldsymbol{k}} (\alpha_{\boldsymbol{k}}^\dagger, \ \beta_{\boldsymbol{k}}^\dagger) \begin{pmatrix} R_{\boldsymbol{k}} & C_{\boldsymbol{k}} \\ C_{\boldsymbol{k}} & T_{\boldsymbol{k}} \end{pmatrix} \begin{pmatrix} \alpha_{\boldsymbol{k}} \\ \beta_{\boldsymbol{k}} \end{pmatrix} \tag{4.11}$$

with the coefficients

$$R_{\boldsymbol{k}} = \tilde{\varepsilon}_{v,\boldsymbol{k}} |u_{\boldsymbol{k}}|^2 + \tilde{\varepsilon}_{c,\boldsymbol{k}} |w_{\boldsymbol{k}}|^2 + 2\Delta_{\boldsymbol{k}} u_{\boldsymbol{k}} w_{\boldsymbol{k}} \tag{4.12}$$

$$T_{\boldsymbol{k}} = \tilde{\varepsilon}_{v,\boldsymbol{k}} |w_{\boldsymbol{k}}|^2 + \tilde{\varepsilon}_{c,\boldsymbol{k}} |u_{\boldsymbol{k}}|^2 - 2\Delta_{\boldsymbol{k}} u_{\boldsymbol{k}} w_{\boldsymbol{k}} \tag{4.13}$$

$$C_{\boldsymbol{k}} = \Delta_{\boldsymbol{k}} (|w_{\boldsymbol{k}}|^2 - |u_{\boldsymbol{k}}|^2) - (\tilde{\varepsilon}_{c,\boldsymbol{k}} - \tilde{\varepsilon}_{v,\boldsymbol{k}}) u_{\boldsymbol{k}} w_{\boldsymbol{k}} \,. \tag{4.14}$$

We can diagonalize the Hamiltonian by forcing the coefficients of the off-diagonal entries $\alpha_{\boldsymbol{k}}^\dagger \beta_{\boldsymbol{k}}$ and $\beta_{\boldsymbol{k}}^\dagger \alpha_{\boldsymbol{k}}$ to be zero. The Hamiltonian enters its diagonal form

$$H = \sum_{\boldsymbol{k}} E_{\alpha,\boldsymbol{k}} \alpha_{\boldsymbol{k}}^\dagger \alpha_{\boldsymbol{k}} + \sum_{\boldsymbol{k}} E_{\beta,\boldsymbol{k}} \beta_{\boldsymbol{k}}^\dagger \beta_{\boldsymbol{k}} \tag{4.15}$$

with the eigenenergies

$$E_{\alpha/\beta,\boldsymbol{k}} = \frac{1}{2} (\tilde{\varepsilon}_{v,\mathbf{k}} + \tilde{\varepsilon}_{c,\mathbf{k}}) \mp \sqrt{\Sigma_{\mathbf{k}}^2 + \Delta_{\mathbf{k}}^2} \,. \tag{4.16}$$

We see that the energies of the new quasi-particles are not only determined by the single-particle energies $\tilde{\varepsilon}_{c/v,\boldsymbol{k}}$ but also by the quantities $\Sigma_{\boldsymbol{k}}$ and $\Delta_{\boldsymbol{k}}$. The term $\pm\sqrt{\Sigma_{\boldsymbol{k}}^2 + \Delta_{\boldsymbol{k}}^2}$ corresponds to the energy to add or remove a particle-hole pair from the condensate with a vanishing total momentum. The gap dispersion $\Sigma_{\boldsymbol{k}}$ reads

$$2\Sigma_{\boldsymbol{k}} = \varepsilon_{c,\boldsymbol{k}} - \varepsilon_{v,\boldsymbol{k}} + \sum_{\boldsymbol{k}'} \mathcal{V}_{\boldsymbol{k}-\boldsymbol{k}'}^{\mathrm{m}} \left(u_{\boldsymbol{k}'}^2 f_{\beta,\boldsymbol{k}'} + w_{\boldsymbol{k}'}^2 f_{\alpha,\boldsymbol{k}'} \right) - \sum_{\boldsymbol{k}'} \mathcal{V}_{\boldsymbol{k}-\boldsymbol{k}'}^{W} \left(u_{\boldsymbol{k}'}^2 f_{\alpha,\boldsymbol{k}'} + w_{\boldsymbol{k}'}^2 f_{\beta,\boldsymbol{k}'} \right) \,, \tag{4.17}$$

where we define $\mathcal{V}^l_{\boldsymbol{k}-\boldsymbol{k}'} = V^l_{\boldsymbol{0}} - V^l_{\boldsymbol{k}-\boldsymbol{k}'} - V_{\boldsymbol{0}} + V_{\boldsymbol{k}-\boldsymbol{k}'}$, $l \in \{\mathrm{m}, W\}$ with molecular and TMDC intralayer Coulomb potentials $V^{\mathrm{m}}_{\boldsymbol{k}}$ and $V^W_{\boldsymbol{k}}$, respectively [199]. The occurring difference of the Coulomb potentials from the distinct materials shows the dipolar nature of the EI [41,247,248]. The difference of the single-particle energies in Eq. (4.17) is renormalized not only by intra- and interlayer Coulomb potentials but also by the occupations of the hybridized pair states $f_{\lambda,\boldsymbol{k}} = \langle \lambda^\dagger_{\boldsymbol{k}} \lambda_{\boldsymbol{k}} \rangle$ with $\lambda \in \{\alpha, \beta\}$. Since the quasi-particles are fermions and the Hamiltonian is in diagonal form the occupations follow Fermi functions with dispersion $E_{\alpha/\beta,\boldsymbol{k}}$. Another quantity entering the new energies Eq. (4.16) is the ordering parameter $\Delta_{\boldsymbol{k}}$. In Bogoliubov basis the parameter $\Delta_{\boldsymbol{k}}$ is determined by the transcendental gap equation

$$\Delta_{\boldsymbol{k}} = \frac{1}{2} \sum_{\boldsymbol{k}'} V_{\boldsymbol{k}-\boldsymbol{k}'} \frac{\Delta_{\boldsymbol{k}'}}{\sqrt{\Sigma^2_{\boldsymbol{k}'} + \Delta^2_{\boldsymbol{k}'}}} \left(f_{\alpha,\boldsymbol{k}'} - f_{\beta,\boldsymbol{k}'} \right) , \tag{4.18}$$

which is obtained by inserting the Bogoliubov transformation into the definition of $\Delta_{\boldsymbol{k}}$. In the following, we will see that this quantity is of special interest and why referred to as ordering parameter. The gap equation is determined by three quantities. The first is the interlayer Coulomb potential. The second quantity are the occupations $f_{\alpha/\beta,\boldsymbol{k}}$, which include a temperature dependence to the gap equation. And finally, the denominator $E_{\boldsymbol{k}} = \sqrt{\Sigma^2_{\boldsymbol{k}} + \Delta^2_{\boldsymbol{k}}}$, which we call Bogoliubov dispersion. The Bogoliubov dispersion describes the excitation spectrum of the new pair states. Since the occupations $f_{\alpha/\beta,\boldsymbol{k}} = \exp(-(E_{\alpha/\beta,\boldsymbol{k}} - \mu)/k_B T)$ depend on the energies $E_{\alpha/\beta,\boldsymbol{k}}$, both equations for the ordering parameter $\Delta_{\boldsymbol{k}}$ and the gap dispersion $\Sigma_{\boldsymbol{k}}$ are coupled and we need to solve Eq. (4.17) and Eq. (4.18) simultaneously, which greatly increases the complexity of the system. This coupling stems from the fact that we include all possible Coulomb renormalizations. The chemical potential μ is adjusted such that the system is charge neutral.

Similar to $\Delta_{\boldsymbol{k}}$ we can specify the quantities $p_{\boldsymbol{k}} = \langle v^\dagger_{\boldsymbol{k}} c_{\boldsymbol{k}} \rangle$ and $f_{\boldsymbol{k}} = \langle v^\dagger_{\boldsymbol{k}} v_{\boldsymbol{k}} \rangle - \langle c^\dagger_{\boldsymbol{k}} c_{\boldsymbol{k}} \rangle$ by inserting the Bogoliubov transformation. We find in equilibrium

$$p^{(0)}_{\boldsymbol{k}} = \frac{1}{2} \frac{\Delta_{\boldsymbol{k}}}{\sqrt{\Sigma^2_{\boldsymbol{k}} + \Delta^2_{\boldsymbol{k}}}} \left(f_{\alpha,\boldsymbol{k}} - f_{\beta,\boldsymbol{k}} \right) \tag{4.19}$$

$$f^{(0)}_{\boldsymbol{k}} = f_{v,\boldsymbol{k}} - f_{c,\boldsymbol{k}} = \frac{\Sigma_{\boldsymbol{k}}}{\sqrt{\Sigma^2_{\boldsymbol{k}} + \Delta^2_{\boldsymbol{k}}}} \left(f_{\alpha,\boldsymbol{k}} - f_{\beta,\boldsymbol{k}} \right). \tag{4.20}$$

Interestingly, for $\Delta_{\boldsymbol{k}} \neq 0$ we observe that the interband transition is non-vanishing what is unexpected for an unexcited semiconductor. Also the inversion differs from one, which we would not anticipate for a Hartree-Fock ground state. In case of $\Delta_{\boldsymbol{k}} = 0$ the microscopic polarization vanishes. Such an on-off switching of an intrinsic microscopic polarization suggests that $\Delta_{\boldsymbol{k}}$ may serve as an ordering parameter. In case of a vanishing $\Delta_{\boldsymbol{k}}$ also the inversion recovers to $f^{(0)}_{\boldsymbol{k}} = f_{v,\boldsymbol{k}} - f_{c,\boldsymbol{k}} = 1$ because $f_{\alpha,\boldsymbol{k}}$ and $f_{\beta,\boldsymbol{k}}$ have as limit $f_{v,\boldsymbol{k}}$ and $f_{c,\boldsymbol{k}}$ for $\Delta_{\boldsymbol{k}} = 0$. Since for an excitonic ground state the microscopic polarization has a finite value and the inversion differs from unity, we mark them as ground state distributions by the superscript (0).

From the diagonalization we obtained also the coefficients

$$|u_{\boldsymbol{k}}|^2 = \frac{1}{2} \left(1 + \frac{\Sigma_{\boldsymbol{k}}}{\sqrt{\Sigma^2_{\boldsymbol{k}} + \Delta^2_{\boldsymbol{k}}}} \right), \quad \text{and} \quad |w_{\boldsymbol{k}}|^2 = \frac{1}{2} \left(1 - \frac{\Sigma_{\boldsymbol{k}}}{\sqrt{\Sigma^2_{\boldsymbol{k}} + \Delta^2_{\boldsymbol{k}}}} \right). \tag{4.21}$$

The coherence factors $|w_{\boldsymbol{k}}|^2$ and $|u_{\boldsymbol{k}}|^2$ describe that the pair states are occupied or unoccupied, respectively. Figure 4.2(a) displays the coherence factors for an excitonic insulating phase.

Figure 4.2(b) shows their limit by increasing the band gap and forcing therefore the ordering parameter to zero. Here, the coherence factors correspond to step functions as expected for a conventional semiconductor. The step lies at the Fermi vector k_F. In contrast, in the EI phase the coherence factors are smeared out, which is required for the pairing interaction. In formal analogy to the BCS superconductivity theory [249] we can construct the EI ground state wave function as [209]

$$|\tilde{\Psi}_0\rangle = \prod_{\boldsymbol{k}} \left(u_{\boldsymbol{k}} - w_{\boldsymbol{k}} c_{\boldsymbol{k}}^\dagger v_{\boldsymbol{k}} \right) |\Psi_0\rangle = \prod_{\boldsymbol{k}} \alpha_{\boldsymbol{k}}^\dagger |0\rangle \tag{4.22}$$

with $|\Psi_0\rangle = \prod_{\boldsymbol{k}} v_{\boldsymbol{k}}^\dagger |0\rangle$ as the conventional semiconducting ground state constructed from the vacuum state $|0\rangle$. These new Bogoliubov quasi-particle operators create (or annihilate) an electron in a linear combination of valence and conduction band. Finally, we discuss the Hamiltonian and ground state wave function together. The mean-field Hamiltonian Eq. (4.4) is $U(1)$ gauge symmetric. This can be seen when applying the transformation $\lambda_{\boldsymbol{k}}^{(\dagger)} \to e^{(\frac{+}{-})i\phi_{\boldsymbol{k}}}$, which corresponds to a $U(1)$ group operation being analogue to a rotational symmetry. For the Hamiltonian any phase is allowed and leaves Eq. (4.4) invariant. However, the new ground state is not invariant under rotation:

$$|\tilde{\Psi}_0\rangle = \prod_{\boldsymbol{k}} \alpha_{\boldsymbol{k}}^\dagger |0\rangle \to \prod_{\boldsymbol{k}} \left(e^{-i\phi_{\boldsymbol{k}}} u_{\boldsymbol{k}} v_{\boldsymbol{k}}^\dagger - e^{-i\phi_{\boldsymbol{k}}} w_{\boldsymbol{k}} c_{\boldsymbol{k}}^\dagger \right) |\Psi_0\rangle = \prod_{\boldsymbol{k}} e^{-i\phi_{\boldsymbol{k}}} \left(u_{\boldsymbol{k}} v_{\boldsymbol{k}}^\dagger - w_{\boldsymbol{k}} c_{\boldsymbol{k}}^\dagger \right) |\Psi_0\rangle \neq |\tilde{\Psi}_0\rangle \,. \tag{4.23}$$

The Hamiltonian and its ground state are not sharing the same symmetry anymore and the system undergoes a spontaneous symmetry breaking. This emphasizes the language of phase transition and ordering parameter. To obtain some more analytical insights into the ordering parameter, we can define the quantity $\varphi_{\boldsymbol{k}} = \Delta_{\boldsymbol{k}} / \sqrt{\Sigma_{\boldsymbol{k}}^2 + \Delta_{\boldsymbol{k}}^2}$ and substitute in the gap equation Eq. (4.18), which yields [209]

$$\sqrt{\Sigma_{\boldsymbol{k}}^2 + \Delta_{\boldsymbol{k}}^2} \varphi_{\boldsymbol{k}} = \sum_{\boldsymbol{k}'} V_{\boldsymbol{k}-\boldsymbol{k}'} \varphi_{\boldsymbol{k}'} \tag{4.24}$$

for the temperature limit of $0\,\mathrm{K}$. When comparing to the Wannier equation

$$(E_{\boldsymbol{k}} - E_B) \varphi_{\boldsymbol{k}} = \sum_{\boldsymbol{k}'} V_{\boldsymbol{k}-\boldsymbol{k}'} \varphi_{\boldsymbol{k}'} \tag{4.25}$$

we can deduce that the gap equation is related to the Wannier equation. Consequently, the ordering parameter is related to the exciton binding energy. When we neglect the Hartree-Fock renormalizations in the gap dispersion and approximate $\Delta_{\boldsymbol{k}} \approx \Delta_0$, we can write for small Δ_0

$$\left(\frac{\hbar^2 \boldsymbol{k}^2}{2m} + E_G + \frac{2\Delta_0^2}{E_G} \right) \varphi_{\boldsymbol{k}} = \sum_{\boldsymbol{k}'} V_{\boldsymbol{k}-\boldsymbol{k}'} \varphi_{\boldsymbol{k}'} \tag{4.26}$$

with the reduced mass m. If we assume that the gap energy is of the same order of magnitude as the exciton binding energy, we can identify $|E_B| \approx E_G + 2\Delta_0^2/E_G$ by comparing Eq. (4.26) with the Wannier equation Eq. (4.25). Resolving for the order parameter yields

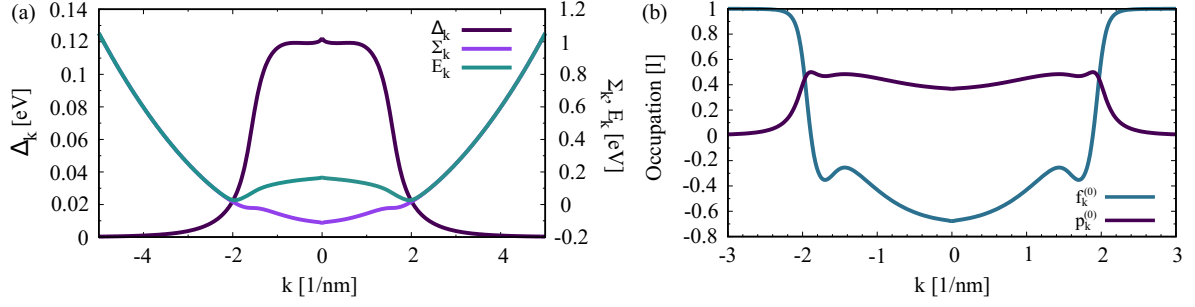$$\Delta_0 = |E_B| \sqrt{\frac{1}{2} \left(1 - \frac{E_G}{|E_B|} \right)} \,. \tag{4.27}$$

Figure 4.3: (a) Numerical solutions for $\Delta_{\boldsymbol{k}}$, $\Sigma_{\boldsymbol{k}}$, and $E_{\boldsymbol{k}}$ at $300\,\mathrm{K}$. $\Delta_{\boldsymbol{k}}$ peaks at the origin and decreases with the wave number. The Bogoliubov dispersion has a sombrero shape and $\Sigma_{\boldsymbol{k}}$ is negative close to the origin due to Hartree-Fock renormalizations. (b) Ground state distributions at $300\,\mathrm{K}$ showing a present microscopic polarization and intrinsic inversion. For $k \to \infty$, the ground state distributions go to the semiconducting limit because $\Delta_{\boldsymbol{k}} = 0$. The ground state distributions peak in the pockets of the Bogoliubov dispersion. Figure appears similarly in Ref. [230].

We see that the ordering parameter is a continuous function of the band gap. For a binding energy smaller than the band gap holds $\Delta_0 = 0$ (semiconductor limit) and increases continuously with diminishing band gap compared to the binding energy. This result suggests, that the EI phase transition is of second order.

Figure 4.3(a) displays the numerical results for the ordering parameter $\Delta_{\boldsymbol{k}}$, gap $\Sigma_{\boldsymbol{k}}$ and Bogoliubov $E_{\boldsymbol{k}}$ dispersion at room temperature. First of all, the ordering parameter is non-vanishing and peaks at $k = 0$. A finite value accounts for a finite probability to create electron-hole pairs, which designates the excitonic instability. The ordering parameter is monotonously decreasing with the wave number. This behavior is in formal analogy to the ordering parameter from s-wave superconductors [249–251]. The Bogoliubov dispersion $E_{\boldsymbol{k}}$ has a sombrero shape, which peaks at $k = 0$ and exhibits two pockets close to $k = \pm 2\,\mathrm{nm}^{-1}$. The strength of the peak at the origin is related to the exciton binding energy and can be understood as gap opening. The gap dispersion $\Sigma_{\boldsymbol{k}}$ has mainly a parabolic shape. Interestingly, we see that around $k = 0$ the gap dispersion turns negative. If we artificially turn off the Hartree-Fock Coulomb corrections, the gap dispersion corresponds to the band gap at the origin. Then the gap dispersion is positive. For a positive gap dispersion we see from Eq. (4.20) that for the inversion holds $f_{\boldsymbol{k}}^{(0)} > 0$. In contrast, with a negative gap dispersion follows $f_{\boldsymbol{k}}^{(0)} < 0$. Therefore, by including all Hartree-Fock renormalizations, we find that the suggested EI structure exhibits an intrinsic inversion close to the band extremum. Figure 4.3(b) plots the ground state distributions. The ground state polarization and occupations peak in the Bogoliubov pocket, which we can identify with a Fermi wave number k_F. Away from the band extremum the inversion goes to one and the polarization vanishes.

Two relevant parameters, which influence the ordering parameter are temperature and band gap. The latter is tunable by an applied voltage. Depending on the choice of these parameters we can expect three different excitonic phases: excitonic insulator, semiconductor, and semi-metal. The excitonic insulator is determined by a finite value of $\Delta_{\boldsymbol{k}}$, while the other two phases exhibit a vanishing $\Delta_{\boldsymbol{k}}$. However, they can be distinguished via the inversion $f_{\boldsymbol{k}}^{(0)}$. For a semiconductor the inversion is one in the Hartree-Fock ground state, but the value is smaller for a semi-metal reflecting the presence of a free electron gas. Figure 4.4
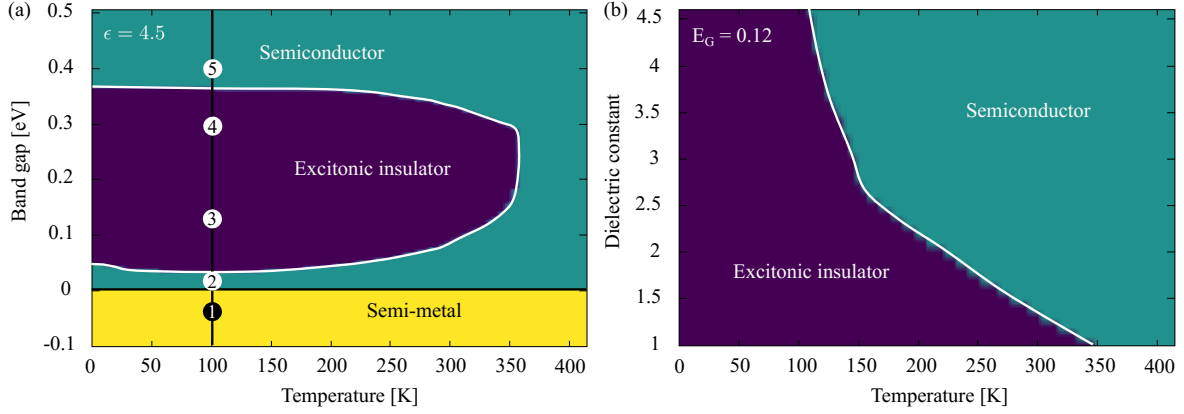
Figure 4.4: (a) Phase diagram of a WS$_2$-F6TCNNQ on hBN and air surrounding. The excitonic insulating phase separates the semiconducting and semi-metal phases. The numbers show where the absorption spectrum is calculated at a later stage. Number 3 corresponds to zero applied electric field. (b) Phase diagram for changing dielectric constant of the supstrate up to hBN encapsulation. A low mean dielectric constant is necessary to keep the EI stable at heigher temperatures. Figure appears similarly in Ref. [230].

shows the phase diagram of the WS$_2$-F6TCNNQ heterostructure. For a guidance of the eye we included the coexistence lines between the different phases. We see that the excitonic insulator is stable up to a temperature of 350 K underlining the possibility of the system to built a high-temperature excitonic insulator. Concerning the band gap, the EI appears in the range of 0.04-0.38 eV. By increasing the band gap the system enters its semiconducting phase. In contrast, by decreasing the band gap we approach the semi-metal case. Interestingly, there is no coexistence of EI and semi-metal, but the heterostructure traverses the semiconducting phase. This results from a fast decrease of the ordering parameter with decreasing band gap and its vanishing prior to a negative band gap. The microscopic origin is the competing effect between the band gap renormalization, which is included in $\Sigma_{\boldsymbol{k}}$, and the strength of the exciton binding energy. The separating area can be understood as excited semiconductor. The reason for this interpretation is that $\Delta_{\boldsymbol{k}} = 0$ and $\Sigma_{\boldsymbol{k}} = \tilde{\varepsilon}_{c,\boldsymbol{k}} - \tilde{\varepsilon}_{v,\boldsymbol{k}} > 0$ as in the semiconducting phase but with $f_{c,\boldsymbol{k}} \neq 0$. To convert the band gap change into a value for applied voltage we use a simple model by approximating the exciton as dipole in a plate capacitor. We use the materials WS$_2$ and F6TCNNQ directly as electrodes and apply the voltage between them. For the band shift due to the Stark effect we assume a simple linear dependence: $\Delta\varepsilon = ER$ [244]. The band shift $\Delta\varepsilon$ is determined by the electric field strength E and the layer separation R. For a plate capacitor the electric field is related to the applied voltage by $U = ER$. To tune the band gap over the full range shown in Fig. 4.4(a) a voltage of 0.5 V needs to be applied. Finally, we recognize a sublimation line – a direct transition of semiconductor to semi-metal without traversing the EI by just high enough temperature. Figure 4.4(b) displays the excitonic phases as function of the two device relevant parameters temperature and dielectric environment at the original band gap $E_G = 0.12$ eV. The heterostructure is placed on an hBN substrate and the dielectric constant of a supstrate is changed continuously. We see that a low mean dielectric constant is necessary to keep the EI phase stable at high operating temperatures.

4.3 Optical response

With the correct many-body ground state, we can now calculate the optical response of the heterostructure. The frequency-dependent and self-consistent absorption coefficient corresponds to Eq. (2.63) derived in Sec. 2.6.2. The linear absorption is determined by the susceptibility. We know that the susceptibility is related to the macroscopic polarization, which itself is determined by the microscopic polarization. However, we do not know exactly how the macroscopic polarization looks for an excitonic insulator. Therefore, we derived the equations of motion before defining the actual observable.

The equation of motion for the optical excitation derived from the Hamiltonian Eq. (4.4) reads

$$i\hbar\frac{d}{dt}p_{\boldsymbol{k}} = (2\Sigma_{\boldsymbol{k}} + ie\boldsymbol{E}(t)\cdot\nabla_{\boldsymbol{k}})\,p_{\boldsymbol{k}} - \Delta_{\boldsymbol{k}}f_{\boldsymbol{k}} + \hbar\Omega_{\boldsymbol{k}}(t)f_{\boldsymbol{k}}\,, \tag{4.28}$$

$$i\hbar\frac{d}{dt}f_{\boldsymbol{k}} = 2i\Im\left(\Delta_{\boldsymbol{k}}p_{\boldsymbol{k}}\right) + e\boldsymbol{E}(t)\cdot\nabla_{\boldsymbol{k}}f_{\boldsymbol{k}} \tag{4.29}$$

with $2\Sigma_{\boldsymbol{k}} = \tilde{\varepsilon}_{c,\boldsymbol{k}} - \tilde{\varepsilon}_{v,\boldsymbol{k}}$. The terms carrying the product of electric field and momentum gradient correspond to optical intraband transitions and terms with $\Delta_{\boldsymbol{k}}$ account for attractive electron-hole Coulomb coupling. Optically induced interband transitions are described by the Rabi-frequency $\Omega_{\boldsymbol{k}}(t)$. We expand the polarization and inversion into orders of the exciting electric field [252, 253]

$$p_{\boldsymbol{k}} = p_{\boldsymbol{k}}^{(0)} + p_{\boldsymbol{k}}^{(1)} + \mathcal{O}(2) \tag{4.30}$$

$$f_{\boldsymbol{k}} = f_{\boldsymbol{k}}^{(0)} + f_{\boldsymbol{k}}^{(1)} + \mathcal{O}(2)\,, \tag{4.31}$$

where we restrict ourself to the first order. The initial conditions arise from the ground state $(p_{\boldsymbol{k}}^{(0)}, f_{\boldsymbol{k}}^{(0)})$. The dynamical correction to first order in the electric field is denoted by $p_{\boldsymbol{k}}^{(1)}$ and $f_{\boldsymbol{k}}^{(1)}$. The HIOS Bloch equations in first order of the electric field read

$$i\hbar\frac{d}{dt}p_{\boldsymbol{k}}^{(1)} = 2\Sigma_{\boldsymbol{k}}^{(0)}p_{\boldsymbol{k}}^{(1)} - \Delta_{\boldsymbol{k}}^{(1)}f_{\boldsymbol{k}}^{(0)} + 2\Sigma_{\boldsymbol{k}}^{(1)}p_{\boldsymbol{k}}^{(0)} - \Delta_{\boldsymbol{k}}^{(0)}f_{\boldsymbol{k}}^{(1)} + \hbar\Omega_{\boldsymbol{k}}(t)f_{\boldsymbol{k}}^{(0)} + ie\boldsymbol{E}(t)\cdot\nabla_{\boldsymbol{k}}p_{\boldsymbol{k}}^{(0)} \tag{4.32}$$

$$i\hbar\frac{d}{dt}f_{\boldsymbol{k}}^{(1)} = 2i\Im\left(\Delta_{\boldsymbol{k}}^{(0)}p_{\boldsymbol{k}}^{(1)} + \Delta_{\boldsymbol{k}}^{(1)}p_{\boldsymbol{k}}^{(0)}\right) + ie\boldsymbol{E}(t)\cdot\nabla_{\boldsymbol{k}}f_{\boldsymbol{k}}^{(0)}\,. \tag{4.33}$$

Since $p_{\boldsymbol{k}}^{(0)}$ and $f_{\boldsymbol{k}}^{(0)}$ describe the ground state their dynamics vanish and we are left with the first order. The first two terms of Eq. (4.32) correspond to the homogeneous semiconductor Bloch equation producing the Wannier equation. The third and fourth term do not exist in the conventional semiconductor Bloch equations and therefore generalize them to the excitonic insulator. They describe a coupling of the polarization to occupations via the ground state polarization. The last two terms correspond to the optical excitation due to inter- and intraband transitions [254]. Analogous, in Eq. (4.33) the first term describes the semiconductor Bloch equation limit, while the second term is specific to the EI. It corresponds to a ground state polarization-assisted source [254]. The last term stems from optically-induced intraband transitions. The static ground state distributions induce a coupling between the linearized equations of the optical polarization $p_{\boldsymbol{k}}^{(1)}$ and inversion $f_{\boldsymbol{k}}^{(1)}$. Both equations can be decoupled by the transformation [253]

$$P_{\boldsymbol{k}}^{(1)} = \frac{E_{\boldsymbol{k}} + \Sigma_{\boldsymbol{k}}^{(0)}}{E_{\boldsymbol{k}}}p_{\boldsymbol{k}}^{(1)} - \frac{E_{\boldsymbol{k}} - \Sigma_{\boldsymbol{k}}^{(0)}}{E_{\boldsymbol{k}}}p_{\boldsymbol{k}}^{*(1)} - \frac{\Delta_{\boldsymbol{k}}^{(0)}}{E_{\boldsymbol{k}}}f_{\boldsymbol{k}}^{(1)} \tag{4.34}$$

$$F_{\boldsymbol{k}}^{(1)} = \frac{\Delta_{\boldsymbol{k}}^{(0)}}{E_{\boldsymbol{k}}}\left(p_{\boldsymbol{k}}^{(1)} + p_{\boldsymbol{k}}^{*(1)}\right) + \frac{\Sigma_{\boldsymbol{k}}^{(0)}}{E_{\boldsymbol{k}}}f_{\boldsymbol{k}}^{(1)}\,. \tag{4.35}$$

We obtain

$$i\hbar \frac{d}{dt} P_{\boldsymbol{k}}^{(1)} = 2E_{\boldsymbol{k}} P_{\boldsymbol{k}}^{(1)} - \sum_{\boldsymbol{k}'} V_{\boldsymbol{k}-\boldsymbol{k}'} P_{\boldsymbol{k}'}^{(1)} + \hbar \Omega_{\boldsymbol{k}}(t) f_{\boldsymbol{k}}^{(0)} + ie\boldsymbol{E}(t) \cdot \nabla_{\boldsymbol{k}} p_{\boldsymbol{k}}^{(0)} \tag{4.36}$$

$$i\hbar \frac{d}{dt} F_{\boldsymbol{k}}^{(1)} = ie\boldsymbol{E}(t) \cdot \nabla_{\boldsymbol{k}} f_{\boldsymbol{k}}^{(0)} \,, \tag{4.37}$$

where we can identify the linear Bogoliubov-Wannier equation

$$2E_{\boldsymbol{k}} \varphi_{\mu,\boldsymbol{k}} - \sum_{\boldsymbol{k}'} V_{\boldsymbol{k}-\boldsymbol{k}'} \varphi_{\mu,\boldsymbol{k}'} = E_{\mu} \varphi_{\mu,\boldsymbol{k}} \,. \tag{4.38}$$

We can now treat the linearized equations of motion for the optical excitation of an EI with the conventional exciton formalism, which we introduced in Sec. 2.6.1. We transform to relative and center-of-mass momentum and project the interband transition onto the Bogoliubov-Wannier wave functions, which yields the excitonic EI equations

$$i\hbar \frac{d}{dt} P_{\mu,0}^{(1)} = E_{\mu} P_{\mu,0}^{(1)} + \sum_{\boldsymbol{k}} f_{\boldsymbol{k}}^{(0)} \varphi_{\mu,\boldsymbol{k}}^{*} \hbar \Omega_{\boldsymbol{k}}(t) + ie\boldsymbol{E}(t) \cdot \sum_{\boldsymbol{k}} \varphi_{\mu,\boldsymbol{k}}^{*} \nabla_{\boldsymbol{k}} p_{\boldsymbol{k}}^{(0)} \tag{4.39}$$

$$i\hbar \frac{d}{dt} F_{\boldsymbol{k}}^{(1)} = ie\boldsymbol{E}(t) \cdot \nabla_{\boldsymbol{k}} f_{\boldsymbol{k}}^{(0)} \,. \tag{4.40}$$

Besides the Bogoliubov-Wannier energy the equation of motion exhibit an interband source scaled by the ground state inversion and an intraband source determined by the momentum gradient of the ground state polarization. By knowing the equations of motion we can make an educated guess for an excitonic light-matter Hamiltonian, which yields Eq. (4.39) and Eq. (4.40). We choose a light-matter Hamiltonian of the form

$$H_{\text{int}} = \sum_{\mu,\boldsymbol{k}} \left(\boldsymbol{d}_{\boldsymbol{k}} \cdot \boldsymbol{E}(t) f_{\boldsymbol{k}}^{(0)} \varphi_{\mu,\boldsymbol{k}}^{*} + ie\boldsymbol{E}(t) \cdot \sum_{\boldsymbol{k}} \varphi_{\mu,\boldsymbol{k}}^{*} \nabla_{\boldsymbol{k}} p_{\boldsymbol{k}}^{(0)} \right) P_{\mu,0}^{\dagger} + \text{H.c}$$
$$+ ie\boldsymbol{E}(t) \sum_{\lambda,\boldsymbol{k}} (\nabla_{\boldsymbol{k}} \lambda_{\boldsymbol{k}}^{\dagger}) \lambda_{\boldsymbol{k}} \,. \tag{4.41}$$

From the definition of the macroscopic polarization, being the functional derivative of the light-matter Hamiltonian with respect to the electric field $\boldsymbol{P}(t) = -\delta H_{\text{int}}/\delta \boldsymbol{E}(t)$ we find for the macroscopic polarization

$$\boldsymbol{P}(t) = -\sum_{\mu,\boldsymbol{k}} \left(\boldsymbol{d}_{\boldsymbol{k}} \varphi_{\mu,\boldsymbol{k}} f_{\boldsymbol{k}}^{(0)} + ie \sum_{\mu,\boldsymbol{k}} \varphi_{\mu,\boldsymbol{k}} \nabla_{\boldsymbol{k}} p_{\boldsymbol{k}}^{(0)} \right) P_{\mu,0} + ie \sum_{\lambda,\boldsymbol{k}} (\nabla_{\boldsymbol{k}} \lambda_{\boldsymbol{k}}^{\dagger}) \lambda_{\boldsymbol{k}} \,. \tag{4.42}$$

From the macroscopic polarization we can also calculate the optical current, which is defined as time derivative of the macroscopic polarization

$$\boldsymbol{j}(t) = \frac{d}{dt} \boldsymbol{P}(t) = -\sum_{\mu,\boldsymbol{k}} \left(\boldsymbol{d}_{\boldsymbol{k}} \varphi_{\mu,\boldsymbol{k}} f_{\boldsymbol{k}}^{(0)} + ie \varphi_{\mu,\boldsymbol{k}} \nabla_{\boldsymbol{k}} p_{\boldsymbol{k}}^{(0)} \right) \frac{d}{dt} P_{\mu,0}(t) + e \sum_{\boldsymbol{k}} \boldsymbol{v}_{\boldsymbol{k}} F_{v,\boldsymbol{k}}^{(1)}(t) \tag{4.43}$$

$$\boldsymbol{j}(\omega) = -\sum_{\mu,\boldsymbol{k}} \left(\boldsymbol{d}_{\boldsymbol{k}} \varphi_{\mu,\boldsymbol{k}} f_{\boldsymbol{k}}^{(0)} + ie \varphi_{\mu,\boldsymbol{k}} \nabla_{\boldsymbol{k}} p_{\boldsymbol{k}}^{(0)} \right) i\omega P_{\mu,0}(\omega) + e \sum_{\boldsymbol{k}} \boldsymbol{v}_{\boldsymbol{k}} F_{v,\boldsymbol{k}}^{(1)}(\omega) \,, \tag{4.44}$$

where we solved the time derivative by Fourier transformation. We defined the particle velocity $\boldsymbol{v}_{\boldsymbol{k}} = \hbar \boldsymbol{k}/m_v$, which is obtained by shuffling the gradient from the operator to the

corresponding eigenenergy. As consequence only the TMDC valence band occupation $F_{v,\boldsymbol{k}}^{(1)}$ contribute to the optical response since the molecule electrons have infinite mass. Additionally, we used that $f_{\boldsymbol{k}} = f_{\boldsymbol{k}}^{(0)} + F_{\boldsymbol{k}}^{(1)}$, whereby $\sum_{\boldsymbol{k}} \boldsymbol{k} \cdot f_{\boldsymbol{k}}^{(0)} = 0$ because $f_{\boldsymbol{k}}^{(0)}$ is even since it depends only on the absolute value of the the wave vector and $\boldsymbol{k}$ being uneven. The first part of Eq. (4.44) can be treated by inserting the Fourier transform of Eq. (4.39).

Some more work requires the second contribution to the optical current. Inserting the Fourier transform of Eq. (4.40) yields for the intraband current

$$\boldsymbol{j}(\omega) = -e \sum_{\boldsymbol{k}} \boldsymbol{v}_{\boldsymbol{k}} \frac{ie\boldsymbol{E}(t) \cdot \nabla_{\boldsymbol{k}} f_{v,\boldsymbol{k}}^{(0)}}{\hbar\omega + i\gamma} = \left(-\frac{ie^2}{\hbar} \sum_{\boldsymbol{k}} \frac{\boldsymbol{v}_{\boldsymbol{k}} \otimes \nabla_{\boldsymbol{k}} f_{v,\boldsymbol{k}}^{(0)}}{\omega + i\gamma/\hbar} \right) \cdot \boldsymbol{E}(t). \qquad (4.45)$$

We added a phenomenological dephasing to the optically excited occupation. The expression in front of the electric field can be identified as the conductivity tensor of a plasma. Equation (4.45) can be seen as Ohm's law, connecting the current and the electric field. With integration by parts, we can move the gradient that instead of acting on the occupation it acts on the particle velocity. The current is now in the form

$$\boldsymbol{j}(\omega) = i\frac{e^2}{m}\frac{n_{el}}{\omega + i\gamma/\hbar}\boldsymbol{E}(\omega) \qquad (4.46)$$

with electron number $n_{el} = \sum_{\boldsymbol{k}} f_{v,\boldsymbol{k}}^{(0)}$. Comparing with the definition of the current $\boldsymbol{j}(\omega) = -i\omega\epsilon_0\chi(\omega)\boldsymbol{E}(\omega)$, we can identify the susceptibility. Together with the interband contribution of Eq. (4.44), we can identify the general susceptibility tensor

$$\chi(\omega) = -\frac{1}{\epsilon_0} \sum_{\mu} \frac{\boldsymbol{d}_{\mu} \otimes \boldsymbol{d}_{\mu} + \boldsymbol{j}_{\mu} \otimes \boldsymbol{j}_{\mu}}{\hbar\omega - E_{\mu} + i\gamma} + \frac{e^2}{\epsilon_0\hbar} \sum_{\boldsymbol{k}} \frac{\boldsymbol{v}_{\boldsymbol{k}} \otimes \nabla_{\boldsymbol{k}} f_{v,\boldsymbol{k}}^{(0)}}{\omega^2 + i\gamma\omega/\hbar}, \qquad (4.47)$$

where we added also a phenomenological dephasing γ to the excited microscopic polarization. While the first term corresponds to a Lorentz response the last term corresponds to the conductivity tensor of a free electron plasma and can be brought to the well-known Drude model for a current density $\chi_{\text{Drude}} = -\omega_{pl}^2/(\omega^2 + i\gamma\omega)$ with plasma frequency $\omega_{pl}^2 = e^2 \sum_{\boldsymbol{k}} f_{v,\boldsymbol{k}}^{(0)}/\epsilon_0 m_v$ by using Eq. (4.46). The matrix elements are defined as $\boldsymbol{d}_{\mu} = \boldsymbol{d} \sum_{\boldsymbol{k}} f_{\boldsymbol{k}}^{(0)} \varphi_{\mu,\boldsymbol{k}}^*$ with electronic dipole moment $\boldsymbol{d}$ and $\boldsymbol{j}_{\mu} = ie \sum_{\boldsymbol{k}} \varphi_{\mu,\boldsymbol{k}} \nabla_{\boldsymbol{k}} p_{\boldsymbol{k}}^{(0)}$. In the following, we assume a perpendicular excitation and project the optical matrix elements on the polarization vector $\boldsymbol{e}$. We can now discuss the optical selection rules included in the susceptibility. For an excitonic insulator with s symmetric ground state the first excited state is of p symmetry. Therefore, excitonic insulators exhibit intraexcitonic s to p transitions [156, 255, 256]. But due to the uneven parity of p states, the interband source d_{μ} vanishes. In contrast, the intraband source j_{μ} is finite. The matrix element can be investigated in more detail. From the gap equation Eq. (4.18) we see that it corresponds to the Bogoliubov-Wannier equation with vanishing exciton binding energy. This suggests that also the ground state polarization could be projected onto the wave function acting as solution for $E_{\mu} = 0$: $p_{\boldsymbol{k}}^{(0)} = \sum_{\mu,E_{\mu}=0} \varphi_{\mu,\boldsymbol{k}} p_{\mu}^{(0)}$. Then the momentum-gradient in the intraband matrix element acts onto the wave function. For a s-type ground state the angular derivative vanishes. Together with an analytical treatment of the angle-sum we obtain for the intraband source

$$j_{\mu} = e\pi\boldsymbol{e} \cdot \sum_{\nu,k} \varphi_{\mu,k}^* \partial_k \varphi_{\nu,k} \begin{pmatrix} 1 \\ \pm i \end{pmatrix}, \qquad (4.48)$$
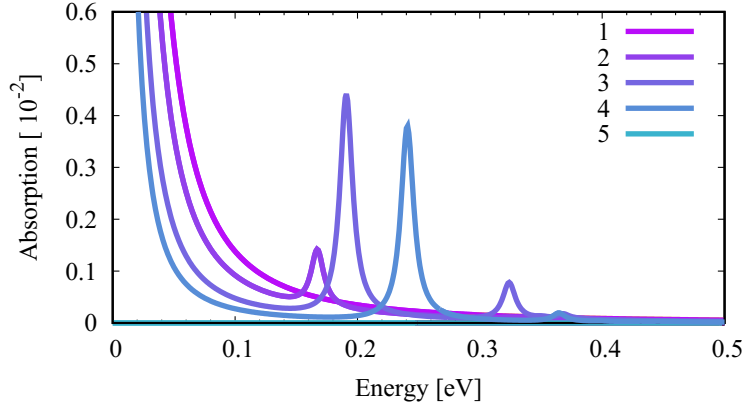
Figure 4.5: Absorption spectrum of the WS$_2$-F6TCNNQ stack in the far-infrared to terahertz regime. (1) Semi-metal phase characterized by a Drude response. (2) First Lorentzian signature due to rising intraexcitonic transitions. (3) EI phase exhibits a Drude response, which is modulated by a p excitonic Rydberg series. (4) EI phase with wider gap showing a blue shift of the resonances and a decreasing oscillator strength. (5) Semiconducting phase shows no optical response due to vanishing small oscillator strength of the interlayer transition and absent free electron gas. Figure appears similarly in Ref. [230].

where the sign stands for $\mu = p_+$ and $\mu = p_-$ final states. These two final states exhibit a circular dichroismic selection rule, comparable to KK and KK$_-$ excitons in monolayer TMDCs.

When entering the semiconducting phase, the Bogoliubov-Wannier equation turns into the conventional Wannier equation, which yields the $1s$ exciton as first excited state. Then the intraband source is zero and the interband source finite. However, since we investigate interlayer transitions, the optical interband transition is expected to be small [257]. For a negative band gap neither of the first two terms contribute. The response is solely given by the last term, which corresponds to the plasma response in a Drude model for a free electron gas. It stems from intraband transitions of the microscopic occupations with plasma frequency ω_{pl}.

Figure 4.5 shows the calculated absorption along the billiard line in Fig. 4.4(a). In the semi-metal phase (1) we observe the well-known Drude response for the free electron gas. Opening the gap (2), we see that an additional feature rises, which stems from the first two sources. The slowly rising microscopic polarization is convoluted with the excitonic wave function, which interpolates at this point between s and p state. Therefore, also the interband source contributes in principle. However, the oscillator strength of the interlayer exciton is weak and the contribution of the interband source is negligible. When entering the excitonic insulating phase (3), we observe that the Drude response, which is still present due to a finite $f_{\boldsymbol{k}}^{(0)}$, is modulated by a p excitonic Rydberg series in the far-infrared to terahertz regime. The resonances correspond to transitions from a $1s$ ground state to excited p states. Since the transition is of intraband nature, it possesses sufficient oscillator strength to be observed in optical experiments. For a further gap opening (4) we observe a blue shift of the resonances accompanied by a decreasing oscillator strength since the ordering parameter and the connected ground state distributions $p_{\boldsymbol{k}}^{(0)}$ and $f_{\boldsymbol{k}}^{(0)}$ decrease. For a band gap of $0.4\,\mathrm{eV}$ the wave function of the lowest excited state changes to s symmetry. As consequence the intraband source vanish and the heterostructure is in its semiconducting phase (5). However, due to the weak hybridization of intra and interlayer exciton, the interlayer exciton has negligible

oscillator strength. Since for the semiconductor also the inversion corresponds to unity, the Drude response vanishes as well and no response at all is observed. The material becomes transparent for large wavelengths. For higher temperatures a similar picture emerges but characterized by generally weaker oscillator strength due to smaller ground state populations and a faster change between the phases with band gap altering.

4.4 Conclusion

In this chapter, we introduced the functionalization of two-dimensional inorganic TMDC semiconductors by organic molecules. The molecules form a flat periodic lattice. This enables a transformation for the molecule electrons into a momentum Bloch basis. We suggest such hybrids to be the ideal candidate to form excitonic insulators. The reasons are the large amount of organic molecules with low dielectric constant from which a HIOS could be built. Additionally, the flat bands of the organic layers are favorable for a large interlayer exciton binding energy. Finally, the easy tunability of the molecular energy levels, compared to the bands of inorganic semiconductors, by an applied electric field enables fine tuning of the excitonic phases.

We developed a Bogoliubov description to properly describe the new many-body ground state. We find that excitonic insulators exhibit an intrinsic non-vanishing polarization due to a correlated $1s$ exciton ground state. Additionally, they exhibit a spontaneous formation of inversion. We calculated the excitonic phase diagram as function of temperature and band gap. The latter is tunable via the static Stark shift induced by an applied voltage. We see that the excitonic insulating phase in WS_2-F6TCNNQ is stable up to room temperature. Since the ordering parameter is connected to the exciton binding energy its stability strongly depends on the dielectric environment.

Due to the applied voltage we can choose between three different phases: semi-metal, semiconductor and excitonic insulator. All show different optical signatures in the far-infrared to terahertz regime measurable by linear absorption. The semi-metal is described by a Drude model. The semiconducting phase shows no optical response due to a negligible small oscillator strength of the interlayer exciton. Finally, for the excitonic insulator we find a Drude response modulated by a p exciton Rydberg series, which is observable in linear absorption due to optical intraband transitions.

Chapter 5

X-ray absorption spectroscopy

X-ray experiments, such as X-ray absorption spectroscopy (XAS), have played a tremendous role in the early times of atomic physics for the characterization of the electronic structure of atoms and the search for new elements [43, 44, 258–260]. XAS is a local probe of the electronic and geometrical structure of materials, which can likewise be applied to gases, liquids, solids, and almost all kind of materials like catalysts, minerals or biological tissues [261–266]. This results in a wide application range of XAS in physics, chemistry, biology, or material science [267, 268]. Today, synchrotron is used as source for the necessary intense tunable X-rays. Prior, the continuous spectra of X-ray tubes had to be used and monochromatized, which made measurements time consuming and difficult compared to related techniques as X-ray photoemission spectroscopy or Auger electron spectroscopy [269]. XAS is a general term including both X-ray absorption near edge structure (XANES) and extended X-ray absorption fine structure (EXAFS). Figure 5.1(a) shows a schematic of the lattice periodic potential in a solid state. Energetically, the solid possesses occupied core and valence bands, unoccupied conduction bands, and the ionization continuum above the ionization threshold of the material.

XANES, or alternatively near-edge X-ray absorption fine structure (NEXAFS), is constituted by transitions of inner-core shell electrons into unoccupied states below the ionization level of the materials, cf. Fig. 5.1(a). Such X-ray induced transitions lead to sharp resonance lines in the absorption spectrum, which are called absorption edges as sketched in Fig. 5.1(b). In the existing literature [270–272], XANES is typically described by Fermi's golden rule for the transition probability from core electrons with wave vector $\boldsymbol{k}$ to unoccupied conduction band states with wave vector $\boldsymbol{k}'$ under illumination with a X-ray frequency ω:

$$P(\omega) \propto \int \int dk dk' \, |\boldsymbol{e} \cdot \boldsymbol{d}_{\boldsymbol{k},\boldsymbol{k}'}|^2 \delta \left(E_{\boldsymbol{k}'} - E_{\boldsymbol{k}} - \hbar\omega \right) . \tag{5.1}$$

The transition probability $P(\omega)$ is determined by the product of the dipole matrix element $\boldsymbol{d}_{\boldsymbol{k},\boldsymbol{k}'}$ projected on the polarization vector $\boldsymbol{e}$ and an energy conserving delta function.

When the absorption spectrum is measured over a large range of photon energy, after the XANES part, starting from the ionization threshold, an oscillatory behavior of the absorption coefficient is observed, cf. Fig. 5.1(b). This part of the spectrum is called EXAFS and stems from transitions of core electrons into the ionization continuum above the ionization threshold of the material, cf. Fig. 5.1(a). The characteristic oscillation were first observed in the 1930's and appears only for molecules and solids but not for single atoms. A quantitative description of the oscillation was only given in 1970 by D. E. Sayers and coworkers [52, 53]. The explanation of the oscillation is based on the theory introduced by R. de L. Kronig for
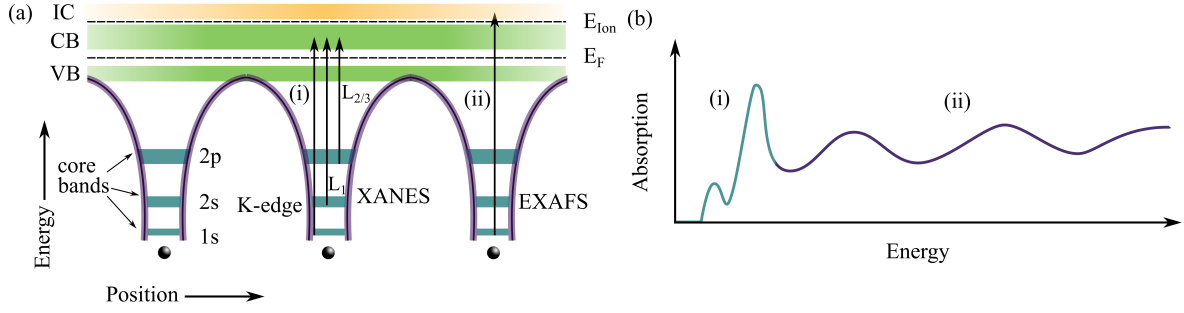
Figure 5.1: (a) Sketch of a lattice periodic potential of a solid state with core, valence (VB), conduction (CB) bands and the ionization continuum (IC). We additionally draw exemplary XANES and EXAFS transitions. (b) Sketch of a typical X-ray absorption spectrum with XANES part (green) exhibiting absorption edges and the EXAFS part (violet) showing the oscillatory behavior. Figure appears similarly in Ref. [274].

small molecular gases [50, 51]. The description interprets the oscillations in the spectrum as interference effects emerging from secondary waves emitted by an X-ray absorbing atom and waves back scattered by neighbored atoms [273]. The corresponding parametrization of the absorption by D. E. Sayers *et. al*

$$\alpha_k = S_0^2 \sum_i N_i \frac{|f_i(k)|}{kR_i^2} \sin\left(2kR_i + \phi_i\right) e^{-2R_i/\lambda_k} e^{-2\sigma_i^2 k^2} \tag{5.2}$$

has become standard in describing EXAFS. The formula gives the absorption cross section as function of the wave number of the photoelectron. For EXAFS the X-ray energy is higher than the ionization energy E_{Ion} of the material and the excess energy is transferred to the excited photoelectron in form of kinetic energy. Consequently, the X-ray excitation frequency ω, can be related to the photoelectron wave number by $k^2 = 2m_0(\hbar\omega - E_{Ion})/\hbar^2$ with the free electron mass m_0. The structural parameters are the number of equivalent scatterers N_i of type i, the interatomic distances R_i, and the bond length σ_i. The discovery of the relation between the oscillation and the interatomic bond length promoted XAS to a structural method. The exponential factor $\exp(-2R_i/\lambda_k)$ accounts for the finite lifetime of the photoelectron, which is only scattered elastically over a short distance. Here, λ_k stands for the X-ray wavelength. The Debye-Waller factor accounts for thermally or disorder induced changes in the bond length. The quantity $|f_i(k)|$ describes the back scattering amplitude, resulting from back scattering of neighboring atoms, and S_0 describes the reduction factor due to multielectron processes. Finally, ϕ_i stand for phase shifts due to the initially excited and the back scattering atom [53, 273]. Although, the development of the Sayers formula is of paramount importance and under extensive use for the analysis of all kind of EXAFS measurement it has one problem: The utilized wave functions for the derivation of Eq. (5.2) do not fulfill the Bloch theorem and are therefore no proper basis functions for solid states. Therefore, in this chapter we derive a Bloch theory for X-ray absorption spectroscopy for atomically-thin materials. Moreover, we aim for a combination of the Bloch formalism with the solution of the Maxwell equations to construct a self-consistent spatio-temporal resolved XAS theory, which describes XANES and EXAFS in one consistent description. The spatial resolution allows for local excitations of the solid with high-energy X-ray light and the temporal resolution accounts for the description of ultrafast phenomena accessible in time-resolved X-ray spectroscopy.

The presented results and parts of the formulation were submitted for publication at Physical Review Research.

5.1 Core electrons

Typically, electrons are separated into two categories: core and valence electrons. Core electrons are strongly bound and often even added to the nucleus. The reason is that core or inner-shell electrons remain largely unaltered when an atom is present in a molecule or crystal whereas valence electrons rearrange and contribute to the bonding properties. An electronic ground state of a solid state crystal is naturally described by Bloch waves – simultaneous eigenstates of the periodic Hamiltonian and of the direct lattice translations and extensively discussed in Sec. 2.2. Here, the electronic wave function is a product of a plane wave and a lattice periodic function labelled by band index λ and wave vector $\boldsymbol{k}$. Because of their plane wave character Bloch waves are rather delocalized over the crystal, which makes their description difficult for core electrons. However, since Bloch functions have different envelope functions at different wave vectors, we can expect to build a localized wave packet by superposing Bloch functions of different wave vectors [275]. A strongly localized wave packet in real space is achieved from a broad $\boldsymbol{k}$-space superposition

$$w_{\lambda,0}(\boldsymbol{r}) = \frac{1}{\sqrt{N}} \int_{UC} d^2k \; \Psi_{\lambda,\boldsymbol{k}}(\boldsymbol{r}) \,, \tag{5.3}$$

where the integral is carried over the 1st Brillouin zone with normalization constant N corresponding to the number of unit cells. The function $w_{\lambda,0}(\boldsymbol{r})$ denotes a Wannier function located at the center atom of the crystal. We can insert into the integral a phase factor $\exp(i\boldsymbol{k} \cdot \boldsymbol{R})$ with the real space lattice vector. This has the effect of translating the real-space Wannier function by $\boldsymbol{R}$ and generates additional Wannier functions at different atom positions

$$w_{\lambda}(\boldsymbol{r} - \boldsymbol{R}) = \frac{1}{\sqrt{N}} \int_{UC} d^2k \; e^{-i\boldsymbol{k}\cdot\boldsymbol{R}} \Psi_{\lambda,\boldsymbol{k}}(\boldsymbol{r}) \,. \tag{5.4}$$

Here, the Wannier function has the form of a Fourier transform. From inverse Fourier transformation and transformation to a discrete grid we can construct the electronic wave functions

$$\Psi_{\lambda,\boldsymbol{k}}(\boldsymbol{r}) = \frac{1}{\sqrt{N}} \sum_{\boldsymbol{R}} e^{i\boldsymbol{k}\cdot\boldsymbol{R}} w_{\lambda}(\boldsymbol{r} - \boldsymbol{R}) \,, \tag{5.5}$$

which form a complete orthonormal set. The Wannier representation is essentially a real-space picture of localized orbitals and assigns as quantum number the lattice vector $\boldsymbol{R}$ of the cell, where the orbital is localized, together with the band index λ. The transition from Eq. (5.4) to Eq. (5.5) constitute a unitary transformation between Bloch and Wannier states. Therefore, both states are an equally valid description of the band subspace. We conclude that Wannier functions provide an attractive option for representing the space spanned by a Bloch band in a crystal, but being localized and still carrying the same information contained in the Bloch functions. Similar to the Bloch functions $u_{\lambda,\boldsymbol{k}}(\boldsymbol{r})$, Wannier functions require computationally expensive methods. A practical solution is to expand the Wannier functions after atomic orbitals, which yields the tight binding wave function approach [276, 277]. We can write for an electronic wave function of band λ

$$\Psi_{\lambda,\boldsymbol{k}}(\boldsymbol{r}) = \frac{1}{\sqrt{N}} \sum_{\beta,j,\boldsymbol{R}_\beta} C_{\beta j,\boldsymbol{k}}^{\lambda} e^{i\boldsymbol{k}\cdot\boldsymbol{R}_\beta} \phi_{\beta,j}^{\lambda}(\boldsymbol{r} - \boldsymbol{R}_\beta) \,. \tag{5.6}$$

The band at sublattice β consists of atomic orbitals $\phi^\lambda_{\beta,j}$ of type j. The atomic orbitals decay spatially with an effective inverse length $\zeta = Z/a_B$ simulating the screening of a many-electron system. a_B corresponds to the hydrogen Bohr radius and Z denotes the nuclear charge. The phase factor ensures the lattice translation symmetry. The tight binding coefficient $C^\lambda_{\beta j, \boldsymbol{k}}$ describes the weight of each orbital to the band. In the following, we will derive the matrix elements formally with Bloch waves and afterwards within a tight-binding approximation. However, a Wannier representation is achievable is desired by expressing the Bloch functions in terms of Wannier functions. After having discussed the wave function, we quickly examine the core dispersion. Because of the strong localization of the core states we can expect a small orbital overlap of neighbored lattice sites. Consequently, the core bands can in good approximation be described by flat bands.

5.2   XANES

As introduced at the beginning of this chapter, XANES consists of transitions of core electrons into unoccupied bands below the ionization threshold of the material. We start with the many-body Hamiltonian in second quantization, which reads

$$H = \sum_{\lambda,\boldsymbol{k}} \varepsilon^\lambda_{\boldsymbol{k}} \lambda^\dagger_{\boldsymbol{k}} \lambda_{\boldsymbol{k}} - \sum_{\lambda,\lambda',\boldsymbol{k},\boldsymbol{k}',\boldsymbol{Q}} \boldsymbol{d}^{\lambda\lambda'}_{\boldsymbol{k},\boldsymbol{k}'}(\boldsymbol{Q}) \cdot \boldsymbol{E}_{\boldsymbol{Q}}(z_0,t) \lambda^\dagger_{\boldsymbol{k}} \lambda'_{\boldsymbol{k}'} + \sum_{\substack{\lambda,\nu,\lambda',\nu' \\ \boldsymbol{k},\boldsymbol{q},\boldsymbol{k}',\boldsymbol{q}'}} V^{\lambda\nu\nu'\lambda'}_{\boldsymbol{k},\boldsymbol{q},\boldsymbol{q}',\boldsymbol{k}'} \lambda^\dagger_{\boldsymbol{k}} \nu^\dagger_{\boldsymbol{q}} \nu'_{\boldsymbol{q}'} \lambda'_{\boldsymbol{k}'} . \quad (5.7)$$

The first term describes the single-particle energy of the electrons in band λ with in-plane wave vector $\boldsymbol{k}$. Here, λ summarizes all bands within the material including core states. The second contribution to the Hamiltonian describes the X-ray-matter interaction with dipole matrix element $\boldsymbol{d}^{\lambda\lambda'}_{\boldsymbol{k},\boldsymbol{k}'}(\boldsymbol{Q})$. In contrast to the definition in the second chapter we explicitly include the spatial in-plane extension of the electric field via the Fourier transform $\boldsymbol{E}(\boldsymbol{r},t) = \sum_{\boldsymbol{Q}} \boldsymbol{E}_{\boldsymbol{Q}}(z_0,t)\exp(i\boldsymbol{Q}\cdot\boldsymbol{r}_\parallel)$ with the X-ray wave vector $\boldsymbol{Q}$. The dipole matrix element reads then

$$\boldsymbol{d}^{\lambda\lambda'}_{\boldsymbol{k},\boldsymbol{k}'}(\boldsymbol{Q}) = e\langle \Psi_{\lambda,\boldsymbol{k}} \mid \boldsymbol{r} \; e^{i\boldsymbol{Q}\cdot\boldsymbol{r}_\parallel} \mid \Psi_{\lambda',\boldsymbol{k}'}\rangle . \quad (5.8)$$

So far, for visible and extreme ultraviolet light up to $20\,\text{eV}$ the spatial variation of the electric field compared to the 1st Brillouin zone could have been seen as constant. As consequence the spatial phase factor was approximated within a Taylor expansion to one. Here, we consider X-ray energies up to $500\,\text{eV}$. This corresponds to a X-ray wave vector of about 10% of the 1st Brillouin zone and might not be negligible anymore. Additionally, this formal definition makes the theory scalable even up to the hard X-ray regime. Since we consider the interaction of X-rays with atomically-thin materials, the dipole approximation can be made in the direction perpendicular to the material. Therefore, the electric field is considered only at the position z_0 of the material.

The definition of the Coulomb matrix element is unaltered compared to the previous chapters and includes all possible interaction pathways.

So far, the dipole matrix elements describes XANES and EXAFS. We start first by deriving an expression for the XANES dipole matrix element.

5.2.1   Plane Bloch waves

XANES is characterized by transitions of core electrons into unoccupied conduction band states below the ionization threshold of the material. Such transitions give rise to sudden

absorption edges in the XAS spectrum. Apart from sufficient excitation energy the transition requires a finite dipole matrix element. We restrict the final state band index to bands lying below the ionization threshold and insert Bloch waves into the formal definition of the dipole element. We obtain an expression for the dipole operator acting partly as a derivative on $a^\dagger_{\lambda,\boldsymbol{k}} a_{\lambda',\boldsymbol{k}'}$ of the form

$$\boldsymbol{X}^{\lambda\lambda'}_{\boldsymbol{k}+\boldsymbol{Q}-\boldsymbol{G},\boldsymbol{k}} = -\frac{ie}{V_{UC}} \langle \begin{pmatrix} \nabla_{\boldsymbol{k}+\boldsymbol{Q}-\boldsymbol{G}} \\ iz \end{pmatrix} u_{\lambda,\boldsymbol{k}+\boldsymbol{Q}-\boldsymbol{G}} \mid e^{i\boldsymbol{G}\cdot\boldsymbol{r}_\parallel} \mid u_{\lambda',\boldsymbol{k}} \rangle \delta_{\lambda',\bar{\lambda}} - ie\delta_{\lambda,\lambda'}\nabla_{\boldsymbol{k}+\boldsymbol{Q}-\boldsymbol{G}}. \quad (5.9)$$

An elaboration of the performed manipulations can be found in the appendix A.2. To highlight that the dipole operator describes solely X-ray induced transitions from core bands into final electronic states within the material ($\boldsymbol{X}$ANES) we introduce the labeling $\boldsymbol{d}^{\lambda\lambda'}_{\boldsymbol{k},\boldsymbol{k}'}(\boldsymbol{Q}) \to \boldsymbol{X}^{\lambda\lambda'}_{\boldsymbol{k}+\boldsymbol{Q}-\boldsymbol{G},\boldsymbol{k}}$. We see that the X-ray transition fulfills the momentum selection rule of $\boldsymbol{k}' = \boldsymbol{k} - \boldsymbol{Q} + \boldsymbol{G}$ for the optical transition. The relaxed momentum conservation accounts for a transfer of the in-plane field momentum to the optically excited electron. However, the momentum is conserved up to a reciprocal lattice vector $\boldsymbol{G}$. In case that the sum of $\boldsymbol{k}$ and $\boldsymbol{Q}$ lies outside of the 1st Brillouin zone the reciprocal lattice vector $\boldsymbol{G} \neq 0$ accounts for Umklapp processes [278].

In Eq. (5.9), the first term describes interband transitions between core and unoccupied conduction band states. According to the Siegbahn notation, the absorption edges are named after the main quantum number of the initially excited core electron. For example K transitions involve $1s$ electrons, while excitation of $2s$ and $2p$ electrons occur at the L edges. The enumeration continues similar to the atomic shell model. In case that the angular quantum number is non zero the edges are indexed with consecutive numbers with increasing total angular momentum. For example the L edge consists of the L_1 ($2s$ electrons), L_2, and L_3 transition. The two latter involve the $2p$ electrons with total angular momentum $J = 1/2$ and $J = 3/2$, respectively.

As already discussed in the second chapter, the second term leads to a wave vector gradient, which changes according to the acceleration theorem with a rate proportional to the X-ray field [279] and describes the coupling strength of X-ray excitation to intraband transitions [86, 280]. The X-ray radiation has excitation energies from a hundred of eV up to tens of keV. Consequently, the intraband dynamics do not significantly change the optical response and the intraband effect can be neglected regarding X-ray radiation.

5.2.2 Tight binding description

For Bloch waves the orbital band composition, the character of the dipole transition, and the lattice geometry are encoded in the lattice periodic function $u_{\lambda,\boldsymbol{k}}(\boldsymbol{r})$. Their calculation requires usually computational expensive methods. To bridge this gap we evaluate the matrix element by using tight binding wave functions. This will give us also some analytical insights into X-ray induced core transitions.

By inserting the tight binding wave function Eq. (5.6) for initial and final state into the formal definition Eq. (5.8) and expanding the integral into a sum over unit cells at the lattice

vector $\boldsymbol{R}_\beta$ yields

$$\boldsymbol{X}^{\lambda\lambda'}_{\boldsymbol{k}+\boldsymbol{Q}-\boldsymbol{G},\boldsymbol{k}} = -e \sum_{\alpha,\beta,i,j} \sum_{\boldsymbol{\delta}_{\beta\alpha}} C^{*\lambda}_{\beta j,\boldsymbol{k}+\boldsymbol{Q}-\boldsymbol{G}} C^{\lambda'}_{\alpha i,\boldsymbol{k}} e^{i\boldsymbol{k}\cdot\boldsymbol{\delta}_{\beta\alpha}} \langle \lambda,\beta,j,0 \mid \boldsymbol{r}\ e^{i\boldsymbol{Q}\cdot\boldsymbol{r}_\parallel} \mid \lambda',\alpha,i,\boldsymbol{\delta}_{\beta\alpha}\rangle$$

$$- ie \sum_{\alpha,\beta,i,j} \sum_{\boldsymbol{\delta}_{\beta\alpha}} C^{*\lambda}_{\beta j,\boldsymbol{k}+\boldsymbol{Q}-\boldsymbol{G}} C^{\lambda'}_{\alpha i,\boldsymbol{k}} e^{i\boldsymbol{k}\cdot\boldsymbol{\delta}_{\beta\alpha}} \langle \lambda,\beta,j,0 \mid e^{i\boldsymbol{Q}\cdot\boldsymbol{r}_\parallel} \mid \lambda',\alpha,i,\boldsymbol{\delta}_{\beta\alpha}\rangle \nabla_{\boldsymbol{k}+\boldsymbol{Q}-\boldsymbol{G}}$$

$$(5.10)$$

providing the same momentum selection rule as previously, Eq. (5.9). A projection onto atomic orbital basis yields $\langle\boldsymbol{r}|\lambda,\beta,j,\boldsymbol{\delta}_{\beta\alpha}\rangle = \phi^\lambda_{\beta j}(\boldsymbol{r}-\boldsymbol{\delta}_{\beta\alpha})$, where $\boldsymbol{\delta}_{\beta\alpha} = \boldsymbol{R}_\beta - \boldsymbol{R}_\alpha$ stands for the next-neighbor vectors connecting the atoms. The sum over the sublattices α, β includes neighboring atoms of arbitrary order. The matrix element is determined by the tight binding coefficients and the phase factor $\exp(i\boldsymbol{k}\cdot\boldsymbol{\delta}_{\beta\alpha})$. The core orbitals are strongly localized and their spatial extent decays quickly even compared to the X-ray wavelength of soft and medium X-rays. Therefore, it reasonable to treat the transition integral in dipole approximation. In the appendix A.5.3 we calculate the onsite transition integral, which forms the dominate contribution, beyond the dipole approximation by including the full spatial phase of the electric field. We find that the dipole approximation for the transition integral holds up to X-ray energies of $\sim 4\text{-}5\,\mathrm{keV}$. Since the spatial decay of atomic orbitals directly depends on the atomic number Z the approximation becomes better the heavier the constituting atoms are. Additionally, the dipole integral recovers the optical selection rules known from atomic spectroscopy. However, thanks to the tight binding wave function we include solid state properties, in particular the lattice periodicity. A second consequence of the smaller spatial extent of core orbitals compared to valence orbitals is that the optical transitions are generally weaker compared to optical transitions lying in the visible range of the electromagnetic spectrum. Within a dipole approximation the integral in the second line turns into an overlap integral. The overlap is generally small and we may assume that the chosen orbitals are orthogonal to each other. Then the second line describes intraband transitions similar to Eq. (5.9).

5.3 EXAFS

5.3.1 Plane Bloch waves

Up to now, we have described all transitions from core states into the conduction bands. Now, we extend the model and include the ionization continuum (IC) starting at the ionization energy of the material. Inserting the orthogonalized plane waves Eq. (2.10) and the Bloch band states Eq. (2.7) into the definition of the dipole matrix element Eq. (5.8) yields

$$\mathbf{Y}^{\lambda k_\perp}_{\boldsymbol{k},\boldsymbol{k}'}(\boldsymbol{Q}) = e\langle\Psi_{\lambda,\boldsymbol{k}} \mid \boldsymbol{r}\ e^{i\boldsymbol{Q}\cdot\boldsymbol{r}_\parallel} \mid \boldsymbol{k}'\rangle + e\sum_{\lambda'} \eta_{\lambda',\boldsymbol{k}',k_\perp} \langle\Psi_{\lambda,\boldsymbol{k}} \mid \boldsymbol{r}\ e^{i\boldsymbol{Q}\cdot\boldsymbol{r}_\parallel} \mid \Psi_{\lambda',\boldsymbol{k}'}\rangle \qquad (5.11)$$

with the notation $\langle\boldsymbol{r}|\boldsymbol{k}\rangle = \exp(i(\boldsymbol{k}\cdot\boldsymbol{r}_\parallel + k_\perp z))/\sqrt{V}$ resulting from the unorthogonalized plane wave character of the final state. The second term stems from the orthogonalization due to the Gram-Schmidt procedure. To distinguish from the XANES matrix element we denote the EXAFS dipole matrix element as $\boldsymbol{d}^{\lambda k_\perp}_{\boldsymbol{k},\boldsymbol{k}'}(\boldsymbol{Q}) \rightarrow \boldsymbol{Y}^{\lambda k_\perp}_{\boldsymbol{k},\boldsymbol{k}'}(\boldsymbol{Q})$. The matrix element can be calculated analogously to the XANES case with the difference that the wave vector of the ionization continuum is three-dimensional. We obtain

$$\boldsymbol{Y}^{\lambda k_\perp}_{\boldsymbol{k}+\boldsymbol{Q}-\boldsymbol{G},\boldsymbol{k}} = -\frac{ie}{\sqrt{V_{UC}}}\left\langle \begin{pmatrix} \nabla_{\boldsymbol{k}+\boldsymbol{Q}-\boldsymbol{G}} \\ iz \end{pmatrix} u_{\lambda,\boldsymbol{k}+\boldsymbol{Q}-\boldsymbol{G}} \mid e^{i\boldsymbol{G}\cdot\boldsymbol{r}_\parallel}e^{ik_\perp z}\right\rangle + \sum_{\lambda'} \eta_{\lambda',\boldsymbol{k},k_\perp} \boldsymbol{X}^{\lambda\lambda'\,(\mathrm{inter})}_{\boldsymbol{k}+\boldsymbol{Q}-\boldsymbol{G},\boldsymbol{k}}. \quad (5.12)$$

As for the XANES dipole element, we find an interband term describing the optical transition between a Bloch and a plane wave state. But in contrast to XANES no intraband interaction is available because of the forced orthogonality of the ionization continuum to all band states. Therefore, the appearing XANES matrix element in Eq. (5.12), stemming from the orthogonalization, is restricted to its interband part.

5.3.2 Tight binding description

As for the XANES transitions, we evaluate the EXAFS matrix element for tight binding wave functions. The starting point is the EXAFS dipole matrix element Eq. (5.11), now with the initial state electronic wave function $\Psi_{\lambda,\boldsymbol{k}}(\boldsymbol{r})$ in the tight binding approach. First we investigate the orthogonalization coefficients, which appear under a sum of all involved bands. The electronic bands are constituted from atomic orbitals. Each atomic orbital is determined by the main n, angular l and magnetic m quantum number and can be written as product of radial function and spherical harmonics. We can then explicitly calculate the orthogonalization coefficients, which read

$$\eta_{\lambda,\boldsymbol{k},k_\perp} = i^l \sqrt{(2\zeta)^{2n+1}/(2n)!} J_{nl}(k) Y_{lm}(\vartheta_k, \varphi_k)/2\pi^2 \tag{5.13}$$

with the spherical harmonics Y_{lm} and the radial function $J_{nl}(k) = \sqrt{\pi/2k}(\zeta^2+k^2)^{-(n+1)/2}\Gamma(n-1+l)P_n^{-l}[\zeta(\zeta^2+l^2)^{-1/2}]$ with the associated Legendre polynomials $P_n^l(x)$. Generally, because the $1s$ orbital has the smallest extent in real space, it determines the strength of the orthogonalization contribution to the EXAFS dipole matrix element. The orthogonalization coefficient to the $1s$ state is proportional to $\eta_{1s,\boldsymbol{k},k_\perp} \propto (\zeta^2 + k^2)^{-2}$. Here, $\eta_{1s,\boldsymbol{k},k_\perp}$ decreases to $10\,\%$ at approximately $k = \sqrt{2}\zeta$. We see that the orthogonalization coefficient depends on the atomic number and gains importance with increasing atomic weight. With an exemplary effective atomic number of $Z = 5.7$, stemming from the Slater rule for carbon [281], we obtain a wave number of $140\,\mathrm{nm}^{-1}$ corresponding to an energy of $5\,\mathrm{eV}$. Starting at the ionization threshold we see that the coefficients decrease rapidly with increasing energy. The reason is that the orthogonalization contributes only close to the surface. Since the coefficients $\eta_{\lambda,\boldsymbol{k},k_\perp}$ decrease rapidly to zero with increasing energy, we use in the following free electronic continuum states for simplicity. The EXAFS matrix element constitutes now only of the first term of Eq. (5.11) and reads

$$\mathbf{Y}_{\boldsymbol{k},\boldsymbol{k}+\boldsymbol{G}}^{\lambda k_\perp} = -\frac{e}{\sqrt{V_{UC}}} \sum_{\beta,j} C_{\beta j,\boldsymbol{k}}^{*\lambda} \langle \lambda, \beta, j, 0 \mid \boldsymbol{r} \mid \boldsymbol{k} + \boldsymbol{G} \rangle. \tag{5.14}$$

However, the plane wave approximation has to be investigated carefully for each material independently.

In the case of graphene the core bands constitute just of $1s$ electrons. Consequently, only K-shell transitions are present. The calculation of the transition integral from a $\lambda = 1s$ core electron to the plane wave state is detailed in the appendix A.5.2. We obtain

$$\mathbf{Y}_{\boldsymbol{k},\boldsymbol{k}+\boldsymbol{G}}^{1s k_\perp} = -\frac{e}{\sqrt{V_{UC}}} \sum_{\beta,n} C_{\beta 1s,\boldsymbol{k}}^{*1s} \frac{32\sqrt{\pi} i \zeta^{5/2}(\boldsymbol{k}+\boldsymbol{G})_n}{(\zeta^2 + (\boldsymbol{k}+\boldsymbol{G})^2)^3} \hat{\boldsymbol{e}}_n \tag{5.15}$$

with the unit vector $\hat{\boldsymbol{e}}_n$ in Cartesian coordinates. Equation (5.15) consists of the tight binding coefficients, which carry the lattice periodicity, and the transition integral, which carries the unit cell informations. The latter resembles a Laue condition for X-ray diffraction and peaks at $\boldsymbol{k} = \boldsymbol{G}$. The magnitude and width of the form factor peaks are determined by the spatial

electron distribution. Therefore, the form factor is weakened by the effective inverse Bohr radius $\zeta = Z/a_B$, cf. Eq. (5.15) denominator. Further, we see that the optical transition into the ionization continuum is unpolarized in contrast to transitions within the material. Therefore, the optical transition into the vacuum are independent of the incident angle of the light.

It is interesting to compare EXAFS to the two complementary techniques X-ray diffraction and electron diffraction used to measure the structure of crystals. The difference between EXAFS and X-ray diffraction lies in the choice of the observable. While for the EXAFS a transmission or reflection setup is used, for X-ray diffraction also the spatially resolved signal is collected. The latter is described by the unit cell contribution to Eq. (5.15), determined by the Fourier transform of the electron distribution, which is often called form factor. As consequence the X-rays are not very sensitive to light atoms with stronger localized and only weakly screened inner shell electrons [282]. For electron diffraction the form factor can be calculated from the X-ray form factor by the Mott-Bethe equation [283, 284], which takes additionally to the elastic scattering at the electron clouds also nucleus scattering into account. Then also crystals of lighter elements can be resolved and measured.

5.4   X-ray Bloch equations and Meitner-Auger recombination

The observable describing the X-ray response of the material is the detected X-ray field, which is given as the incident light field interfering with the excited dipole density in the sample in reflection or transmission geometry. As already discussed in the previous chapters, the dipole density $\boldsymbol{P}(\boldsymbol{r}, t)$ as a function of the electric field $\boldsymbol{E}(\boldsymbol{r}, t)$ can be derived from the light-matter interaction Hamiltonian. We can identify the two-dimensional macroscopic polarization density

$$\boldsymbol{P}_{\boldsymbol{Q}}^{2D}(t) = \frac{1}{A} \sum_{\lambda_1 \neq \lambda_2, \boldsymbol{G}, \boldsymbol{k}} \boldsymbol{d}_{\boldsymbol{k}+\boldsymbol{Q}-\boldsymbol{G}, \boldsymbol{k}}^{\lambda_1 \lambda_2} p_{\boldsymbol{k}+\boldsymbol{Q}-\boldsymbol{G}, \boldsymbol{k}}^{\lambda_1 \lambda_2}(t) \,, \tag{5.16}$$

which determines the X-ray response. Here, we explicitly exclude the intraband contribution since it is not altering the X-ray response. As expected, the two-dimensional macroscopic polarization is determined by the microscopic transition $p_{\boldsymbol{k}+\boldsymbol{Q}-\boldsymbol{G}, \boldsymbol{k}}^{\lambda_1 \lambda_2}(t) = \langle a_{\lambda_1, \boldsymbol{k}+\boldsymbol{Q}-\boldsymbol{G}}^{\dagger} a_{\lambda_2, \boldsymbol{k}} \rangle(t)$, which includes now all available bands of the solid, and can be excited if the corresponding dipole matrix element $\mathbf{d}_{\boldsymbol{k}+\boldsymbol{Q}-\boldsymbol{G}, \boldsymbol{k}}^{\lambda_1 \lambda_2}$ does not vanish. Due to the spatial resolution of the X-ray light the non-diagonal character of the microscopic transition and densities in momentum space is included. For a better readability, we introduce the abbreviations $\boldsymbol{k}_1 = \boldsymbol{k} + \boldsymbol{Q} - \boldsymbol{G}$ and $\boldsymbol{k}_2 = \boldsymbol{k}$ and derive the equation of motion for the microscopic polarization from the Heisenberg's equation of motion:

$$
\begin{aligned}
i\hbar \frac{d}{dt} p_{\boldsymbol{k}_1, \boldsymbol{k}_2}^{\lambda_1 \lambda_2} &= \left(\varepsilon_{\boldsymbol{k}_2}^{\lambda_2} - \varepsilon_{\boldsymbol{k}_1}^{\lambda_1} \right) p_{\boldsymbol{k}_1, \boldsymbol{k}_2}^{\lambda_1 \lambda_2} + i\hbar \partial_t p_{\boldsymbol{k}_1, \boldsymbol{k}_2}^{\lambda_1 \lambda_2} \big|_{\text{coll}} \\
&\quad - \sum_{\lambda, \boldsymbol{Q}', \boldsymbol{G}'} \mathbf{E}_{\boldsymbol{Q}'}(t) \cdot \left(\boldsymbol{d}_{\boldsymbol{k}_2, \boldsymbol{k}_2 + \boldsymbol{Q}' + \boldsymbol{G}'}^{\lambda_2 \lambda} \sigma_{\boldsymbol{k}_1, \boldsymbol{k}_2 - \boldsymbol{Q}' + \boldsymbol{G}'}^{\lambda_1 \lambda} - \boldsymbol{d}_{\boldsymbol{k}_1 + \boldsymbol{Q}' - \boldsymbol{G}', \boldsymbol{k}_1}^{\lambda \lambda_1} \sigma_{\boldsymbol{k}_1 + \boldsymbol{Q}' - \boldsymbol{G}', \boldsymbol{k}_2}^{\lambda \lambda_2} \right) \\
&\quad + \sum_{\substack{\lambda_a, \lambda_b, \lambda_c \\ \boldsymbol{k}_a, \boldsymbol{k}_b, \boldsymbol{k}_c}} \left(V_{\boldsymbol{k}_2, \boldsymbol{k}_a, \boldsymbol{k}_b, \boldsymbol{k}_c}^{\lambda_2 \lambda_a \lambda_b \lambda_c} - V_{\boldsymbol{k}_2, \boldsymbol{k}_a, \boldsymbol{k}_c, \boldsymbol{k}_b}^{\lambda_2 \lambda_a \lambda_c \lambda_b} \right) \sigma_{\boldsymbol{k}_a, \boldsymbol{k}_c}^{\lambda_a \lambda_c} \sigma_{\boldsymbol{k}_1, \boldsymbol{k}_b}^{\lambda_1 \lambda_b} \\
&\quad - \sum_{\substack{\lambda_a, \lambda_b, \lambda_c \\ \boldsymbol{k}_a, \boldsymbol{k}_b, \boldsymbol{k}_c}} \left(V_{\boldsymbol{k}_a, \boldsymbol{k}_b, \boldsymbol{k}_1, \boldsymbol{k}_c}^{\lambda_a \lambda_b \lambda_1 \lambda_c} - V_{\boldsymbol{k}_b, \boldsymbol{k}_a, \boldsymbol{k}_1, \boldsymbol{k}_c}^{\lambda_b \lambda_a \lambda_1 \lambda_c} \right) \sigma_{\boldsymbol{k}_b, \boldsymbol{k}_c}^{\lambda_b \lambda_c} \sigma_{\boldsymbol{k}_a, \boldsymbol{k}_2}^{\lambda_a \lambda_2} \,. \tag{5.17}
\end{aligned}
$$

The first term incorporates the free oscillation of the transition amplitude with the single-particle energies of initial and final state. The second line of Eq. (5.17) describes the coupling to the X-ray field. Here, $\sigma_{\boldsymbol{k},\boldsymbol{k}'}^{\lambda\lambda'} = \langle a_{\lambda,\boldsymbol{k}}^{\dagger} a_{\lambda',\boldsymbol{k}'} \rangle$ describes a general transition amplitude. This expectation value turns into an interband transition $p_{\boldsymbol{k},\boldsymbol{k}'}^{\lambda\lambda'}$ for $\lambda \neq \lambda'$ and into a non-local occupation $f_{\boldsymbol{k},\boldsymbol{k}'}^{\lambda}$ for $\lambda = \lambda'$. The third and fourth line describe the Coulomb contribution. The Coulomb interaction is divided in Hartree-Fock and collision $p_{\boldsymbol{k}+\boldsymbol{Q}-\boldsymbol{G},\boldsymbol{k}}^{\lambda_1\lambda_2}\big|_{\mathrm{coll}}$ contributions including many-body interaction and scattering-induced dephasing beyond the Hartree-Fock level. Depending on the band index combination of the Coulomb matrix element, the third and fourth line implicitly includes band and field renormalization. The renormalizations lead to a shift of the absorption peak. Restricting the equation of motion to the linear optics limit sources of the microscopic transition being quadratic in the occupation can be neglected. Generally, depending on the excitation conditions and band structure, one has to carefully investigate, which terms contribute to the dynamics of the X-ray induced transition.

Investigating the transition between the bands λ_1 and λ_2, for example due to a spectral sharp X-ray pulse, the band sums in Eq. (5.17) can be restricted exclusively to these bands. Neglecting sources, which rotate with twice of the transition frequency the X-ray Bloch equation reads

$$
\begin{aligned}
i\hbar\frac{d}{dt}p_{\boldsymbol{k}_1,\boldsymbol{k}_2}^{\lambda_1\lambda_2} = {}& \left(\varepsilon_{\boldsymbol{k}_2}^{\lambda_2} - \varepsilon_{\boldsymbol{k}_1}^{\lambda_1}\right) p_{\boldsymbol{k}_1,\boldsymbol{k}_2}^{\lambda_1\lambda_2} + i\hbar\partial_t p_{\boldsymbol{k}_1,\boldsymbol{k}_2}^{\lambda_1\lambda_2}\big|_{\mathrm{coll}} \\
& - \sum_{\boldsymbol{Q}',\boldsymbol{G}'} \boldsymbol{E}_{\boldsymbol{Q}'}(t) \cdot \left(\boldsymbol{d}_{\boldsymbol{k}_2,\boldsymbol{k}_2+\boldsymbol{Q}'+\boldsymbol{G}'}^{\lambda_2\lambda_1} f_{\boldsymbol{k}_1,\boldsymbol{k}_2-\boldsymbol{Q}'+\boldsymbol{G}'}^{\lambda_1} - \boldsymbol{d}_{\boldsymbol{k}_1+\boldsymbol{Q}'-\boldsymbol{G}',\boldsymbol{k}_1}^{\lambda_2\lambda_1} f_{\boldsymbol{k}_1+\boldsymbol{Q}'-\boldsymbol{G}',\boldsymbol{k}_2}^{\lambda_2}\right) \\
& + \sum_{\boldsymbol{k}',\boldsymbol{q}} \left(V_{\boldsymbol{k}_1+\boldsymbol{q},\boldsymbol{k}',\boldsymbol{k}'+\boldsymbol{q},\boldsymbol{k}_1}^{\lambda_1\lambda_1\lambda_1\lambda_1} f_{\boldsymbol{k}_1+\boldsymbol{q},\boldsymbol{k}'+\boldsymbol{q}}^{\lambda_1} p_{\boldsymbol{k}',\boldsymbol{k}_2+\boldsymbol{q}}^{\lambda_1\lambda_2} - V_{\boldsymbol{k}_2,\boldsymbol{k}'-\boldsymbol{q},\boldsymbol{k}'-\boldsymbol{q},\boldsymbol{k}_2}^{\lambda_2\lambda_2\lambda_2\lambda_2} f_{\boldsymbol{k}'+\boldsymbol{q},\boldsymbol{k}_2+\boldsymbol{q}}^{\lambda_2} p_{\boldsymbol{k}_1,\boldsymbol{k}'}^{\lambda_1\lambda_2}\right) \\
& + \sum_{\boldsymbol{k}',\boldsymbol{q}} \left(V_{\boldsymbol{k}_1+\boldsymbol{q},\boldsymbol{k}',\boldsymbol{k}'+\boldsymbol{q},\boldsymbol{k}_1}^{\lambda_1\lambda_2\lambda_2\lambda_1} f_{\boldsymbol{k}',\boldsymbol{k}_2}^{\lambda_2} p_{\boldsymbol{k}_1+\boldsymbol{q},\boldsymbol{k}'+\boldsymbol{q}}^{\lambda_1\lambda_2} - V_{\boldsymbol{k}'+\boldsymbol{q},\boldsymbol{k}_2,\boldsymbol{k}_2+\boldsymbol{q},\boldsymbol{k}'}^{\lambda_1\lambda_2\lambda_2\lambda_1} f_{\boldsymbol{k}_1,\boldsymbol{k}'}^{\lambda_1} p_{\boldsymbol{k}'+\boldsymbol{q},\boldsymbol{k}_2+\boldsymbol{q}}^{\lambda_1\lambda_2}\right) . \quad (5.18)
\end{aligned}
$$

From the second line we see that the X-ray transition is initiated by the core occupation $f_{\mathbf{k}_1,\mathbf{k}_2-\boldsymbol{q}'+\boldsymbol{G}'}^{\lambda_1}$ and blocked by the final band occupation $f_{\mathbf{k}_1+\boldsymbol{q}'-\boldsymbol{G}',\mathbf{k}_2}^{\lambda_2}$. The two different indices indicate the existence of spatial correlations in a spatially inhomogeneous system. The third line describes an energy renormalization, due to intraband Coulomb interaction, which includes the effect of core-holes [285]. The fourth line corresponds to the excitonic contribution as in Eq. (2.49) but for an inhomogeneous system. Such core-hole excitons can play a considerable role in the interpretation of X-ray spectroscopy [286–289]. For local excitations it can be advantageous to transform into real space by exploiting the Wigner representation [290]. The densities and polarization can be Fourier transformed with respect to their relative momentum. Performing a gradient expansion of the Fourier phase factor and going beyond the zeroth order yields spatially resolved Bloch equations for occupation and polarization [290]. Higher-order contributions to the Coulomb interaction, which are included in the collision term, need to be treated on the same level. It describes dephasing of polarization and relaxation of carrier distribution to a local quasi-equilibrium [291]. In the following we present in a first approximation the electron scattering contribution in a homogeneous system, where $f_{\boldsymbol{k}_1,\boldsymbol{k}_2}^{\lambda} \to \delta_{\boldsymbol{k}_1,\boldsymbol{k}_2} f_{\boldsymbol{k}_1}^{\lambda}(\boldsymbol{R})$ and $f_{\boldsymbol{k}_1}^{\lambda}$ depends only parametrically on $\boldsymbol{R}$.

The contribution $\partial_t p_{\boldsymbol{k}_1,\boldsymbol{k}_2}^{\lambda_1\lambda_2}\big|_{\mathrm{coll}}$ describes the many-particle scattering beyond the Hartree-Fock interaction. The collision term contributes to diagonal $\gamma_{\boldsymbol{k}_1,\boldsymbol{k}_2}$ and off-diagonal $\mathcal{U}_{\boldsymbol{k}_1,\boldsymbol{k}_2}^{\lambda_1\lambda_2}$

(a) Impact ionization I   (b) Impact ionization II   (c) Meitner-Auger I   (d) Meitner-Auger II
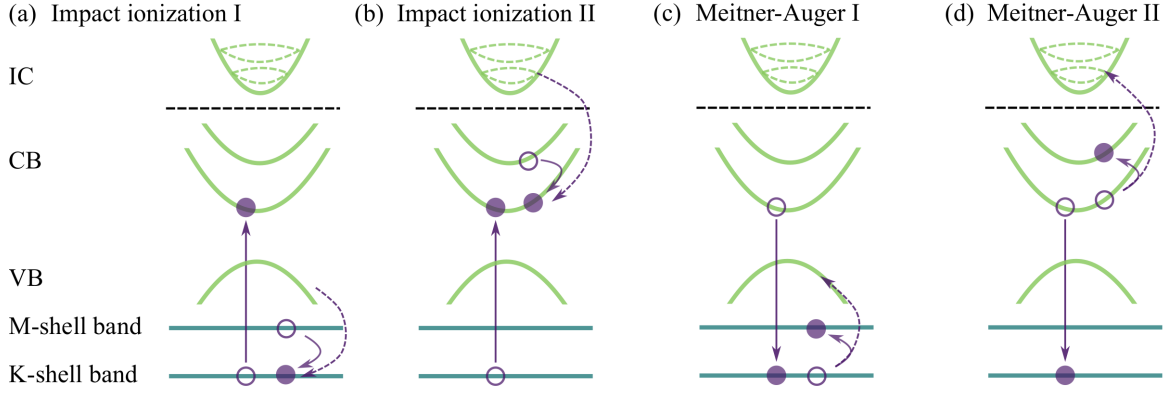

Figure 5.2: (a) and (b) Sketch of possible impact ionization transitions involving the core bands. (c) and (d) are drawing possible Meitner-Auger recombinations involving core states. The dashed lines draw alternative transitions to the solid line. Figure appears similarly in Ref. [274].

dephasing [292] of the microscopic polarization and acts as a first estimation for the dephasing:

$$\frac{d}{dt} p_{\boldsymbol{k}_1,\boldsymbol{k}_2}^{\lambda_1\lambda_2}|_{\text{coll}} = -\gamma_{\boldsymbol{k}_1,\boldsymbol{k}_2}(t) p_{\boldsymbol{k}_1,\boldsymbol{k}_2}^{\lambda_1\lambda_2} + \mathcal{U}_{\boldsymbol{k}_1,\boldsymbol{k}_2}^{\lambda_1\lambda_2}(t) \,. \tag{5.19}$$

The diagonal part is determined by the time- and momentum-dependent Coulomb scattering rates

$$\gamma_{\boldsymbol{k}_1,\boldsymbol{k}_2} = \frac{1}{2}\left(\Gamma_{\lambda_1,\boldsymbol{k}_1}^{\text{in}} + \Gamma_{\lambda_1,\boldsymbol{k}_1}^{\text{out}} + \Gamma_{\lambda_2,\boldsymbol{k}_2}^{\text{in}} + \Gamma_{\lambda_2,\boldsymbol{k}_2}^{\text{out}} \right) \,. \tag{5.20}$$

The in and out scattering rates read

$$\Gamma_{\lambda,\boldsymbol{k}_\lambda}^{\text{in}}(t) = \frac{2\pi}{\hbar} \sum_{\substack{\lambda_a,\lambda_b,\lambda_c \\ \boldsymbol{k}_c,\boldsymbol{q}}} V_{\boldsymbol{k}_\lambda,\boldsymbol{k}_c-\boldsymbol{q},\boldsymbol{k}_c,\boldsymbol{k}_\lambda-\boldsymbol{q}}^{\lambda\lambda_a\lambda_c\lambda_b} \tilde{V}_{\boldsymbol{k}_\lambda-\boldsymbol{q},\boldsymbol{k}_c,\boldsymbol{k}_c-\boldsymbol{q},\boldsymbol{k}_\lambda}^{\lambda_b\lambda_c\lambda_a\lambda} R_{\boldsymbol{k}_c,\boldsymbol{k}_\lambda,\boldsymbol{q}}^{\lambda_a\lambda_b\lambda_c} \delta\left(\varepsilon_{\boldsymbol{k}_\lambda}^{\lambda} + \varepsilon_{\boldsymbol{k}_c-\boldsymbol{q}}^{\lambda_a} - \varepsilon_{\boldsymbol{k}_\lambda-\boldsymbol{q}}^{\lambda_b} - \varepsilon_{\boldsymbol{k}_c}^{\lambda_c} \right)$$
$$\tag{5.21}$$

$$\Gamma_{\lambda,\boldsymbol{k}_\lambda}^{\text{out}}(t) = \frac{2\pi}{\hbar} \sum_{\substack{\lambda_a,\lambda_b,\lambda_c \\ \boldsymbol{k}_c,\boldsymbol{q}}} V_{\boldsymbol{k}_\lambda,\boldsymbol{k}_c-\boldsymbol{q},\boldsymbol{k}_c,\boldsymbol{k}_\lambda-\boldsymbol{q}}^{\lambda\lambda_a\lambda_c\lambda_b} \tilde{V}_{\boldsymbol{k}_\lambda-\boldsymbol{q},\boldsymbol{k}_c,\boldsymbol{k}_c-\boldsymbol{q},\boldsymbol{k}_\lambda}^{\lambda_b\lambda_c\lambda_a\lambda} \tilde{R}_{\boldsymbol{k}_b,\boldsymbol{k}_\lambda,\boldsymbol{q}}^{\lambda_a\lambda_b\lambda_c} \delta\left(\varepsilon_{\boldsymbol{k}_\lambda}^{\lambda} + \varepsilon_{\boldsymbol{k}_c-\boldsymbol{q}}^{\lambda_a} - \varepsilon_{\boldsymbol{k}_\lambda-\boldsymbol{q}}^{\lambda_b} - \varepsilon_{\boldsymbol{k}_c}^{\lambda_c} \right)$$
$$\tag{5.22}$$

with $R_{\boldsymbol{k}_c,\boldsymbol{k}_\lambda,\boldsymbol{q}}^{\lambda_a\lambda_b\lambda_c} = (1-f_{\boldsymbol{k}_c-\boldsymbol{q}}^{\lambda_a}) f_{\boldsymbol{k}_\lambda-\boldsymbol{q}}^{\lambda_b} f_{\boldsymbol{k}_c}^{\lambda_c}$ and $\tilde{R}_{\boldsymbol{k}_b,\boldsymbol{k}_\lambda,\boldsymbol{q}}^{\lambda_a\lambda_b\lambda_c} = f_{\boldsymbol{k}_c-\boldsymbol{q}}^{\lambda_a}(1-f_{\boldsymbol{k}_\lambda-\boldsymbol{q}}^{\lambda_b})(1-f_{\boldsymbol{k}_c}^{\lambda_c})$, which explicitly include Pauli-blocking terms [293]. In the scattering rates, we used the abbreviation $\tilde{V}_{abcd} = V_{abcd} - V_{bacd}$. The off-diagonal contribution couples to all coherences in the Brillouin zone and reads

$$\mathcal{U}_{\boldsymbol{k}_1,\boldsymbol{k}_2}^{\lambda_1\lambda_2} = \sum_{\boldsymbol{k}_a,\boldsymbol{k}_b} \left(\mathcal{V}_{\boldsymbol{k}_1,\boldsymbol{k}_2,\boldsymbol{k}_a,\boldsymbol{k}_b}^{\lambda_1\lambda_2} p_{\boldsymbol{k}_a,\boldsymbol{k}_b}^{\lambda_1\lambda_2} + \text{c.c} \right) \,. \tag{5.23}$$

For the carrier relaxation processes the Coulomb interaction is treated up to second order Born-Markov approximation and

$$\mathcal{V}_{\boldsymbol{k}_1,\boldsymbol{k}_2,\boldsymbol{k}_a,\boldsymbol{k}_b}^{\lambda_1\lambda_2} = \frac{\pi}{\hbar} \sum_{\substack{\lambda_B,\lambda_C \\ \boldsymbol{k}_B,\boldsymbol{k}_C}} \sum_{\lambda=\{\lambda_1,\lambda_2\}} \left[\tilde{V}_{\boldsymbol{k}_2,\boldsymbol{k}_C,\boldsymbol{k}_B,\boldsymbol{k}_b}^{\lambda_2\lambda_C\lambda_B\lambda_2} \tilde{V}_{\boldsymbol{k}_a,\boldsymbol{k}_B,\boldsymbol{k}_C,\boldsymbol{k}_1}^{\lambda_1\lambda_B\lambda_C\lambda_1} T_{\boldsymbol{k}_\lambda,\boldsymbol{k}_B,\boldsymbol{k}_C}^{\lambda\lambda_B\lambda_C} \delta^+ \right.$$
$$\left. - V_{\boldsymbol{k}_2,\boldsymbol{k}_a,\boldsymbol{k}_C,\boldsymbol{k}_B}^{\lambda_2\lambda_1\lambda_C\lambda_B} \tilde{V}_{\boldsymbol{k}_B,\boldsymbol{k}_C,\boldsymbol{k}_b,\boldsymbol{k}_1}^{\lambda_B\lambda_C\lambda_1\lambda_2} \tilde{T}_{\boldsymbol{k}_\lambda,\boldsymbol{k}_B\boldsymbol{k}_C}^{\lambda\lambda_B\lambda_C} \delta^- \right] \tag{5.24}$$

with $T^{\lambda\lambda_B\lambda_C}_{\boldsymbol{k}_\lambda,\boldsymbol{k}_B,\boldsymbol{k}_C} = f^\lambda_{\mathbf{k}_\lambda}(1-f^{\lambda_B}_{\boldsymbol{k}_B})f^{\lambda_C}_{\boldsymbol{k}_C} + (1-f^\lambda_{\boldsymbol{k}_\lambda})(1-f^{\lambda_C}_{\boldsymbol{k}_C})f^{\lambda_B}_{\boldsymbol{k}_B}$ and $\tilde{T}^{\lambda\lambda_B\lambda_C}_{\boldsymbol{k}_\lambda,\boldsymbol{k}_B,\boldsymbol{k}_C} = (1-f^\lambda_{\boldsymbol{k}_\lambda})f^{\lambda_B}_{\boldsymbol{k}_B}f^{\lambda_C}_{\boldsymbol{k}_C} + f^\lambda_{\boldsymbol{k}_\lambda}(1-f^{\lambda_B}_{\boldsymbol{k}_B})(1-f^{\lambda_C}_{\boldsymbol{k}_C})$. The delta functions read $\delta^\pm = \delta\left(\varepsilon^\lambda_{\boldsymbol{k}_\lambda} + \sigma^\lambda_{\lambda_1}\varepsilon^\lambda_{\boldsymbol{k}_\lambda} - \varepsilon^{\lambda_B}_{\boldsymbol{k}_B} \pm \varepsilon^{\lambda_C}_{\boldsymbol{k}_C}\right)$, where $\sigma^\lambda_{\lambda_1} = 1$ if $\lambda = \lambda_1$, otherwise $\sigma^\lambda_{\lambda_1} = -1$. The efficiency of the scattering channels is determined by the Coulomb matrix element and the occupation probabilities $f^\lambda_{\boldsymbol{k}}$ of the involved states. The scattering rates feature a sum over different band indices, which include all possible Meitner-Auger relaxation channels, which fulfill momentum and energy conservation at the same time [293, 294]. The Meitner-Auger effect [54, 295–297] as relaxation mechanism of the core-hole is characterized by the filling of the inner-shell vacancy accompanied by the emission of an electron into the unoccupied conduction band states and possibly even out of the sample into the ionization continuum. Figure 5.2 visualize the possible Meitner-Auger processes appearing in Eq. (5.20) and Eq. (5.23) as well as the inverse impact ionization processes.

Finally, we present the dynamics of the homogeneous occupations:

$$\frac{d}{dt}f^{\lambda_1}_{\boldsymbol{k}_1} = -2\Im\mathfrak{m}\left(\Omega^{\lambda_1\lambda_2}_{\boldsymbol{k}_1,\boldsymbol{k}_2}p^{\lambda_1\lambda_2}_{\boldsymbol{k}_1,\boldsymbol{k}_2}\right) - \frac{2}{\hbar}\Im\mathfrak{m}\left(\left[V^{\lambda_1\lambda_2\lambda_2\lambda_1}_{\boldsymbol{k}_1,\boldsymbol{k}_2,\boldsymbol{k}_2,\boldsymbol{k}_1} - V^{\lambda_1\lambda_2\lambda_1\lambda_2}_{\boldsymbol{k}_1,\boldsymbol{k}_2,\boldsymbol{k}_1,\boldsymbol{k}_2}\right]p^{\lambda_2\lambda_1}_{\boldsymbol{k}_2,\boldsymbol{k}_1}p^{\lambda_1\lambda_2}_{\boldsymbol{k}_1,\boldsymbol{k}_2}\right)$$
$$+ \Gamma^{\text{in}}_{\lambda_1,\boldsymbol{k}_1}\left(1-f^{\lambda_1}_{\boldsymbol{k}_1}\right) - \Gamma^{\text{out}}_{\lambda_1,\boldsymbol{k}_1}f^{\lambda_1}_{\boldsymbol{k}_1}. \tag{5.25}$$

The first term describes the excitation of a non-equilibrium electron distribution in the band λ_1. The second term describes the nonlinear Coulomb sources of the carrier population. The last line expresses the Coulomb interaction described by a microscopic Boltzmann-like scattering equation.

The last missing ingredient to calculate the X-ray absorption is the electric field. In the following section we solve the wave equation to determine the electric field as self-consistent observable.

5.5 Nonlocal absorption

5.5.1 Wave equation

The optical property, which is usually available directly from the experiment is the frequency-dependent reflectance or transmittance. To relate to the experimental observable it is necessary to investigate the wave equation for the optical exciting field. The fundamental equations of electromagnetism are Maxwell's equations [298–300]. In the presence of dielectric and non-magnetic matter they read

$$\nabla \cdot \boldsymbol{D}(\boldsymbol{r},t) = 0\,, \tag{5.26}$$

$$\nabla \cdot \boldsymbol{B}(\boldsymbol{r},t) = 0\,, \tag{5.27}$$

$$\nabla \times \boldsymbol{E}(\boldsymbol{r},t) = -\frac{\partial}{\partial t}\boldsymbol{B}(\boldsymbol{r},t)\,, \tag{5.28}$$

$$\nabla \times \boldsymbol{H}(\boldsymbol{r},t) = \frac{\partial}{\partial t}\boldsymbol{D}(\boldsymbol{r},t)\,. \tag{5.29}$$

The electric displacement is defined as $\boldsymbol{D}(\boldsymbol{r},t) = \epsilon_0\epsilon(\boldsymbol{r})\boldsymbol{E}(\boldsymbol{r},t) + \boldsymbol{P}(\boldsymbol{r},t)$ with electric field $\boldsymbol{E}(\boldsymbol{r},t)$, the polarization of the material $\boldsymbol{P}(\boldsymbol{r},t)$, and the dielectric function $\epsilon(\boldsymbol{r})$ of a spatially inhomogeneous medium [301]. The first partial differential equation is identical to Gaussian law but written in a form that makes explicit the fact that the medium responds to the electric field by becoming polarized. All charges that arises due to polarization are included to the displacement field. With the assumption of no free charges the displacement has no sources, cf. Eq. (5.26). Equation (5.29) corresponds to Ampere's law. If an electric flux density changes in

time it gives rise to a magnetic field that whirl around the displacement field. In non-magnetic media the magnetization field is related to the magnetic field by $\boldsymbol{B}(\boldsymbol{r},t) = \boldsymbol{H}(\boldsymbol{r},t)/\mu_0$ with the magnetic vacuum permittivity μ_0. Equation (5.28) corresponds to Faraday's law, which states that changing a magnetic field in time induces an electric field circulating around it. If we take the curl of Faraday's law, insert the definition for the magnetization field and exploit Ampere's law we obtain

$$\nabla \times \nabla \times \boldsymbol{E}(\boldsymbol{r},t) = -\mu_0 \frac{\partial^2}{\partial t^2} \boldsymbol{D}(\boldsymbol{r},t) \,. \tag{5.30}$$

By inserting the definition of the displacement field we obtain the general wave equation [302–304]

$$\nabla \times \nabla \times \boldsymbol{E}(\boldsymbol{r},t) + \frac{\epsilon(\boldsymbol{r})}{c^2} \frac{\partial^2}{\partial t^2} \boldsymbol{E}(\boldsymbol{r},t) = -\mu_0 \frac{\partial^2}{\partial t^2} \boldsymbol{P}(\boldsymbol{r},t) \tag{5.31}$$

with the speed of light in vacuum c. Under the assumption of an uniform background we can take $\epsilon(\boldsymbol{r}) = \epsilon$ as constant. Subsequently, we can use Eq. (5.26) to obtain a relation for the divergence of the electric field of the form $\nabla \cdot \boldsymbol{E}(\boldsymbol{r},t) = -\nabla \cdot \boldsymbol{P}(\boldsymbol{r},t)/\epsilon_0\epsilon$. Rewriting $\nabla \times \nabla \times \boldsymbol{E} = \nabla(\nabla \cdot \boldsymbol{E}) - \Delta \boldsymbol{E}$ and inserting the expression for the divergence of the electric field yields

$$\Delta \boldsymbol{E}(\boldsymbol{r},t) - \frac{\epsilon}{c^2} \frac{\partial^2}{\partial t^2} \boldsymbol{E}(\boldsymbol{r},t) = \mu_0 \frac{\partial^2}{\partial t^2} \boldsymbol{P}(\boldsymbol{r},t) - \frac{1}{\epsilon_0\epsilon} \nabla \left(\nabla \cdot \boldsymbol{P}(\boldsymbol{r},t) \right) \,. \tag{5.32}$$

In comparison to Sec. 2.6.2 the wave equation displays as an additional source the divergence of the polarization of the material. Since we are interested in non-local phenomena and a non-perpendicular excitation geometry this term does not vanish. The wave equation can be solved with help of Green's theorem [305, 306] through

$$\boldsymbol{E}(\boldsymbol{r},t) = \int d^3r' \int dt' \, \mathcal{G}(\boldsymbol{r}-\boldsymbol{r}',t-t')\boldsymbol{\Pi}(\boldsymbol{r}',t') \tag{5.33}$$

with the inhomogeneity $\boldsymbol{\Pi}(\boldsymbol{r},t)$ corresponding to the right hand side of Eq. (5.32). The equation gives the solution in real and time space and is determined by a convolution of the inhomogeneity and the Greens function tensor $\mathcal{G}(\boldsymbol{r},\boldsymbol{r}',t-t')$. From the convolution theorem we can expect a simple form in momentum and frequency space. Performing a Fourier transformation yields

$$\boldsymbol{E}_{\boldsymbol{Q}}(Q_z,\omega) = \mathcal{G}_{\boldsymbol{Q}}(Q_z,\omega)\boldsymbol{\Pi}_{\boldsymbol{Q}}(Q_z,\omega) \,. \tag{5.34}$$

By Fourier transforming the wave equation Eq. (5.32) in space and time allows us to identify the scalar Green's function

$$\left(\frac{\epsilon\omega^2}{c^2} - \boldsymbol{Q}^2 - Q_z^2 \right) \boldsymbol{E}_{\boldsymbol{Q}}(Q_z,\omega) = \boldsymbol{\Pi}_{\boldsymbol{Q}}(Q_z\omega) \tag{5.35}$$

$$\boldsymbol{E}_{\boldsymbol{Q}}(Q_z,\omega) = \frac{1}{\epsilon\omega^2/c^2 - \boldsymbol{Q}^2 - Q_z^2} \boldsymbol{\Pi}_{\boldsymbol{Q}}(Q_z,\omega) = \mathcal{G}_{\boldsymbol{Q}}(Q_z,\omega)\boldsymbol{\Pi}_{\boldsymbol{Q}}(Q_z,\omega) \,. \tag{5.36}$$

Finally, we apply an inverse Fourier transform to the electric field with respect to Q_z to obtain a field propagating in z-direction [307, 308], yielding

$$\boldsymbol{E_Q}(z,\omega) = \int dz' \; \mathcal{G}_{\boldsymbol{Q}}(z-z',\omega)\boldsymbol{\Pi_Q}(z',\omega) \tag{5.37}$$

$$\mathcal{G}_{\boldsymbol{Q}}(z-z',\omega) = \frac{1}{2\pi}\int dQ_z \; e^{-iQ_z(z-z')}\left(\frac{\epsilon\omega^2}{c^2} - \boldsymbol{Q}^2 - Q_z^2\right)^{-1}$$

$$= \frac{1}{2\pi}\int dQ_z \; e^{-iQ_z(z-z')}\left(\kappa^2 - Q_z^2\right)^{-1} \tag{5.38}$$

$$= \frac{i}{2\kappa}e^{-i\kappa|z-z'|} \tag{5.39}$$

as final expression for the Green's function and where $\kappa^2 = \epsilon\omega^2/c^2 - \boldsymbol{Q}^2$. The integral was solved with help of the residue theorem. The last missing piece to fully determine the electric field is the inhomogeneity $\boldsymbol{\Pi_Q}(z,\omega)$. Performing a two-dimensional Fourier transformation in space and a Fourier transformation in time yields from the right-hand side of Eq. (5.32)

$$\boldsymbol{\Pi_Q}(z,\omega) = -\mu_0\omega^2 \boldsymbol{P_Q}(z,\omega) - \frac{1}{\epsilon_0\epsilon}\begin{pmatrix}i\boldsymbol{Q}\\ \partial_z\end{pmatrix}\left[i\boldsymbol{Q}\cdot\boldsymbol{P}_{\|\boldsymbol{Q}}(z,\omega) + \frac{\partial}{\partial z}P_{\perp\boldsymbol{Q}}(z,\omega)\right], \tag{5.40}$$

where $\boldsymbol{P}_{\|\boldsymbol{Q}}(z,\omega)$ and $P_{\perp\boldsymbol{Q}}(z,\omega)$ are the in- and out-of-plane component of the macroscopic polarization. With this, the electric field Eq. (5.37) is known:

$$\boldsymbol{E}_{\|\boldsymbol{Q}}(z,\omega) = -\frac{i\mu_0\omega^2}{2\kappa}\int dz' \; e^{-i\kappa|z-z'|}\boldsymbol{P}_{\|\boldsymbol{Q}}(z',\omega)$$

$$+ \frac{\boldsymbol{Q}}{2\kappa\epsilon_0\epsilon}\int dz' \; e^{-i\kappa|z-z'|}\left(i\boldsymbol{Q}\cdot\boldsymbol{P}_{\|\boldsymbol{Q}}(z',\omega) + \frac{\partial}{\partial z'}P_{\perp\boldsymbol{Q}}(z',\omega)\right) \tag{5.41}$$

$$E_{\perp\boldsymbol{Q}}(z,\omega) = -\frac{i\mu_0\omega^2}{2\kappa}\int dz' \; e^{-i\kappa|z-z'|}P_{\perp\boldsymbol{Q}}(z',\omega)$$

$$- \frac{i}{2\kappa\epsilon_0\epsilon}\int dz' \; e^{-i\kappa|z-z'|}\left(i\boldsymbol{Q}\cdot\frac{\partial}{\partial z'}\boldsymbol{P}_{\|\boldsymbol{Q}}(z',\omega) + \frac{\partial^2}{\partial z'^2}P_{\perp\boldsymbol{Q}}(z',\omega)\right). \tag{5.42}$$

To further evaluate the electric field, we assume an infinitely thin layer located at $z = z_0$. The material response is then described by the two-dimensional polarization $\boldsymbol{P}(\boldsymbol{r}) = \boldsymbol{P}^{2D}(\boldsymbol{r}_\|)\delta(z - z_0)$. Inserting this into Eq. (5.41) and Eq. (5.42) and solving the z-integrals yields

$$\boldsymbol{E}_{\|\boldsymbol{Q}}(z,\omega) = \frac{i}{2\kappa}\left(\frac{\boldsymbol{Q}\otimes\boldsymbol{Q}}{\epsilon_0\epsilon} - \mu_0\omega^2\right)\boldsymbol{P}^{2D}_{\|\boldsymbol{Q}}(\omega)e^{-i\kappa|z-z_0|}$$

$$- \frac{i\boldsymbol{Q}}{2\epsilon_0\epsilon}\mathrm{sgn}(z-z_0)e^{-i\kappa|z-z_0|}P^{2D}_{z\boldsymbol{Q}}(\omega) \tag{5.43}$$

$$E_{z\boldsymbol{Q}}(\omega) = \frac{i}{2}e^{-i\kappa|z-z_0|}P^{2D}_{z\boldsymbol{Q}}(\omega)\left(\frac{\kappa}{\epsilon_0\epsilon} - \frac{\mu_0\omega^2}{\kappa}\right)$$

$$- \frac{i}{2\epsilon_0\epsilon}\mathrm{sgn}(z-z_0)e^{-i\kappa|z-z_0|}\boldsymbol{Q}\cdot\boldsymbol{P}^{2D}_{\|\boldsymbol{Q}}(\omega) \tag{5.44}$$

with the sign function, which is equal to $+1$ for $z > z_0$ and -1 if $z < z_0$. In the limit of a vanishing wave vector $\boldsymbol{Q}$ we retrieve the result of a perpendicular incidence of the electric field on a material, where the wave travels as a plane wave varying in propagation direction.

5.5.2   Self-consistent Maxwell-X-ray Bloch formalism

As in Sec. 2.6.2, our goal is to obtain an absorption coefficient from a self-consistent coupling of electric field and material equation, now extended by a spatial resolution. We start by separating the equations Eq. (5.43) and (5.44) into their Cartesian coordinates and formulating them in matrix form:

$$
\boldsymbol{E_Q}(z,\omega) = \frac{e^{-i\kappa|z-z_0|}}{2i}
\begin{pmatrix}
\frac{\mu_0\omega^2}{\kappa} - \frac{Q_x^2}{\epsilon_0\epsilon\kappa} & -\frac{Q_xQ_y}{\epsilon_0\epsilon\kappa} & \frac{Q_x}{\epsilon_0\epsilon}\mathrm{sgn}(z-z_0) \\
-\frac{Q_yQ_x}{\epsilon_0\epsilon\kappa} & \frac{\mu_0\omega^2}{\kappa} - \frac{Q_y^2}{\epsilon_0\epsilon\kappa} & \frac{Q_y}{\epsilon_0\epsilon}\mathrm{sgn}(z-z_0) \\
\frac{Q_x}{\epsilon_0\epsilon}\mathrm{sgn}(z-z_0) & \frac{Q_y}{\epsilon_0\epsilon}\mathrm{sgn}(z-z_0) & \frac{\mu_0\omega^2}{\kappa} - \frac{\kappa}{\epsilon_0\epsilon}
\end{pmatrix}
\begin{pmatrix}
P^{2D}_{xQ}(\omega) \\
P^{2D}_{yQ}(\omega) \\
P^{2D}_{\perp Q}(\omega)
\end{pmatrix}
$$
$$
+ \mathbf{E}^0_{\boldsymbol{Q}}(z,\omega) \tag{5.45}
$$

with the homogeneous solution $\boldsymbol{E}^0_{\boldsymbol{Q}}(z,\omega) = \boldsymbol{E}_0\exp(-i\kappa z) + \mathbf{r}\exp(i\kappa z)$ and for a free standing layer $\boldsymbol{E}^0_{\boldsymbol{Q}}(z,\omega) = \boldsymbol{E}_0\exp(-i\kappa z)$. If we name the appearing matrix as $K_{\boldsymbol{Q}}(z,\omega)$ then Eq. (5.45) reads

$$
\boldsymbol{E_Q}(z,\omega) = K_{\boldsymbol{Q}}(z,\omega)\boldsymbol{P}^{2D}_{\boldsymbol{Q}}(\omega) + \boldsymbol{E}^0_{\boldsymbol{Q}}(z,\omega) = K_{\boldsymbol{Q}}(z,\omega)\left(\epsilon_0\chi_{\boldsymbol{Q}}(\omega)\boldsymbol{E_Q}(z_0,\omega)\right) + \boldsymbol{E}^0_{\boldsymbol{Q}}(z,\omega), \tag{5.46}
$$

where we inserted the definition of the linear macroscopic polarization $\boldsymbol{P}^{2D}_{\boldsymbol{Q}}(\omega) = \epsilon_0\chi_{\boldsymbol{Q}}(\omega)\boldsymbol{E_Q}(z_0,\omega)$ at the position of the material in the second step. In the above equation, the incident electric field $\boldsymbol{E}^0_{\boldsymbol{Q}}(z,\omega)$ from the homogeneous solution of the wave equation, the linear susceptibility $\chi_{\boldsymbol{Q}}(\omega)$ via the microscopic X-ray Bloch equations as well as the matrix $K_{\boldsymbol{Q}}(z,\omega)$ are known. Missing is an expression for the electric field at position z_0 of the material layer. Therefore, we evaluate Eq. (5.46) at position z_0:

$$
\boldsymbol{E_Q}(z_0,\omega) = K_{\boldsymbol{Q}}(z_0,\omega)\left(\epsilon_0\chi_{\boldsymbol{Q}}(\omega)\boldsymbol{E_Q}(z_0,\omega)\right) + \boldsymbol{E}^0_{\boldsymbol{Q}}(z_0,\omega) \tag{5.47}
$$
$$
\boldsymbol{E_Q}(z_0,\omega) = \left(\mathbb{1} - \epsilon_0 K_{\boldsymbol{Q}}(z_0,\omega)\chi_{\boldsymbol{Q}}(\omega)\right)^{-1}\boldsymbol{E}^0_{\boldsymbol{Q}}(z_0,\omega) \tag{5.48}
$$

and insert it back into Eq. (5.46) to obtain a self-consistent expression for the electric field of the form

$$
\boldsymbol{E_Q}(z,\omega) = \epsilon_0 K_{\boldsymbol{Q}}(z,\omega)\chi_{\boldsymbol{Q}}(\omega)\left(\mathbb{1} - \epsilon_0 K_{\boldsymbol{Q}}(z_0,\omega)\chi_{\boldsymbol{Q}}(\omega)\right)^{-1}\boldsymbol{E}^0_{\boldsymbol{Q}}(z_0,\omega) + \boldsymbol{E}^0_{\boldsymbol{Q}}(z,\omega). \tag{5.49}
$$

Important to note is that the susceptibility is no scalar function anymore, but a second rank tensor. The reason is that the polarization depends on the light wave vector. Therefore, it is not independent of the orientation of the electric field. The dielectric is said to be anisotropic and the polarization and electric field are not necessarily collinear anymore. Figure 5.3 sketches the investigated geometry: An atomically-thin material irradiated by X-ray light under a certain angle of incidence θ. The incoming electric field $\boldsymbol{E}^0_{\boldsymbol{Q}}(z,\omega)$ is reflected ($\boldsymbol{E}^R_{\boldsymbol{Q}}(z,\omega)$) and transmitted ($\boldsymbol{E}^T_{\boldsymbol{Q}}(z,\omega)$), both described by Eq. (5.49), and induces a two-dimensional polarization determining the response of the material to the X-ray radiation. The reflection is defined by the reflected intensity of the left propagating field in front of the graphene sheet $r_{\boldsymbol{Q}}(\omega) = I^L_{\boldsymbol{Q}}(\omega)/I^0_{\boldsymbol{Q}}(\omega)$ and the transmission by the intensity of the right propagating electric field behind the graphene sheet $t_{\boldsymbol{Q}}(\omega) = I^R_{\boldsymbol{Q}}(\omega)/I^0_{\boldsymbol{Q}}(\omega)$. The intensities are determined by the electric field Eq. (5.49).

From the self-consistent coupling of the Maxwell and X-ray Bloch equations we can derive an expression for the radiative dephasing: Here, a core-hole recombines with an electron under emission of a photon. Besides Meitner-Auger recombination this process contributes to the
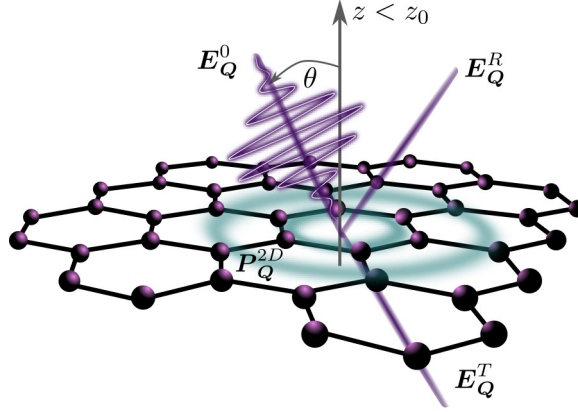
Figure 5.3: Atomically-thin material at z_0 irradiated by X-rays under an angle of incidence θ. The incident electric field $\boldsymbol{E}_Q^0$ is reflected ($\boldsymbol{E}_Q^R$) and transmitted ($\boldsymbol{E}_Q^T$), and induces a macroscopic polarization $\boldsymbol{P}_Q^{2D}$ of the material. Figure appears similarly in Ref. [274].

core-hole lifetime and forms the basis of, for example, X-ray fluorescence [309]. Inserting the emitted electric field Eq. (5.43) and Eq. (5.44) into the X-ray Bloch equation Eq. (5.18) yields

$$i\hbar \frac{d}{dt} p_{\boldsymbol{k}_1,\boldsymbol{k}_2}^{\lambda_1\lambda_2}\big|_{\mathrm{rad}} = -\frac{i}{2}(f_{\boldsymbol{k}_1}^{\lambda_1} - f_{\boldsymbol{k}_2}^{\lambda_2}) \sum_{\boldsymbol{k}',\boldsymbol{G}'} \left[\frac{\mu_0\omega^2}{\kappa} \boldsymbol{d}_{\boldsymbol{k}_2,\boldsymbol{k}_1}^{\|\lambda_2\lambda_1} \cdot \boldsymbol{d}_{\boldsymbol{k}'+\boldsymbol{Q}-\boldsymbol{G}',\boldsymbol{k}'}^{\|\lambda_1\lambda_2} \right.$$
$$\left. -\frac{1}{\epsilon_0\kappa}\left(\boldsymbol{d}_{\boldsymbol{k}_2,\boldsymbol{k}_1}^{\|\lambda_2\lambda_1} \cdot \boldsymbol{Q}\right)\left(\boldsymbol{Q} \cdot \boldsymbol{d}_{\boldsymbol{k}'+\boldsymbol{Q}-\boldsymbol{G}',\boldsymbol{k}'}^{\|\lambda_1\lambda_2}\right) + \left(\frac{\mu_0\omega^2}{\kappa} - \frac{\kappa}{\epsilon_0}\right) d_{\boldsymbol{k}_2,\boldsymbol{k}_1}^{\perp\lambda_2\lambda_1} d_{\boldsymbol{k}'+\boldsymbol{Q}-\boldsymbol{G}',\boldsymbol{k}'}^{\perp\lambda_1\lambda_2} \right] p_{\boldsymbol{k}'+\boldsymbol{q}-\boldsymbol{G}',\boldsymbol{k}'}^{\lambda_1\lambda_2} \cdot$$
$$\tag{5.50}$$

We see that the radiative interaction couples all X-ray induced transitions. The radiative dephasing of the transition $p_{\boldsymbol{k}+\boldsymbol{Q}-\boldsymbol{G},\boldsymbol{k}}^{\lambda_1\lambda_2}$ is implicitly included in Eq. (5.50). Since we do not transform into the excitonic basis, the coupling cannot be resolved easily. However, to gain more insights we can perform a rotating wave approximation together with a random phase approximation and determine the main contribution to the dephasing from its diagonal part $\boldsymbol{k}' = \boldsymbol{k}$ and $\boldsymbol{G}' = \boldsymbol{G}$. For a plane wave excitation the term is imaginary, describing only a dephasing and no renormalizations of the dispersion. The diagonal dephasing explicitly reads

$$\gamma_{\boldsymbol{k}+\boldsymbol{Q}-\boldsymbol{G},\boldsymbol{k}}^{\mathrm{rad}} = \frac{1}{2}\left(\frac{\omega^2}{\epsilon_0\kappa c^2}|d_{\boldsymbol{k}+\boldsymbol{Q}-\boldsymbol{G},\boldsymbol{k}}^{\|\lambda_1\lambda_2}|^2 - \frac{1}{\epsilon_0\kappa}|\boldsymbol{q}\cdot\boldsymbol{d}_{\boldsymbol{k}+\boldsymbol{Q}-\boldsymbol{G},\boldsymbol{k}}^{\|\lambda_1\lambda_2}|^2 + \left(\frac{\omega^2}{\epsilon_0\kappa c^2} - \frac{\kappa}{\epsilon_0}\right)|d_{\boldsymbol{k}+\boldsymbol{Q}-\boldsymbol{G},\boldsymbol{k}}^{\perp\lambda_1\lambda_2}|^2\right) \cdot$$
$$\tag{5.51}$$

For a vanishing $\boldsymbol{Q}$ only the first term of Eq. (5.51) survives. In accordance to a first order perturbation theory, we obtain Fermi's golden rule for the radiative broadening, where the radiative dephasing is determined by the square of the dipole matrix element.

To the end of this section, we can compare with the current literature concerning the core-hole recombination channels. With regard to the radiative recombination, the rate of spontaneous emission W_X between an initial band λ and the $1s$-band for atoms is usually described in dipole approximation by Fermi's golden rule [310, 311]:

$$W_X \propto \omega^3 \sum_{\beta,j} |\langle 1s, \beta, 1s, 0 \mid \boldsymbol{r} \mid \lambda, \beta, j, 0\rangle|^2 , \tag{5.52}$$

where ω stands for the transition energy between initial and final state. The rigorously derived result from a self-consistent treatment of the Maxwell and X-ray Bloch equations for two-dimensional semiconductors yields a ω-dependence for the radiative dephasing, cf. Eq. (5.51) with inserted $\boldsymbol{Q}$. However, for atoms a ω^3-dependence is well known, cf. Eq. (5.52). The difference originates from the different dimensionality. Investigating Eq. (5.52), for atoms we can argue that the electronic wave functions have strongly contributing values only for $|\boldsymbol{r}| < a_B/Z$ and we can roughly approximate the transition integral to be proportional to Z^{-1}. From Moseley's law [260] we know that the transition energy ω is proportional to Z^2. Consequently, we see that the spontaneous K-shell emission rate is proportional to Z^4 [312]. It can be shown that for atoms the Meitner-Auger yield W_A is almost independent of the effective nuclear charge [313]. A semi-empirical expression for the X-ray yield is

$$w_X = \frac{W_X}{W_X + W_A} \tag{5.53}$$

which is proportional to Z^4 [55]. Hence, for atomic systems with low Z the core-hole recombination is dominated by Meitner-Auger transitions. In contrast for atoms with higher nuclear charge fluorescence is more likely to occur. Using the presented formalism for core electron interactions, it might be possible to extent and establish similar statements for crystalline solids. Moreover, the extension to core-electron phonon interaction is straightforward.

5.6   Graphene

The band structure properties of graphene form the basis of understanding the electronic spectra of carbon-based allotropes. Graphene is a monolayer of carbon atoms arranged in a two-dimensional hexagonal lattice. The free carbon atom has six electrons with an electronic configuration $1s^2$, $2s^2$, $2p^2$. The $1s$ electrons form the core bands. In contrast, the $2s$ and $2p$ electrons constitute the valence (and conduction) bands around the Fermi level, which is set to $0\,\text{eV}$. For the bonding of the carbon atoms, the $2s$ and the $2p_{x/y}$ electrons undergo a sp^2-hybridization with one electron left in the $2p_z$ orbital. Because of the in-plane orientation of the former they form σ bands, which are responsible for the covalent in-plane bonding between the atom [166]. σ bonds are the strongest type of covalent bonding since they form by the overlap of orbitals in an end-to-end fashion, with the electron density concentrated between the nuclei of the bonding atoms. The $2p_z$ electrons form the π bands, which are formed by the overlap of orbitals in a side-by-side fashion with the electron density concentrated above and below the plane of the nuclei of the bonding atoms.

The unit cell of graphene is spanned by the lattice vectors $\boldsymbol{a}_1$ and $\boldsymbol{a}_2$ and contains two atoms, constituting the equivalent sublattices A and B, which are rotated by $\pi/3$. The lattice vectors read

$$\boldsymbol{a}_1 = \frac{a_0}{2}\begin{pmatrix} \sqrt{3} \\ 2 \end{pmatrix} \quad \text{and} \quad \boldsymbol{a}_2 = \frac{a_0}{2}\begin{pmatrix} -\sqrt{3} \\ 1 \end{pmatrix}. \tag{5.54}$$

The vectors $\boldsymbol{R}_A$ and $\boldsymbol{R}_B$ denote the position of the corresponding atoms. In nearest-neighbour approximation the constructed vectors $\boldsymbol{\delta}_{BA} = \boldsymbol{R}_{Bi} - \boldsymbol{R}_A \equiv \boldsymbol{\delta}_i$ connect the atoms on sublattice A with the three surrounding atoms on sublattice B. A sketch of the graphene lattice is shown in Fig 5.4(a), where white circles denote atoms on sublattice A and green circles stand for atoms of sublattice B. As can be seen, the six second next-neighbors however lie again on the same sublattice. The electronic and optical properties of graphene for low energies are mostly determined by the π bands. Therefore, theoretical descriptions often include only this band.

However, for X-ray absorption, which goes over a large energy range of several hundred of eV, also bands further away from the Fermi level need to be considered.

The energy dispersion and corresponding tight binding coefficients are obtained from the Schrödinger equation Eq. (2.3). Therefore, we multiply the Schrödinger equation by the complex conjugate of one Bloch basis function $\Phi_{\alpha i, \boldsymbol{k}}(\boldsymbol{r}) = \sum_{\boldsymbol{R}_\alpha} \exp(i\boldsymbol{k} \cdot \boldsymbol{R}_\alpha)\phi_{\alpha i}^\nu(\boldsymbol{r})/\sqrt{N}$ (with orbital i and sublattice α) and integrate over all space:

$$\sum_{\beta,j} \left(\mathcal{H}_{\beta j, \boldsymbol{k}}^{\alpha i} - E_{\boldsymbol{k}} \mathcal{S}_{\beta j, \boldsymbol{k}}^{\alpha i} \right) C_{\beta j, \boldsymbol{k}} = 0 \,. \tag{5.55}$$

Here, we defined the Hamiltonian matrix $\mathcal{H}_{\beta j, \boldsymbol{k}}^{\alpha i} = \langle \Phi_{\alpha i, \boldsymbol{k}} | H_0 | \Phi_{\beta j, \boldsymbol{k}} \rangle$ and overlap matrix $\mathcal{S}_{\beta j, \boldsymbol{k}}^{\alpha i} = \langle \Phi_{\alpha i, \boldsymbol{k}} | \Phi_{\beta j, \boldsymbol{k}} \rangle$. Since the overlap matrix is generally small we approximate it by an identity matrix. The Hamiltonian matrix for graphene reads

$$\mathcal{H}(\boldsymbol{k}) = \begin{pmatrix} \mathcal{H}_{AA}(\boldsymbol{k}) & \mathcal{H}_{AB}(\boldsymbol{k}) \\ \mathcal{H}_{BA}(\boldsymbol{k}) & \mathcal{H}_{BB}(\boldsymbol{k}) \end{pmatrix} = \begin{pmatrix} \mathcal{H}_{AA}(\boldsymbol{k}) & \mathcal{H}_{AB}(\boldsymbol{k}) \\ \mathcal{H}_{AB}^\dagger(\boldsymbol{k}) & \mathcal{H}_{AA}(\boldsymbol{k}) \end{pmatrix}, \tag{5.56}$$

where each entry is organized in 5×5 block matrices. In the second step we used the symmetry of the equivalent sublattices due to identical carbon atoms in the unit cell. The diagonal entries are onsite matrices. We calculate exemplary one entry:

$$\mathcal{H}_{AA}^{11}(\boldsymbol{k}) = \langle \Phi_{1sA, \boldsymbol{k}} | H_0 | \Phi_{1sA, \boldsymbol{k}} \rangle = \varepsilon_{1s} \langle \Phi_{1sA, \boldsymbol{k}} | \Phi_{1sA, \boldsymbol{k}} \rangle = \varepsilon_{1s} \,. \tag{5.57}$$

The total diagonal on-site matrix becomes

$$\mathcal{H}_{AA}(\boldsymbol{k}) = \begin{pmatrix} \begin{array}{c|ccccc} & 1s^A & 2p_z^A & 2s^A & 2p_x^A & 2p_y^A \\ \hline 1s^A & \varepsilon_{1s} & 0 & 0 & 0 & 0 \\ 2p_z^A & 0 & \varepsilon_{2p} & 0 & 0 & 0 \\ 2s^A & 0 & 0 & \varepsilon_{2s} & 0 & 0 \\ 2p_x^A & 0 & 0 & 0 & \varepsilon_{2p} & 0 \\ 2p_y^A & 0 & 0 & 0 & 0 & \varepsilon_{2p} \end{array} \end{pmatrix} \tag{5.58}$$

describing onsite hoppings between the basis functions with the energies $\varepsilon_{1s} = -283\,\text{eV}$, $\varepsilon_{2p} = 0\,\text{eV}$ and $\varepsilon_{2s} = 8.7\,\text{eV}$ [314, 315]. Next, we calculate the offsite matrix, which describes hoppings between different sublattices. It reads

$$\mathcal{H}_{AB}(\boldsymbol{k}) = \begin{pmatrix} \begin{array}{c|ccccc} & 1s^B & 2p_z^B & 2s^B & 2p_x^B & 2p_y^B \\ \hline 1s^A & t_{1s}\xi_{\boldsymbol{k}} & 0 & 0 & 0 & 0 \\ 2p_z^A & 0 & t_\pi \xi_{\boldsymbol{k}} & 0 & 0 & 0 \\ 2s^A & 0 & 0 & \mathcal{H}_{33}(\boldsymbol{k}) & \mathcal{H}_{34}(\boldsymbol{k}) & \mathcal{H}_{35}(\boldsymbol{k}) \\ 2p_x^A & 0 & 0 & \mathcal{H}_{43}(\boldsymbol{k}) & \mathcal{H}_{44}(\boldsymbol{k}) & \mathcal{H}_{45}(\boldsymbol{k}) \\ 2p_y^A & 0 & 0 & \mathcal{H}_{53}(\boldsymbol{k}) & \mathcal{H}_{54}(\boldsymbol{k}) & \mathcal{H}_{55}(\boldsymbol{k}) \end{array} \end{pmatrix}. \tag{5.59}$$

An expression for the hopping between two $1s$ or two $2p_z$ orbitals of different lattice sites were already calculated and inserted in Eq. (5.59). The calculation is straightforward and reads

$$\langle \Phi_{2p_z A, \boldsymbol{k}} | H_0 | \Phi_{2p_z B, \boldsymbol{k}} \rangle = \frac{1}{N} \sum_{\boldsymbol{R}_A, \boldsymbol{R}_B} e^{i\boldsymbol{k} \cdot (\boldsymbol{R}_A - \boldsymbol{R}_B)} \langle \phi_{2p_z}(\boldsymbol{r} - \boldsymbol{R}_A) | H_0 | \phi_{2p_z}(\boldsymbol{r} - \boldsymbol{R}_B) \rangle = t_\pi \xi_{\boldsymbol{k}} \,, \tag{5.60}$$

where we shifted the spatial integral on top of $\boldsymbol{R}_A$ by $\boldsymbol{r}_\parallel \to \boldsymbol{r}_\parallel + \boldsymbol{R}_A$ and used the definition of the next-neighbor vector. Then we defined the hopping parameter $t_\pi =$
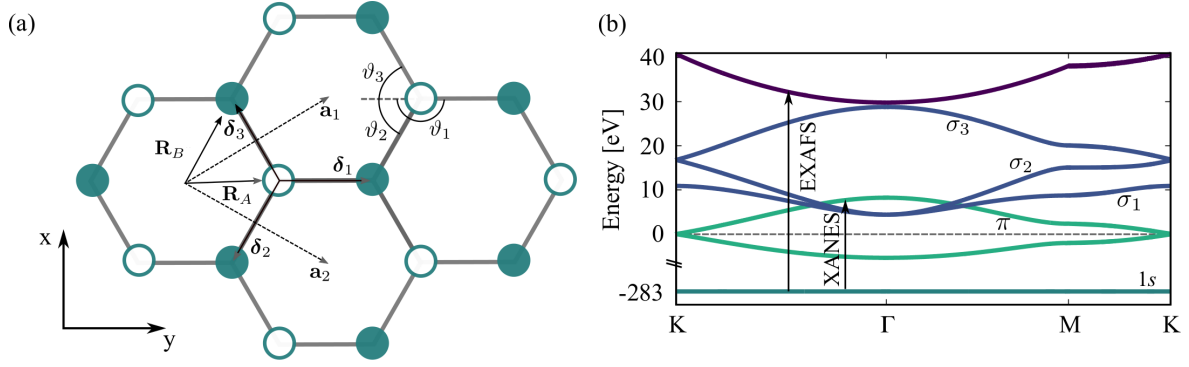
Figure 5.4: (a) Honeycomb lattice of graphene with carbon atom on lattice site A (white) and B (green). Shown are the basis vectors $\boldsymbol{a}_i$, the lattice vectors $\boldsymbol{R}_{A/B}$, the next-neighbor vectors $\boldsymbol{\delta}_i$, and the angles ϑ_i of the bonding directions with respect to the y axis. (b) Calculated band structure of graphene. Shown are the used unoccupied bands above the Fermi level (grey dashed), the occupied π valence band below the Fermi level for orientation and the 1s core band. XANES constitutes of core transitions into the unoccupied states below the ionization threshold of the material and EXAFS of core transitions into the ionization continuum. Figure appears similarly in Ref. [274].

$\langle \phi_{2p_z}(\boldsymbol{r})|H_0|\phi_{2p_z}(\boldsymbol{r}-\boldsymbol{\delta})\rangle$ and the next-neighbor form factor $\xi_{\boldsymbol{k}} = \sum_i \exp(i\boldsymbol{k}\cdot\boldsymbol{\delta}_i)$. In the same way we can calculate the entry for the core orbital. From the offsite matrix Eq. (5.59) we can see that the 1s, $2p_z$ and the in-plane hybridized orbitals decouple. The reason is that for the core orbitals, we assume due to the spatial localization a negligible overlap with other orbitals. For the other orbitals we have symmetry reasons. The Hamiltonian of graphene is symmetric with respect to reflection in the x-y plane. Consequently, the π bands and the σ bands decouple since the former have an odd symmetry and the latter are even with respect to the reflection [272]. We can therefore diagonalize the core, π and σ bands individually. For the π band we find analytically

$$\varepsilon_{\pi,\boldsymbol{k}} = \pm t_\pi \xi_{\boldsymbol{k}} \tag{5.61}$$

with the positive solution describing the valence and the negative solution corresponding to the conduction band. The shape of the dispersion depends solely on the lattice symmetry included by the form factor $\xi_{\boldsymbol{k}}$. Because we neglected the influence of the overlap matrix, we have an electron-hole symmetry for the π bands. The core band can be obtained as limiting case for vanishing lattice site hopping $t_\pi \to 0$: $\varepsilon_{1s}^\pm = \varepsilon_{1s}$. Because of the vanishing hopping the bonding and anti-bonding core bands degenerate.

We turn now our attention to the σ bands. Here, the calculation of the matrix entries are more complicated since the involved orbitals do not all point out of the plane as for $2p_z$ orbitals. In contrast, they lie within the plane and are oriented along the bonding axis. The matrix elements for the Bloch orbitals between the A and B atoms are obtained by taking the components of the $2p_x$ and $2p_y$ orbitals in the σ and π basis. Such a type of (orbital) decomposition is called Slater-Koster method [138]. By these means we obtain a semi-empirical tight binding model, where the Slater-Koster parameters (corresponding to the hopping parameters) are fitted to *ab initio* band structures. We start by calculating the the matrix element for hoppings between two 2s orbitals at different lattice sites. Here we can proceed analogously to the $2p_z$ case and obtain $\mathcal{H}_{33}(\boldsymbol{k}) = V_{ss\sigma}\xi_{\boldsymbol{k}}$. Next, we investigate

hoppings including in-plane $2p$ orbitals. For this, we decompose the p orbital into a component parallel $|p_\delta\rangle$ and perpendicular $|p_n\rangle$ to the line joining two neighbored carbon atoms:

$$|p\rangle = \cos\vartheta|p_\delta\rangle + \sin\vartheta|p_n\rangle\,. \tag{5.62}$$

A sketch defining the nearest neighbour vectors $\boldsymbol{\delta}_i$ and the corresponding angles ϑ_i is shown in Fig. 5.4(a). For the hopping matrix element between $2s$ and $2p_x$ we find:

$$
\begin{aligned}
\mathcal{H}_{34}(\boldsymbol{k}) &= \langle\Phi_{2sA}|H_0|\Phi_{2p_xB}\rangle \\
&= \frac{1}{N}\sum_{\boldsymbol{R}_A,\boldsymbol{R}_B} e^{i\boldsymbol{k}\cdot(\boldsymbol{R}_A-\boldsymbol{R}_B)}\langle\phi_{2s}(\boldsymbol{r}-\boldsymbol{R}_A)|H_0|\phi_{2p_x}(\boldsymbol{r}-\boldsymbol{R}_B)\rangle \\
&= \sum_i e^{i\boldsymbol{k}\cdot\boldsymbol{\delta}_i}\langle\phi_{2s}(\boldsymbol{r})|H_0|\phi_{2p_x}(\boldsymbol{r}-\boldsymbol{\delta}_i)\rangle \\
&= \sum_i e^{i\boldsymbol{k}\cdot\boldsymbol{\delta}_i}\cos\vartheta_i\langle\phi_{2s}|H_0|\phi_{2p_x,\delta}\rangle + \sum_i e^{i\boldsymbol{k}\cdot\boldsymbol{\delta}_i}\sin\vartheta_i\langle\phi_{2s}|H_0|\phi_{2p_x,n}\rangle \\
&= V_{sp\sigma}\sum_i e^{i\boldsymbol{k}\cdot\boldsymbol{\delta}_i}\cos\vartheta_i\,.
\end{aligned}
\tag{5.63}
$$

For the hopping integrals, we define $\langle\phi_{2s}|H_0|\phi_{2p_x,\delta}\rangle = V_{sp\sigma}$ and from symmetry the second hopping integral vanishes. For the other hoppings we find

$$\mathcal{H}_{18}(\boldsymbol{k}) = \langle\Phi_{2sA}|H_0|\Phi_{2p_yB}\rangle = V_{sp\sigma}\sum_i e^{i\boldsymbol{k}\cdot\boldsymbol{\delta}_i}\sin\vartheta_i\,, \tag{5.64}$$

$$\mathcal{H}_{27}(\boldsymbol{k}) = \langle\Phi_{2p_xA}|H_0|\Phi_{2p_xB}\rangle = \sum_i \left(V_{pp\sigma}\cos^2\vartheta_i + t_\pi\sin^2\vartheta_i\right)e^{i\boldsymbol{k}\cdot\boldsymbol{\delta}_i}\,, \tag{5.65}$$

$$\mathcal{H}_{28}(\boldsymbol{k}) = \langle\Phi_{2p_xA}|H_0|\Phi_{2p_yB}\rangle = \sum_i \left(V_{pp\sigma} - t_\pi\right)\cos\vartheta_i\sin\vartheta_i e^{i\boldsymbol{k}\cdot\boldsymbol{\delta}_i}\,, \tag{5.66}$$

$$\mathcal{H}_{38}(\boldsymbol{k}) = \langle\Phi_{2p_yA}|H_0|\Phi_{2p_yB}\rangle = \sum_i \left(V_{pp\sigma}\sin^2\vartheta_i + t_\pi\cos^2\vartheta_i\right)e^{i\boldsymbol{k}\cdot\boldsymbol{\delta}_i}\,. \tag{5.67}$$

We see that the hoppings are weighted by the bonding orientation. The signs of the exponential form factors reflect the underlying triangular symmetry of the lattice. A more detailed derivation of the decomposition of s and p orbitals in constituents parallel and perpendicular to the bonding direction is shown in the appendix A.4. The Slater-Koster parametrized tight binding Hamiltonian is diagonalized numerically exploiting the zgeev routine.

Figure 5.4(b) displays the calculated band structure along the high symmetry traces. For the π band we show addiotnally to the unoccpied conduction band also the occupied valence band below the Fermi level for a better orientation. The π band exhibits Dirac cone-like minima at the K points, saddle points at the M points and a maximum at the Γ point. As discussed in Sec. 5.1, the core dispersion is treated as a flat band $\varepsilon_{1s} = -283\,\text{eV}$ [315]. The tight binding coefficients in nearest-neighbor approximation for the unoccupied π and and $1s$ state read $C_{A,\boldsymbol{k}}^{\pi/1s} = -\xi_{\boldsymbol{k}}/\sqrt{2}|\xi_{\boldsymbol{k}}|$ and $C_{B,\boldsymbol{k}}^{\pi/1s} = 1/\sqrt{2}$. Furthermore, Fig. 5.4(b) displays the unoccupied σ bands, where we see that two of the σ bands cross the π band and lie at the Γ point slightly below the π band. The coefficients of the σ bands are obtained from the numerical diagonalization. The ionization continuum is treated as parabola and starts artificially at the highest included band, which corresponds to the third σ band, cf. Fig. 5.4(b).

With the tight-binding coefficients $C_{j\beta,\boldsymbol{k}}^{\lambda}$ we can calculate the XANES dipole matrix element Eq. (5.10) for the core-conduction band transitions. We restrict the next-neighbor

sum to the nearest-neighbors and obtain in dipole approximation for the K-edge dipole matrix elements

$$\boldsymbol{X}^{1s\lambda}_{\boldsymbol{k}+\boldsymbol{Q}-\boldsymbol{G},\boldsymbol{k}} = -e \sum_{\alpha,\beta,i} C^{*1s}_{\beta 1s,\boldsymbol{k}+\boldsymbol{Q}-\boldsymbol{G}} C^{\lambda}_{\alpha i,\boldsymbol{k}}$$

$$\times \left(\langle 1s, \beta, 1s, 0 \mid \boldsymbol{r} \mid \lambda, \alpha, i, 0 \rangle \, \delta_{\alpha,\beta} + e^{i\boldsymbol{k}\cdot\boldsymbol{\delta}_{\beta\alpha}} \langle 1s, \beta, 1s, 0 \mid \boldsymbol{r} \mid \lambda, \alpha, i, \boldsymbol{\delta}_{\beta\alpha} \rangle \right) . \quad (5.68)$$

The first term of the dipole matrix element exhibits an onsite transition and the second term corresponds to an offsite contribution. The band $\lambda = \pi$ consists just of the $i = 2p_z$ orbital. The $\lambda = \sigma$ band is built by $i = 2s, 2p_x, 2p_y$ orbitals. The offsite transition integral between sublattices A and B can be calculated analytically by transforming the integral to prolate spheroidal coordinates helping to handle the two-center nature of the integral. The z-polarized π transition depends only on the absolute value of the next-neighbor vectors, which is $\delta_i = 0.14$ nm for the nearest-neighbors. The corresponding integral has a value of

$$\langle 1s, A, 1s, 0 \mid \mathbf{r} \mid \pi, B, 2p_z, 0.14 \rangle = \begin{pmatrix} 0 \\ 0 \\ 0.14 \end{pmatrix} \mathrm{pm} . \quad (5.69)$$

In contrast, the transition into the σ bands are in-plane polarized because of the mirror symmetry of the graphene plane. The in-plane transitions are differently weighted for each next-neighbor vector depending on its angular orientation ϑ_i to the y-axis, cf. Fig. 5.4(a). We find

$$\langle 1s, A, 1s, 0 \mid \boldsymbol{r} \mid \sigma, B, 2p_x, \boldsymbol{\delta}_i \rangle = \begin{pmatrix} \cos^2 \vartheta_i & \sin^2 \vartheta_i & 0 \\ \sin \vartheta_i \cos \vartheta_i & -\sin \vartheta_i \cos \vartheta_i & 0 \\ 0 & 0 & 1 \end{pmatrix} \begin{pmatrix} -0.12 \\ 0.14 \\ 0 \end{pmatrix} \mathrm{pm}$$

$$\langle 1s, A, 1s, 0 \mid \boldsymbol{r} \mid \sigma, B, 2p_y, \boldsymbol{\delta}_i \rangle = \begin{pmatrix} \sin \vartheta_i \cos \vartheta_i & -\sin \vartheta_i \cos \vartheta_i & 0 \\ \sin^2 \vartheta_i & \cos^2 \vartheta_i & 0 \\ 0 & 0 & 1 \end{pmatrix} \begin{pmatrix} -0.12 \\ 0.14 \\ 0 \end{pmatrix} \mathrm{pm} . \quad (5.70)$$

In the $\delta \to 0$ limit the prolate spheroidal coordinates evolve into the spherical coordinates. The onsite transitions for the $2p_x$, $2p_y$ and $2p_z$-integrals are purely x, y and z-polarized, respectively, and have the value of 4.00 pm. Finally, the $1s$ to $2s$ transition does not contribute for vanishing connection vector because of there even symmetry and the uneven parity of the dipole vector. For the offsite transition we obtain

$$\langle 1s, A, 1s, 0 \mid \boldsymbol{r} \mid \sigma, B, 2s, \boldsymbol{\delta}_i \rangle = -0.5 \begin{pmatrix} \cos \vartheta_i \\ \sin \vartheta_i \\ 0 \end{pmatrix} \mathrm{pm} . \quad (5.71)$$

The result is negative because of the node of the $2s$ orbital. Obviously, offsite transition integrals are smaller than onsite transition integrals because of the small overlap of the core orbital with other orbitals. At last, we want to point out that we performed a dipole approximation for the transition integral. However, transitions forbidden by the dipole selection rule are accessible via higher-order terms in the $\exp(i\boldsymbol{Q} \cdot \boldsymbol{r}_\parallel)$ expansion. But their intensity is usually much less than the intensity of the dipole allowed transitions.

5.7 X-ray absorption of graphene

We finally have all necessary quantities for the description of the X-ray absorption. For a weak excitation density the homogeneous occupation in initial and final band can be set to

one and zero, respectively. Then, in linear optics, the solution of the microscopic X-ray Bloch equation Eq. (5.18) reads in frequency space

$$p_{\boldsymbol{k}+\boldsymbol{Q}-\boldsymbol{G},\boldsymbol{k}}^{\lambda_1\lambda_2}(\omega) = \frac{-\boldsymbol{X}_{\boldsymbol{k}+\boldsymbol{Q}-\boldsymbol{G},\boldsymbol{k}}^{\lambda_2\lambda_1} \cdot \boldsymbol{E}_{\boldsymbol{Q}}(\omega)}{\hbar\omega - \varepsilon_{\boldsymbol{k}}^{\lambda_2} + \varepsilon_{\boldsymbol{k}+\boldsymbol{Q}-\boldsymbol{G}}^{\lambda_1} + i\gamma} \tag{5.72}$$

$$p_{\boldsymbol{k}+\boldsymbol{Q}-\boldsymbol{G},\boldsymbol{k}}^{\lambda k_\perp}(\omega) = \frac{-\boldsymbol{Y}_{\boldsymbol{k}+\boldsymbol{Q}-\boldsymbol{G},\boldsymbol{k}}^{k_\perp\lambda} \cdot \boldsymbol{E}_{\boldsymbol{Q}}(\omega)}{\hbar\omega - \varepsilon_{\boldsymbol{k}}^{k_\perp} + \varepsilon_{\boldsymbol{k}+\boldsymbol{Q}-\boldsymbol{G}}^{\lambda} + i\gamma} \tag{5.73}$$

divided into XANES and EXAFS transitions, respectively. In the case of $\lambda_1 = 1s$ core states, the former equation will yield the sudden K absorption edges at the energy differences between two-dimensional $1s$ and conduction bands λ_2. The second equation yields the absorption of $1s$ to vacuum transitions and should inhered the experimentally observed oscillations. Since the core bands are flat bands, we shifted the momenta such that the vector addition is performed in the flat band to be numerically exact. Additionally, we introduced a phenomenological dephasing constant γ attributing to the finite lifetime of the electronic transition and leading to a broadening of the absorption line. The dephasing consists of a Coulomb-induced and a radiative dephasing. The radiative dephasing can be included by Eq. (5.51). The dephasing depends on the position in the electronic Brillouin zone by $\boldsymbol{k}$ and the X-ray wave vector $\boldsymbol{Q}$. Generally, the calculated radiative lifetime is of a few picoseconds. Different studies report a core-hole lifetime in graphite and carbon-based molecules of around 10 fs [316, 317] suggesting that other recombination mechanism are dominating. These relaxation channels are considered phenomenologically by adjusting the dephasing rate γ. Together with the definition of the two-dimensional macroscopic polarization, being proportional to the electric field, we can identify the dyadic susceptibility

$$\chi_{\boldsymbol{Q}}(\omega) = \sum_{\lambda_1,\lambda_2,\boldsymbol{k},\boldsymbol{G}} \frac{\boldsymbol{X}_{\boldsymbol{k},\boldsymbol{k}+\boldsymbol{Q}-\boldsymbol{G}}^{\lambda_1\lambda_2} \otimes \boldsymbol{X}_{\boldsymbol{k}+\boldsymbol{Q}-\boldsymbol{G},\boldsymbol{k}}^{\lambda_2\lambda_1}}{\hbar\omega - \varepsilon_{\boldsymbol{k}}^{\lambda_2} + \varepsilon_{\boldsymbol{k}+\boldsymbol{Q}-\boldsymbol{G}}^{\lambda_1} + i\gamma} + \sum_{\lambda,\boldsymbol{k},\boldsymbol{G},k_\perp} \frac{\boldsymbol{Y}_{\boldsymbol{k},\boldsymbol{k}+\boldsymbol{Q}-\boldsymbol{G}}^{\lambda k_\perp} \otimes \boldsymbol{Y}_{\boldsymbol{k}+\boldsymbol{Q}-\boldsymbol{G},\boldsymbol{k}}^{k_\perp\lambda}}{\hbar\omega - \varepsilon_{\boldsymbol{k}}^{k_\perp} + \varepsilon_{\boldsymbol{k}+\boldsymbol{Q}-\boldsymbol{G}}^{\lambda} + i\gamma} \tag{5.74}$$

with the dyadic product of the vector-valued dipole matrix elements yielding a 3×3 matrix for the susceptibility. The XANES dipole matrix element $\boldsymbol{X}_{\boldsymbol{k}+\boldsymbol{Q}-\boldsymbol{G},\boldsymbol{k}}^{\lambda_2\lambda_1}$ is determined by Eq. (5.68) and the EXAFS matrix element $\boldsymbol{Y}_{\boldsymbol{k},\boldsymbol{k}+\boldsymbol{Q}-\boldsymbol{G}}^{\lambda k_\perp}$ by Eq. (5.15). The X-ray wave number and the excitation frequency are related by the relation $Q^2 = \omega^2 \sin\theta/c^2$, where θ denotes the incident angle of the X-ray radiation. Consequently, we perform no further approximation and include all $\boldsymbol{Q}$ over the full range of the absorption spectrum. The response of the material to the weak excitation is investigated by calculating the absorption. Therefore, we introduce the absorption coefficient $\alpha_{\boldsymbol{Q}}(\omega) = 1 - r_{\boldsymbol{Q}}(\omega) - t_{\boldsymbol{Q}}(\omega)$ defined by reflection $r_{\boldsymbol{Q}}$ and transmission $t_{\boldsymbol{Q}}$.

Since the susceptibility is determined by a dyadic product all possible components of the dipole matrix elements are coupled, which leads to a rather difficult expression for the absorption suggesting a numerical treatment. We start by investigating the XANES spectrum, i.e. the susceptibility in Eq. (5.74) is restricted to the first term. Figure 5.5(a) displays the calculated XANES spectrum of graphene for different angles of incidence θ. The absorption starts at 283 eV corresponding to the binding energy of the core electrons relative to the Fermi surface of graphene. The first peak at 286 eV rises with increasing angle. It stems from the transition of $1s$ electrons into the π band close to the M-point, which exhibits a van Hove singularity due to a saddle point and therefore a large density of states. The following three peaks at 293 eV, 298 eV, and 303 eV stem from transitions into the three σ bands and are decreasing with increasing angle of incidence. All four peaks are observed in
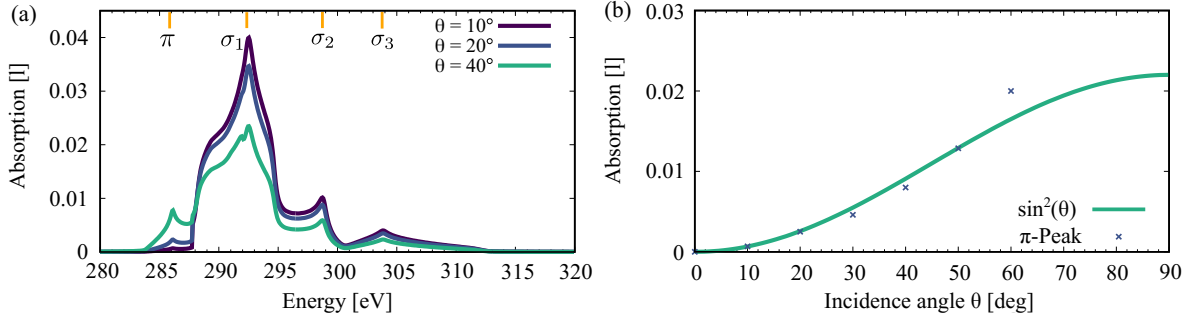
Figure 5.5: (a) XANES of graphene for different angles of incidence. The first peak stems from absorption into the π bands, while the three succeeding peaks are transitions into the σ bands. (b) The π peak shows a $\sin^2\theta$-behavior. The deviation at higher angles stems from the fact that we assumed an infinite thin graphene layer. Figure appears similarly in Ref. [274].

experiment [318–321] and match with the here calculated energetic positions and spectral structure. However, one difference between calculated and measured absorption spectrum can be noticed, namely the appearance of a plateau after the second peak in the measured absorption spectrum, which is absent in the calculated spectrum, cf. Fig. 5.5(a). This can be traced back to the point that we limited our approach to orbitals up to the $2p$ orbitals. Including more orbitals [322] leads to a continuum of close lying bands and should form an almost continuous absorption.

Figure 5.5(b) shows the peak height of the π peak as a function of the angle of incidence. We obtain that the absorption follows a $\sin^2\theta$-behavior before deviating from this trend at about $60\,^\circ$. The polarization-dependent absorption can be explained by the symmetry of the orbital composition of the final band [272,318,323,324]. When considering only transitions into the $2p_z$ orbital we can exploit the z-polarization of the dipole transition due to the out-of-plane character of the $2p_z$ orbital. This greatly simplify the susceptibility tensor. Consequently, we can find an analytical expression for the absorption into the π band. Without loss of generality we assume for the in-plane incidence angle zero degree, such that $Q_y = 0$. Then we obtain for the absorption

$$\alpha_{\boldsymbol{Q}}(\omega) = \frac{\Delta_{\boldsymbol{Q}}(\omega)\Im\mathfrak{m}\left(\chi_{\boldsymbol{Q}}^{33}(\omega)\right) - \frac{Q_x^2}{2\epsilon}|\chi_{\boldsymbol{Q}}^{33}(\omega)|^2}{|1 - \frac{i}{2}\Delta_{\boldsymbol{Q}}(\omega)\chi_{\boldsymbol{Q}}^{33}(\omega)|^2} \tag{5.75}$$

with $\Delta_{\boldsymbol{Q}}(\omega) = \frac{\omega^2}{c^2\kappa} - \frac{\kappa}{\epsilon}$ and $\chi_{\boldsymbol{Q}}^{33}(\omega)$ as the zz-entry of the susceptibility tensor. The coefficient $\Delta_{\boldsymbol{Q}}(\omega)$ stems from the matrix $K_{\boldsymbol{Q}}(\omega)$ carrying all prefactors. In particular, the denominator arises from the self-consistent treatment of the Maxwell and Bloch equations and includes for instance the radiative coupling in the sample. The in-plane light wave vector Q_x^2 is proportional to $\sin^2\theta$. When inserting the definition for κ and express the X-ray wave vector as function of the angle of incidence we obtain for the prefactor $\Delta(\theta,\omega) = \omega^2 \sin^2\theta/\epsilon c^2\sqrt{\epsilon - \sin^2\theta}$. Now, we explicitly see the $\sin^2$-dependence of the true absorption coefficient. For a perpendicular irradiation of the sample ($\theta = 0°$) we immediately see that $\Delta_{\boldsymbol{Q}}(\omega)$ and Q_x vanish and consequently also the absorption vanishes as expected from the z-polarized transition. On the other side the derived absorption formula diverges for an incident angle of $\theta = 90°$ in the case of $\epsilon = 1$, explaining the observed deviation in Fig. 5.5(b). The fact that the singularity does not explicitly appear anymore for $\epsilon > 1$, suggests that the origin lies in the assumption of an infinitely thin layer in a uniform background. The divergence might be lifted by starting with
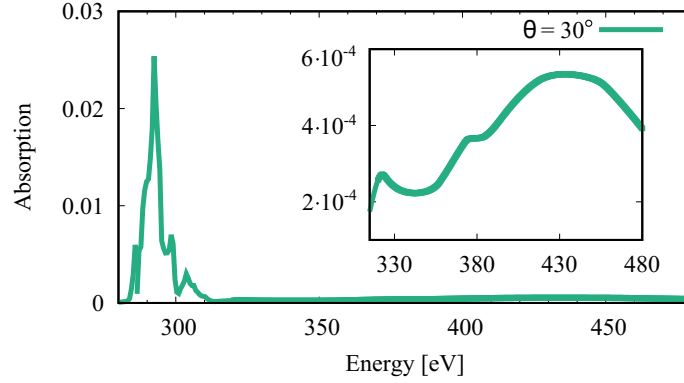
Figure 5.6: X-ray absorption spectrum of graphene for 30° irradiation. We obtain a dominating XANES contribution stemming from transition between core and conduction bands. Also, the weaker transitions into the ionization continuum, displayed in the inset, are obtained. The absorption into the three-dimensional continuum is modulated by oscillations with maxima at different energies. Figure appears similarly in Ref. [274].

a three layer model – supstrate, layer, substrate – all with finite thickness and by solving the Maxwell equation for each region with corresponding continuity conditions [325].

After investigating the XANES contribution, we compute the full X-ray absorption spectrum by including also the EXAFS part, described by the second line of Eq. (5.74). The ionization threshold is set artificially to the maximum of the energetically highest lying σ band. Figure 5.6 shows the full absorption spectrum ($\theta = 30°$) and a zoom into the EXAFS part, corresponding to the absorption involving the three-dimensional electronic continuum of vacuum states as final states. We recognize that the absorption curve is modulated with oscillations. For the particular situation plotted here we recognize three maxima. Following the pioneering work by D. E. Sayers *et al.* it is widely recognized that these wiggles could be used to obtain quantitative information about the local structure of the lattice. The current interpretation in literature is that these oscillations stem from a modulation of the absorption cross section due to interference of the X-ray waves between neighboring atoms. Here, we calculate the absorption using the susceptibility determined by the second term of Eq. (5.74), which includes the full lattice symmetry. For a constant EXAFS dipole matrix element the second line of Eq. (5.74) summed over the electronic wave vectors describes a square-root like absorption into the three-dimensional continuum states of the vacuum electrons. However, this simplified absorption line is modulated by the dyadic product of the EXAFS matrix elements, cf. Eq. (5.74). To obain more insights we abbreviate the occurring form factor in the EXAFS matrix element Eq. (5.15) as $f_n(\boldsymbol{k} - \boldsymbol{G}) = 8\pi i \zeta^{3/2} (\boldsymbol{k} - \boldsymbol{G})_n \hat{\boldsymbol{e}}_n / (\zeta^2 + (\boldsymbol{k} - \boldsymbol{G})^2)^3$. Analytically, we obtain for the squared dipole matrix element of the entry nm in the susceptibility tensor

$$|(C^{*1s}_{A1s,\boldsymbol{k}} + C^{*1s}_{B1s,\boldsymbol{k}})|^2 f_n(\boldsymbol{k} - \boldsymbol{G}) f_m(\boldsymbol{k} - \boldsymbol{G}) = \left(1 + \frac{1}{|\xi_{\boldsymbol{k}}|} \sum_i \cos(\boldsymbol{k} \cdot \boldsymbol{\delta}_i)\right) f_n(\boldsymbol{k} - \boldsymbol{G}) f_m(\boldsymbol{k} - \boldsymbol{G}), \tag{5.76}$$

where we inserted the definitions for the tight binding coefficients. Similar to the work of D. E. Sayers, we clearly find an oscillating behavior in $\boldsymbol{k}$ with the lattice vector frequency $\boldsymbol{\delta}_i$ comparable to Eq. (5.2). The prefactor $f_n(\boldsymbol{k} - \boldsymbol{G})$, in conjunction with the reciprocal lattice vector sum in the susceptibility, describes a train of Lorentzians peaking at multiples of the

reciprocal lattice vector encoding the direct position of the atoms. However, because of the small nuclear number, the broadening of the form factor f_n is so strong that f_n is almost constant, i.e. $f_n(\boldsymbol{k} - \boldsymbol{G}) \equiv f_n$. Therefore, the reciprocal lattice geometry is not resolved and its influence on $\alpha_{\boldsymbol{Q}}(\omega)$ is negligible. Consequently, Eq. (5.76) is determined solely by the squared tight binding coefficients $(1 + \sum_i \cos(\boldsymbol{k} \cdot \boldsymbol{\delta}_i)/|\xi_{\boldsymbol{k}}|)$, which are responsible for the cosine-like oscillations. From a physical point of view, the tight binding coefficients describe the orbital contribution of a specific lattice site to the band composition. Due to the lattice periodicity, the tight binding coefficients are a function of the wave vector $\boldsymbol{k}$, which is determined by the lattice geometry. We can therefore understand the absorption, which is proportional to Eq. (5.76) and summing over all wave vectors (Eq. (5.74)), as showing the quantum interference between orbital electronic wave functions, which can be constructive or destructive depending on the sign of the coefficients.

Summarizing this discussion, we can conclude that the EXAFS oscillations stem from an interference of standing electronic wave functions of the graphene sublattices A and B. In contrast to current interpretations [53, 273, 326–328], the interference is spatially stationary, since it is independent of the X-ray excitation.

This discussion rises the question why such oscillations are not observed also in XANES. For XANES excitations the tight binding coefficients of the initial and final states are multiplied and the XANES dipole matrix element consists of a sum of onsite and offsite contributions, cf. Eq. (5.68). For diagonal transitions, where $\boldsymbol{k}_1 = \boldsymbol{k}_2 = \boldsymbol{k}$, the lattice geometry-dependent phase cancels for the onsite contribution due to the product of the tight binding coefficients. However, the offsite contribution still carries a phase with included lattice geometry: $-\boldsymbol{X}_{\boldsymbol{k},\boldsymbol{k}}^{1s\pi} = \boldsymbol{d}_{\mathrm{on}} \left(|\xi_{\boldsymbol{k}}| + 1\right)/2 + \boldsymbol{d}_{\mathrm{off}} \sum_i \cos(\boldsymbol{k} \cdot \boldsymbol{\delta}_i)/|\xi_{\boldsymbol{k}}|$, where $\boldsymbol{d}_{\mathrm{on}}$ and $\boldsymbol{d}_{\mathrm{off}}$ stand for the onsite and offsite dipole transition integrals occurring in Eq. (5.68). In the case of non-diagonal transitions the phase is non-vanishing even for the onsite contribution. However, due to the k-space restriction of the 1st Brillouin zone, the bandwidth is not large enough that the oscillating behavior of the phase becomes visible in the absorption spectrum. This is different for the ionization continuum since it lacks the translational invariance of the lattice.

EXAFS is often expressed in terms of wave number k. Since the X-ray light has an excitation energy higher than the threshold energy we can express the energy of the free electron as $\omega(k) = \hbar k^2/2m_0 + E_{Ion}/\hbar$. To discuss the spatial interference, we apply a Fourier transform to the absorption coefficient, i.e. $\int d^2k \, \alpha_{\boldsymbol{Q}(k)}(\boldsymbol{k}) \exp(i\boldsymbol{k} \cdot \boldsymbol{r}_\parallel)$, to real space with respect to the wave number. Consequently, Eq. (5.76) exhibits maxima at the nearest-neighbor distance. To increase the visibility and access more conveniently the oscillations at higher k, the absorption spectrum as function of wave number is multiplied by k^m with typically $m \in [1, 2, 3]$ and a Fourier transform is applied subsequently [329–331]. In the following, we discuss the Fourier transform of the absorption spectrum evaluated by our description, which involves the Bloch theorem for solid states.

The blue curve in Fig. 5.7(a) displays the Fourier amplitude of the k-weighted and background corrected EXAFS spectrum [332] in first neighbor approximation. The effective radial distribution function clearly displays a peak at the distance of the first neighbor. The second peak at 0.28 nm is the second harmonic lying at twice of the nearest-neighbor distance. Higher harmonics are barely visible due to the overall decrease of the spectrum with increasing r. The higher harmonics stem from the fact that the Fourier transformation is performed on a limited space.

So far we have considered only the nearest-neighbor hoppings for the calculation of the matrix elements. As a result we obtain a peak at the first neighbor distance and corresponding peaks at the higher harmonics. However, calculating the matrix elements beyond the nearest-
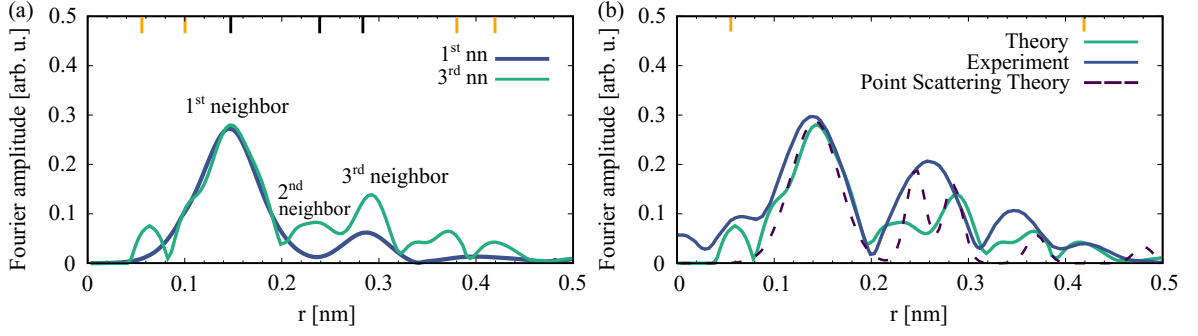
Figure 5.7: (a) Fourier amplitude of the EXAFS spectrum. The blue curve includes only the first nearest-neighbor (nn). It peaks at the first nearest-neighbor distance and its higher harmonics. The green curve includes also the second and third next-neighbors. The peaks stem from the first three neighbors (black) and interferences among themselves (yellow). (b) Comparison of Bloch theory, experiment (adapted from Ref. [319]) and point scattering theory (Eq. (5.78)). Figure appears similarly in Ref. [274].

neighbor approximation should add additional features to the Fourier amplitude of the EXAFS. To go beyond the nearest-neighbor hopping we introduce the second $\xi_{\boldsymbol{k}}^{(2)} = \eta_2 \sum_{i=4}^{9} \exp(i\boldsymbol{k} \cdot \boldsymbol{\delta}_i)$ and third $\xi_{\boldsymbol{k}}^{(3)} = \eta_3 \sum_{i=10}^{12} \exp(i\boldsymbol{k} \cdot \boldsymbol{\delta}_i)$ next-neighbor form factors. For the free parameters of second and third next-neighbor hoppings we reasonably choose $\eta_2 = 0.05$ and $\eta_3 = 0.01$, respectively. The ratios of η_2 and η_3 with respect to the hopping parameter to the nearest-neighbor are chosen such that they coincide with the relative deviation of the hoppings between $2p_z$ orbitals with increasing order of neighbors [333, 334]. By this assumption the peak heights are uncertain, but the peak positions – which is of most importance in our study – are unaffected by that. The tight binding coefficients up to the third neighbor hopping read

$$C_{A1s,\boldsymbol{k}}^{1s} = \frac{\xi_{\boldsymbol{k}} + \xi_{\boldsymbol{k}}^{(3)}}{\sqrt{2}\left(|\xi_{\boldsymbol{k}} + \xi_{\boldsymbol{k}}^{(3)}| + \xi_{\boldsymbol{k}}^{(2)}\right)}, \quad \text{and} \quad C_{B1s}^{1s} = \frac{1}{\sqrt{2}}, \tag{5.77}$$

which now include 12 neighbors instead of three and enter the matrix element, described by the left-hand side of Eq. (5.76). The green line in Fig. 5.7(a) displays the effective radial distribution function including hoppings up to the third neighbor coupling in the EXAFS matrix element. In contrast to the calculation with first neighbor hopping, we find additional peaks at the second and third neighbor distance of 0.24 nm and 0.28 nm, respectively, as well as the corresponding higher harmonics. For instance, the third peak at 0.28 nm is a combination of the third neighbor and higher harmonic of the first neighbor. Interestingly, also peaks appear, which do not correspond to next neighbor distances, but do correspond to interferences of different next neighbor vectors. Exemplary, we obtain a peak at 0.38 nm corresponding to the sum of the first and second neighbor distance. Since 0.38 nm also correspond to the fourth neighbor distance in graphene, this peak could also be interpreted as the fourth neighbor in experiments. At 0.05 nm we can resolve a peak, which arises from the difference of third and second neighbor. So far, this peak has been explained via a phase shift stemming from a difference between measured and geometrical interatomic distances and required a theoretical or experimental correction [273]. In contrast, in our approach, we show that the peak can be interpreted as a quantum interference between electronic Bloch wave functions of first and second neighbor. The slight sideband of the first nearest-neighbor peak at 0.1 nm stems from

the difference of the second and first neighbor. Further, we observe a peak at 0.42 nm, which can be understood as interference of the first with third neighbor.

To manifest our interpretation, in Fig. 5.7(b) we provide a direct comparison of our full computational result up to the third nearest-neighbor to experiment, adapted from Ref. [319], and additionally display the outcome obtained from the point scattering theory [53]. In point scattering theory the oscillatory part of the EXAFS is solely described by the matrix element squared corresponding to Eq. (5.2). The Fourier transform yields the structure-related function [53]

$$S(r) = \frac{1}{2} \sum_i \frac{N_i}{R_i^2} e^{-\gamma R_i} e^{-2(r-R_i)^2/\sigma_i^2} \tag{5.78}$$

displayed as dashed line in Fig. 5.7(b). The γ-factor accounts for the photoelectron scattering range and leads to an overall decrease with increasing distance. The result is a sum of Gaussian functions lying at the next-neighbor distances R_i.

The blue curve in Fig. 5.7(b) corresponds to the Fourier transform of a measured EXAFS with an isolated soft X-ray pulse produced by high harmonic generation. The measurements were performed by Barbara Buades and Jens Biegert from the Institute of photonic sciences (ICFO) in Barcelona and published in reference [319], who provided us the data for a comparison.

Prior to the Fourier transformation, the measured EXAFS data were background corrected. This correction consists of an approximation of the EXAFS data by an adjustable smooth function, which represents the absorption coefficient without neighboring atoms. The spline function is then subtracted from the measured data. To achieve a fair comparison between the two theories and the experiment we perform the same manipulations. Additionally, we force the first neighbor peak to match the experimental one in height. The experimental curve in Fig. 5.7(b) displays three major peaks: The first at 0.14 nm reflects the first neighbor. The second peak around 0.26 nm consists of a sum of second and third neighbor. The reason for that is the spectral resolution of the used table top water window X-ray laser, which is a new technology [319, 335]. With a broader spectral range of the laser it might be possible to resolve both close-lying peaks individually. Lastly, the maximum at 0.38 nm can be interpreted as fourth neighbor. All three peaks are well reproduced by our Bloch as well as the point scattering theory. However, a close look to the experiment reveals clear additional spectral features around 0.05 nm and at 0.42 nm, both distances that do not exist in the graphene lattice. While those spectral features are absent in a point scattering theory, our theory reproduces them in good agreement in position: Following the description above, these features rely on the use of the Bloch theorem and can be explained as quantum interference between electronic Bloch wave functions. Although the interference peaks are observed in experiment [319] they have not been discussed so far and require a detailed solid state theory involving the full solid state lattice symmetry to be interpreted. Thus the central result of our approach is a solid state generalization of Eq. (5.2).

Summarizing, the EXAFS oscillations are encoded in the dipole matrix element, which modulate the square root-like absorption line into the three-dimensional continuum. The modulations can only be understood by a solid state specific theory that confirms the relation between the EXAFS oscillations and the local real space configuration of the crystalline material [53]. However, these oscillations does not originate from an interference of the X-ray waves but from quantum interferences of electronic wave functions of neighbored atoms.

5.8 Conclusion

X-ray absorption spectroscopy is a spectroscopic techniques, which probes the core electrons of materials. XAS has played a tremendous role at the beginning of the 20th century by investigating atomic energy levels and discovering new rare elements. XAS is usually divided into two parts: The first corresponds to XANES and desribes the transition of core electrons into unoccupied conduction band states in the material. Each transition gives rise to sudden absorption edges in the spectrum. The current literature typically consults Fermi's golden rule to describe XANES. The second part is EXAFS, which stems from transitions of core-electrons into the ionization continuum. Here, the absorption into the three-dimensional continuum is modulated by oscillations. In the 1970s D. E. Sayers *el. al.* discovered that these oscillation can be related to the local structure of the sample. Therefore, EXAFS oscillations appear only in molecules or solid states. Problematic is that the basis functions of the Sayers formalism does not fulfill the Bloch theorem and are therefore no appropriate basis for crystalline materials. Therefore, we derived a solid state theory of X-ray absorption spectroscopy by self-consistently coupling the Maxwell and X-ray Bloch equations. Here, we took into account the in-plane wave vector of X-ray radiation and spatial variations in the unit cell, which give rise to a non-local optical response of the material. Moreover, we show that the polarization dependence of the electronic core transitions give rise to a strong dependence of the angle of incidence of the light. For EXAFS, we find that the oscillations indeed give information about the local structure of the material, but appear due to interference effects of Bloch waves from neighbored atoms. Consequently, the Fourier transform does not show only peaks at the neighbor distances but also at sums or differences of the distances. This demands a careful analysis of X-ray measurements of solid states.

The self-consistent coupling of the Maxwell and X-ray Bloch equations enables a calculation of the radiative dephasing of core-holes beyond Fermi's golden rule. As second mechanism for atomic recombination of core-holes the literature discusses Meitner-Auger recombination. The X-ray Bloch formalism naturally incorporates such scattering channels. Moreover, the formalism can treat all kind of Coulomb interaction and includes also core excitons and core-hole effects.

Chapter 6

Conclusion

We discussed high energy spectroscopic techniques namely time and angle resolved photoemission spectroscopy and X-ray absorption spectroscopy.

In case of tr-ARPES we raised the questions whether excitons, as correlated electron-hole quasi-particles, are visible in photoemission. Developing an excitonic photoemission theory based on the unit operator method, which expands each electron after electron-hole pairs, we can answer the question with yes. Additionally, after 40 years of tr-ARPES history the experimental realization of this theoretical proposition has been realized [176, 180]. We find that the coherent excitons lead to an intriguing signal, namely a valence band replica, at the exciton energy. The intensity distribution along this signal reflects the exciton wave function squared in momentum space. Therefore, tr-ARPES can directly visualize the square of the exciton wave function. Moreover, we can access also incoherent excitons and trace their phonon-induced scattering throughout the Brillouin zone. We expect that the direct, momentum resolved, access of tr-ARPES to excitons will give new insights into exciton physics and material science. In this contribution, we focused on the low excitation regime linear in the exciton density. However, the theory is scalable to higher excitation conditions. Unfortunately, tr-ARPES experiment are to date limited by their energy resolution. Therefore, information encoded in higher orders of the exciton expansion will be experimentally unresolved. But with increasing energy resolution, in the future such theoretical studies might become necessary.

Secondly, we built a solid state conform self-consistent theory for X-ray absorption spectroscopy by combining the Maxwell and X-ray Bloch equations. With this, we present the first theory, which can describe XANES and EXAFS in a unified way. We applied the derived theory to the exemplary material of graphene. We showed that XANES displays the density of states of bound electronic states and how core transitions show a strong dependence on the angle of incidence of the exciting X-ray light. EXAFS, which corresponds to unpolarized core transitions into the ionization continuum, displays oscillations in the spectrum. We confirmed the assumption of D. E. Sayers and coworker from 1970 that these oscillations are related to the local geometry of the sample. However, we find that in case of crystalline solids these oscillations stem from interference of core Bloch wave functions from neighbored atoms instead of interfering X-ray waves. This leads to the fact that we can assign so far overlooked peaks in the Fourier transformed EXAFS spectrum, which displays not only peaks at the neighbor distances but also at interferences between them. Moreover, our XAS theory is compatible with DFT methods, which are the main theoretical instrument in XAS theory. For example all electronic parameters and matrix elements can be calculated with Quantum Espresso and a Wannier90 interpolation and the results can be combined with the self-consistent XAS theory. We believe that this new X-ray-matter theory will shed new light on the analysis of XAS

experiments. One limitation of the presented theory is, although the solution of the wave equation inherits linear and nonlinear excitations, that the derived self-consistent electric field is restricted to the linear regime. Here lies a further possible extension of the theory, also to nonlinear time-resolved XAS experiments on two-dimensional crystalline solids.

As third topic we investigated excitons in van der Waals heterostructures. For a WSe$_2$-graphene stack, we studied interfacial energy and charge transfer processes. We find that Förster transfer acts on a long time scale, while Dexter transfer is extremely unlikely. In contrast, phonon-assisted tunneling of electrons and holes happens on short time scales. Additionally, we identify a new type of interlayer energy transfer mechanism, which we name interfacial Meitner-Auger energy transfer. Here, a TMDC exciton recombines non-radiatively and excites intraband transitions in graphene. This theoretical study was triggered by tr-ARPES measurements, which found intriguing and inexplicable results [200]. In such a way, the circle closes as we stated at the beginning that tr-ARPES will boost the amount of new insights into exciton physics and material science. Secondly, we investigated hybrids of inorganic semiconductors and organic molecules. We propose HIOS to be the ideal candidate for the long time searched excitonic insulator built by interlayer excitons and uniquely provable by far-infrared to terahertz spectroscopy. Recently, their has been a lot of studies on the excitonic insulator in TMDC homobilayer and heterostructures, but compelling experimental evidence is still missing. With HIOS we propose an additional promising candidate and showed how to detect the phase transition. The excitonic insulator forms a new type of material phase characterized by spontaneous formation of excitons. The excitonic insulating phase exhibits an excitonic ground state, which requires a proper description, for example in a Bogoliubov formalism. Within this framework we showed how to optically characterize excitonic phases, which are tunable by an externally applied electric field. By these means we can switch between (semi-) metallic phase, described by a Drude response, semiconductor phase, described by a Lorentz response (vanishing small for interlayer excitons) and excitonic insulator exhibiting a p-type Rydberg series from intraexcitonic transitions. The developed excitonic insulator Bogoliubov theory is derived in a mean-field approximation. But an excitonic insulator exhibits high electron-hole occupations and as in our case even an electronic inversion. Here, the question rises about non-linear contributions, or even a biexcitonic ground state. Therefore, a description beyond the mean-field limit might be interesting for future research.

Appendices

A.1 Optical selection rules from group theory

Table 1 displays the character table of the point group C_{3h}. A single prime indicates that a representation is symmetric with respect to a σ_h plane and a double prime indicates its antisymmetry. This is comparable to the subscripts g (gerade) and u (ungerade) if an inversion center is present. Checking the basis function in column of Tab. 1 we see that

Table 1: Character table of the C_3 point group with $\varepsilon = \exp(2\pi i/3)$.

C_3	E	$C_3(z)$	C_3^2	σ_h	S_3	$(S_3)^5$	quadratic function
A'	1	1	1	1	1	1	$x^2 + y^2,\ z^2$
E'	1	ε	ε^*	1	ε	ε^*	$(x^2 - y^2, xy)$
	1	ε^*	ε	1	ε^*	ε	
A"	1	1	1	-1	-1	-1	-
E"	1	ε	ε^*	-1	$-\varepsilon$	$-\varepsilon^*$	(xz, yz)
	1	ε^*	ε	-1	$-\varepsilon^*$	$-\varepsilon$	

$(d_{x^2-y^2} i \pm d_{z^2})/\sqrt{2}$ transforms according to the representation E'. The two rows consider the plus and minus case. The dipole vector transforms in the C_{3h} point group according to $E' + A''$. Then the direct product reads

$$\Gamma_v \otimes \Gamma_r = A' \otimes (E' + A'') = A'E' + A'A''. \tag{A.1.1}$$

The characters $\chi_{A'} \otimes \chi_{E'+A''}$ is summarized in Tab. 2 We consider $\chi_{A'} \otimes \chi_{E'+A''}$ as reducible

Table 2: Character table of the $\Gamma_v \otimes \Gamma_r$

E	$C_3(z)$	C_3^2	σ_h	S_3	$(S_3)^5$
2	$1+\varepsilon$	$1+\varepsilon^*$	0	ε-1	ε^*-1

representation of the group C_{3h}. The decomposition formula reads [138]

$$n(i) = \frac{1}{h} \sum_c g_c \chi_i \chi_r. \tag{A.1.2}$$

It gives the amount of times a symmetry species occurs in the reducible representation $n(i)$. The sum runs over all symmetry operations c and h is the order of the group. The order just corresponds to the total number of symmetry operations. The relevant numbers for the decomposition are the number of symmetry operations g_c, the character of the irreducible representation χ_i and the character of the reducible representation χ_r. Together with the character tables we obtain

$$n(A') = \frac{1}{3} \left(1 \cdot 1 \cdot 2 + 1 \cdot 1 \cdot (1 + e^{2\pi i/3}) + 1 \cdot 1 \cdot (1 + e^{-2\pi i/3}) \right) = 1, \tag{A.1.3}$$

$$n(E') = \frac{1}{3} \left(1 \cdot 1 \cdot 2 + 1 \cdot e^{2\pi i/3} \cdot (1 + e^{2\pi i/3}) + 1 \cdot e^{-2\pi i/3} \cdot (1 + e^{-2\pi i/3}) \right) = 0. \tag{A.1.4}$$

We see that transitions into final states transforming according to the irreducible representation A' are allowed, as is the case for the d_{z^2} orbital, but optical transition into states transforming

according to E' forbidden. For the sake of completeness we provide also

$$n(A'') = \frac{1}{3}\left(1 \cdot (-1) \cdot 0 + 1 \cdot (-1) \cdot (e^{2\pi i/3} - 1) + 1 \cdot (-1) \cdot (e^{-2\pi i/3} - 1)\right) = 1, \qquad (A.1.5)$$

$$n(E'') = \frac{1}{3}\left(1 \cdot (-1) \cdot 0 + 1 \cdot (-e^{2\pi i/3}) \cdot (e^{2\pi i/3} - 1) + 1 \cdot (-e^{-2\pi i/3}) \cdot (e^{-2\pi i/3} - 1)\right) = 0.$$
$$(A.1.6)$$

Next, we investigate the photoemission selection rules. The final state continuum wave function should be symmetric with respect to all mirror planes of the surface. The valence band transforms according to E' and the ionization continuum to A' and E'. We obtain for the character product $E' \cdot A' = 1 \mid \varepsilon \mid \varepsilon^* \mid 1 \mid \varepsilon \mid \varepsilon^*$. In order that the integral is symmetric the polarization projected dipole vector needs to transform according to E'. To check

$$\chi_{E'}\chi_{E'}\chi_{A'} = 1 \mid 1 \mid 1 \mid 1 \mid 1 \mid 1. \qquad (A.1.7)$$

In case that the polarization is perpendicular to the sample the final state needs to be antisymmetric, which gives a contradiction and is therefore dipole forbidden.

A.2 Dipole matrix element

The general light-matter interaction Hamiltonian as defined in Chap. 5 with inserted Bloch functions yields

$$H = -\frac{e}{Al_z}\sum_{\lambda,\lambda'}\sum_{\boldsymbol{k},\boldsymbol{k}',\boldsymbol{Q}} \boldsymbol{E}_{\boldsymbol{Q}}(z_0,t) \cdot \int d^3r \; e^{-i\boldsymbol{k}\cdot\boldsymbol{r}_\parallel} u^*_{\lambda,\boldsymbol{k}}(\boldsymbol{r}) \; \boldsymbol{r} \; e^{i\boldsymbol{Q}\cdot\boldsymbol{r}_\parallel} \; e^{i\boldsymbol{k}'\cdot\boldsymbol{r}_\parallel} u_{\lambda',\boldsymbol{k}'}(\boldsymbol{r}) \; a^\dagger_{\lambda,\boldsymbol{k}} a_{\lambda',\boldsymbol{k}'},$$
$$(A.2.1)$$

where we pulled the quantization length l_z in z-direction out of the lattice periodic Bloch functions. Expanding the integral into a sum over elementary cells at the lattice vector $\boldsymbol{R}_n$: $\boldsymbol{r} \rightarrow \boldsymbol{r}_n + \boldsymbol{R}_n$ yields

$$H = -\frac{e}{Al_z}\sum_{\lambda,\lambda'}\sum_{\boldsymbol{k},\boldsymbol{k}',\boldsymbol{Q}} \boldsymbol{E}_{\boldsymbol{Q}}(z_0,t)$$

$$\times \sum_{\boldsymbol{R}_n} e^{i(\boldsymbol{k}'+\boldsymbol{Q}-\boldsymbol{k})\cdot\boldsymbol{R}_n} \int_{UC} d^3r \; e^{i(\boldsymbol{k}'+\boldsymbol{Q}-\boldsymbol{k})\cdot\boldsymbol{r}_{n\parallel}} u^*_{\lambda,\boldsymbol{k}}(\boldsymbol{r}_n) \; \boldsymbol{r}_n \; u_{\lambda',\boldsymbol{k}'}(\boldsymbol{r}_n) \; a^\dagger_{\lambda,\boldsymbol{k}} a_{\lambda',\boldsymbol{k}'}$$

$$- \frac{e}{Al_z}\sum_{\lambda,\lambda'}\sum_{\boldsymbol{k},\boldsymbol{k}',\boldsymbol{Q}} \boldsymbol{E}_{\boldsymbol{Q}}(z_0,t)$$

$$\times \sum_{\boldsymbol{R}_n} e^{i(\boldsymbol{k}'+\boldsymbol{Q}-\boldsymbol{k})\cdot\boldsymbol{R}_n}\boldsymbol{R}_n \int_{UC} d^3r \; e^{i(\boldsymbol{k}'+\boldsymbol{Q}-\boldsymbol{k})\cdot\boldsymbol{r}_{n\parallel}} u^*_{\lambda,\boldsymbol{k}}(\boldsymbol{r}_n) u_{\lambda',\boldsymbol{k}'}(\boldsymbol{r}_n) \; a^\dagger_{\lambda,\boldsymbol{k}} a_{\lambda',\boldsymbol{k}'}$$

$$= -e\frac{N}{Al_z}\sum_{\lambda,\lambda'}\sum_{\boldsymbol{k}',\boldsymbol{Q}} \boldsymbol{E}_{\boldsymbol{Q}}(z_0,t) \cdot \sum_{\boldsymbol{G}} \int_{UC} d^3r \; e^{i\boldsymbol{G}\cdot\boldsymbol{r}_{n\parallel}} u^*_{\lambda,\boldsymbol{k}'+\boldsymbol{Q}-\boldsymbol{G}}(\boldsymbol{r}_n) \; \boldsymbol{r}_n \; u_{\lambda',\boldsymbol{k}'}(\boldsymbol{r}_n) \; a^\dagger_{\lambda,\boldsymbol{k}'+\boldsymbol{Q}-\boldsymbol{G}} a_{\lambda',\boldsymbol{k}'}$$

$$- i\frac{e}{Al_z}\sum_{\lambda,\lambda'}\sum_{\boldsymbol{k},\boldsymbol{k}',\boldsymbol{Q}} \boldsymbol{E}_{\boldsymbol{Q}}(z_0,t)$$

$$\times \sum_{\boldsymbol{R}_n} \left(\nabla_{\boldsymbol{k}} e^{i(\boldsymbol{k}'+\boldsymbol{Q}-\boldsymbol{k})\cdot\boldsymbol{R}_n}\right) \int_{UC} d^3r \; e^{i(\boldsymbol{k}'+\boldsymbol{Q}-\boldsymbol{k})\cdot\boldsymbol{r}_{n\parallel}} u^*_{\lambda,\boldsymbol{k}}(\boldsymbol{r}_n) u_{\lambda',\boldsymbol{k}'}(\boldsymbol{r}_n) \; a^\dagger_{\lambda,\boldsymbol{k}} a_{\lambda',\boldsymbol{k}'}$$

$$
\begin{aligned}
= -e\frac{N}{Al_z}\sum_{\lambda,\lambda'}\sum_{\boldsymbol{k'},\boldsymbol{Q}}\boldsymbol{E_Q}(z_0,t)\cdot\sum_{\boldsymbol{G}}\int_{UC}d^3r\; e^{i\boldsymbol{G}\cdot\boldsymbol{r}_{n\parallel}}u^*_{\lambda,\boldsymbol{k'}+\boldsymbol{Q}-\boldsymbol{G}}(\boldsymbol{r}_n)\;\boldsymbol{r}_n\;u_{\lambda',\boldsymbol{k'}}(\boldsymbol{r}_n)\;a^\dagger_{\lambda,\boldsymbol{k'}+\boldsymbol{Q}-\boldsymbol{G}}a_{\lambda',\boldsymbol{k'}} \\
-ie\frac{N}{Al_z}\sum_{\lambda,\lambda'}\sum_{\boldsymbol{k},\boldsymbol{k'},\boldsymbol{Q}}\boldsymbol{E_Q}(z_0,t) \\
\times\sum_{\boldsymbol{G}}\left(\nabla_{\boldsymbol{k}}\delta_{\boldsymbol{k'}+\boldsymbol{Q}-\boldsymbol{k},\boldsymbol{G}}\right)\int_{UC}d^3r\; e^{i(\boldsymbol{k'}+\boldsymbol{Q}-\boldsymbol{k})\cdot\boldsymbol{r}_{n\parallel}}u^*_{\lambda,\boldsymbol{k}}(\boldsymbol{r}_n)u_{\lambda',\boldsymbol{k'}}(\boldsymbol{r}_n)\;a^\dagger_{\lambda,\boldsymbol{k}}a_{\lambda',\boldsymbol{k'}}\,, \quad\text{(A.2.2)}
\end{aligned}
$$

where we indexed $\boldsymbol{r}_n$ to clarify that the vector is defined locally in the nth Brillouin zone. Writing the $\boldsymbol{k}$-sum as integral and transforming the Kronecker delta to a delta function, we can exploit the product rule to obtain

$$
\begin{aligned}
H = &-e\frac{N}{Al_z}\sum_{\lambda,\lambda'}\sum_{\boldsymbol{k},\boldsymbol{k'},\boldsymbol{Q}}\boldsymbol{E_Q}(z_0,t)\cdot\sum_{\boldsymbol{G}}\int_{UC}d^3r\; e^{i\boldsymbol{G}\cdot\boldsymbol{r}_{n\parallel}}u^*_{\lambda,\boldsymbol{k'}+\boldsymbol{Q}-\boldsymbol{G}}(\boldsymbol{r}_n)\;\boldsymbol{r}_n\;u_{\lambda',\boldsymbol{k'}}(\boldsymbol{r}_n)\;a^\dagger_{\lambda,\boldsymbol{k'}+\boldsymbol{Q}-\boldsymbol{G}}a_{\lambda',\boldsymbol{k'}} \\
&-ie\frac{N}{Al_z}\sum_{\substack{\lambda,\lambda'\\\boldsymbol{k'},\boldsymbol{Q},\boldsymbol{G}}}\boldsymbol{E_Q}(z_0,t) \\
&\times\int d^2k\;\nabla_{\boldsymbol{k}}\left(\delta(\boldsymbol{k'}+\boldsymbol{Q}-\boldsymbol{k}-\boldsymbol{G})\int_{UC}d^3r\; e^{i(\boldsymbol{k'}+\boldsymbol{Q}-\boldsymbol{k})\cdot\boldsymbol{r}_{n\parallel}}u^*_{\lambda,\boldsymbol{k}}(\boldsymbol{r}_n)u_{\lambda',\boldsymbol{k'}}(\boldsymbol{r}_n)\right)\;a^\dagger_{\lambda,\boldsymbol{k}}a_{\lambda',\boldsymbol{k'}} \\
&+ie\frac{N}{Al_z}\sum_{\substack{\lambda,\lambda'\\\boldsymbol{k'},\boldsymbol{Q},\boldsymbol{G}}}\boldsymbol{E_Q}(z_0,t) \\
&\times\int d^2k\;\delta(\boldsymbol{k'}+\boldsymbol{Q}-\boldsymbol{k}-\boldsymbol{G})\int_{UC}d^3r\;\left(\nabla_{\boldsymbol{k}}e^{i(\boldsymbol{k'}+\boldsymbol{Q}-\boldsymbol{k})\cdot\boldsymbol{r}_{n\parallel}}\right)u^*_{\lambda,\boldsymbol{k}}(\boldsymbol{r}_n)u_{\lambda',\boldsymbol{k'}}(\boldsymbol{r}_n)\;a^\dagger_{\lambda,\boldsymbol{k}}a_{\lambda',\boldsymbol{k'}} \\
&+ie\frac{N}{Al_z}\sum_{\substack{\lambda,\lambda'\\\boldsymbol{k'},\boldsymbol{Q},\boldsymbol{G}}}\boldsymbol{E_Q}(z_0,t) \\
&\times\int d^2k\;\delta(\boldsymbol{k'}+\boldsymbol{Q}-\boldsymbol{k}-\boldsymbol{G})\int_{UC}d^3r\; e^{i(\boldsymbol{k'}+\boldsymbol{Q}-\boldsymbol{k})\cdot\boldsymbol{r}_{n\parallel}}\left(\nabla_{\boldsymbol{k}}u^*_{\lambda,\boldsymbol{k}}(\boldsymbol{r}_n)\right)u_{\lambda',\boldsymbol{k'}}(\boldsymbol{r}_n)\;a^\dagger_{\lambda,\boldsymbol{k}}a_{\lambda',\boldsymbol{k'}} \\
&+ie\frac{N}{Al_z}\sum_{\substack{\lambda,\lambda'\\\boldsymbol{k'},\boldsymbol{Q},\boldsymbol{G}}}\boldsymbol{E_Q}(z_0,t) \\
&\times\int d^2k\;\delta(\boldsymbol{k'}+\boldsymbol{Q}-\boldsymbol{k}-\boldsymbol{G})\int_{UC}d^3r\; e^{i(\boldsymbol{k'}+\boldsymbol{Q}-\boldsymbol{k})\cdot\boldsymbol{r}_{n\parallel}}u^*_{\lambda,\boldsymbol{k}}(\boldsymbol{r}_n)u_{\lambda',\boldsymbol{k'}}(\boldsymbol{r}_n)\left(\nabla_{\boldsymbol{k}}a^\dagger_{\lambda,\boldsymbol{k}}\right)a_{\lambda',\boldsymbol{k'}}\,. \\
&\quad\text{(A.2.3)}
\end{aligned}
$$

The second line vanishes at the boundaries and the results reads

$$
\begin{aligned}
H = &\;ie\frac{N}{Al_z}\sum_{\lambda,\lambda'}\sum_{\boldsymbol{k'},\boldsymbol{Q}}\boldsymbol{E_Q}(z_0,t) \\
&\times\sum_{\boldsymbol{G}}\int_{UC}d^3r\; e^{i\boldsymbol{G}\cdot\boldsymbol{r}_{n\parallel}}\left(\begin{pmatrix}\nabla_{\boldsymbol{k'}+\boldsymbol{Q}-\boldsymbol{G}}\\iz\end{pmatrix}u^*_{\lambda,\boldsymbol{k'}+\boldsymbol{Q}-\boldsymbol{G}}(\boldsymbol{r}_n)\right)u_{\lambda',\boldsymbol{k'}}(\boldsymbol{r}_n)\;a^\dagger_{\lambda,\boldsymbol{k'}+\boldsymbol{Q}-\boldsymbol{G}}a_{\lambda',\boldsymbol{k'}} \\
&+ie\frac{N}{Al_z}\sum_{\lambda,\lambda'}\sum_{\boldsymbol{k'},\boldsymbol{Q}}\boldsymbol{E_Q}(z_0,t) \\
&\times\sum_{\boldsymbol{G}}\int_{UC}d^3r\; e^{i\boldsymbol{G}\cdot\boldsymbol{r}_{n\parallel}}u^*_{\lambda,\boldsymbol{k'}+\boldsymbol{Q}-\boldsymbol{G}}(\boldsymbol{r}_n)u_{\lambda',\boldsymbol{k'}}(\boldsymbol{r}_n)\left(\nabla_{\boldsymbol{k'}+\boldsymbol{Q}-\boldsymbol{G}}a^\dagger_{\boldsymbol{k'}+\boldsymbol{Q}-\boldsymbol{G}}\right)a_{\boldsymbol{k'}}\,. \quad\text{(A.2.4)}
\end{aligned}
$$

Exploiting the periodicity of the Bloch factors in reciprocal space and their orthogonality yields the Hamiltonian

$$
\begin{aligned}
H = \sum_{\lambda,\lambda'} \sum_{\mathbf{k}',\mathbf{Q}} \boldsymbol{E}_{\mathbf{Q}}(z_0,t) \cdot \sum_{\mathbf{G}} \frac{ie}{V_{UC}} & \left[\int_{UC} d^3r \; e^{i\mathbf{G}\cdot\mathbf{r}_{n\|}} \left(\begin{pmatrix} \nabla_{\mathbf{k}'+\mathbf{Q}-\mathbf{G}} \\ iz \end{pmatrix} u^*_{\lambda,\mathbf{k}'+\mathbf{Q}-\mathbf{G}}(\mathbf{r}_n) \right) u_{\lambda',\mathbf{k}'}(\mathbf{r}_n) \right. \\
& \left. + V_{UC}\delta_{\lambda,\lambda'} \nabla_{\mathbf{k}'+\mathbf{Q}-\mathbf{G}} \right] a^\dagger_{\lambda,\mathbf{k}'+\mathbf{Q}-\mathbf{G}} a_{\lambda',\mathbf{k}'} \,.
\end{aligned}
\tag{A.2.5}
$$

with the unit cell volume $V_{UC} = V/N$. Taking the limit $\mathbf{Q} = \mathbf{G} = 0$ yields the Hamiltonian shown Chap. 2.

A.3 Energy and charge transfer matrix elements

A.3.1 Dexter transfer

Before deriving the Dexter matrix element, we define the heterostructure Coulomb potential. We introduce a layer index l. The Coulomb potential reads

$$
V^{ll'}_{\mathbf{q}} = \frac{e_0^2}{2\epsilon_0 A |\mathbf{q}| \epsilon^{ll'}_{\mathbf{q}}}; \quad \epsilon^{ll'}_{\mathbf{q}} = \begin{cases} \epsilon_{\mathbf{q}}, & l \neq l' \\ \epsilon^i_{\mathbf{q}}, & l = l' \equiv i \end{cases}
\tag{A.3.1}
$$

with $i = \{0,1\}$ for the two material layers. The dielectric functions read

$$
\epsilon_{\mathbf{q}} = \kappa g^0_{|\mathbf{q}|} g^1_{|\mathbf{q}|} f_{|\mathbf{q}|} \quad \text{and} \quad \epsilon^i_{\mathbf{q}} = \frac{\kappa g^{1-i}_{|\mathbf{q}|} f_{|\mathbf{q}|}}{\cosh(\delta_{1-i}|\mathbf{q}|/2) h^i_{|\mathbf{q}|}}
\tag{A.3.2}
$$

for the intra- and interlayer Coulomb potential, respectively. The abbreviations read

$$
\begin{aligned}
f_{\mathbf{q}} = 1 + \frac{1}{2} & \left((\frac{\kappa_0}{\kappa} + \frac{\kappa}{\kappa_0}) \tanh(\delta_0|\mathbf{q}|) + (\frac{\kappa_1}{\kappa} + \frac{\kappa}{\kappa_1}) \tanh(\delta_1|\mathbf{q}|) + (\frac{\kappa_0}{\kappa_1} \right. \\
& \left. + \frac{\kappa_1}{\kappa_0}) \tanh(d_0|\mathbf{q}|) \tanh(\delta_1|\mathbf{q}|) \right)
\end{aligned}
\tag{A.3.3}
$$

$$
h^i_{\mathbf{q}} = 1 + \frac{\kappa}{\kappa_i} \tanh(\delta_i|\mathbf{q}|) + \frac{\kappa}{\kappa_{1-i}} \tanh(\delta_{1-i}|\mathbf{q}|/2) + \frac{\kappa_i}{\kappa_{1-i}} \tanh(\delta_i|\mathbf{q}|) \tanh(\delta_{1-i}|\mathbf{q}|/2)
\tag{A.3.4}
$$

$$
g^i_{\mathbf{q}} = \frac{\cosh(\delta_i|\mathbf{q}|)}{\cosh(\delta_{1-i}|\mathbf{q}|/2)} \left(1 + \frac{\kappa}{\kappa_i} \tanh(\delta_i|\mathbf{q}|/2) \right).
\tag{A.3.5}
$$

The parameters are $\kappa_i = \sqrt{\epsilon^i_\| \epsilon^i_\perp}$ as dielectric environment of the material and κ for the dielectric background. Additionally, we define $\alpha_i = \sqrt{\epsilon^i_\| / \epsilon^i_\perp}$ and $\delta_i = \alpha_i d_i$ with the layer thickness d_i.

For the Dexter matrix element, we start from Eq. (3.14). We decompose the z and z' integration into two integrals over the two materials

$$
\begin{aligned}
V^{cvvc}_{\mathbf{k},\mathbf{q},\mathbf{k}',\mathbf{q}'} = \frac{1}{A} \sum_{\mathbf{K}} \delta_{\mathbf{k},\mathbf{q}'+\mathbf{K}} \delta_{\mathbf{q},\mathbf{k}'-\mathbf{K}} & \left(\int_W dz \int_W dz' \; \chi_c(z)\chi_v(z') V_{\mathbf{K}}(z,z') \right. \\
& + \int_W dz \int_G dz' \; \chi_c(z)\chi_v(z') V_{\mathbf{K}}(z,z') + \int_G dz \int_W dz' \; \chi_c(z)\chi_v(z') V_{\mathbf{K}}(z,z') \\
& \left. + \int_G dz \int_G dz' \; \chi_c(z)\chi_v(z') V_{\mathbf{K}}(z,z') \right).
\end{aligned}
\tag{A.3.6}
$$

Since the Coulomb potential varies only weakly in each layer, we take the Coulomb potential directly at the position of the layer $V_{\boldsymbol{K}}(z^{(')} = z_l)$ and take the potential out of the integral. Then, we write for the wave function overlap $\chi_{\lambda,l} = \int_l dz \, \chi_\lambda(z)$. When assuming that both layers contribute equally to the wave function overlap we can use $\chi_{\lambda,W} = \chi_{\lambda,G} = \chi_\lambda/2$ and obtain for the matrix element

$$V^{cvvc}_{\boldsymbol{k},\boldsymbol{q},\boldsymbol{k}',\boldsymbol{q}'} = \frac{1}{4A}\chi_c\chi_v \sum_{\boldsymbol{K}} \delta_{\boldsymbol{k},\boldsymbol{q}'+\boldsymbol{K}} \delta_{\boldsymbol{q},\boldsymbol{k}'-\boldsymbol{K}} V^{\text{Dex}}_{\boldsymbol{K}} \tag{A.3.7}$$

with

$$V^{\text{Dex}}_{\boldsymbol{K}} = V_{\boldsymbol{K}}(z_W, z'_W) + V_{\boldsymbol{K}}(z_W, z'_G) + V_{\boldsymbol{K}}(z_G, z'_W) + V_{\boldsymbol{K}}(z_G, z'_G) \,. \tag{A.3.8}$$

When reinserting into the Hamiltonian and resolving the momentum Kronecker we obtain

$$H = \sum_{\boldsymbol{k},\boldsymbol{q},\boldsymbol{K}} \frac{1}{4A}\chi_c\chi_v \sum_{\boldsymbol{K}} V^{\text{Dex}}_{\boldsymbol{K}+\boldsymbol{k}-\boldsymbol{q}} c^{\dagger W}_{\boldsymbol{k}+\boldsymbol{K}} v^{\dagger W}_{\boldsymbol{k}} v^W_{\boldsymbol{k}} c^G_{\boldsymbol{q}} + \text{H.c.} \tag{A.3.9}$$

Here, we indexed the operators according to the layers since due to momentum conservation the notation breaks down. At this point, the wave vectors are defined with respect to the Γ point in WSe$_2$ and graphene. We can shift the coordinate system on the K points by $\boldsymbol{k} \to \boldsymbol{K}_W + \boldsymbol{k}$, $\boldsymbol{q} \to \boldsymbol{K}_G + \boldsymbol{q}$. Together with an exciton basis we obtain

$$H = -\sum_{\boldsymbol{q},\boldsymbol{K}} \left(\frac{1}{4\sqrt{A}}\chi_c\chi_v \sum_{\boldsymbol{k}} \varphi^*_{\mu,\boldsymbol{K}_W+\boldsymbol{k}} V^{\text{Dex}}_{\boldsymbol{K}_W-\boldsymbol{K}_G+\boldsymbol{K}+\boldsymbol{k}-\boldsymbol{q}} \right) P^\dagger_{\mu,\boldsymbol{K}} R^{\boldsymbol{K}_G+\boldsymbol{q}}_{\boldsymbol{K}} + \text{H.c.} \tag{A.3.10}$$

When neglecting the local wave vector sum $\boldsymbol{K} + \boldsymbol{k} - \boldsymbol{q}$, which is way smaller than the distance $|\boldsymbol{K}_G - \boldsymbol{K}_W|$ we obtain the Dexter matrix element from the main text.

A.3.2 Phonon-assisted tunnel

We start from Eq. (3.23) and insert the compounds $a/b = (\lambda_{a/b}, \boldsymbol{k}_{a/b}, l_{a/b})$, and $c = (\boldsymbol{K}_c, \alpha_c, l_c)$, and use the selection rules

$$t^{\lambda_b\lambda_d l_b l_d}_{\boldsymbol{k}_b\boldsymbol{k}_d} = t^{\lambda_b\lambda_d l_b d_d} \delta^{l_b\bar{l}_d}_{\boldsymbol{k}_b\boldsymbol{k}_d} \delta_{\lambda_b\lambda_d} \quad \text{and} \quad g^{\lambda_a\lambda_d l_a l_d l_c}_{\boldsymbol{k}_a\boldsymbol{k}_d\boldsymbol{K}_c} = g^{\lambda_a\lambda_d l_a l_d l_c}_{\boldsymbol{K}_c} \delta^{l_a l_d}_{\lambda_a\lambda_d} \delta_{\boldsymbol{K}_c,\boldsymbol{k}_a-\boldsymbol{k}_d} \,. \tag{A.3.11}$$

We obtain

$$H = \frac{1}{2} \sum_{\lambda,\alpha,l,\boldsymbol{k},\boldsymbol{K}} \lambda^{\dagger\bar{l}}_{\boldsymbol{k}+\boldsymbol{K}} \lambda^l_{\boldsymbol{k}} \left(t^{\lambda\bar{l}l} g^{\bar{l}\alpha}_{\boldsymbol{K}} (\alpha^{\lambda\bar{l}l}_{\boldsymbol{k}} + \gamma^{\bar{l}\alpha}_{\boldsymbol{k},\boldsymbol{K}}) b^{\bar{l}\alpha}_{\boldsymbol{K}} + t^{\lambda\bar{l}l} g^{\bar{l}\alpha}_{\boldsymbol{K}} (\alpha^{\lambda\bar{l}l}_{\boldsymbol{k}} + \beta^{\bar{l}\alpha}_{\boldsymbol{k},\boldsymbol{K}}) b^{\dagger\bar{l}\alpha}_{-\boldsymbol{K}} \right)$$

$$- \frac{1}{2} \sum_{\lambda,\alpha,l,\boldsymbol{k},\boldsymbol{K}} \lambda^{\dagger\bar{l}}_{\boldsymbol{k}+\boldsymbol{K}} \lambda^l_{\boldsymbol{k}} \left(t^{\lambda l\bar{l}} g^{\lambda l\alpha}_{\boldsymbol{K}} (\alpha^{\lambda\bar{l}l}_{\boldsymbol{k}+\boldsymbol{K}} + \gamma^{\lambda\alpha}_{\boldsymbol{k},\boldsymbol{K}}) b^{l\alpha}_{\boldsymbol{K}} + t^{\lambda\bar{l}l} g^{\lambda l\alpha}_{\boldsymbol{K}} (\alpha^{\lambda\bar{l}l}_{\boldsymbol{k}+\boldsymbol{K}} + \beta^{\lambda l\alpha}_{\boldsymbol{k},\boldsymbol{K}}) b^{\dagger\bar{l}\alpha}_{-\boldsymbol{K}} \right) \tag{A.3.12}$$

with

$$\alpha^{\lambda ij}_{\boldsymbol{k}} = \frac{1}{\varepsilon^{\lambda i}_{\boldsymbol{k}} - \varepsilon^{\lambda j}_{\boldsymbol{k}}} \tag{A.3.13}$$

$$\beta^{\lambda i\alpha}_{\boldsymbol{k},\boldsymbol{K}} = \frac{1}{\varepsilon^{\lambda i}_{\boldsymbol{k}+\boldsymbol{K}} - \varepsilon^{\lambda i}_{\boldsymbol{k}} + \hbar\Omega^{i\alpha}_{-\boldsymbol{K}}} \tag{A.3.14}$$

$$\gamma^{\lambda i\alpha}_{\boldsymbol{k},\boldsymbol{K}} = \frac{1}{\varepsilon^{\lambda i}_{\boldsymbol{k}+\boldsymbol{K}} - \varepsilon^{\lambda i}_{\boldsymbol{k}} - \hbar\Omega^{i\alpha}_{\boldsymbol{K}}} \tag{A.3.15}$$

107

Carrying out the layer sum yields

$$
\begin{aligned}
H = {} & \frac{1}{2} \sum_{\lambda,\alpha,\boldsymbol{k},\boldsymbol{K}} \lambda^{\dagger W}_{\boldsymbol{k}+\boldsymbol{K}} \lambda^{G}_{\boldsymbol{k}} \left(t^{\lambda GW} g^{\lambda W\alpha}_{\boldsymbol{K}} (\alpha^{\lambda GW}_{\boldsymbol{k}} + \gamma^{\lambda W\alpha}_{\boldsymbol{k},\boldsymbol{K}}) b^{W\alpha}_{\boldsymbol{K}} + t^{\lambda GW} g^{\lambda W\alpha}_{\boldsymbol{K}} (\alpha^{\lambda GW}_{\boldsymbol{k}} + \beta^{\lambda W\alpha}_{\boldsymbol{k},\boldsymbol{K}}) b^{\dagger W\alpha}_{-\boldsymbol{K}} \right) \\
& - \frac{1}{2} \sum_{\lambda,\alpha,\boldsymbol{k},\boldsymbol{K}} \lambda^{\dagger G}_{\boldsymbol{k}+\boldsymbol{K}} \lambda^{W}_{\boldsymbol{k}} \left(t^{\lambda GW} g^{\lambda W\alpha}_{\boldsymbol{K}} (\alpha^{\lambda WG}_{\boldsymbol{k}} + \gamma^{\lambda W\alpha}_{\boldsymbol{k},\boldsymbol{K}}) b^{W\alpha}_{\boldsymbol{K}} + t^{\lambda GW} g^{\lambda W\alpha}_{\boldsymbol{K}} (\alpha^{\lambda WG}_{\boldsymbol{k}} + \beta^{\lambda W\alpha}_{\boldsymbol{k},\boldsymbol{K}}) b^{\dagger W\alpha}_{-\boldsymbol{K}} \right) \\
& + \frac{1}{2} \sum_{\lambda,\alpha,\boldsymbol{k},\boldsymbol{K}} \lambda^{\dagger G}_{\boldsymbol{k}+\boldsymbol{K}} \lambda^{W}_{\boldsymbol{k}} \left(t^{\lambda WG} g^{\lambda G\alpha}_{\boldsymbol{K}} (\alpha^{\lambda WG}_{\boldsymbol{k}} + \gamma^{\lambda G\alpha}_{\boldsymbol{k},\boldsymbol{K}}) b^{G\alpha}_{\boldsymbol{K}} + t^{\lambda WG} g^{\lambda G\alpha}_{\boldsymbol{K}} (\alpha^{\lambda WG}_{\boldsymbol{k}} + \beta^{\lambda G\alpha}_{\boldsymbol{k},\boldsymbol{K}}) b^{\dagger G\alpha}_{-\boldsymbol{K}} \right) \\
& - \frac{1}{2} \sum_{\lambda,\alpha,\boldsymbol{k},\boldsymbol{K}} \lambda^{\dagger W}_{\boldsymbol{k}+\boldsymbol{K}} \lambda^{G}_{\boldsymbol{k}} \left(t^{\lambda WG} g^{\lambda G\alpha}_{\boldsymbol{K}} (\alpha^{\lambda GW}_{\boldsymbol{k}} + \gamma^{\lambda G\alpha}_{\boldsymbol{k},\boldsymbol{K}}) b^{G\alpha}_{\boldsymbol{K}} + t^{\lambda WG} g^{\lambda G\alpha}_{\boldsymbol{K}} (\alpha^{\lambda GW}_{\boldsymbol{k}} + \beta^{\lambda G\alpha}_{\boldsymbol{k},\boldsymbol{K}}) b^{\dagger G\alpha}_{-\boldsymbol{K}} \right) .
\end{aligned}
\tag{A.3.16}
$$

We fix the momenta to the vicinity of the K point. The factor $\alpha^{c\bar{l}l}_{\boldsymbol{k}\approx K_l}$ can be read out from DFT calculations. For the prefactors $\beta^{\lambda l\alpha}_{\boldsymbol{k},\boldsymbol{K}}$ and $\gamma^{\lambda l\alpha}_{\boldsymbol{k},\boldsymbol{K}}$ we recognize that ΔE_{K_G} appears when WSe$_2$ phonons are involved and ΔE_{K_W} when graphene phonons are involved. The value of $\Delta E_{K_G} \approx 250\,\mathrm{meV}$ is large compared to the typical WSe$_2$ phonon energy of $30\,\mathrm{meV}$, and $\Delta E_{K_W} \approx 1\,\mathrm{eV}$ is large compared to the graphene phonon energy of $200\,\mathrm{meV}$. Therefore, the phonon energies can be neglected in $\beta^{\lambda l\alpha}_{\boldsymbol{k},\boldsymbol{K}}$ and $\gamma^{\lambda l\alpha}_{\boldsymbol{k},\boldsymbol{K}}$. These approximations yield the Hamiltonian in the main text.

A.3.3 Interlayer Meitner-Auger energy transfer

The Coulomb matrix elements reads

$$
\begin{aligned}
V^{\nu_1 \lambda_1 \lambda_2 \nu_2}_{\boldsymbol{q}_1,\boldsymbol{k}_1,\boldsymbol{k}_2,\boldsymbol{q}_2} &= \int d^3r \int d^3r' \; \Psi^*_{\nu_1,\boldsymbol{q}_1}(\boldsymbol{r}) \Psi^*_{\lambda_1,\boldsymbol{k}_1}(\boldsymbol{r}') V(\boldsymbol{r}-\boldsymbol{r}') \Psi_{\lambda_2,\boldsymbol{k}_2}(\boldsymbol{r}') \Psi_{\nu_2,\boldsymbol{q}_2}(\boldsymbol{r}) \\
&= \sum_{\boldsymbol{q}} V_{\boldsymbol{q}} \int d^3r \; \Psi^*_{\nu_1,\boldsymbol{q}_1}(\boldsymbol{r}) e^{i\boldsymbol{q}\cdot\boldsymbol{r}_\parallel} \Psi_{\nu_2,\boldsymbol{q}_2}(\boldsymbol{r}) \int d^3r' \; \Psi^*_{\lambda_1,\boldsymbol{k}_1}(\boldsymbol{r}') e^{-i\boldsymbol{q}\cdot\boldsymbol{r}'_\parallel} \Psi_{\lambda_2,\boldsymbol{k}_2}(\boldsymbol{r}') .
\end{aligned}
\tag{A.3.17}
$$

$V_{\boldsymbol{q}}$ corresponds to the interlayer Coulomb potential. First, we investigate the r-integral. For the TMDC we know that $\nu_1 \neq \nu_2$ due to the interband transition. We write

$$
\begin{aligned}
I^{\nu_1 \nu_2}_{\boldsymbol{q},\boldsymbol{q}_1,\boldsymbol{q}_2} &= \int d^3r \; \Psi^*_{\nu_1,\boldsymbol{q}_1}(\boldsymbol{r}) e^{i\boldsymbol{q}\cdot\boldsymbol{r}_\parallel} \Psi_{\nu_2,\boldsymbol{q}_2}(\boldsymbol{r}) \\
&= \sum_{\boldsymbol{R}} e^{i\boldsymbol{R}\cdot(\boldsymbol{q}-\boldsymbol{q}_1+\boldsymbol{q}_2)} \int_{UC} d^3r \; u^*_{\nu_1,\boldsymbol{q}_1}(\boldsymbol{r}) u_{\nu_2,\boldsymbol{q}_2}(\boldsymbol{r}) e^{i\boldsymbol{r}_\parallel\cdot(\boldsymbol{q}-\boldsymbol{q}_1+\boldsymbol{q}_2)} \\
&= \delta_{\boldsymbol{q}-\boldsymbol{q}_1+\boldsymbol{q}_2,0} \frac{N}{V} \int_{UC} d^3r \; u^*_{\nu_1,\boldsymbol{q}_1}(\boldsymbol{r}) u_{\nu_2,\boldsymbol{q}_2}(\boldsymbol{r}) \\
&= \delta_{\boldsymbol{q},\boldsymbol{q}_1-\boldsymbol{q}_2} \frac{1}{e} \boldsymbol{d}^{\nu_1 \nu_2}(\boldsymbol{q}_1 - \boldsymbol{q}_2)
\end{aligned}
\tag{A.3.18}
$$

with a $k \cdot p$-expansion for $\nu_1 \neq \nu_2$ in the last step. Next, we calculate the graphene integral, where $\lambda_1 = \lambda_2$ holds. We find

$$
\begin{aligned}
I_{q,k_1,k_2}^{\lambda_1\lambda_2} &= \int d^3r' \; \Psi_{\lambda_1,k_1}^*(\boldsymbol{r}')e^{-i\boldsymbol{q}\cdot\boldsymbol{r}'_\parallel}\Psi_{\lambda_2,k_2}(\boldsymbol{r}') \\
&= \sum_{\boldsymbol{R}} e^{i\boldsymbol{R}\cdot(-\boldsymbol{q}-\boldsymbol{k}_1+\boldsymbol{k}_2)} \int_{UC} d^3r' \; u_{\lambda_1,k_1}^*(\boldsymbol{r}')u_{\lambda_2,k_2}(\boldsymbol{r}')e^{i\boldsymbol{r}_\parallel\cdot(-\boldsymbol{q}+\boldsymbol{k}_1+\boldsymbol{k}_2)} \\
&= \delta_{-\boldsymbol{q}-\boldsymbol{k}_1+\boldsymbol{k}_2,0}\frac{N}{V}\int_{UC}d^3r' \; u_{\lambda_1,k_1}^*(\boldsymbol{r}')u_{\lambda_2,k_2}(\boldsymbol{r}') \\
&= \delta_{\boldsymbol{k}_2-\boldsymbol{k}_1,\boldsymbol{q}}\,,
\end{aligned}
\tag{A.3.19}
$$

where we treated the integral for $\lambda_1 = \lambda_2$ in a low wave number approximation corresponding to the zeroth order of the $k \cdot p$ expansion.

A.4 Slater-Koster tight binding method

For the Hamiltonian we need the electronic hopping between different atomic orbitals at different interatomic distances. σ and π bondings are defined such that the axes of the involved p orbitals are parallel and normal to the interatomic vector, respectively. The hopping integrals for p orbitals are parameterized into parallel and normal component to the bonding directions. We need to decompose the Cartesian p orbital into the bond-parallel and the bond-normal p orbital.

We start with the projection of s-p integrals. Let $\hat{\boldsymbol{\delta}}$ be the unit vector along the bond from the first to the second atom. Let $\hat{\boldsymbol{e}}$ be the unit vector along the Cartesian axes. We first decompose p orbitals along $\hat{\boldsymbol{e}}$ into two p orbitals that are parallel and normal to $\hat{\boldsymbol{\delta}}$:

$$
|p_i\rangle = \hat{\boldsymbol{e}} \cdot \hat{\boldsymbol{\delta}}|p_\delta\rangle + \hat{\boldsymbol{e}} \cdot \hat{\boldsymbol{n}}|p_n\rangle
\tag{A.4.1}
$$

with $i \in \{x, y, z\}$. The unit vector $\hat{\boldsymbol{n}}$ perpendicular to $\hat{\boldsymbol{\delta}}$. The relation $\langle s|H|p\rangle = -\langle p|H|s\rangle$ is simply obtained by inverting the direction of the bonding unit vector, i.e. changing the sign of the directional cosines.

We continue with the projection of p-p integrals. This time we consider two unit vectors for the coordinate system and the bond between two atoms. The p orbital along $\hat{\boldsymbol{a}}_1$ can be decomposed into two p orbitals that are parallel and normal to $\hat{\boldsymbol{\delta}}$:

$$
|p_i\rangle = \hat{\boldsymbol{e}}_1 \cdot \hat{\boldsymbol{\delta}}|p_{\delta_1}\rangle + \hat{\boldsymbol{e}}_1 \cdot \hat{\boldsymbol{n}}_1|p_{n_1}\rangle\,,
\tag{A.4.2}
$$

where the unit vector $\hat{\boldsymbol{n}}$ normal to $\hat{\boldsymbol{\delta}}$ within the plane spanned by $\boldsymbol{\delta}$ and $\boldsymbol{a}_1$. We define the origins of $|p_{\delta_1}\rangle$ and $|p_{n_1}\rangle$ to be at the first atom. The second p orbital can be handled in a similar manner. Then we obtain

$$
\begin{aligned}
\langle p_1|H|p_2\rangle &= (\hat{\boldsymbol{e}}_1 \cdot \hat{\boldsymbol{\delta}}\langle p_{\delta_1}| + \hat{\boldsymbol{e}}_1 \cdot \hat{\boldsymbol{n}}_1\langle p_{n_1}|)H(\hat{\boldsymbol{e}}_2 \cdot \hat{\boldsymbol{\delta}}|p_{\delta_2}\rangle + \hat{\boldsymbol{e}}_2 \cdot \hat{\boldsymbol{n}}_2|p_{n_2}\rangle) \\
&= (\hat{\boldsymbol{e}}_1 \cdot \hat{\boldsymbol{\delta}})(\hat{\boldsymbol{e}}_2 \cdot \hat{\boldsymbol{\delta}})\langle p_{\delta_1}|H|p_{\delta_2}\rangle + (\hat{\boldsymbol{e}}_1 \cdot \hat{\boldsymbol{n}}_1\langle p_{n_1}|)H(\hat{\boldsymbol{e}}_2 \cdot \hat{\boldsymbol{n}}_2|p_{n_2}\rangle)
\end{aligned}
\tag{A.4.3}
$$

with the matrix element between orthogonal p orbitals as zero. We define $\langle p_{\delta_1}|H|p_{\delta_2}\rangle = V_{pp\sigma}$ and write

$$
(\hat{\boldsymbol{e}}_1 \cdot \hat{\boldsymbol{n}}_1\langle p_{n_1}|)H(\hat{\boldsymbol{e}}_2 \cdot \hat{\boldsymbol{n}}_2|p_{n_2}\rangle) = ((\hat{\boldsymbol{e}}_1 \cdot \hat{\boldsymbol{n}}_1)((\hat{\boldsymbol{e}}_2 \cdot \hat{\boldsymbol{n}}_2)\langle p_{n_1}|H|p_{n_2}\rangle
\tag{A.4.4}
$$

$$
= (\hat{\boldsymbol{e}}_1 \cdot \hat{\boldsymbol{n}}_1)((\hat{\boldsymbol{e}}_2 \cdot \hat{\boldsymbol{n}}_2))(\hat{\boldsymbol{n}}_1 \cdot \hat{\boldsymbol{n}}_2)t_\pi
\tag{A.4.5}
$$

$$
= ((\hat{\boldsymbol{e}}_1 \cdot \hat{\boldsymbol{n}}_1)\hat{\boldsymbol{n}}_1) \cdot ((\hat{\boldsymbol{e}}_2 \cdot \hat{\boldsymbol{n}}_2)\hat{\boldsymbol{n}}_2)\,t_\pi
\tag{A.4.6}
$$

$$
= \left(\hat{\boldsymbol{e}}_1 - (\hat{\boldsymbol{e}}_1 \cdot \hat{\boldsymbol{\delta}})\hat{\boldsymbol{\delta}}\right) \cdot \left(\hat{\boldsymbol{e}}_2 - (\hat{\boldsymbol{e}}_2 \cdot \hat{\boldsymbol{\delta}})\hat{\boldsymbol{\delta}}\right)t_\pi
\tag{A.4.7}
$$
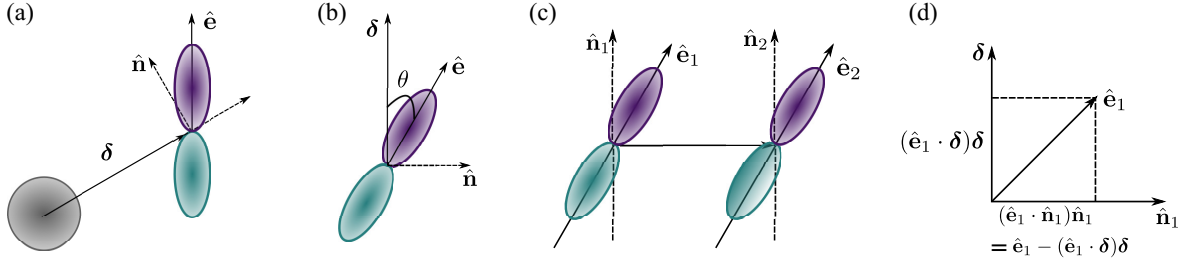
Figure A.4.1: (a) Decomposition of a p-orbital. (b) Angle θ between the vectors $\boldsymbol{\delta}$ and $\hat{\boldsymbol{e}}$. (c) Side view of vector $\boldsymbol{\delta}$. (d) Sketch of the used relation for hoppings between two p orbitals.

We end up with

$$\langle p_1|H|p_2\rangle = (\hat{\boldsymbol{e}}_1 \cdot \hat{\boldsymbol{\delta}})(\hat{\boldsymbol{e}}_2 \cdot \hat{\boldsymbol{\delta}})V_{pp\sigma} + \left(\hat{\boldsymbol{e}}_1 - (\hat{\boldsymbol{e}}_1 \cdot \hat{\boldsymbol{\delta}})\hat{\boldsymbol{\delta}}\right) \cdot \left(\hat{\boldsymbol{e}}_2 - (\hat{\boldsymbol{e}}_2 \cdot \hat{\boldsymbol{\delta}})\hat{\boldsymbol{\delta}}\right) t_\pi. \tag{A.4.8}$$

For example, we can calculate now

$$\begin{aligned}
\langle 2p_x|H|2p_y\rangle &= \cos\theta_1 \sin\theta_2 V_{pp\sigma} + (\hat{\boldsymbol{e}}_1 - \cos\theta_1\boldsymbol{\delta}) \cdot (\hat{\boldsymbol{e}}_2 - \sin\theta_2\boldsymbol{\delta})t_\pi \\
&= \cos\theta_1 \sin\theta_2 V_{pp\sigma} + (\hat{\boldsymbol{e}}_1 \cdot \hat{\boldsymbol{e}}_2 - \hat{\boldsymbol{e}}_1 \cdot \boldsymbol{\delta}\sin\theta_1 - \hat{\boldsymbol{e}}_2 \cdot \boldsymbol{\delta}\cos\theta_1 + \cos\theta_1\sin\theta_2\boldsymbol{\delta} \cdot \boldsymbol{\delta})t_\pi \\
&= \cos\theta_1 \sin\theta_2 V_{pp\sigma} + (-\cos\theta_1\sin\theta_1 - \sin\theta_2\cos\theta_1 + \cos\theta_1\sin\theta_2) \\
&= \cos\theta_1 \sin\theta_2 V_{pp\sigma} - \cos\theta_1\sin\theta_2 t_\pi \\
&= (V_{pp\sigma} - t_\pi)\cos\theta\sin\theta. \tag{A.4.9}
\end{aligned}$$

The other integrals can be treated in similar manner.

A.5 Integrals

A.5.1 XANES offsite transition integral

We start by calculating the $1s$-$2p_z$ transition:

$$\boldsymbol{d}_{\text{off}} = \int d^3r \; \phi_{1s} \begin{pmatrix} x \\ y \\ z \end{pmatrix} \boldsymbol{r} \; \phi_{2p_z} \begin{pmatrix} x - \delta\cos\vartheta \\ y - \delta\sin\vartheta \\ z \end{pmatrix}. \tag{A.5.1}$$

First, we shift the dipole moment between the atoms of sublattice A and B by $\boldsymbol{r} \to \boldsymbol{r} - \boldsymbol{\delta}/2$

$$\boldsymbol{d}_{\text{off}} = \int d^3r \; \phi_{1s}(\boldsymbol{r}) \begin{pmatrix} x - \frac{\delta}{2}\cos\vartheta \\ y - \frac{\delta}{2}\sin\vartheta \\ z \end{pmatrix} \phi_{2p_z} \begin{pmatrix} x - \delta\cos\vartheta \\ y - \delta\sin\vartheta \\ z \end{pmatrix}. \tag{A.5.2}$$

Then, we rotate the coordinate system in direction of $\boldsymbol{\delta}$ and shift $x' \to x' + \delta/2$, where the prime indicates the new coordinate system. We obtain

$$\boldsymbol{d}_{\text{off}} = \int d^3r \; \phi_{1s} \begin{pmatrix} (x' + \frac{\delta}{2})\cos\vartheta - y'\sin\vartheta \\ (x' + \frac{\delta}{2})\sin\vartheta + y'\cos\vartheta \\ z \end{pmatrix} \begin{pmatrix} x'\cos\vartheta - y'\sin\vartheta \\ x'\sin\vartheta + y'\cos\vartheta \\ z \end{pmatrix}$$

$$\times \phi_{2p_z} \begin{pmatrix} (x' - \frac{\delta}{2})\cos\vartheta - y'\sin\vartheta \\ (x' - \frac{\delta}{2})\sin\vartheta + y'\cos\vartheta \\ z \end{pmatrix}. \tag{A.5.3}$$

110

We define the radii $r_1 = \left[\left(x' - \frac{\delta}{2}\right)^2 + y'^2 + z'^2\right]^{1/2}$ and $r_2 = \left[\left(x' + \frac{\delta}{2}\right)^2 + y'^2 + z'^2\right]^{1/2}$. Then, we introduce the prolate spheroidal coordinates $\xi = (r_1 + r_2)/\delta$ and $\eta = (r_1 - r_2)/\delta$. This yields $r_1 = \frac{\delta}{2}(\xi + \eta)$ and $r_2 = \frac{\delta}{2}(\xi - \eta)$. Now $\phi_i(\xi, \eta)$ is defined. For our coordinate system, the Cartesian coordinates as function of prolate spheroidal coordinates are $z = \frac{\delta}{2}\sqrt{(\xi^2 - 1)(1 - \eta^2)}\cos\phi$, $y = \frac{\delta}{2}\sqrt{(\xi^2 - 1)(1 - \eta^2)}\sin\phi$ and $x = \frac{\delta}{2}\xi\eta$. Inserting the hydrogen-type orbitals we see that the angle-integral eliminates the x and y components. The z-component of the integral reads in prolate spheroidal coordinates

$$
\begin{aligned}
d_{\text{off}}^{\perp} = {}& N_{1s}N_{2p_z}\left(\frac{\delta}{2}\right)^5 \int_1^\infty \int_{-1}^1 \int_0^{2\pi} d\xi d\eta d\phi\, (\xi^2 - \eta^2)e^{-\zeta_{1s}\delta(\xi-\eta)/2}e^{-\zeta_{2p}\delta(\xi+\eta)/4} \\
& \times (\xi^2 - 1)(1 - \eta^2)\cos^2\phi \\
= {}& N_{1s}N_{2p_z}\left(\frac{\delta}{2}\right)^5 \pi \int_1^\infty \int_{-1}^1 d\xi d\eta\, (\xi^2 - \eta^2)e^{-\zeta_{1s}\delta(\xi-\eta)/2}e^{-\zeta_{2p}\delta(\xi+\eta)/4}(\xi^2 - 1)(1 - \eta^2),
\end{aligned}
$$
$$(A.5.4)$$

where N_{1s} and N_{2p_z} are the normalization constants of the hydrogen-like orbitals. The left integral is only a sum of integrals consisting of a product of exponential functions, which can easily be evaluated. We find

$$
\boldsymbol{d}_{\text{off}} = \begin{pmatrix} 0 \\ 0 \\ 0.14 \end{pmatrix} \text{pm}.
$$
$$(A.5.5)$$

After having shown the concept, we evaluate also the $1s$-$2p_x$ integral. The first steps are identical. We shift the dipole moment into the center of the atoms, rotate the coordinate system and introduce prolate spheroidal coordinates. We end up with

$$
\begin{aligned}
\boldsymbol{d}_{\text{off}} = {}& N_{1s}N_{2p_x} \int \int \int_0^{2\pi} d\xi d\eta d\phi\, \left(\frac{\delta}{2}\right)^3 (\xi^2 - \eta^2)e^{-\zeta_{1s}\delta(\xi-\eta)/2}e^{-\zeta_{2p}\delta(\xi+\eta)/4} \\
& \times \begin{pmatrix} \frac{\delta}{2}\xi\eta\cos\vartheta - \frac{\delta}{2}\sqrt{(\xi^2 - 1)(1 - \eta^2)}\sin\phi\sin\vartheta \\ \frac{\delta}{2}\xi\eta\sin\vartheta + \frac{\delta}{2}\sqrt{(\xi^2 - 1)(1 - \eta^2)}\sin\phi\cos\vartheta \\ \frac{\delta}{2}\sqrt{(\xi^2 - 1)(1 - \eta^2)}\cos\phi \end{pmatrix} \\
& \times \left[\left(\frac{\delta}{2}\xi\eta - \frac{\delta}{2}\right)\cos\vartheta - \frac{\delta}{2}\sqrt{(\xi^2 - 1)(1 - \eta^2)}\sin\phi\sin\vartheta\right]
\end{aligned}
$$
$$(A.5.6)$$

$$
\begin{aligned}
\boldsymbol{d}_{\text{off}} = {}& N_{1s}N_{2p}\left(\frac{\delta}{2}\right)^5 \pi \int_1^\infty \int_{-1}^1 d\xi d\eta\, (\xi^2 - \eta^2)e^{-\zeta_{1s}\delta(\xi-\eta)/2}e^{-\zeta_{2p}\delta(\xi+\eta)/4} \\
& \times \begin{pmatrix} 2\xi\eta(\xi\eta - 1)\cos^2\vartheta + (\xi^2 - 1)(1 - \eta^2)\sin^2\vartheta \\ 2\xi\eta(\xi\eta - 1)\sin\vartheta\cos\vartheta - (\xi^2 - 1)(1 - \eta^2)\sin\vartheta\cos\vartheta \\ 0 \end{pmatrix}.
\end{aligned}
$$
$$(A.5.7)$$

Alternatively, we can write

$$
\begin{aligned}
\boldsymbol{d}_{\text{off}} = {}& N_{1s}N_{2p}\left(\frac{\delta}{2}\right)^5 \pi \begin{pmatrix} \cos^2\vartheta & \sin^2\vartheta & 0 \\ \cos\vartheta\sin\vartheta & -\sin\vartheta\cos\vartheta & 0 \\ 0 & 0 & 1 \end{pmatrix} \\
& \times \int_1^\infty \int_{-1}^1 d\xi d\eta\, (\xi^2 - \eta^2)e^{-\zeta_{1s}\delta(\xi-\eta)/2}e^{-\zeta_{2p}\delta(\xi+\eta)/4} \begin{pmatrix} 2\xi\eta(\xi\eta - 1) \\ (\xi^2 - 1)(1 - \eta^2) \\ 0 \end{pmatrix}
\end{aligned}
$$
$$(A.5.8)$$

The last two integrals can again easily be evaluate, yielding the result Eq. (38). The integrals involving the $2s$ and $2p_y$ can be calculated analogously.

A.5.2 EXAFS transition integral

Next, we calculate the remaining integral in Eq. (5.14) for $j = 1s$. We substitute $(\boldsymbol{k} + \boldsymbol{G}) + k_\perp \hat{\boldsymbol{e}}_z = \boldsymbol{p}$ and write

$$\boldsymbol{I}(\boldsymbol{p}) = \int d^3r \ \phi_{1s}(\boldsymbol{r}) \ \boldsymbol{r} \ e^{i\boldsymbol{p}\cdot\boldsymbol{r}} \, . \tag{A.5.9}$$

In spherical coordinates we can substitute for the x-component $\sin\vartheta\cos\varphi = -\sqrt{2\pi/3}(Y_{11}(\vartheta,\varphi) - Y_{1-1}(\vartheta,\varphi))$, for the y-component $\sin\vartheta\sin\varphi = i\sqrt{2\pi/3}(Y_{11}(\vartheta,\varphi) + Y_{1-1}(\vartheta,\varphi))$, and for the z-component $\cos\vartheta = \sqrt{4\pi/3}Y_{10}(\vartheta,\varphi)$. We calculate exemplary the z-component:

$$I_z = \frac{8\pi}{\sqrt{3}}\zeta^{3/2} \int dr \ r^3 e^{-\zeta r} \sum_l \sum_{m=-l}^{l} i^l j_l(pr) Y_{lm}(\theta,\phi) \int\int d\vartheta d\varphi \ \sin\vartheta \ Y_{l'm'}^*(\vartheta,\varphi) Y_{lm}^*(\vartheta,\varphi)$$

$$= \frac{8\pi}{\sqrt{3}}\zeta^{3/2} \int dr \ r^3 e^{-\zeta r} \sum_l \sum_{m=-l}^{l} (-1)^m i^l j_l(pr) Y_{lm}(\theta,\phi) \int\int d\vartheta d\varphi \ \sin\vartheta \ Y_{l'm'}^*(\vartheta,\varphi) Y_{lm}(\vartheta,\varphi)$$

$$= \frac{8\pi}{\sqrt{3}}\zeta^{3/2} i^{l'} Y_{l'm'}(\theta,\phi) \int dr \ r^3 j_{l'}(pr) e^{-\zeta r} \, , \tag{A.5.10}$$

where we exploited in the last step the orthogonality of the spherical harmonics. Next, we insert $l' = 1$ and $m' = 0$:

$$\begin{aligned} I_z &= \frac{8\pi}{\sqrt{3}}\zeta^{3/2} i Y_{10}(\theta,\phi) \int dr \ r^3 j_1(pr) e^{-\zeta r} \\ &= \frac{8\pi}{\sqrt{3}}\zeta^{3/2} i Y_{10}(\theta,\phi) \frac{8\zeta p}{(\zeta^2 + p^2)^3} \\ &= 32\sqrt{\pi}\zeta^{5/2} i \frac{k_z}{(\zeta^2 + (\boldsymbol{k} + \boldsymbol{G})^2)^3} \, . \end{aligned} \tag{A.5.11}$$

The x and y-components can be obtained analogously.

A.5.3 Onsite transition integral beyond the dipole approximation

Here, we calculate the z-polarized optical onsite transition between $1s$ and $2p_z$ orbital beyond the electric dipole approximation:

$$d_{\text{on}}^\perp(\boldsymbol{Q}) = \int d^3r \ \phi_{1s}(\boldsymbol{r}) z \phi_{2p_z}(\boldsymbol{r}) e^{i\boldsymbol{Q}\cdot\boldsymbol{r}_\parallel} \, . \tag{A.5.12}$$

For reasons of simplicity, we drop the index β. First, we extend the integral into the third dimension. We stress that $\boldsymbol{k}$ and $\boldsymbol{G}$ are now three-dimensional. Writing $\phi_{1s}(\boldsymbol{r})z = \phi_{1s}(r,\vartheta,\varphi) r \cos\vartheta = \tilde{R}_{21}(r) Y_{10}(\vartheta,\varphi)$ with $\tilde{R}_{21}(r) = \sqrt{4/3}\zeta^{3/2} r \exp(-\zeta r)$ and using $\exp(i\boldsymbol{Q} \cdot \boldsymbol{r}) = 4\pi \sum_{l=0}^{\infty} \sum_{m=-l}^{l} i^l j_l(Qr) Y_{lm}^*(\theta,\phi) Y_{lm}(\vartheta,\varphi)$ we obtain generally

$$d_{\text{on}}^\perp = 4\pi \int_0^\infty \int_0^\pi \int_0^{2\pi} dr d\vartheta d\varphi \ r^2 \sin\vartheta \sum_{l=0}^{\infty} \sum_{m=-l}^{l} i^l j_l(Qr) R_{n_1 l_1}(r) R_{n_2 l_2}(r) Y_{l_1 m_1}^*(\vartheta,\varphi) Y_{l_2 m_2}(\vartheta,\varphi)$$

$$\times Y_{lm}^*(\vartheta,\varphi) Y_{lm}(\theta,\phi) \, , \tag{A.5.13}$$

where θ and ϕ are the polar and azimuthal angles of the light wave vector. The angular integral yields

$$
\int\int d\vartheta d\varphi \ \sin\vartheta Y^*_{l_1 m_1}(\vartheta,\varphi) Y_{l_2 m_2}(\vartheta,\varphi) Y^*_{lm}(\vartheta,\varphi) = \int\int d\vartheta d\varphi \ \sin\vartheta Y^*_{lm}(\vartheta,\varphi)
$$

$$
\times \sum_{L=|l_1-l_2|}^{l_1+l_2} \sum_{M=-L}^{L} \sqrt{\frac{(2l_1+1)(2l_2+1)(2L+1)}{4\pi}} \begin{bmatrix} l_1 & l_2 & L \\ 0 & 0 & 0 \end{bmatrix} \begin{bmatrix} l_1 & l_2 & L \\ m_1 & m_2 & M \end{bmatrix} Y^*_{LM}(\vartheta,\varphi)
$$

$$
= \int\int d\vartheta d\varphi \ \sin\vartheta (-1)^m Y_{l,-m}(\vartheta,\varphi) \sum_{L=|l_1-l_2|}^{l_1+l_2} \sum_{M=-L}^{L} \sqrt{\frac{(2l_1+1)(2l_2+1)(2L+1)}{4\pi}}
$$

$$
\times \begin{bmatrix} l_1 & l_2 & L \\ 0 & 0 & 0 \end{bmatrix} \begin{bmatrix} l_1 & l_2 & L \\ m_1 & m_2 & M \end{bmatrix} Y^*_{LM}(\vartheta,\varphi)
$$

$$
= (-1)^{m_2} \sum_{L=|l_1-l_2|} \sqrt{\frac{(2L+1)(2l_1+1)(2l_2+1)}{4\pi}} \begin{bmatrix} l_1 & l_2 & L \\ 0 & 0 & 0 \end{bmatrix} \begin{bmatrix} l_1 & l_2 & L \\ m_1 & m_2 & m_1-m_2 \end{bmatrix} \delta_{l,L}\delta_{m,m_2-m_1}
$$

$$(A.5.14)$$

where we used the orthogonality of the spherical harmonics and the Wigner 3j-symbols. We have now

$$
d^\perp_{\mathrm{on}}(Q,\theta,\phi) = (-1)^{m_2} \sum_{L=|l_1-l_2|}^{l_1+l_2} \sqrt{(2L+1)(2l_1+1)(2l_2+1)} \begin{bmatrix} l_1 & l_2 & L \\ 0 & 0 & 0 \end{bmatrix} \begin{bmatrix} l_1 & l_2 & L \\ m_1 & m_2 & m_1-m_2 \end{bmatrix}
$$

$$
\times I^L(Q) Y_{L,m_2-m_1}(\theta,\phi) \tag{A.5.15}
$$

with

$$
I^L(Q) = i^L 8\sqrt{\pi} \frac{(\zeta_1 \zeta_2)^{3/2}}{n_1^2 n_2^2} \sqrt{(n_1-l_1-1)!(n_1+l_1)!(n_2-l_2-1)!(n_2+n_2)!} \times
$$

$$
\times \sum_{s_1=0}^{n_1-l_1-1} \sum_{s_2=0}^{n_2-l_2-1} \frac{(-1)^{s_1+s_2}(2\zeta_1/n_1)^{l_1+s_1}(2\zeta_2/n_2)^{l_2+s_2} I_{L\omega}(\gamma,Q)}{s_1!(n_1-l_1-s_1-1)!(s_1+2l_1+1)!s_2!(n_2-l_2-s_2-1)!(s_2+2l_2+1)!}
$$

$$(A.5.16)$$

with inserted radial functions and

$$
I_{L\omega}(\gamma,Q) = \int_0^\infty dr \ r^{\omega+2} e^{-\gamma r} j_L(Qr) = \sqrt{\frac{\pi}{2Q}} \frac{\Gamma(L+\omega+3)}{(\gamma^2+Q^2)^{(\omega+5/2)/2}} P^{-(L+1/2)}_{\omega+3/2}[\gamma(\gamma^2+Q^2)^{-1/2}]
$$

$$(A.5.17)$$

where $P^\mu_\nu(x)$ stands for the associated Legendre polynomial, $\gamma = \zeta_1/n_1 + \zeta_2/n_2$ and $\omega = l_1 + s_1 + l_2 + s_2 \geq L$. Now, we have to insert the wave functions for the $2p_z$ orbitals $\phi_{2p_z} = R_{21}(r) Y_{10}(\vartheta,\varphi)$ and obtain

$$
d^\perp_{\mathrm{on}} = \frac{1}{2\sqrt{\pi}} \left(I^0(Q) + (3\cos^2\theta - 1) I^2(Q) \right) \tag{A.5.18}
$$

$$
\text{with} \quad I^0(Q) = \frac{\sqrt{\pi}}{12} (\zeta_1 \zeta_2)^{5/2} I_{02}(\zeta_1/2 + \zeta_2/2, Q) \quad \text{and}
$$

$$
I^2(Q) = -\frac{\sqrt{\pi}}{12} (\zeta_1 \zeta_2)^{5/2} I_{22}(\zeta_1/2 + \zeta_2/2, Q). \tag{A.5.19}
$$

Note that $\zeta_1 = 2Z/a_B = 2\zeta$ and $\zeta_2 = Z/a_B = \zeta$. We find

$$d_{\text{on}}^{\perp} = \frac{3}{2} \frac{(2\zeta^2)^{5/2}\zeta}{((\frac{3\zeta}{2})^2 + Q^2)^4} \left(\frac{9}{4}\zeta^2 - 2Q^2 - 3Q^2 \cos(2\theta) \right) . \tag{A.5.20}$$

Going back to the two-dimensional case $\theta = \pi/2$ and multiplying with a constant $N = 4\sqrt{6}\pi/(3\zeta)$ that $N\phi_{2p_z} = z\phi_{1s}$, we obtain finally

$$d_{\text{on}}^{\perp}(Q_{\parallel}) = \frac{16\sqrt{3\pi}\zeta^5}{\left(\left(\frac{3\zeta}{2}\right)^2 + Q_{\parallel}^2 \right)^3} \tag{A.5.21}$$

A.6   Parameters

Table 3: Electronic TMDC parameters and the free electron mass $m_0 = 5.68568\,\text{fs}^2\text{eV}/\text{nm}^2$. The parameters stem from the references [140], [8], and [336].

Parameter	Symbol	WSe$_2$	MoSe$_2$	WS$_2$	MoS$_2$
Lattice constant	a_0/nm	0.332	0.332	0.318	0.319
Thickness	d_0/nm	0.347	0.344	0.315	0.312
Electron mass	$m_c^{\uparrow K}/m_0$	0.29	0.50	0.27	0.44
Electron mass	$m_c^{\uparrow \Lambda}/m_0$	0.56	0.71	0.62	0.81
Hole mass	$m_v^{\uparrow K}/m_0$	0.36	0.6	0.36	0.54
Dielectric constant	ϵ	13.63	15.27	11.75	13.36
Plasmon energy peak	E_{pl}/eV	22.6	22.0	22.8	22.5

The phonon parameters can be found in the references [113], [104], and [105].

Table 4: Electronic parameters for graphene from the references [166], [315], [337], and [314].

Parameter	Symbol	Graphene
Lattice constant	a_0/nm	0.246
Fermi velocity	v_F fs/nm	1
Core binding energy	$\varepsilon_{1s}/\text{eV}$	-283.0
2s onsite energy	$\varepsilon_{2s}/\text{eV}$	8.7
2p onsite energy	$\varepsilon_{2p}/\text{eV}$	0.0
2p$_z$-2p$_z$ hopping	t_π/eV	-3.1
2s-2s hopping	$V_{ss\sigma}/\text{eV}$	-6.7
2s-2p$_{x/y}$ hopping	$V_{sp\sigma}/\text{eV}$	-5.5
2p$_{x/y}$-2p$_{x/y}$ hopping	$V_{pp\sigma}/\text{eV}$	5.1

Bibliography

[1] K. E. Drexler, "Nanotechnology: from feynman to funding," *Bulletin of Science, Technology & Society*, vol. 24, no. 1, pp. 21–27, 2004.

[2] K. S. Novoselov, A. K. Geim, S. V. Morozov, D.-e. Jiang, Y. Zhang, S. V. Dubonos, I. V. Grigorieva, and A. A. Firsov, "Electric field effect in atomically thin carbon films," *science*, vol. 306, no. 5696, pp. 666–669, 2004.

[3] K. F. Mak, C. Lee, J. Hone, J. Shan, and T. F. Heinz, "Atomically thin mos 2: a new direct-gap semiconductor," *Physical review letters*, vol. 105, no. 13, p. 136805, 2010.

[4] A. Splendiani, L. Sun, Y. Zhang, T. Li, J. Kim, C.-Y. Chim, G. Galli, and F. Wang, "Emerging photoluminescence in monolayer mos2," *Nano letters*, vol. 10, no. 4, pp. 1271–1275, 2010.

[5] S. Lebegue and O. Eriksson, "Electronic structure of two-dimensional crystals from ab initio theory," *Physical Review B*, vol. 79, no. 11, p. 115409, 2009.

[6] T. Cheiwchanchamnangij and W. R. Lambrecht, "Quasiparticle band structure calculation of monolayer, bilayer, and bulk mos 2," *Physical Review B*, vol. 85, no. 20, p. 205302, 2012.

[7] R. Roldán, J. A. Silva-Guillén, M. P. López-Sancho, F. Guinea, E. Cappelluti, and P. Ordejón, "Electronic properties of single-layer and multilayer transition metal dichalcogenides mx2 (m= mo, w and x= s, se)," *Annalen der Physik*, vol. 526, no. 9-10, pp. 347–357, 2014.

[8] T. C. Berkelbach, M. S. Hybertsen, and D. R. Reichman, "Theory of neutral and charged excitons in monolayer transition metal dichalcogenides," *Physical Review B*, vol. 88, no. 4, p. 045318, 2013.

[9] A. Chernikov, T. C. Berkelbach, H. M. Hill, A. Rigosi, Y. Li, O. B. Aslan, D. R. Reichman, M. S. Hybertsen, and T. F. Heinz, "Exciton binding energy and nonhydrogenic rydberg series in monolayer ws 2," *Physical review letters*, vol. 113, no. 7, p. 076802, 2014.

[10] G. Berghäuser and E. Malic, "Analytical approach to excitonic properties of mos 2," *Physical Review B*, vol. 89, no. 12, p. 125309, 2014.

[11] X. Liu, T. Galfsky, Z. Sun, F. Xia, E.-c. Lin, Y.-H. Lee, S. Kéna-Cohen, and V. M. Menon, "Strong light–matter coupling in two-dimensional atomic crystals," *Nature Photonics*, vol. 9, no. 1, pp. 30–34, 2015.

[12] D. Xiao, G.-B. Liu, W. Feng, X. Xu, and W. Yao, "Coupled spin and valley physics in monolayers of mos 2 and other group-vi dichalcogenides," *Physical review letters*, vol. 108, no. 19, p. 196802, 2012.

[13] A. Molina-Sánchez, D. Sangalli, K. Hummer, A. Marini, and L. Wirtz, "Effect of spin-orbit interaction on the optical spectra of single-layer, double-layer, and bulk mos 2," *Physical Review B*, vol. 88, no. 4, p. 045412, 2013.

[14] H. Zeng, J. Dai, W. Yao, D. Xiao, and X. Cui, "Valley polarization in mos 2 monolayers by optical pumping," *Nature nanotechnology*, vol. 7, no. 8, pp. 490–493, 2012.

[15] T. Cao, G. Wang, W. Han, H. Ye, C. Zhu, J. Shi, Q. Niu, P. Tan, E. Wang, B. Liu, *et al.*, "Valley-selective circular dichroism of monolayer molybdenum disulphide," *Nature communications*, vol. 3, no. 1, pp. 1–5, 2012.

[16] K. F. Mak, K. He, J. Shan, and T. F. Heinz, "Control of valley polarization in monolayer mos 2 by optical helicity," *Nature nanotechnology*, vol. 7, no. 8, pp. 494–498, 2012.

[17] X. Xu, W. Yao, D. Xiao, and T. F. Heinz, "Spin and pseudospins in layered transition metal dichalcogenides," *Nature Physics*, vol. 10, no. 5, pp. 343–350, 2014.

[18] M. Gmitra and J. Fabian, "Proximity effects in bilayer graphene on monolayer wse 2: field-effect spin valley locking, spin-orbit valve, and spin transistor," *Physical review letters*, vol. 119, no. 14, p. 146401, 2017.

[19] T. Zhou, J. Zhang, H. Jiang, I. Žutić, and Z. Yang, "Giant spin-valley polarization and multiple hall effect in functionalized bismuth monolayers," *npj Quantum Materials*, vol. 3, no. 1, pp. 1–7, 2018.

[20] J. Lindlau, M. Selig, A. Neumann, L. Colombier, J. Förste, V. Funk, M. Förg, J. Kim, G. Berghäuser, T. Taniguchi, *et al.*, "The role of momentum-dark excitons in the elementary optical response of bilayer wse 2," *Nature communications*, vol. 9, no. 1, pp. 1–7, 2018.

[21] M. Feierabend, G. Berghäuser, M. Selig, S. Brem, T. Shegai, S. Eigler, and E. Malic, "Molecule signatures in photoluminescence spectra of transition metal dichalcogenides," *Physical Review Materials*, vol. 2, no. 1, p. 014004, 2018.

[22] Z. Khatibi, M. Feierabend, M. Selig, S. Brem, C. Linderälv, P. Erhart, and E. Malic, "Impact of strain on the excitonic linewidth in transition metal dichalcogenides," *2D Materials*, vol. 6, no. 1, p. 015015, 2018.

[23] A. Raja, M. Selig, G. Berghauser, J. Yu, H. M. Hill, A. F. Rigosi, L. E. Brus, A. Knorr, T. F. Heinz, E. Malic, *et al.*, "Enhancement of exciton–phonon scattering from monolayer to bilayer ws2," *Nano letters*, vol. 18, no. 10, pp. 6135–6143, 2018.

[24] R. Rosati, K. Wagner, S. Brem, R. Perea-Causin, E. Wietek, J. Zipfel, J. D. Ziegler, M. Selig, T. Taniguchi, K. Watanabe, *et al.*, "Temporal evolution of low-temperature phonon sidebands in transition metal dichalcogenides," *ACS Photonics*, vol. 7, no. 10, pp. 2756–2764, 2020.

[25] M. Selig, F. Katsch, S. Brem, G. F. Mkrtchian, E. Malic, and A. Knorr, "Suppression of intervalley exchange coupling in the presence of momentum-dark states in transition metal dichalcogenides," *Physical Review Research*, vol. 2, no. 2, p. 023322, 2020.

[26] M. Puppin, Y. Deng, C. Nicholson, J. Feldl, N. Schröter, H. Vita, P. Kirchmann, C. Monney, L. Rettig, M. Wolf, *et al.*, "Time-and angle-resolved photoemission spectroscopy of solids in the extreme ultraviolet at 500 khz repetition rate," *Review of Scientific Instruments*, vol. 90, no. 2, p. 023104, 2019.

[27] A. K. Geim and I. V. Grigorieva, "Van der waals heterostructures," *Nature*, vol. 499, no. 7459, pp. 419–425, 2013.

[28] K. Novoselov, o. A. Mishchenko, o. A. Carvalho, and A. C. Neto, "2d materials and van der waals heterostructures," *Science*, vol. 353, no. 6298, 2016.

[29] Y. K. Luo, J. Xu, T. Zhu, G. Wu, E. J. McCormick, W. Zhan, M. R. Neupane, and R. K. Kawakami, "Opto-valleytronic spin injection in monolayer mos2/few-layer graphene hybrid spin valves," *Nano letters*, vol. 17, no. 6, pp. 3877–3883, 2017.

[30] Y. Cao, V. Fatemi, S. Fang, K. Watanabe, T. Taniguchi, E. Kaxiras, and P. Jarillo-Herrero, "Unconventional superconductivity in magic-angle graphene superlattices," *Nature*, vol. 556, no. 7699, pp. 43–50, 2018.

[31] M. Gmitra and J. Fabian, "Graphene on transition-metal dichalcogenides: A platform for proximity spin-orbit physics and optospintronics," *Physical Review B*, vol. 92, no. 15, p. 155403, 2015.

[32] S. Bertolazzi, D. Krasnozhon, and A. Kis, "Nonvolatile memory cells based on mos2/graphene heterostructures," *ACS nano*, vol. 7, no. 4, pp. 3246–3252, 2013.

[33] A. Avsar, J. Y. Tan, T. Taychatanapat, J. Balakrishnan, G. Koon, Y. Yeo, J. Lahiri, A. Carvalho, A. Rodin, E. O'Farrell, *et al.*, "Spin–orbit proximity effect in graphene," *Nature communications*, vol. 5, no. 1, pp. 1–6, 2014.

[34] M. Lv, J. J. Jasieniak, J. Zhu, and X. Chen, "A hybrid organic–inorganic three-dimensional cathode interfacial material for organic solar cells," *RSC advances*, vol. 7, no. 45, pp. 28513–28519, 2017.

[35] L. Krieg, F. Meierhofer, S. Gorny, S. Leis, D. Splith, Z. Zhang, H. von Wenckstern, M. Grundmann, X. Wang, J. Hartmann, *et al.*, "Toward three-dimensional hybrid inorganic/organic optoelectronics based on gan/ocvd-pedot structures," *Nature communications*, vol. 11, no. 1, pp. 1–10, 2020.

[36] D. Ban, S. Han, Z. Lu, A. J. SpringThorpe, and H. Liu, "Inorganic/organic hybrid optical upconversion device," in *2007 Conference on Lasers and Electro-Optics (CLEO)*, pp. 1–2, IEEE, 2007.

[37] R. Knox, *Solid state physics, suppl. 5: Theory of excitons.* Academic Press, 1963.

[38] H. Cercellier, C. Monney, F. Clerc, C. Battaglia, L. Despont, M. Garnier, H. Beck, P. Aebi, L. Patthey, H. Berger, *et al.*, "Evidence for an excitonic insulator phase in 1 t-tise 2," *Physical review letters*, vol. 99, no. 14, p. 146403, 2007.

[39] Y. Wakisaka, T. Sudayama, K. Takubo, T. Mizokawa, M. Arita, H. Namatame, M. Taniguchi, N. Katayama, M. Nohara, and H. Takagi, "Excitonic insulator state in ta 2 nise 5 probed by photoemission spectroscopy," *Physical review letters*, vol. 103, no. 2, p. 026402, 2009.

[40] L. Ma, P. X. Nguyen, Z. Wang, Y. Zeng, K. Watanabe, T. Taniguchi, A. H. MacDonald, K. F. Mak, and J. Shan, "Strongly correlated excitonic insulator in atomic double layers," *arXiv preprint arXiv:2104.05066*, 2021.

[41] J. Gu, L. Ma, S. Liu, K. Watanabe, T. Taniguchi, J. C. Hone, J. Shan, and K. F. Mak, "Dipolar excitonic insulator in a moire lattice," *arXiv preprint arXiv:2108.06588*, 2021.

[42] Z. Zhang, E. C. Regan, D. Wang, W. Zhao, S. Wang, M. Sayyad, K. Yumigeta, K. Watanabe, T. Taniguchi, S. Tongay, *et al.*, "Correlated interlayer exciton insulator in double layers of monolayer wse2 and moir\'e ws2/wse2," *arXiv preprint arXiv:2108.07131*, 2021.

[43] O. Lundquist, "Über die kβ-linien in den röntgenemissionsspektra der elemente phosphor und kalium," *Zeitschrift für Physik*, vol. 33, no. 1, pp. 901–915, 1925.

[44] D. Coster and M. Druyvesteyn, "Über die satelliten der röntgendiagrammlinien," *Zeitschrift für Physik*, vol. 40, no. 10, pp. 765–774, 1927.

[45] J. Röhler, "Handbook on the physics and chemistry of rare earths," *edited by KA Gschneider Jr, L. Eyring and S. H üfner)(North-Holland, Amsterdam 1987)*, vol. 10, 1987.

[46] G. A. Lindsay and H. Voorhees, "Lxxxix. the k x-ray absorption edge of iron," *The London, Edinburgh, and Dublin Philosophical Magazine and Journal of Science*, vol. 6, no. 38, pp. 910–920, 1928.

[47] D. Coster and M. Wolf, "The fine structure of x-ray absorption edges," *Nature*, vol. 124, no. 3130, pp. 652–653, 1929.

[48] B. Kievit and G. A. Lindsay, "Fine structure in the x-ray absorption spectra of the k series of the elements calcium to gallium," *Physical Review*, vol. 36, no. 4, p. 648, 1930.

[49] J. Hanawalt, "The dependence of x-ray absorption spectra upon chemical and physical state," *Physical Review*, vol. 37, no. 6, p. 715, 1931.

[50] R. d. L. Kronig, "Zur theorie der feinstruktur in den röntgenabsorptionsspektren," *Zeitschrift für Physik*, vol. 70, no. 5-6, pp. 317–323, 1931.

[51] R. d. L. Kronig, "Zur theorie der feinstruktur in den röntgenabsorptionsspektren. iii," *Zeitschrift für Physik*, vol. 75, no. 7, pp. 468–475, 1932.

[52] D. Sayers, F. Lytle, and E. Stern, "Point scattering theory of x-ray k-absorption fine structure," *Advances in X-ray Analysis*, vol. 13, pp. 248–271, 1969.

[53] D. E. Sayers, E. A. Stern, and F. W. Lytle, "New technique for investigating noncrystalline structures: Fourier analysis of the extended x-ray—absorption fine structure," *Physical review letters*, vol. 27, no. 18, p. 1204, 1971.

[54] D. Briggs and J. T. Grant, *Surface analysis by Auger and X-ray photoelectron spectroscopy.* SurfaceSpectra, 2012.

[55] R. Fink, R. Jopson, H. Mark, and C. Swift, "Atomic fluorescence yields," *Reviews of Modern Physics*, vol. 38, no. 3, p. 513, 1966.

[56] Y.-Y. Luk, N. L. Abbott, J. N. Crain, and F. J. Himpsel, "Dipole-induced structure in aromatic-terminated self-assembled monolayers—a study by near edge x-ray absorption fine structure spectroscopy," *The Journal of chemical physics*, vol. 120, no. 22, pp. 10792–10798, 2004.

[57] P. S. Johnson, J. M. García-Lastra, C. K. Kennedy, N. J. Jersett, I. Boukahil, F. Himpsel, and P. L. Cook, "Crystal fields of porphyrins and phthalocyanines from polarization-dependent 2p-to-3d multiplets," *The Journal of chemical physics*, vol. 140, no. 11, p. 114706, 2014.

[58] M. Cardona and Y. Y. Peter, *Fundamentals of semiconductors*, vol. 619. Springer, 2005.

[59] C. Kittel and C.-y. Fong, *Quantum theory of solids*, vol. 5. Wiley New York, 1963.

[60] W. A. Harrison, "Pseudopotentials in the theory of metals," *1966, 336 P. W. A. BENJAMIN, INC., NEW YORK*, 1966.

[61] U. Von Barth and C. Gelatt, "Validity of the frozen-core approximation and pseudopotential theory for cohesive energy calculations," *Physical Review B*, vol. 21, no. 6, p. 2222, 1980.

[62] M. Born and R. Oppenheimer, "Zur quantentheorie der molekeln," *Annalen der physik*, vol. 389, no. 20, pp. 457–484, 1927.

[63] M. Tinkham, *Group theory and quantum mechanics.* Courier Corporation, 2003.

[64] E. Dobardžić, M. Dimitrijević, and M. Milovanović, "Generalized bloch theorem and topological characterization," *Physical Review B*, vol. 91, no. 12, p. 125424, 2015.

[65] M. Kira and S. W. Koch, *Semiconductor quantum optics.* Cambridge University Press, 2011.

[66] H. Haug and S. W. Koch, *Quantum theory of the optical and electronic properties of semiconductors.* World Scientific Publishing Company, 2009.

[67] C. Herring, "A new method for calculating wave functions in crystals," *Physical Review*, vol. 57, no. 12, p. 1169, 1940.

[68] J. Callaway, "Orthogonalized plane wave method," *Physical Review*, vol. 97, no. 4, p. 933, 1955.

[69] T. O. Woodruff, "The orthogonalized plane-wave method," in *Solid state physics*, vol. 4, pp. 367–411, Elsevier, 1957.

[70] M. Schüler, U. De Giovannini, H. Hübener, A. Rubio, M. A. Sentef, T. P. Devereaux, and P. Werner, "How circular dichroism in time-and angle-resolved photoemission can be used to spectroscopically detect transient topological states in graphene," *Physical Review X*, vol. 10, no. 4, p. 041013, 2020.

[71] J. H. Ryoo and C.-H. Park, "Momentum-dependent spin selection rule in photoemission with glide symmetry," *Physical Review B*, vol. 98, no. 23, p. 235403, 2018.

[72] C. Caroli, D. Lederer-Rozenblatt, B. Roulet, and D. Saint-James, "Inelastic effects in photoemission: microscopic formulation and qualitative discussion," *Physical Review B*, vol. 8, no. 10, p. 4552, 1973.

[73] P. J. Feibelman and D. Eastman, "Photoemission spectroscopy—correspondence between quantum theory and experimental phenomenology," *Physical Review B*, vol. 10, no. 12, p. 4932, 1974.

[74] G. Mahan, "Theory of photoemission in simple metals," *Physical Review B*, vol. 2, no. 11, p. 4334, 1970.

[75] E. Perfetto, S. Bianchi, and G. Stefanucci, "Time-resolved arpes spectra of nonequilibrium excitonic insulators: Revealing macroscopic coherence with ultrashort pulses," *Physical Review B*, vol. 101, no. 4, p. 041201, 2020.

[76] J. B. Pendry, *Low energy electron diffraction: the theory and its application to determination of surface structure*. 2, Academic Press, 1974.

[77] A. Liebsch, "Theory of angular resolved photoemission from adsorbates," *Physical Review Letters*, vol. 32, no. 21, p. 1203, 1974.

[78] J. Pendtry, "Angular dependence of electron emission from surfaces," *Journal of Physics C: Solid State Physics*, vol. 8, no. 15, p. 2413, 1975.

[79] M. Schüler, Y. Pavlyukh, and J. Berakdar, "Nuclear-wave-packet dynamics mapped out by two-center interference in the he h 2+ molecule," *Physical Review A*, vol. 89, no. 6, p. 063421, 2014.

[80] M. D. Schwartz, *Quantum field theory and the standard model*. Cambridge University Press, 2014.

[81] W. Nolting and W. D. Brewer, *Fundamentals of Many-body Physics*. Springer, 2008.

[82] W. Greiner and J. Reinhardt, *Field quantization*. Springer Science & Business Media, 2013.

[83] C. Cohen-Tannoudji, J. Dupont-Roc, and G. Grynberg, *Atom-photon interactions: basic processes and applications*. John Wiley & Sons, 1998.

[84] T. C. Berkelbach, M. S. Hybertsen, and D. R. Reichman, "Bright and dark singlet excitons via linear and two-photon spectroscopy in monolayer transition-metal dichalcogenides," *Physical Review B*, vol. 92, no. 8, p. 085413, 2015.

[85] M. Glazov, L. Golub, G. Wang, X. Marie, T. Amand, and B. Urbaszek, "Intrinsic exciton-state mixing and nonlinear optical properties in transition metal dichalcogenide monolayers," *Physical Review B*, vol. 95, no. 3, p. 035311, 2017.

[86] D. Golde, T. Meier, and S. W. Koch, "High harmonics generated in semiconductor nanostructures by the coupled dynamics of optical inter-and intraband excitations," *Physical Review B*, vol. 77, no. 7, p. 075330, 2008.

[87] P. Földi, "Gauge invariance and interpretation of interband and intraband processes in high-order harmonic generation from bulk solids," *Physical Review B*, vol. 96, no. 3, p. 035112, 2017.

[88] W. Schäfer and M. Wegener, *Semiconductor optics and transport phenomena*. Springer Science & Business Media, 2013.

[89] D. Golde, M. Kira, T. Meier, and S. W. Koch, "Microscopic theory of the extremely nonlinear terahertz response of semiconductors," *physica status solidi (b)*, vol. 248, no. 4, pp. 863–866, 2011.

[90] W. Vogel and D.-G. Welsch, *Quantum optics.* John Wiley & Sons, 2006.

[91] N. Koch, S. Duhm, J. P. Rabe, A. Vollmer, and R. L. Johnson, "Optimized hole injection with strong electron acceptors at organic-metal interfaces," *Physical review letters*, vol. 95, no. 23, p. 237601, 2005.

[92] N. S. Rytova, "The screened potential of a point charge in a thin film," *Moscow University Physics Bulletin*, vol. 3, no. 3, p. 18, 1967.

[93] L. Keldysh, "Coulomb interaction in thin semiconductor and semimetal films," *Soviet Journal of Experimental and Theoretical Physics Letters*, vol. 29, p. 658, 1979.

[94] P. Cudazzo, I. V. Tokatly, and A. Rubio, "Dielectric screening in two-dimensional insulators: Implications for excitonic and impurity states in graphane," *Physical Review B*, vol. 84, no. 8, p. 085406, 2011.

[95] D. Van Tuan, M. Yang, and H. Dery, "Coulomb interaction in monolayer transition-metal dichalcogenides," *Physical Review B*, vol. 98, no. 12, p. 125308, 2018.

[96] M. L. Trolle, T. G. Pedersen, and V. Véniard, "Model dielectric function for 2d semiconductors including substrate screening," *Scientific reports*, vol. 7, no. 1, pp. 1–9, 2017.

[97] G. Cappellini, R. Del Sole, L. Reining, and F. Bechstedt, "Model dielectric function for semiconductors," *Physical Review B*, vol. 47, no. 15, p. 9892, 1993.

[98] S. Latini, T. Olsen, and K. S. Thygesen, "Excitons in van der waals heterostructures: The important role of dielectric screening," *Physical Review B*, vol. 92, no. 24, p. 245123, 2015.

[99] F. Katsch, *Theory of exciton-exciton interactions in monolayer transition metal dichalcogenides.* Technische Universitaet Berlin (Germany), 2020.

[100] K. Andersen, S. Latini, and K. S. Thygesen, "Dielectric genome of van der waals heterostructures," *Nano letters*, vol. 15, no. 7, pp. 4616–4621, 2015.

[101] T. Basak and A. Shukla, "Optical signatures of electric-field-driven magnetic phase transitions in graphene quantum dots," *Physical Review B*, vol. 93, no. 23, p. 235432, 2016.

[102] K. S. Thygesen, "Calculating excitons, plasmons, and quasiparticles in 2d materials and van der waals heterostructures," *2D Materials*, vol. 4, no. 2, p. 022004, 2017.

[103] K. Kaasbjerg, K. S. Thygesen, and K. W. Jacobsen, "Phonon-limited mobility in n-type single-layer mos 2 from first principles," *Physical Review B*, vol. 85, no. 11, p. 115317, 2012.

[104] X. Li, J. T. Mullen, Z. Jin, K. M. Borysenko, M. B. Nardelli, and K. W. Kim, "Intrinsic electrical transport properties of monolayer silicene and mos 2 from first principles," *Physical Review B*, vol. 87, no. 11, p. 115418, 2013.

[105] Z. Jin, X. Li, J. T. Mullen, and K. W. Kim, "Intrinsic transport properties of electrons and holes in monolayer transition-metal dichalcogenides," *Physical Review B*, vol. 90, no. 4, p. 045422, 2014.

[106] S. Baroni, S. De Gironcoli, A. Dal Corso, and P. Giannozzi, "Phonons and related crystal properties from density-functional perturbation theory," *Reviews of modern Physics*, vol. 73, no. 2, p. 515, 2001.

[107] J. Bardeen and W. Shockley, "Deformation potentials and mobilities in non-polar crystals," *Physical review*, vol. 80, no. 1, p. 72, 1950.

[108] G. D. Mahan, *9. Many-Particle Systems.* Princeton University Press, 2008.

[109] K. Kaasbjerg, K. S. Thygesen, and A.-P. Jauho, "Acoustic phonon limited mobility in two-dimensional semiconductors: Deformation potential and piezoelectric scattering in monolayer mos 2 from first principles," *Physical Review B*, vol. 87, no. 23, p. 235312, 2013.

[110] H. Peelaers and C. G. Van de Walle, "Effects of strain on band structure and effective masses in mos 2," *Physical Review B*, vol. 86, no. 24, p. 241401, 2012.

[111] K. He, C. Poole, K. F. Mak, and J. Shan, "Experimental demonstration of continuous electronic structure tuning via strain in atomically thin mos2," *Nano letters*, vol. 13, no. 6, pp. 2931–2936, 2013.

[112] H. J. Conley, B. Wang, J. I. Ziegler, R. F. Haglund Jr, S. T. Pantelides, and K. I. Bolotin, "Bandgap engineering of strained monolayer and bilayer mos2," *Nano letters*, vol. 13, no. 8, pp. 3626–3630, 2013.

[113] M. Selig, *Exciton-phonon coupling in monolayers of transition metal dichalcogenides.* Technische Universitaet Berlin (Germany), 2018.

[114] H. Hertz, "Ueber einen einfluss des ultravioletten lichtes auf die electrische entladung," *Annalen der Physik*, vol. 267, no. 8, pp. 983–1000, 1887.

[115] A. Einstein, "Über einem die erzeugung und verwandlung des lichtes betreffenden heuristischen gesichtspunkt," *Annalen der physik*, vol. 4, 1905.

[116] A. Damascelli, Z. Hussain, and Z.-X. Shen, "Angle-resolved photoemission studies of the cuprate superconductors," *Reviews of modern physics*, vol. 75, no. 2, p. 473, 2003.

[117] R. Haight, J. Bokor, J. Stark, R. Storz, R. Freeman, and P. Bucksbaum, "Picosecond time-resolved photoemission study of the inp (110) surface," *Physical review letters*, vol. 54, no. 12, p. 1302, 1985.

[118] R. Haight and J. Silberman, "Surface intervalley scattering on gaas (110): direct observation with picosecond laser photoemission," *Physical review letters*, vol. 62, no. 7, p. 815, 1989.

[119] S.-D. Chen, M. Hashimoto, Y. He, D. Song, K.-J. Xu, J.-F. He, T. P. Devereaux, H. Eisaki, D.-H. Lu, J. Zaanen, *et al.*, "Incoherent strange metal sharply bounded by a critical doping in bi2212," *Science*, vol. 366, no. 6469, pp. 1099–1102, 2019.

[120] A. Tamai, W. Meevasana, P. King, C. Nicholson, A. De La Torre, E. Rozbicki, and F. Baumberger, "Spin-orbit splitting of the shockley surface state on cu (111)," *Physical Review B*, vol. 87, no. 7, p. 075113, 2013.

[121] I. Cucchi, A. Marrazzo, E. Cappelli, S. Riccò, F. Bruno, S. Lisi, M. Hoesch, T. Kim, C. Cacho, C. Besnard, *et al.*, "Bulk and surface electronic structure of the dual-topology semimetal pt 2 hgse 3," *Physical review letters*, vol. 124, no. 10, p. 106402, 2020.

[122] J. L. Webb, L. S. Hart, D. Wolverson, C. Chen, J. Avila, and M. C. Asensio, "Electronic band structure of res 2 by high-resolution angle-resolved photoemission spectroscopy," *Physical Review B*, vol. 96, no. 11, p. 115205, 2017.

[123] J. Lobo-Checa, J. E. Ortega, A. Mascaraque, E. G. Michel, and E. E. Krasovskii, "Effect of photoelectron mean free path on the photoemission cross-section of cu (111) and ag (111) shockley states," *Physical Review B*, vol. 84, no. 24, p. 245419, 2011.

[124] J. Minár, S. Mankovsky, J. Braun, and H. Ebert, "One-step model of photoemission at finite temperatures: Spin fluctuations of fe (001)," *Physical Review B*, vol. 102, no. 3, p. 035107, 2020.

[125] D. Christiansen, M. Selig, E. Malic, R. Ernstorfer, and A. Knorr, "Theory of exciton dynamics in time-resolved arpes: Intra-and intervalley scattering in two-dimensional semiconductors," *Physical Review B*, vol. 100, no. 20, p. 205401, 2019.

[126] R. Bertoni, C. W. Nicholson, L. Waldecker, H. Hübener, C. Monney, U. De Giovannini, M. Puppin, M. Hoesch, E. Springate, R. T. Chapman, *et al.*, "Generation and evolution of spin-, valley-, and layer-polarized excited carriers in inversion-symmetric wse 2," *Physical review letters*, vol. 117, no. 27, p. 277201, 2016.

[127] C. Papp, L. Plucinski, J. Minar, J. Braun, H. Ebert, C. Schneider, and C. Fadley, "Band mapping in x-ray photoelectron spectroscopy: An experimental and theoretical study of w (110) with 1.25 kev excitation," *Physical Review B*, vol. 84, no. 4, p. 045433, 2011.

[128] S. Hüfner, *Photoelectron spectroscopy: principles and applications.* Springer Science & Business Media, 2013.

[129] J. Ribeiro-Soares, R. Almeida, E. B. Barros, P. T. Araujo, M. S. Dresselhaus, L. G. Cançado, and A. Jorio, "Group theory analysis of phonons in two-dimensional transition metal dichalcogenides," *Physical Review B*, vol. 90, no. 11, p. 115438, 2014.

[130] Q. H. Wang, K. Kalantar-Zadeh, A. Kis, J. N. Coleman, and M. S. Strano, "Electronics and optoelectronics of two-dimensional transition metal dichalcogenides," *Nature nanotechnology*, vol. 7, no. 11, pp. 699–712, 2012.

[131] D. Jariwala, V. K. Sangwan, L. J. Lauhon, T. J. Marks, and M. C. Hersam, "Emerging device applications for semiconducting two-dimensional transition metal dichalcogenides," *ACS nano*, vol. 8, no. 2, pp. 1102–1120, 2014.

[132] G. Wang, A. Chernikov, M. M. Glazov, T. F. Heinz, X. Marie, T. Amand, and B. Urbaszek, "Colloquium: Excitons in atomically thin transition metal dichalcogenides," *Reviews of Modern Physics*, vol. 90, no. 2, p. 021001, 2018.

[133] R. Dong and I. Kuljanishvili, "Progress in fabrication of transition metal dichalcogenides heterostructure systems," *Journal of Vacuum Science & Technology B, Nanotechnology and Microelectronics: Materials, Processing, Measurement, and Phenomena*, vol. 35, no. 3, p. 030803, 2017.

[134] O. M. Van't Erve, A. T. Hanbicki, A. L. Friedman, K. M. McCreary, E. Cobas, C. H. Li, J. T. Robinson, and B. T. Jonker, "Graphene and monolayer transition-metal dichalcogenides: properties and devices," *Journal of Materials Research*, vol. 31, no. 7, pp. 845–877, 2016.

[135] S. Ahmed and J. Yi, "Two-dimensional transition metal dichalcogenides and their charge carrier mobilities in field-effect transistors," *Nano-micro letters*, vol. 9, no. 4, pp. 1–23, 2017.

[136] F. Manghi, G. Riegler, C. M. Bertoni, and G. Bachelet, "Band-structure calculation for gaas and si beyond the local-density approximation," *Physical Review B*, vol. 31, no. 6, p. 3680, 1985.

[137] M. Koshino and E. McCann, "Parity and valley degeneracy in multilayer graphene," *Physical Review B*, vol. 81, no. 11, p. 115315, 2010.

[138] M. S. Dresselhaus, G. Dresselhaus, and A. Jorio, *Group theory: application to the physics of condensed matter.* Springer Science & Business Media, 2007.

[139] P. Li, I. Appelbaum, *et al.*, "Illuminating" spin-polarized" bloch wave-function projection from degenerate bands in decomposable centrosymmetric lattices," *Physical Review B*, vol. 97, no. 12, p. 125434, 2018.

[140] A. Kormányos, G. Burkard, M. Gmitra, J. Fabian, V. Zólyomi, N. D. Drummond, and V. Fal'ko, "k · p theory for two-dimensional transition metal dichalcogenide semiconductors," *2D Materials*, vol. 2, no. 2, p. 022001, 2015.

[141] E. Cappelluti, R. Roldán, J. Silva-Guillén, P. Ordejón, and F. Guinea, "Tight-binding model and direct-gap/indirect-gap transition in single-layer and multilayer mos 2," *Physical Review B*, vol. 88, no. 7, p. 075409, 2013.

[142] T. Deilmann, P. Krüger, and M. Rohlfing, "Ab initio studies of exciton g factors: monolayer transition metal dichalcogenides in magnetic fields," *Physical review letters*, vol. 124, no. 22, p. 226402, 2020.

[143] C. M. Gilardoni, F. Hendriks, C. H. van der Wal, and M. H. Guimarães, "Symmetry and control of spin-scattering processes in two-dimensional transition metal dichalcogenides," *Physical Review B*, vol. 103, no. 11, p. 115410, 2021.

[144] P. Avouris, T. F. Heinz, and T. Low, *2D Materials.* Cambridge University Press, 2017.

[145] A. Damascelli, "Probing the electronic structure of complex systems by arpes," *Physica Scripta*, vol. 2004, no. T109, p. 61, 2004.

[146] P. Ayria, A. R. Nugraha, E. H. Hasdeo, T. R. Czank, S.-i. Tanaka, and R. Saito, "Photon energy dependence of angle-resolved photoemission spectroscopy in graphene," *Physical Review B*, vol. 92, no. 19, p. 195148, 2015.

[147] P. Ayria, S.-i. Tanaka, A. R. Nugraha, M. S. Dresselhaus, and R. Saito, "Phonon-assisted indirect transitions in angle-resolved photoemission spectra of graphite and graphene," *Physical Review B*, vol. 94, no. 7, p. 075429, 2016.

[148] G. F. Mkrtchian, A. Knorr, and M. Selig, "Theory of second-order excitonic nonlinearities in transition metal dichalcogenides," *Physical Review B*, vol. 100, no. 12, p. 125401, 2019.

[149] F. Katsch, M. Selig, A. Carmele, and A. Knorr, "Theory of exciton–exciton interactions in monolayer transition metal dichalcogenides," *physica status solidi (b)*, vol. 255, no. 12, p. 1800185, 2018.

[150] M. Selig, F. Katsch, R. Schmidt, S. M. de Vasconcellos, R. Bratschitsch, E. Malic, and A. Knorr, "Ultrafast dynamics in monolayer transition metal dichalcogenides: interplay of dark excitons, phonons, and intervalley exchange," *Physical Review Research*, vol. 1, no. 2, p. 022007, 2019.

[151] V. M. Axt and A. Stahl, "A dynamics-controlled truncation scheme for the hierarchy of density matrices in semiconductor optics," *Zeitschrift für Physik B Condensed Matter*, vol. 93, no. 2, pp. 195–204, 1994.

[152] M. Lindberg, Y. Hu, R. Binder, and S. Koch, "χ (3) formalism in optically excited semiconductors and its applications in four-wave-mixing spectroscopy," *Physical Review B*, vol. 50, no. 24, p. 18060, 1994.

[153] J. Fricke, "Transport equations including many-particle correlations for an arbitrary quantum system: A general formalism," *Annals of Physics*, vol. 252, no. 2, pp. 479–498, 1996.

[154] F. Katsch, M. Selig, and A. Knorr, "Theory of coherent pump–probe spectroscopy in monolayer transition metal dichalcogenides," *2D Materials*, vol. 7, no. 1, p. 015021, 2019.

[155] F. Katsch, M. Selig, and A. Knorr, "Exciton-scattering-induced dephasing in two-dimensional semiconductors," *Physical Review Letters*, vol. 124, no. 25, p. 257402, 2020.

[156] M. Kira and S. Koch, "Many-body correlations and excitonic effects in semiconductor spectroscopy," *Progress in quantum electronics*, vol. 30, no. 5, pp. 155–296, 2006.

[157] V. M. Axt and T. Kuhn, "Femtosecond spectroscopy in semiconductors: a key to coherences, correlations and quantum kinetics," *Reports on Progress in Physics*, vol. 67, no. 4, p. 433, 2004.

[158] M. Selig, G. Berghäuser, A. Raja, P. Nagler, C. Schüller, T. F. Heinz, T. Korn, A. Chernikov, E. Malic, and A. Knorr, "Excitonic linewidth and coherence lifetime in monolayer transition metal dichalcogenides," *Nature communications*, vol. 7, no. 1, pp. 1–6, 2016.

[159] D. Christiansen, M. Selig, G. Berghäuser, R. Schmidt, I. Niehues, R. Schneider, A. Arora, S. M. de Vasconcellos, R. Bratschitsch, E. Malic, *et al.*, "Phonon sidebands in monolayer transition metal dichalcogenides," *Physical review letters*, vol. 119, no. 18, p. 187402, 2017.

[160] I. Niehues, R. Schmidt, M. Drüppel, P. Marauhn, D. Christiansen, M. Selig, G. Berghäuser, D. Wigger, R. Schneider, L. Braasch, *et al.*, "Strain control of exciton–phonon coupling in atomically thin semiconductors," *Nano letters*, vol. 18, no. 3, pp. 1751–1757, 2018.

[161] S. Shree, M. Semina, C. Robert, B. Han, T. Amand, A. Balocchi, M. Manca, E. Courtade, X. Marie, T. Taniguchi, *et al.*, "Exciton-phonon coupling in mose2 monolayers," *arXiv preprint arXiv:1804.06340*, 2018.

[162] I. Niehues, P. Marauhn, T. Deilmann, D. Wigger, R. Schmidt, A. Arora, S. M. de Vasconcellos, M. Rohlfing, and R. Bratschitsch, "Strain tuning of the stokes shift in atomically thin semiconductors," *Nanoscale*, vol. 12, no. 40, pp. 20786–20796, 2020.

[163] M. Selig, G. Berghäuser, M. Richter, R. Bratschitsch, A. Knorr, and E. Malic, "Dark and bright exciton formation, thermalization, and photoluminescence in monolayer transition metal dichalcogenides," *2D Materials*, vol. 5, no. 3, p. 035017, 2018.

[164] S. Brem, A. Ekman, D. Christiansen, F. Katsch, M. Selig, C. Robert, X. Marie, B. Urbaszek, A. Knorr, and E. Malic, "Phonon-assisted photoluminescence from indirect excitons in monolayers of transition-metal dichalcogenides," *Nano letters*, vol. 20, no. 4, pp. 2849–2856, 2020.

[165] T. Stroucken, A. Knorr, P. Thomas, and S. Koch, "Coherent dynamics of radiatively coupled quantum-well excitons," *Physical Review B*, vol. 53, no. 4, p. 2026, 1996.

[166] E. Malic and A. Knorr, *Graphene and carbon nanotubes: ultrafast optics and relaxation dynamics.* John Wiley & Sons, 2013.

[167] F. Katsch and A. Knorr, "Optical preparation and coherent control of ultrafast nonlinear quantum superpositions in exciton gases: A case study for atomically thin semiconductors," *Physical Review X*, vol. 10, no. 4, p. 041039, 2020.

[168] M. Eckstein and M. Kollar, "Measuring correlated electron dynamics with time-resolved photoemission spectroscopy," *Physical Review B*, vol. 78, no. 24, p. 245113, 2008.

[169] J. Braun, R. Rausch, M. Potthoff, J. Minár, and H. Ebert, "One-step theory of pump-probe photoemission," *Physical Review B*, vol. 91, no. 3, p. 035119, 2015.

[170] J. Freericks, H. Krishnamurthy, and T. Pruschke, "Theoretical description of time-resolved photoemission spectroscopy: application to pump-probe experiments," *Physical review letters*, vol. 102, no. 13, p. 136401, 2009.

[171] M. Weinelt, "Time-resolved two-photon photoemission from metal surfaces," *Journal of Physics: Condensed Matter*, vol. 14, no. 43, p. R1099, 2002.

[172] S. Ramakrishna, F. Willig, and A. Knorr, "Photoinduced bulk-surface dynamics: time resolved two photon photoemission signals at semiconductor surfaces," *Surface science*, vol. 558, no. 1-3, pp. 159–173, 2004.

[173] A. Ivanov and H. Haug, "Self-consistent theory of the biexciton optical nonlinearity," *Physical Review B*, vol. 48, no. 3, p. 1490, 1993.

[174] T. Usui, "Excitations in a high density electron gas. i," *Progress of Theoretical Physics*, vol. 23, no. 5, pp. 787–798, 1960.

[175] A. Fischer, D. Kim, J. Hays, W. Shan, J. Song, D. Eason, J. Ren, J. Schetzina, H. Luo, J. Furdyna, *et al.*, "Femtosecond coherent spectroscopy of bulk znse and zncdse/znse quantum wells," *Physical review letters*, vol. 73, no. 17, p. 2368, 1994.

[176] S. Dong, M. Puppin, T. Pincelli, S. Beaulieu, D. Christiansen, H. Hübener, C. W. Nicholson, R. P. Xian, M. Dendzik, Y. Deng, *et al.*, "Direct measurement of key exciton properties: Energy, dynamics, and spatial distribution of the wave function," *Natural Sciences*, p. e10010, 2021.

[177] A. Rustagi and A. F. Kemper, "Photoemission signature of excitons," *Physical Review B*, vol. 97, no. 23, p. 235310, 2018.

[178] M. K. Man, J. Madéo, C. Sahoo, K. Xie, M. Campbell, V. Pareek, A. Karmakar, E. L. Wong, A. Al-Mahboob, N. S. Chan, *et al.*, "Experimental measurement of the intrinsic excitonic wave function," *Science Advances*, vol. 7, no. 17, p. eabg0192, 2021.

[179] J. Zipfel, J. Holler, A. A. Mitioglu, M. V. Ballotin, P. Nagler, A. V. Stier, T. Taniguchi, K. Watanabe, S. A. Crooker, P. C. Christianen, *et al.*, "Spatial extent of the excited exciton states in ws 2 monolayers from diamagnetic shifts," *Physical Review B*, vol. 98, no. 7, p. 075438, 2018.

[180] J. Madéo, M. K. Man, C. Sahoo, M. Campbell, V. Pareek, E. L. Wong, A. Al-Mahboob, N. S. Chan, A. Karmakar, B. M. K. Mariserla, *et al.*, "Directly visualizing the momentum-forbidden dark excitons and their dynamics in atomically thin semiconductors," *Science*, vol. 370, no. 6521, pp. 1199–1204, 2020.

[181] A. Steinhoff, M. Florian, M. Rösner, G. Schönhoff, T. O. Wehling, and F. Jahnke, "Exciton fission in monolayer transition metal dichalcogenide semiconductors," *Nature communications*, vol. 8, no. 1, pp. 1–11, 2017.

[182] E. Perfetto, D. Sangalli, A. Marini, and G. Stefanucci, "First-principles approach to excitons in time-resolved and angle-resolved photoemission spectra," *Physical Review B*, vol. 94, no. 24, p. 245303, 2016.

[183] A. Rustagi and A. F. Kemper, "Coherent excitonic quantum beats in time-resolved photoemission measurements," *Physical Review B*, vol. 99, no. 12, p. 125303, 2019.

[184] J. Freericks and A. F. Kemper, "What do the two times in two-time correlation functions mean for interpreting tr-arpes?," *Journal of Electron Spectroscopy and Related Phenomena*, vol. 251, p. 147104, 2021.

[185] K.-D. Park, T. Jiang, G. Clark, X. Xu, and M. B. Raschke, "Radiative control of dark excitons at room temperature by nano-optical antenna-tip purcell effect," *Nature nanotechnology*, vol. 13, no. 1, pp. 59–64, 2018.

[186] J. M. Blatt, K. Böer, and W. Brandt, "Bose-einstein condensation of excitons," *Physical Review*, vol. 126, no. 5, p. 1691, 1962.

[187] L. Keldysh, "The electron-hole liquid in semiconductors," *Contemporary physics*, vol. 27, no. 5, pp. 395–428, 1986.

[188] A. C. Neto, F. Guinea, N. M. Peres, K. S. Novoselov, and A. K. Geim, "The electronic properties of graphene," *Reviews of modern physics*, vol. 81, no. 1, p. 109, 2009.

[189] J.-H. Chen, C. Jang, S. Xiao, M. Ishigami, and M. S. Fuhrer, "Intrinsic and extrinsic performance limits of graphene devices on sio 2," *Nature nanotechnology*, vol. 3, no. 4, pp. 206–209, 2008.

[190] P. Goli, H. Ning, X. Li, C. Y. Lu, K. S. Novoselov, and A. A. Balandin, "Strong enhancement of thermal properties of copper films after chemical vapor deposition of graphene," *arXiv preprint arXiv:1311.6029*, 2013.

[191] H. Zhou, Y. Chen, and H. Zhu, "Deciphering asymmetric charge transfer at transition metal dichalcogenide–graphene interface by helicity-resolved ultrafast spectroscopy," *Science Advances*, vol. 7, no. 34, p. eabg2999, 2021.

[192] S. Fu, I. du Fossé, X. Jia, J. Xu, X. Yu, H. Zhang, W. Zheng, S. Krasel, Z. Chen, Z. M. Wang, *et al.*, "Long-lived charge separation following pump-wavelength–dependent ultrafast charge transfer in graphene/ws2 heterostructures," *Science advances*, vol. 7, no. 9, p. eabd9061, 2021.

[193] R. Krause, M. Chávez-Cervantes, S. Aeschlimann, S. Forti, F. Fabbri, A. Rossi, C. Coletti, C. Cacho, Y. Zhang, P. E. Majchrzak, *et al.*, "Ultrafast charge separation in bilayer ws2/graphene heterostructure revealed by time-and angle-resolved photoemission spectroscopy," *Frontiers in Physics*, vol. 2021, no. 9, p. 668149, 2021.

[194] S. Aeschlimann, A. Rossi, M. Chávez-Cervantes, R. Krause, B. Arnoldi, B. Stadtmüller, M. Aeschlimann, S. Forti, F. Fabbri, C. Coletti, *et al.*, "Direct evidence for efficient ultrafast charge separation in epitaxial ws2/graphene heterostructures," *Science Advances*, vol. 6, no. 20, p. eaay0761, 2020.

[195] D. Luo, J. Tang, X. Shen, F. Ji, J. Yang, S. Weathersby, M. E. Kozina, Z. Chen, J. Xiao, Y. Ye, *et al.*, "Twist-angle-dependent ultrafast charge transfer in mos2-graphene van der waals heterostructures," *Nano Letters*, 2021.

[196] T. Förster, "Zwischenmolekulare energiewanderung und fluoreszenz," *Annalen der physik*, vol. 437, no. 1-2, pp. 55–75, 1948.

[197] J. F. Specht, E. Verdenhalven, B. Bieniek, P. Rinke, A. Knorr, and M. Richter, "Theory of excitation transfer between two-dimensional semiconductor and molecular layers," *Physical Review Applied*, vol. 9, no. 4, p. 044025, 2018.

[198] M. Selig, E. Malic, K. J. Ahn, N. Koch, and A. Knorr, "Theory of optically induced förster coupling in van der waals coupled heterostructures," *Physical Review B*, vol. 99, no. 3, p. 035420, 2019.

[199] S. Ovesen, S. Brem, C. Linderälv, M. Kuisma, T. Korn, P. Erhart, M. Selig, and E. Malic, "Interlayer exciton dynamics in van der waals heterostructures," *Communications Physics*, vol. 2, no. 1, pp. 1–8, 2019.

[200] S. Dong, S. Beaulieu, M. Selig, P. Rosenzweig, D. Christiansen, T. Pincelli, M. Dendzik, J. D. Ziegler, J. Maklar, R. P. Xian, *et al.*, "Observation of ultrafast interfacial meitner-auger energy transfer in a van der waals heterostructure," *arXiv preprint arXiv:2108.06803*, 2021.

[201] D. L. Dexter, "A theory of sensitized luminescence in solids," *The journal of chemical physics*, vol. 21, no. 5, pp. 836–850, 1953.

[202] J. F. Specht, A. Knorr, and M. Richter, "Two-dimensional spectroscopy: An approach to distinguish förster and dexter transfer processes in coupled nanostructures," *Physical Review B*, vol. 91, no. 15, p. 155313, 2015.

[203] S. Piscanec, M. Lazzeri, F. Mauri, A. Ferrari, and J. Robertson, "Kohn anomalies and electron-phonon interactions in graphite," *Physical review letters*, vol. 93, no. 18, p. 185503, 2004.

[204] P. Drude, "Zur elektronentheorie der metalle," *Annalen der physik*, vol. 306, no. 3, pp. 566–613, 1900.

[205] D. S. Wiersma, P. Bartolini, A. Lagendijk, and R. Righini, "Localization of light in a disordered medium," *Nature*, vol. 390, no. 6661, pp. 671–673, 1997.

[206] C. S. Hellberg and S. C. Erwin, "Strongly correlated electrons on a silicon surface: Theory of a mott insulator," *Physical review letters*, vol. 83, no. 5, p. 1003, 1999.

[207] J. E. Moore, "The birth of topological insulators," *Nature*, vol. 464, no. 7286, pp. 194–198, 2010.

[208] L. Keldysh and Y. Kopaev, "Soviet physics solid state," *USSR*, vol. 6, no. 9, p. 2219, 1965.

[209] D. Jérome, T. Rice, and W. Kohn, "Excitonic insulator," *Physical Review*, vol. 158, no. 2, p. 462, 1967.

[210] S. Gupta, A. Kutana, and B. I. Yakobson, "Heterobilayers of 2d materials as a platform for excitonic superfluidity," *Nature communications*, vol. 11, no. 1, pp. 1–7, 2020.

[211] E. Perfetto and G. Stefanucci, "Ultrafast creation and melting of nonequilibrium excitonic condensates in bulk wse 2," *Physical Review B*, vol. 103, no. 24, p. L241404, 2021.

[212] R. Parmenter and W. Henson, "Superconductive properties of the excitonic insulator," *Physical Review B*, vol. 2, no. 1, p. 140, 1970.

[213] R. Wang, O. Erten, B. Wang, and D. Xing, "Prediction of a topological p+ ip excitonic insulator with parity anomaly," *Nature communications*, vol. 10, no. 1, pp. 1–9, 2019.

[214] H. Cercellier, C. Monney, F. Clerc, C. Battaglia, L. Despont, M. Garnier, H. Beck, P. Aebi, L. Patthey, H. Berger, *et al.*, "Evidence for an excitonic insulator phase in 1 t-tise 2," *Physical review letters*, vol. 99, no. 14, p. 146403, 2007.

[215] C. Monney, E. Schwier, M. G. Garnier, N. Mariotti, C. Didiot, H. Cercellier, J. Marcus, H. Berger, A. Titov, H. Beck, *et al.*, "Probing the exciton condensate phase in 1t-tise2 with photoemission," *New Journal of Physics*, vol. 12, no. 12, p. 125019, 2010.

[216] Y. Wakisaka, T. Sudayama, K. Takubo, T. Mizokawa, M. Arita, H. Namatame, M. Taniguchi, N. Katayama, M. Nohara, and H. Takagi, "Excitonic insulator state in ta 2 nise 5 probed by photoemission spectroscopy," *Physical review letters*, vol. 103, no. 2, p. 026402, 2009.

[217] Y. Lu, H. Kono, T. Larkin, A. Rost, T. Takayama, A. Boris, B. Keimer, and H. Takagi, "Zero-gap semiconductor to excitonic insulator transition in ta 2 nise 5," *Nature communications*, vol. 8, no. 1, pp. 1–7, 2017.

[218] D. Werdehausen, T. Takayama, M. Höppner, G. Albrecht, A. W. Rost, Y. Lu, D. Manske, H. Takagi, and S. Kaiser, "Coherent order parameter oscillations in the ground state of the excitonic insulator ta2nise5," *Science advances*, vol. 4, no. 3, p. eaap8652, 2018.

[219] B. Bucher, P. Steiner, and P. Wachter, "Excitonic insulator phase in tmse 0.45 te 0.55," *Physical review letters*, vol. 67, no. 19, p. 2717, 1991.

[220] F. X. Bronold and H. Fehske, "Possibility of an excitonic insulator at the semiconductor-semimetal transition," *Physical Review B*, vol. 74, no. 16, p. 165107, 2006.

[221] K. Fukutani, R. Stania, C. I. Kwon, J. S. Kim, K. J. Kong, J. Kim, and H. W. Yeom, "Detecting photoelectrons from spontaneously formed excitons," *arXiv preprint arXiv:2105.11101*, 2021.

[222] K. Rossnagel, L. Kipp, and M. Skibowski, "Charge-density-wave phase transition in 1 t-tise 2: Excitonic insulator versus band-type jahn-teller mechanism," *Physical Review B*, vol. 65, no. 23, p. 235101, 2002.

[223] B. Zenker, H. Fehske, and H. Beck, "Fate of the excitonic insulator in the presence of phonons," *Physical Review B*, vol. 90, no. 19, p. 195118, 2014.

[224] Z. Jiang, Y. Li, S. Zhang, and W. Duan, "Realizing an intrinsic excitonic insulator by decoupling exciton binding energy from the minimum band gap," *Physical Review B*, vol. 98, no. 8, p. 081408, 2018.

[225] P. A. Volkov, M. Ye, H. Lohani, I. Feldman, A. Kanigel, and G. Blumberg, "Failed excitonic quantum phase transition in ta $\_2$ ni (se $\_{1-x}$ s $\_x$) $\_5$," *arXiv preprint arXiv:2104.07032*, 2021.

[226] Z. Song, T. Schultz, Z. Ding, B. Lei, C. Han, P. Amsalem, T. Lin, D. Chi, S. L. Wong, Y. J. Zheng, *et al.*, "Electronic properties of a 1d intrinsic/p-doped heterojunction in a 2d transition metal dichalcogenide semiconductor," *ACS nano*, vol. 11, no. 9, pp. 9128–9135, 2017.

[227] N. Koch, "Organic electronic devices and their functional interfaces," *ChemPhysChem*, vol. 8, no. 10, pp. 1438–1455, 2007.

[228] M. Fahlman, S. Fabiano, V. Gueskine, D. Simon, M. Berggren, and X. Crispin, "Interfaces in organic electronics," *Nature Reviews Materials*, vol. 4, no. 10, pp. 627–650, 2019.

[229] S. Torabi, F. Jahani, I. Van Severen, C. Kanimozhi, S. Patil, R. W. Havenith, R. C. Chiechi, L. Lutsen, D. J. Vanderzande, T. J. Cleij, *et al.*, "Strategy for enhancing the dielectric constant of organic semiconductors without sacrificing charge carrier mobility and solubility," *Advanced Functional Materials*, vol. 25, no. 1, pp. 150–157, 2015.

[230] D. Christiansen, M. Selig, M. Rossi, and A. Knorr, *Excitonic insulator formed by hybrid excitations in molecular functionalized atomically-thin semiconductors*. in preparation, 2021.

[231] R. Kuhrt, M. Hantusch, M. Knupfer, and B. Büchner, "Charge transfer characteristics of f6tcnnq–gold interface," *Surface and Interface Analysis*, vol. 52, no. 12, pp. 953–956, 2020.

[232] J. Li, I. Duchemin, O. M. Roscioni, P. Friederich, M. Anderson, E. Da Como, G. Kociok-Köhn, W. Wenzel, C. Zannoni, D. Beljonne, *et al.*, "Host dependence of the electron affinity of molecular dopants," *Materials Horizons*, vol. 6, no. 1, pp. 107–114, 2019.

[233] R. Schlesinger, Y. Xu, O. T. Hofmann, S. Winkler, J. Frisch, J. Niederhausen, A. Vollmer, S. Blumstengel, F. Henneberger, P. Rinke, *et al.*, "Controlling the work function of zno and the energy-level alignment at the interface to organic semiconductors with a molecular electron acceptor," *Physical Review B*, vol. 87, no. 15, p. 155311, 2013.

[234] D. Waas, F. Rückerl, and M. Knupfer, "Charge transfer at the interface between mnpc and f6tcnnq," *physica status solidi (b)*, vol. 256, no. 2, p. 1800245, 2019.

[235] S. Park, T. Schultz, X. Xu, B. Wegner, A. Aljarb, A. Han, L.-J. Li, V. C. Tung, P. Amsalem, and N. Koch, "Demonstration of the key substrate-dependent charge transfer mechanisms between monolayer mos 2 and molecular dopants," *Communications Physics*, vol. 2, no. 1, pp. 1–8, 2019.

[236] J. F. Specht, *Theory of multidimensional spectroscopy and excitation transfer processes in nanostructures.* Technische Universitaet Berlin (Germany), 2018.

[237] J. Heyd, G. E. Scuseria, and M. Ernzerhof, "Hybrid functionals based on a screened coulomb potential," *The Journal of chemical physics*, vol. 118, no. 18, pp. 8207–8215, 2003.

[238] V. Blum, R. Gehrke, F. Hanke, P. Havu, V. Havu, X. Ren, K. Reuter, and M. Scheffler, "Ab initio molecular simulations with numeric atom-centered orbitals," *Computer Physics Communications*, vol. 180, no. 11, pp. 2175–2196, 2009.

[239] X. Ren, P. Rinke, V. Blum, J. Wieferink, A. Tkatchenko, A. Sanfilippo, K. Reuter, and M. Scheffler, "Resolution-of-identity approach to hartree–fock, hybrid density functionals, rpa, mp2 and gw with numeric atom-centered orbital basis functions," *New Journal of Physics*, vol. 14, no. 5, p. 053020, 2012.

[240] S. V. Levchenko, X. Ren, J. Wieferink, R. Johanni, P. Rinke, V. Blum, and M. Scheffler, "Hybrid functionals for large periodic systems in an all-electron, numeric atom-centered basis framework," *Computer Physics Communications*, vol. 192, pp. 60–69, 2015.

[241] H. Wang, S. V. Levchenko, T. Schultz, N. Koch, M. Scheffler, and M. Rossi, "Modulation of the work function by the atomic structure of strong organic electron acceptors on h-si (111)," *Advanced Electronic Materials*, vol. 5, no. 5, p. 1800891, 2019.

[242] S. Park, H. Wang, T. Schultz, D. Shin, R. Ovsyannikov, M. Zacharias, D. Maksimov, M. Meissner, Y. Hasegawa, T. Yamaguchi, *et al.*, "Temperature-dependent electronic ground-state charge transfer in van der waals heterostructures," *Advanced Materials*, p. 2008677, 2021.

[243] R. Gillen, "Interlayer excitonic spectra of vertically stacked mose2/wse2 heterobilayers," *physica status solidi (b)*, p. 2000614, 2021.

[244] T. Deilmann and K. S. Thygesen, "Interlayer excitons with large optical amplitudes in layered van der waals materials," *Nano letters*, vol. 18, no. 5, pp. 2984–2989, 2018.

[245] A. Altland and B. D. Simons, *Condensed matter field theory.* Cambridge university press, 2010.

[246] Y. Nambu, "Quasi-particles and gauge invariance in the theory of superconductivity," *Physical Review*, vol. 117, no. 3, p. 648, 1960.

[247] R. Zimmermann and C. Schindler, "Exciton–exciton interaction in coupled quantum wells," *Solid state communications*, vol. 144, no. 9, pp. 395–398, 2007.

[248] C. Schindler and R. Zimmermann, "Analysis of the exciton-exciton interaction in semiconductor quantum wells," *Physical Review B*, vol. 78, no. 4, p. 045313, 2008.

[249] J. Bardeen, L. N. Cooper, and J. R. Schrieffer, "Theory of superconductivity," *Physical review*, vol. 108, no. 5, p. 1175, 1957.

[250] M. Tinkham, *Introduction to superconductivity*. Courier Corporation, 2004.

[251] D. Reyes, M. A. Continentino, C. Thomas, and C. Lacroix, "s-and d-wave superconductivity in a two-band model," *Annals of Physics*, vol. 373, pp. 257–272, 2016.

[252] M. Moeferdt, T. Kiel, T. Sproll, F. Intravaia, and K. Busch, "Plasmonic modes in nanowire dimers: a study based on the hydrodynamic drude model including nonlocal and nonlinear effects," *Physical Review B*, vol. 97, no. 7, p. 075431, 2018.

[253] T. Stroucken and S. W. Koch, "Optically bright p-excitons indicating strong coulomb coupling in transition-metal dichalcogenides," *Journal of Physics: Condensed Matter*, vol. 27, no. 34, p. 345003, 2015.

[254] T. Stroucken, J. Grönqvist, and S. Koch, "Optical response and ground state of graphene," *Physical Review B*, vol. 84, no. 20, p. 205445, 2011.

[255] J. Bhattacharyya, S. Zybell, F. Eßer, M. Helm, H. Schneider, L. Schneebeli, C. Böttge, B. Breddermann, M. Kira, S. W. Koch, *et al.*, "Magnetic control of coulomb scattering and terahertz transitions among excitons," *Physical Review B*, vol. 89, no. 12, p. 125313, 2014.

[256] P. Steinleitner, P. Merkl, A. Graf, P. Nagler, K. Watanabe, T. Taniguchi, J. Zipfel, C. Schüller, T. Korn, A. Chernikov, *et al.*, "Dielectric engineering of electronic correlations in a van der waals heterostructure," *Nano letters*, vol. 18, no. 2, pp. 1402–1409, 2018.

[257] E. Lorchat, M. Selig, F. Katsch, K. Yumigeta, S. Tongay, A. Knorr, C. Schneider, and S. Höfling, "Excitons in bilayer mos 2 displaying a colossal electric field splitting and tunable magnetic response," *Physical Review Letters*, vol. 126, no. 3, p. 037401, 2021.

[258] N. Bohr, "I. on the constitution of atoms and molecules," *The London, Edinburgh, and Dublin Philosophical Magazine and Journal of Science*, vol. 26, no. 151, pp. 1–25, 1913.

[259] A. Sommerfeld, "Zur quantentheorie der spektrallinien," *Annalen der Physik*, vol. 356, no. 17, pp. 1–94, 1916.

[260] H. G. J. Moseley, "Xciii. the high-frequency spectra of the elements," *The London, Edinburgh, and Dublin Philosophical Magazine and Journal of Science*, vol. 26, no. 156, pp. 1024–1034, 1913.

[261] P. Eisenberger, R. Shulman, B. Kincaid, G. Brown, and S. Ogawa, "Extended x-ray absorption fine structure determination of iron nitrogen distances in haemoglobin," *Nature*, vol. 274, no. 5666, pp. 30–34, 1978.

[262] J. Yano and V. K. Yachandra, "X-ray absorption spectroscopy," *Photosynthesis research*, vol. 102, no. 2, pp. 241–254, 2009.

[263] P. M. Kraus, M. Zürch, S. K. Cushing, D. M. Neumark, and S. R. Leone, "The ultrafast x-ray spectroscopic revolution in chemical dynamics," *Nature Reviews Chemistry*, vol. 2, no. 6, pp. 82–94, 2018.

[264] K. Diller, R. J. Maurer, M. Müller, and K. Reuter, "Interpretation of x-ray absorption spectroscopy in the presence of surface hybridization," *The Journal of chemical physics*, vol. 146, no. 21, p. 214701, 2017.

[265] Y. Pertot, C. Schmidt, M. Matthews, A. Chauvet, M. Huppert, V. Svoboda, A. Von Conta, A. Tehlar, D. Baykusheva, J.-P. Wolf, *et al.*, "Time-resolved x-ray absorption spectroscopy with a water window high-harmonic source," *Science*, vol. 355, no. 6322, pp. 264–267, 2017.

[266] W. Hua, S. Mukamel, and Y. Luo, "Transient x-ray absorption spectral fingerprints of the s1 dark state in uracil," *The journal of physical chemistry letters*, vol. 10, no. 22, pp. 7172–7178, 2019.

[267] K. Witte, I. Mantouvalou, R. Sánchez-de Armas, H. Lokstein, J. Lebendig-Kuhla, A. Jonas, F. Roth, B. Kanngießer, and H. Stiel, "On the electronic structure of cu chlorophyllin and its breakdown products: a carbon k-edge x-ray absorption spectroscopy study," *The Journal of Physical Chemistry B*, vol. 122, no. 6, pp. 1846–1851, 2018.

[268] A. Jonas, K. Dammer, H. Stiel, B. Kanngiesser, R. Sánchez-de Armas, and I. Mantouvalou, "Transient sub-nanosecond soft x-ray nexafs spectroscopy on organic thin films," *Analytical Chemistry*, vol. 92, no. 23, pp. 15611–15615, 2020.

[269] W. Malzer, C. Schlesiger, and B. Kanngießer, "A century of laboratory x-ray absorption spectroscopy–a review and an optimistic outlook," *Spectrochimica Acta Part B: Atomic Spectroscopy*, p. 106101, 2021.

[270] C. S. Schnohr and M. C. Ridgway, *X-ray absorption spectroscopy of semiconductors*. Springer, 2015.

[271] J. Stöhr, *NEXAFS spectroscopy*, vol. 25. Springer Science & Business Media, 1992.

[272] M. Chowdhury, R. Saito, and M. Dresselhaus, "Polarization dependence of x-ray absorption spectra in graphene," *Physical Review B*, vol. 85, no. 11, p. 115410, 2012.

[273] J. J. Rehr and R. C. Albers, "Theoretical approaches to x-ray absorption fine structure," *Reviews of modern physics*, vol. 72, no. 3, p. 621, 2000.

[274] D. Christiansen, M. Selig, J. Biegert, and A. Knorr, *Theory of X-ray absorption spectroscopy: a microscopic Bloch equation approach for two-dimensional solid states*. under review, 2021.

[275] N. Marzari, A. A. Mostofi, J. R. Yates, I. Souza, and D. Vanderbilt, "Maximally localized wannier functions: Theory and applications," *Reviews of Modern Physics*, vol. 84, no. 4, p. 1419, 2012.

[276] H. Jones, N. Mott, and H. Skinner, "A theory of the form of the x-ray emission bands of metals," *Physical Review*, vol. 45, no. 6, p. 379, 1934.

[277] J. C. Slater and G. F. Koster, "Simplified lcao method for the periodic potential problem," *Physical Review*, vol. 94, no. 6, p. 1498, 1954.

[278] O. Madelung, *Introduction to solid-state theory*, vol. 2. Springer Science & Business Media, 2012.

[279] F. Bloch, "Über die quantenmechanik der elektronen in kristallgittern," *Zeitschrift für physik*, vol. 52, no. 7, pp. 555–600, 1929.

[280] X. Song, S. Yang, R. Zuo, T. Meier, and W. Yang, "Enhanced high-order harmonic generation in semiconductors by excitation with multicolor pulses," *Physical Review A*, vol. 101, no. 3, p. 033410, 2020.

[281] J. C. Slater, "Atomic shielding constants," *Physical Review*, vol. 36, no. 1, p. 57, 1930.

[282] Y. Wang, Y. Chen, C. Jia, B. Moritz, and T. P. Devereaux, "Time-resolved resonant inelastic x-ray scattering in a pumped mott insulator," *Physical Review B*, vol. 101, no. 16, p. 165126, 2020.

[283] N. F. Mott, "The scattering of fast electrons by atomic nuclei," *Proceedings of the Royal Society of London. Series A, Containing Papers of a Mathematical and Physical Character*, vol. 124, no. 794, pp. 425–442, 1929.

[284] H. Bethe, "Zur theorie des durchgangs schneller korpuskularstrahlen durch materie," *Annalen der Physik*, vol. 397, no. 3, pp. 325–400, 1930.

[285] J. Carlisle, E. L. Shirley, L. Terminello, J. Jia, T. Callcott, D. Ederer, R. Perera, and F. Himpsel, "Band-structure and core-hole effects in resonant inelastic soft-x-ray scattering: Experiment and theory," *Physical Review B*, vol. 59, no. 11, p. 7433, 1999.

[286] H. P. Hjalmarson, H. Büttner, and J. D. Dow, "Theory of core excitons," *Physical Review B*, vol. 24, no. 10, p. 6010, 1981.

[287] P. Brühwiler, A. Maxwell, C. Puglia, A. Nilsson, S. Andersson, and N. Mårtensson, "π^* and σ^* excitons in c 1 s absorption of graphite," *Physical review letters*, vol. 74, no. 4, p. 614, 1995.

[288] R. Ahuja, P. Brühwiler, J. Wills, B. Johansson, N. Mårtensson, and O. Eriksson, "Theoretical and experimental study of the graphite 1s x-ray absorption edges," *Physical Review B*, vol. 54, no. 20, p. 14396, 1996.

[289] W. Olovsson, I. Tanaka, T. Mizoguchi, P. Puschnig, and C. Ambrosch-Draxl, "All-electron bethe-salpeter calculations for shallow-core x-ray absorption near-edge structures," *Physical Review B*, vol. 79, no. 4, p. 041102, 2009.

[290] O. Hess and T. Kuhn, "Spatio-temporal dynamics of semiconductor lasers: Theory, modelling and analysis," *Progress in quantum electronics*, vol. 20, no. 2, pp. 85–179, 1996.

[291] O. Hess and T. Kuhn, "Maxwell-bloch equations for spatially inhomogeneous semiconductor lasers. i. theoretical formulation," *Physical Review A*, vol. 54, no. 4, p. 3347, 1996.

[292] F. Rossi and T. Kuhn, "Theory of ultrafast phenomena in photoexcited semiconductors," *Reviews of Modern Physics*, vol. 74, no. 3, p. 895, 2002.

[293] E. Malic, T. Winzer, E. Bobkin, and A. Knorr, "Microscopic theory of absorption and ultrafast many-particle kinetics in graphene," *Physical Review B*, vol. 84, no. 20, p. 205406, 2011.

[294] T. Winzer, A. Knorr, and E. Malic, "Carrier multiplication in graphene," *Nano letters*, vol. 10, no. 12, pp. 4839–4843, 2010.

[295] L. Meitner, "Über die entstehung der β-strahlspektren radioaktiver substanzen," *Zeitschrift für Physik*, vol. 9, no. 1, pp. 131–144, 1922.

[296] P. Auger, "Sur les rayons β secondaires produits dans un gaz par des rayons x.," *CR Acad. Sci.(F)*, vol. 177, p. 169, 1923.

[297] D. Matsakis, A. Coster, B. Laster, and R. Sime, "A renaming proposal: The auger-meitner effect," *Physics Today*, vol. 72, no. 9, pp. 10–11, 2019.

[298] J. C. Maxwell, "Viii. a dynamical theory of the electromagnetic field," *Philosophical transactions of the Royal Society of London*, no. 155, pp. 459–512, 1865.

[299] J. D. Jackson, "Classical electrodynamics," 1999.

[300] S. R. Franke, *Quantization of quasinormal modes in dissipative media*. Technische Universitaet Berlin (Germany), 2020.

[301] S. Franke, J. Ren, S. Hughes, and M. Richter, "Fluctuation-dissipation theorem and fundamental photon commutation relations in lossy nanostructures using quasinormal modes," *Physical Review Research*, vol. 2, no. 3, p. 033332, 2020.

[302] S. Y. Buhmann, *Dispersion Forces I: Macroscopic quantum electrodynamics and ground-state Casimir, Casimir–Polder and van der Waals forces*, vol. 247. Springer, 2013.

[303] S. Hughes, S. Franke, C. Gustin, M. Kamandar Dezfouli, A. Knorr, and M. Richter, "Theory and limits of on-demand single-photon sources using plasmonic resonators: a quantized quasinormal mode approach," *ACS Photonics*, vol. 6, no. 8, pp. 2168–2180, 2019.

[304] S. Franke, M. Richter, J. Ren, A. Knorr, and S. Hughes, "Quantized quasinormal-mode description of nonlinear cavity-qed effects from coupled resonators with a fano-like resonance," *Physical Review Research*, vol. 2, no. 3, p. 033456, 2020.

[305] L. Novotny and B. Hecht, *Principles of nano-optics*. Cambridge university press, 2012.

[306] S. Franke, S. Hughes, M. K. Dezfouli, P. T. Kristensen, K. Busch, A. Knorr, and M. Richter, "Quantization of quasinormal modes for open cavities and plasmonic cavity quantum electrodynamics," *Physical review letters*, vol. 122, no. 21, p. 213901, 2019.

[307] A. Maradudin and D. Mills, "Scattering and absorption of electromagnetic radiation by a semi-infinite medium in the presence of surface roughness," *Physical Review B*, vol. 11, no. 4, p. 1392, 1975.

[308] A. Knorr, F. Steininger, B. Hanewinkel, S. Kuckenburg, P. Thomas, and S. Koch, "Theory of ultrafast spatio-temporal dynamics in semiconductor quantum wells: Electronic wavepackets and near-field optics," *physica status solidi (b)*, vol. 206, no. 1, pp. 139–151, 1998.

[309] J. Baumann, Y. Kayser, and B. Kanngießer, "Grazing emission x-ray fluorescence: Novel concepts and applications for nano-analytics," *physica status solidi (b)*, vol. 258, no. 3, p. 2000471, 2021.

[310] B. Henderson and G. F. Imbusch, *Optical spectroscopy of inorganic solids*, vol. 44. Oxford University Press, 2006.

[311] S. Franke, J. Ren, M. Richter, A. Knorr, and S. Hughes, "Fermi's golden rule for spontaneous emission in absorptive and amplifying media," *Physical Review Letters*, vol. 127, no. 1, p. 013602, 2021.

[312] H. Kuzmany, *Solid-state spectroscopy: an introduction.* Springer Science & Business Media, 2009.

[313] L. C. Feldman and J. W. Mayer, "Fundamentals of surface and thin film analysis," *North Holland, Elsevier Science Publishers, P. O. Box 211, 1000 AE Amsterdam, The Netherlands, 1986.*, 1986.

[314] G. Dresselhaus, M. S. Dresselhaus, and R. Saito, *Physical properties of carbon nanotubes.* World scientific, 1998.

[315] T. Susi, D. J. Mowbray, M. P. Ljungberg, and P. Ayala, "Calculation of the graphene c 1 s core level binding energy," *Physical Review B*, vol. 91, no. 8, p. 081401, 2015.

[316] Y. Harada, T. Tokushima, Y. Takata, T. Takeuchi, Y. Kitajima, S. Tanaka, Y. Kayanuma, and S. Shin, "Dynamical symmetry breaking under core excitation in graphite: Polarization correlation in soft x-ray recombination emission," *Physical review letters*, vol. 93, no. 1, p. 017401, 2004.

[317] M. Mucke, V. Zhaunerchyk, L. Frasinski, R. J. Squibb, M. Siano, J. H. Eland, P. Linusson, P. Salén, P. Vd Meulen, R. Thomas, *et al.*, "Covariance mapping of two-photon double core hole states in c2h2 and c2h6 produced by an x-ray free electron laser," *New Journal of Physics*, vol. 17, no. 7, p. 073002, 2015.

[318] R. Rosenberg, P. Love, and V. Rehn, "Polarization-dependent c (k) near-edge x-ray-absorption fine structure of graphite," *Physical Review B*, vol. 33, no. 6, p. 4034, 1986.

[319] B. Buades, D. Moonshiram, T. P. Sidiropoulos, I. León, P. Schmidt, I. Pi, N. Di Palo, S. L. Cousin, A. Picón, F. Koppens, *et al.*, "Dispersive soft x-ray absorption fine-structure spectroscopy in graphite with an attosecond pulse," *Optica*, vol. 5, no. 5, pp. 502–506, 2018.

[320] D. Pacilé, M. Papagno, A. F. Rodríguez, M. Grioni, L. Papagno, Ç. Girit, J. Meyer, G. Begtrup, and A. Zettl, "Near-edge x-ray absorption fine-structure investigation of graphene," *Physical review letters*, vol. 101, no. 6, p. 066806, 2008.

[321] M. Papagno, A. F. Rodríguez, Ç. Girit, J. Meyer, A. Zettl, and D. Pacilé, "Polarization-dependent ck near-edge x-ray absorption fine-structure of graphene," *Chemical Physics Letters*, vol. 475, no. 4-6, pp. 269–271, 2009.

[322] R. Willis, B. Fitton, and G. Painter, "Secondary-electron emission spectroscopy and the observation of high-energy excited states in graphite: Theory and experiment," *Physical Review B*, vol. 9, no. 4, p. 1926, 1974.

[323] J. Schiessling, L. Kjeldgaard, F. Rohmund, L. Falk, E. Campbell, J. Nordgren, and P. A. Brühwiler, "Synchrotron radiation study of the electronic structure of multiwalled carbon nanotubes," *Journal of Physics: Condensed Matter*, vol. 15, no. 38, p. 6563, 2003.

[324] T. Hemraj-Benny, S. Banerjee, S. Sambasivan, M. Balasubramanian, D. A. Fischer, G. Eres, A. A. Puretzky, D. B. Geohegan, D. H. Lowndes, W. Han, *et al.*, "Near-edge x-ray absorption fine structure spectroscopy as a tool for investigating nanomaterials," *small*, vol. 2, no. 1, pp. 26–35, 2006.

[325] W. C. Chew, "Vector potential electromagnetics with generalized gauge for inhomogeneous media: Formulation," *Progress In Electromagnetics Research*, vol. 149, pp. 69–84, 2014.

[326] C. Ashley and S. Doniach, "Theory of extended x-ray absorption edge fine structure (exafs) in crystalline solids," *Physical Review B*, vol. 11, no. 4, p. 1279, 1975.

[327] P. Lee and J. Pendry, "Theory of the extended x-ray absorption fine structure," *Physical Review B*, vol. 11, no. 8, p. 2795, 1975.

[328] A. Filipponi, A. Di Cicco, and C. R. Natoli, "X-ray-absorption spectroscopy and n-body distribution functions in condensed matter. i. theory," *Physical Review B*, vol. 52, no. 21, p. 15122, 1995.

[329] G. Ertl, H. Knözinger, J. Weitkamp, *et al.*, *Handbook of heterogeneous catalysis*, vol. 2. VCH Weinheim, 1997.

[330] J. A. Van Bokhoven and C. Lamberti, *X-ray absorption and X-ray emission spectroscopy: theory and applications*, vol. 1. John Wiley & Sons, 2016.

[331] A. Britz, B. Abraham, E. Biasin, T. B. van Driel, A. Gallo, A. T. Garcia-Esparza, J. Glownia, A. Loukianov, S. Nelson, M. Reinhard, *et al.*, "Resolving structures of transition metal complex reaction intermediates with femtosecond exafs," *Physical Chemistry Chemical Physics*, vol. 22, no. 5, pp. 2660–2666, 2020.

[332] B. Ravel and M. Newville, "Athena, artemis, hephaestus: data analysis for x-ray absorption spectroscopy using ifeffit," *Journal of synchrotron radiation*, vol. 12, no. 4, pp. 537–541, 2005.

[333] R. Kundu, "Tight-binding parameters for graphene," *Modern Physics Letters B*, vol. 25, no. 03, pp. 163–173, 2011.

[334] V.-T. Tran, J. Saint-Martin, P. Dollfus, and S. Volz, "Third nearest neighbor parameterized tight binding model for graphene nano-ribbons," *AIP Advances*, vol. 7, no. 7, p. 075212, 2017.

[335] M. Kördel, A. Dehlinger, C. Seim, U. Vogt, E. Fogelqvist, J. A. Sellberg, H. Stiel, and H. M. Hertz, "Laboratory water-window x-ray microscopy," *Optica*, vol. 7, no. 6, pp. 658–674, 2020.

[336] A. Kumar and P. Ahluwalia, "Tunable dielectric response of transition metals dichalco-genides mx2 (m= mo, w; x= s, se, te): Effect of quantum confinement," *Physica B: Condensed Matter*, vol. 407, no. 24, pp. 4627–4634, 2012.

[337] B. Gharekhanlou and S. Khorasani, "An overview of tight-binding method for two-dimensional carbon structures," *Graphene Prop. Synth. Appl*, pp. 1–37, 2011.

Danksagung

Bedanken möchte ich mich zu aller erst bei Prof. Andreas Knorr, der mir diese Arbeit ermöglicht hat. Während dieser Zeit brachte er viele verschiedene Themen und Vorschläge ein und half mit viel Engagement, fachlichen Diskussionen und stets ruhiger Art bei der Umsetzung. Dankbar bin ich auch für die viele Unterstützung, Förderung und entgegengebrachte Vertrauen seit der Bachelorarbeit.

Mein Dank geht auch an Prof. Torsten Meier für die Begutachtung dieser Arbeit und Prof. Birgit Kanngießer für das Übernehmen des Vorsitzes des Promotionsausschusses.

Ein besonderer Dank gilt Dr. Malte Selig für viele schöne Jahre, eine spaßige Zeit während einer langen gemeinsamen Büroära und unendliche Unterstützung was Physik, Numerik und alles darum herum angeht. Auch Dr. Florian Katsch möchte ich in dieser Hinsicht danken, der mir in vielen fachlichen Fragen eine große Hilfe und willkommener Debattierpartner während der Erkundung der interessanten Welt der Exzitonphysik war.

Neben Florian, gilt mein Dank auch Dr. Sebastian Franke und Dr. Oliver Kästle für eine unvergessliche Zeit, viele physikalische Gespräche und zahlreiche Kaffeepausen.

Bedanken möchte ich mich auch bei Dr. Shuo Dong und Prof. Ralph Ernstorfer für die interessante und fruchtbare Zusammenarbeit zwischen Experiment und Theorie.

Meinen herzlichen Dank möchte ich weiterhin Lara Greten, Sebastian und Robert Salzwedel aussprechen. Ihr aufmerksames Lesen der Arbeit mit vielen kritische Anmerkungen haben der Arbeit zu ihrer finalen Form verholfen.

Nicht zu vergessen sind Manuel Katzer und Kisa Barkemeyer, die als Mitglieder der AG zu einem sehr schönen Arbeitsklima beigetragen haben, in welchem man gerne den Tag verbrachte.

Zuletzt danke ich von ganzem Herzen meinen Eltern und Geschwistern, die mich auf meinem Weg bekräftigt und unermüdliche unterstützt haben.